สัญญาเลขที่ RSA5980026

รายงานวิจัยฉบับสมบูรณ์

โครงการการออกแบบและการสังเคราะห์โครงข่ายโลหะแลนทาไนด์-อินทรีย์ โมเลกุลชนิดใหม่เพื่อการประยุกต์ใช้ในการกักเก็บคาร์บอนไดออกไซด์

รองศาสตราจารย์ ดร. อภินภัส รุจิวัตร์

ภาควิชาเคมี คณะวิทยาศาสตร์

มหาวิทยาลัยเชียงใหม่

สนับสนุนโดยสำนักงานกองทุนสนับสนุนการวิจัย

(ความเห็นในรายงานนี้เป็นของผู้วิจัย สกว. ไม่จำเป็นต้องเห็นด้วยเสมอไป)

ACKNOWLEDGEMENTS

This report has been prepared and submitted as part of the fulfillment to the grant supported by the Thailand Research Fund, grant number RSA5980026 entitled "*Design and synthesis of new lanthanide metal-organic frameworks for carbon dioxide capture applications*". This research project led to four high impact Q1 (ISI) and one Q2 (ISI) international publications, as well as the established knowledge on gas sorption and ratiometric photoluminescent sensing properties of the lanthanide benzene dicarboxylate frameworks which consequently lead to an extension to a new project with practical implementation.

Here, I would like to declare sincere gratitude to the Thailand Research Fund and Chiang Mai University for the financial support and therefore opportunity to conduct research in this field which is extremely rare in Thailand and not in the main stream of the national research and technology scheme. I would also like to thank the members of the Materials Research Laboratory (or previously known as Inorganic Materials Research), Department of Chemistry, Faculty of Science, Chiang Mai University, for the dedication and determination so that this project has become a success.

(Apinpus Rujiwatra)

March 27, 2019

TABLE OF CONTENT

ABSTRACT

Massive release of greenhouse carbon dioxide from anthropogenic activities has imposed a grave threat to our global warming and environments, leading to an earnest demand for novel technologies to mitigate carbon dioxide emission including the capture and sequestration. Whilst the sequestration technologies have been well developed, the capture technologies require a lot more research works as none of the existing technologies fulfills the target performance criteria. By virtue of exceptionally high active surface area, remarkably large void volume, structural and chemical tunability and potential scalability to industrial scale, porous coordination polymers and metal organic frameworks have surfaced with a great new hope for unprecedented carbon dioxide capture performance. In order to achieve the target performance criteria, high adsorption capacity and selectivity are required. Several strategies have been proposed including the installing of desired functionalities on the organic linkers, the generation of coordinative unsaturated or open metal sites to the frameworks and the introduction of framework flexibility without disrupting framework hydrothermal stability.

Here, new coordination polymers/metal organic frameworks have been designed and synthesized by putting two major strategies into practice, including the generation of coordinative unsaturated or open metal sites using lanthanide nodes and the introduction of framework flexibility through the use of mixed rigid and flexible dicarboxylates. Through the attempts to synthesize the porous coordination polymers for carbon dioxide capture application, the recently emerging ratiometric-photoluminescent properties of the yielded coordination polymers has been revealed leading to an extension of the project to include the ratiometric photoluminescent temperature sensing. The inherent multifunctional nature of lanthanide coordination polymers/metal organic frameworks has therefore been acknowledged.

Through the employment of benzene-1,4-dicarboxylate (BDC^{2-}), 2-nitro-benzene-1,4-dicarboxylate (NO_2-BDC^{2-}), phthalic acid (H_2phth), adipic acid (H_2ad) and pyridine-2,6-

dicarboxylic acid (H_2pdc),* eleven series of lanthanide coordination polymers have been synthesized, including

- $[La_2(NO_2\text{-}BDC)_3(H_2O)_4]$,
- $[Ln(L)_{0.5}(NO_2\text{-}BDC)(H_2O)]\cdot 3H_2O$ (Ln=Eu, Tb, Dy, Ho; L=BDC^{2-}, $BDC^{2-}/NO_2\text{-}BDC^{2-}$),
- $[Tm(NO_2\text{-}BDC)_{1.5}(H_2O)]\cdot H_2O$,
- $[Ln_2(BDC)_3(DMF)_2(H_2O)_2]_n$ (Ln = Gd, Eu, Tb),
- $[Ln_xGd_{2-x}(BDC)_3(DMF)_2(H_2O)_2]_n$ (Ln = Eu, Tb),
- $[Ln(pdc)(H_2O)_4]_3\cdot 3Cl$ (Ln = Pr, Nd, Sm, Eu, Gd),
- $[Ln(pdc)(Hpdc)(H_2O)_2]\cdot 3H_2O$ (Ln = Pr, Nd, Sm),
- $[Ln(pdc)(H_2O)_4]_3\cdot 3Cl$ (Ln = Sm, Eu),
- $[Nd_2(ad)(phth)_2(H_2O)_4]$,
- $[Ln(ad)_{0.5}(phth)(H_2O)_2]$ (Ln = Eu, Gd, Tb, Dy, Er, Tm, Eu/Tb), and
- $[Ln(bdc)_{0.5}(phth)(H_2O)_2]$ (Ln = Eu, Tb, Ho, Er, Tm, Gd, Eu/Tb).

Among these complexes, $[Ln(L)_{0.5}(NO_2\text{-}BDC)(H_2O)]\cdot 3H_2O$ (Ln=Eu, Tb, Dy, Ho; L=BDC^{2-}, $BDC^{2-}/NO_2\text{-}BDC^{2-}$) are microporous in nature and show excellent selectivity toward carbon dioxide through the open metal site mechanism. The other dense framework complexes exhibit outstanding ratiometric photoluminescent temperature sensing performance.

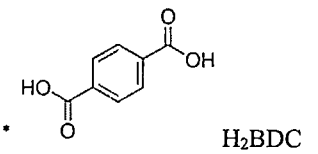

H_2BDC

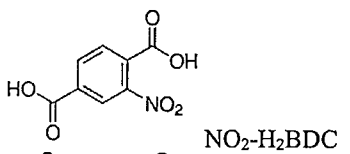

$NO_2\text{-}H_2BDC$

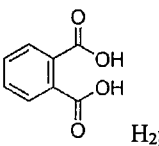

H_2phth

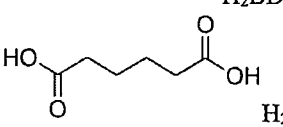

H_2ad

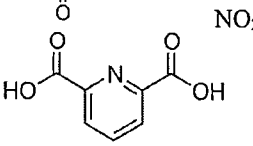

H_2pydc

EXECUTIVE SUMMARY

Project Title: Design and synthesis of new lanthanide metal-organic frameworks for carbon dioxide capture applications

Area of Study: Solid state chemistry/Materials chemistry; Chemical crystallography Coordination chemistry

Keywords: Metal-organic framework; Coordination polymer; Lanthanide Dicarboxylate; Carbon dioxide capture; Photoluminescence

Project Budget: 1.4 MB

Project Duration: 16 June 2016 – 15 March 2019

Project Rational & Significance:

Global warming is one of the major vivid threats encountering human civilization nowadays.[†,‡] The burning of the fossil fuel and therefore the emission of the greenhouse gases especially carbon dioxide has been alleged to be the primary culprits for the rising of the global temperature, earnestly leading to a demand for technologies to control and/or reduce the atmospheric emission of carbon dioxide.[§] The capture and sequestration of the gas have accordingly been intensively investigated during the last two decades.[3,**] Whist the sequestration technologies have been well developed, the capture technologies require a lot more research works as none of the existing technologies fulfills the target performance criteria: (*i*) large capture capacity (*ii*) high selectivity (*iii*) optimal affinity (*iv*) high stability under capture and regeneration conditions.[††] The dominating capture technologies to date are based on the use of aqueous alkanolamine absorbents, of which the studies revealed several drawbacks: (*i*) instability of the absorbents toward heating and water vapor (*ii*) corrosive toward containing vessels (*iii*) restricted absorbent concentration per use and therefore the restriction in capture performance (*iv*) large regeneration energy penalty and therefore costly regeneration process.[‡‡] The drawbacks of aqueous alkanolamine absorbents have therefore

[†]J.D. Figueroa, T. Fout, S. Plasyski, H. McIvried, R.D. Srivastava, *Inter. J. Greenh. Gas Control* **2** (2008) 9-20.
[‡]R. Sabouni,, H. Kazemian, S. Rohani, *Environ. Sci. Pollut. Res.* **21** (2014) 5427.
[§]A.B. Rao, E.S. Rubin, *Environ. Sci. Tehnol.* **36** (2002) 4467-4475.
[**]M.T. Ho, G.W. Allinson, D.E. Wiley, *Ind. Eng. Chem. Res.* **47**(14) (2008) 4883-4890.
[††]E.F. da Silva, H.F. Svendsen, *Inter. J. Greenh. Gas Control* **1** (2007) 151-157.
[‡‡]Y. Liu, Z.U. Wang, H.-C. Zhou, *Greenhouse Sci. Technol.* **2** (2012) 239-259.

drawn attention toward the research on adsorbents as the alternative technologies. Most of the early studies have been focused on the conventional adsorbents like zeolites and activated carbon, from which the shortcomings of these conventional adsorbents, *i.e.* low capture capacities and difficulty in regeneration processing, have been revealed.[§§,***]

The milestone work by A.R. Milward and O.M. Yaghi on the unprecedentedly high carbon dioxide capture capacities of the metal organic framework materials (MOFs), this new class of materials have attracted great attention worldwide.[†††] MOFs are coordination complexes possessing an infinitive coordination frameworks and permanent porosity. They can be regarded as the sub-class of the coordination polymers (CPs). The major reasons presenting MOFs as the rising candidate for new carbon dioxide capture materials are; (*i*) the unprecedentedly high active surface area and remarkably large void volume, (*ii*) their structural and chemical tunability (*iii*) potential scalability to industrial scale.[‡‡‡] One particular advantage on the use of MOFs is reportedly to be the greatly reduced generation energy penalty compared to the aqueous alkanolamine absorbents.[10] In the context of carbon dioxide capture, however, two crucial parameters demanding earnest attentions and further investigation before MOFs can be placed in the real-world carbon dioxide capture processes includes are the design and synthesis of the structures with improved (*i*) adsorption capacities at two different pressure ranges, *i.e.* high and near ambient, (*ii*) selectivity toward carbon dioxide (*iii*) framework stability after the removal of occluded solvents.[10,§§§] In approaching such goals, several strategies have been proposed: (*i*) installing desired functionalities, *e.g.* amines, electron donating groups, polarizing groups and hydrogen bonding donating motifs, on the organic linkers (*ii*) generating coordinative unsaturated or open metal sites to the frameworks (iii) increasing framework flexibility without disrupting framework hydrothermal stability (iv) including extraframework metal nanoparticles or cations.[8,10,11,****] Despite the acknowledgement of various strategies or principles, none of the current MOFs or CPs has reached such requirement yet.

Research Objectives

The primary objective of the research is to design and synthesize new lanthanide coordination polymers/metal organic frameworks for use in carbon dioxide capture application. To achieve the desired objective, two strategies have been adopted in the design and synthesis of new lanthanide CPs and lanthanide MOFs, *i.e.* (i) the generation of

---

[§§]M. Sevilla, A.B. Fuertes, *J. Colloid Interface Sci.* **366**(1) (2012) 147-154.
[***]S.R. Batten, N.R. Champness, X.-M. Chen, J. Garcia-Martinez, S. Kitagawa, L. Ohrstrom, M. O'Keeffe, M.P. Suh, J. Reedijk, *Pure Appl. Chem.* **85**(8) (2013) 1715-1724.
[†††]J.L.C. Rowsell, O.M. Yaghi, *Micropor. Mesopor. Mater.* **73** (2004) 3-14.
[‡‡‡]S. Choi, J.H. Drese, C.W. Jones, *ChemSusChem.* **2**(9) (2009) 796-854.
[§§§]H. Li, M. Eddaoudi, M. O'Keeffe, O.M. Yaghi, *Nature* **402** (1999) 276-279.
[****]H. Li, M. Eddaoudi, T.L. Groy, O.M. Yaghi, *J. Am. Chem. Soc.* **120**(33) (1998) 8571-8572.

coordinative unsaturated or open metal sites by using lanthanide as nodes and (ii) the introduction of framework flexibility without disrupting their hydrothermal stability by using mixed rigid/flexible dicarboxylate linkers.

Research Scope & Methodology

Target applications	▪ Carbon dioxide gas capture applications ▪ Ratiometric photoluminescent sensing
Designed nodes	▪ Trivalent lanthanide metal ions (Ln^{III})
Designed linkers	Mixed flexible and rigid dicarboxylate ligands:
Methodologies	▪ Generation of open metal sites during the work up process in prior to the carbon dioxide gas adsorption experiments ▪ Modulation of photoluminescent emission through variation in antenna and emitting centers

Research Outputs:

No.	Article Title	Journal Matrix	
		JIF (Q)	Citation
1	T. Chuasaard, K. Panyarat, P. Rodlamul, K. Chainok, S. Yimklan, A. Rujiwatra*, Structural Variation and Preference in Lanthanide-pyridine-2,6-dicarboxylate Coordination Polymers, *Crystal Growth & Design* 17 (2017) 1045-1054.	3.972 (Q1)	5
2	K. Panyarat, S. Surinwong, T.J. Prior, T. Konno, A. Rujiwatra*, Crystal Structure and Gas Adsorption Behavior of New Lanthanide-benzene-1,4-dicarboxylate Frameworks, *Microporous Mesoporous Materials* 251 (2017) 155-164.	3.649 (Q1)	5
3	T. Chuasaard, A. Ngamjarurojana, S. Surinwong, T. Konno, S. Bureekaew, A. Rujiwatra*, Lanthanide Coordination Polymers of Mixed Phthalate/Adipate for Ratiometric Temperature Sensing in the Upper-Intermediate Temperature Range, *Inorganic Chemistry* 57 (2018) 2620-2630.	4.700 (Q1)	9
4	K. Panyarat, A. Ngamjarurojana, A. Rujiwatra*, Colorimetric Analysis: A New Strategy to Improve Ratiometric Temperature Sensing Performance of Lanthanide Benzenedicarboxylates, *Journal of Photochemistry and Photobiology A – Chemistry*, Accepted.	2.891 (Q2)	-
5	T. Chuasaard, A. Ngamjarurojana, T. Konno, A. Rujiwatra*, Influences of Mixed Antennae on Ratiometric Thermometry of Lanthanide Benzenedicarboxylates, *Inorganic Chemistry*, Submitted (as of March 22, 2019).	4.700 (Q1)	-

CHAPTER 1

Lanthanide Metal Organic Frameworks & Carbon Dioxide Capture Application

1.1 Introduction to research problem and its significance

Global warming is one of the major vivid threats encountering human civilization nowadays [1,2]. The burning of the fossil fuel and therefore the emission of the greenhouse gases especially carbon dioxide has been alleged to be the primary culprits for the rising of the global temperature [1-7], earnestly leading to a demand for technologies to control and/or reduce the atmospheric emission of carbon dioxide [8,9]. The capture and sequestration of the gas have accordingly been intensively investigated during the last two decades [8,9]. Whist the sequestration technologies have been well developed, the capture technologies require a lot more research works as none of the existing technologies fulfills the target performance criteria: (*i*) large capture capacity (*ii*) high selectivity (*iii*) optimal affinity (*iv*) high stability under capture and regeneration conditions [5]. The dominating capture technologies to date are based on the use of aqueous alkanolamine absorbents, of which the studies revealed several drawbacks: (*i*) instability of the absorbents toward heating and water vapor (*ii*) corrosive toward containing vessels (*iii*) restricted absorbent concentration per use and therefore the restriction in capture performance (*iv*) large regeneration energy penalty and therefore costly regeneration process [10]. The drawbacks of aqueous alkanolamine absorbents as listed have therefore drawn attention toward the research on adsorbents as the alternative technologies. Most of the early studies have been focused on the conventional adsorbents like zeolites and activated carbon, from which the shortcomings of these conventional adsorbents, *i.e.* low capture capacities and difficulty in regeneration processing, have been revealed [9-12].

The milestone work by A.R. Milward and O.M. Yaghi on the unprecedentedly high carbon dioxide capture capacities of the metal-organic framework materials (MOFs) [13], this new class of materials have attracted great attention worldwide. MOFs are coordination complexes possessing an infinitive coordination frameworks and permanent porosity. They can be regarded as the sub-class of the coordination polymers (CPs). The major reasons presenting MOFs as the rising candidate for new carbon dioxide capture materials are; (*i*) the unprecedentedly high active surface area and remarkably large void volume, (*ii*) their structural and chemical tunability (*iii*) potential scalability to industrial scale [10,14-18]. One particular advantage on the use of MOFs is reportedly to be the greatly reduced generation energy penalty compared to the aqueous alkanolamine

absorbents [10]. In the context of carbon dioxide capture, however, two crucial parameters demanding earnest attentions and further investigation before MOFs can be placed in the real-world carbon dioxide capture processes includes are the design and synthesis of the structures with improved (*i*) adsorption capacities at two different pressure ranges, *i.e.* high and near ambient, (*ii*) selectivity toward carbon dioxide (*iii*) framework stability after the removal of occluded solvents [10,17]. In approaching such goals, several strategies have been proposed: (*i*) installing desired functionalities, *e.g.* amines, electron donating groups, polarizing groups and hydrogen bonding donating motifs, on the organic linkers (*ii*) generating coordinative unsaturated or open metal sites to the frameworks (iii) increasing framework flexibility without disrupting framework hydrothermal stability (iv) including extraframework metal nanoparticles or cations [10,12,17,18].

1.2 Literature survey on carbon capture technology

Current technologies for carbon dioxide capture are primarily directed toward the reduction of carbon dioxide emission from power production at three stages, namely post-combustion, pre-combustion and oxy-combustion, among which post-combustion has the greatest near-term potential [9,11]. The dominating capture technologies for the post-combustion processes to date are based on aqueous alkanolamine absorbents [10,19]. In the process, the amine functional groups will participate in nucleophilic attack on the carbon atom of the carbon dioxide forming C–N bond in the forms of either carbamate or bicarbonate species (Fig. 1.1) [10,19,20]. Due to the nature of the amine and the involvement of the C–N bond formation, several drawbacks need attentions: (*i*) instability of the absorbents toward heating and water vapor (*ii*) corrosive toward containing vessels (*iii*) restricted absorbent concentration per use and therefore the restriction in capture performance (*iv*) large regeneration energy penalty and therefore costly regeneration process [10,21-23].

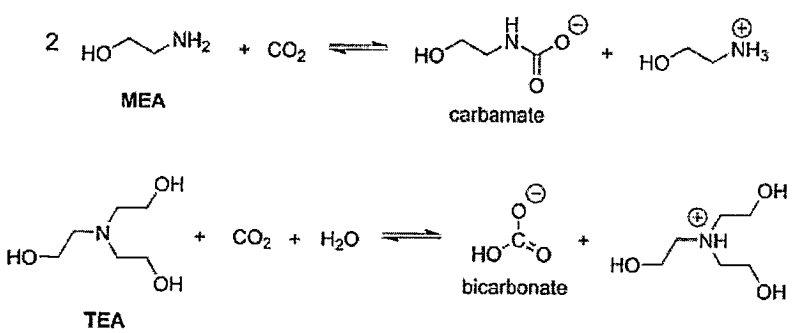

Fig. 1.1 Schematic illustration of the reactions between CO2 with monoethanolamine (MEA) and triethanolamine (TEA) [10]

Despise several pros; the cons of the processes as listed above especially the large regeneration energy penalty and costly regeneration process have brought about the need in finding the other alternative technologies including also the use of adsorbents of which the carbon dioxide gas is captured by physical interactions rather than chemical bonding. Strategic plan for several potential carbon dioxide capture technologies and innovations have been proposed (Fig. 1.2).

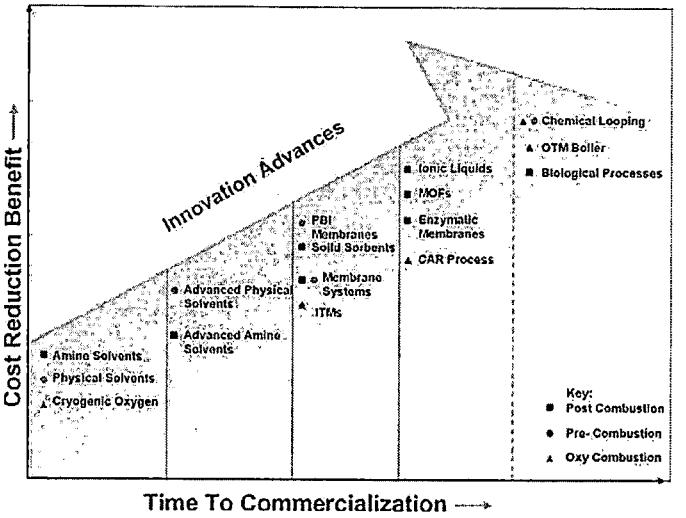

Fig. 1.2 Cost reduction benefits versus time to commercialization for carbon dioxide capture technologies [24]

At the early stage of investigation for carbon dioxide adsorbents, activated carbons, zeolites and zeolite-like materials have been solemnly investigated [10,11,20]. Important criteria have been set for materials to be considered as appropriate carbon dioxide adsorbents [10,19,24,25]: (*i*) high adsorption capacities (≥2-4 mmol·g^{-1}) (*ii*) high selectivity toward carbon dioxide (*iii*) adequate adsorption/desorption kinetics (*iv*) stability during repeated adsorption/desorption cycling (*v*) possessing stable microstructure and morphology under several operating conditions (*vi*) economic production and regeneration process. According to literatures, although some adsorbents exhibited high adsorption capacities, *e.g.* 4.9 mmol·g^{-1} (273 *K*, 0.1 bar) for Na-Y zeolite [26] and 3.2 mmol·g^{-1} (298 *K*, 0.1 bar) for activated carbons [27], these adsorbents always exhibit downside in one way or another.

1.3 Literature survey on porous CPs and MOFs as carbon dioxide capture materials

MOFs, are the coordination networks of one-, two- or three-dimension, built up of metals or metal clusters as nodes and organic ligands as linkers [28]. For materials to be classified as

MOFs, it is recommended that the materials should display strong bonding providing robustness (thermal and chemical stabilities), and comprise of linking units that are available for modification, geometrically well-defined structures and potential to be engineered both structures and properties [30]. MOFs are also known as porous coordination polymers (PCPs) [30,31]. Owing to remarkably high active surface area (up to 5,000 $m^2 \cdot g^{-1}$ [31]), exceptionally large void volume (up to 90% [17]), ability to be structurally and chemically engineered and scalability to industrial scale, MOFs are located at the forefront for several technological applications, *e.g.* gas storage, catalysis, magnetism, drug delivery, molecular separation and sensor [31,32].

In terms of carbon dioxide capture applications, the first report appeared less than two decade ago by H. Li *et al.*, and the material was the microporous $Zn(BDC) \cdot (DMF)(H_2O)$ (BDC = 1,4-benzenedicarboxylate and DMF = N,N′-dimethylformamide) [13]. The following investigation on a series of MOFs by A.R. Milward and O.M. Yaghi seven years later has, however, set a milestone step in the field [33]. Nine compounds as shown in Fig. 1.3 including the square channel MOF2, the open metal site occupied MOF-505 and $Cu_3(BTC)_2$ (BTC = 1,3,5-benzenetricarboxylate), the hexagonally packed cylindrical channel MOF-74, the interpenetrating framework IRMOF-11, the functionalized IRMOF-3 and IRMOF-6, and the extra-highly porous IRMOF-1 and MOF-177 [20]. In this work, the carbon dioxide adsorption capacity of 33.5 $mmol \cdot g^{-1}$, which is far greater than that of any precedent porous materials; 7.4 $mmol \cdot g^{-1}$ at 32 bar for zeolite 13X [34], and 25 $mmol \cdot g^{-1}$ at 35 bar for MAXSORB amorphous carbon [14]. Two more important features of carbon dioixde capture materials have been proposed following this study: (*i*) a periodic structure of the materials for which the sorption and desorption of carbon dioxide is fully reversible (*ii*) a flexibility with which the chemical functionalization and molecular-level fine-tuning can be achieved for optimized capacities [33]. Since the discovery of MOF-177 [33], a huge number of MOFs have been designed, synthesized and characterized for this specific purpose within only the last decade.

According to several reviews [10,11,12,14,18,25], proposed strategies to enhance carbon dioxide adsorption capacities and selectivity can be summarized as follows: (*i*) installing desired functionalities, *e.g.* amines, electron donating groups, polarizing groups and hydrogen bonding donating motifs, on the organic linkers (*ii*) generating coordinative unsaturated or open metal sites to the frameworks (*iii*) increasing framework flexibility without disrupting framework hydrothermal stability (*iv*) including extraframework metal nanoparticles or cations.

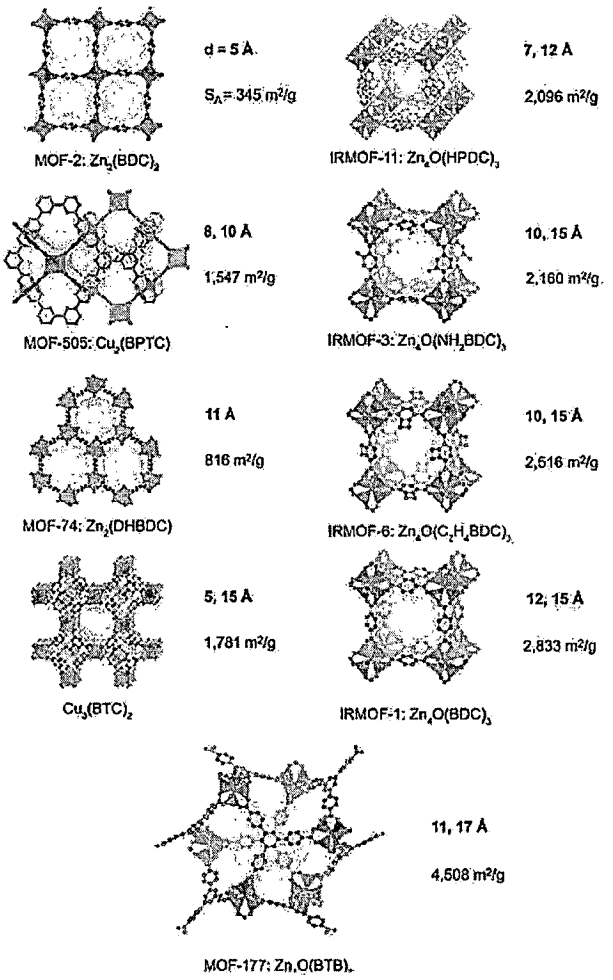

(a)

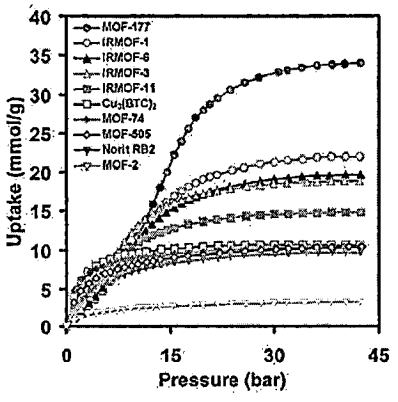

(b)

Fig. 1.3 A series of MOFs and IRMOFs investigated for CO_2 adsorption capacities by A.R. Milward and O.M. Yaghi in 2005 [34], (b) high pressure isotherm measured at 298 *K* of MOF-210 [35]

Based on literatures [10,11,12,14,18,25 and references therein], two observations can be generalized. The metal and metal clusters employed in the fabrication of these MOFs are mostly the first row transition metals with Zn at the lead. Some of the reported MOFs exhibit gravimetric capacity of approximately 70% or higher at high pressures, e.g. $Zn_4O(BTE)_{0.75}(BPDC)$ (MOF-210, Fig. 1.4; 74.2% at 50 bar) and $Zn_4O(BDC)2(H_2O)_3$ (MOF-200; 73.9% at 50 bar) both of which are built up of Zn_4O node and BDC linkers [35], Cu_3(TCEPEB) (Nu-100; 69.8% at 40 bar; TCEPEB = 1,3,5-tris[(1,3-carboxylic acid-5-(4-ethynyl)phenyl))-ethynyl]benzene) [36], and Zn_4O(FMA) (69% at 29 bar; FMA = fumarate) [37]. These MOFs would be potential for post-combustion processes as high pressures are required for such high capacities. Adsorption capacities of the existing MOFs at near-ambient pressures are noticeably not as high as those reported for the high pressure processes. Only few examples exhibit gravimetric capacity close to 30%: $Cu_3(BTC)_2(H_2O)_{1.5}$ (HKUST-1; 27% at 1 bar and 298 *K*) [28], and Mg_2(dobdc) (Mg-MOF-74; 27.5% at 1 bar and 298 *K*; dobdc = 2,5-dioxido-1,4-benzenedicarboxylate) [38]. Note that both the HKUST-1 and Mg-MOF-74 contain the open site metal ions [39,38]. It has been concluded that MOFs possessing a high density of open metal sites tend to adsorb significant amounts of carbon dioxide even at low pressure [38].

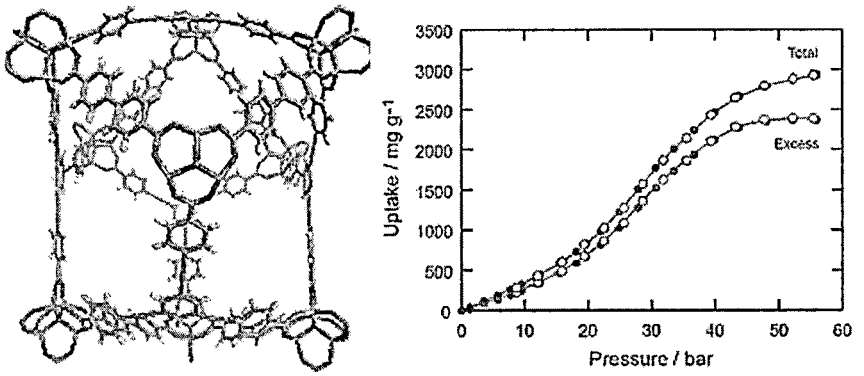

Fig. 1.4 Framework of MOF-210 and its high pressure isotherm measured at 298 *K* [25]

It is also apparent that most of the linkers employed in the fabrication of MOFs aiming at carbon dioxide capture applications are polycarboxylates with the predominance of the dicarboxylates. Some of the dicarboxylate linkers are illustrated in Fig. 1.5, being classified in to rigid and flexible types. Although this is not exhaustively summarized, the predominance of the rigid linkers is apparent. This should be due to the fact that these rigid linkers provide long range ordering as well as stability to the derived MOFs. Functionalization of these linkers will add functionality for specific applications. The use of the flexible linkers in these carbon dioxide

Rigid dicarboxylate ligands

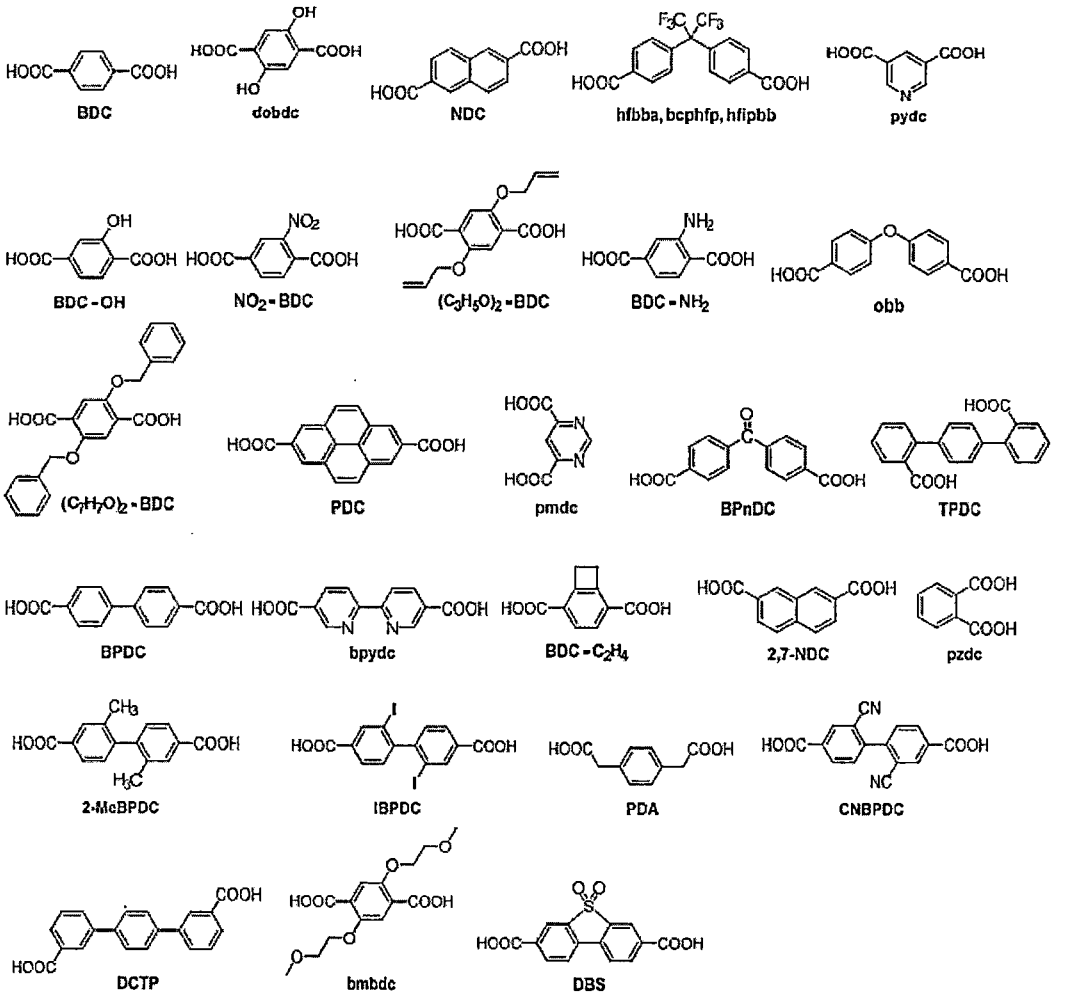

Flexible dicarboxylate ligands

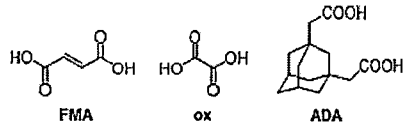

Fig. 1.5 Some dicarboxylate linkers employed in the syntheses of MOFs characterized for carbon dioxide adsorption (Summarized from Refs. 10,11,12,14,18,25 and references therein)

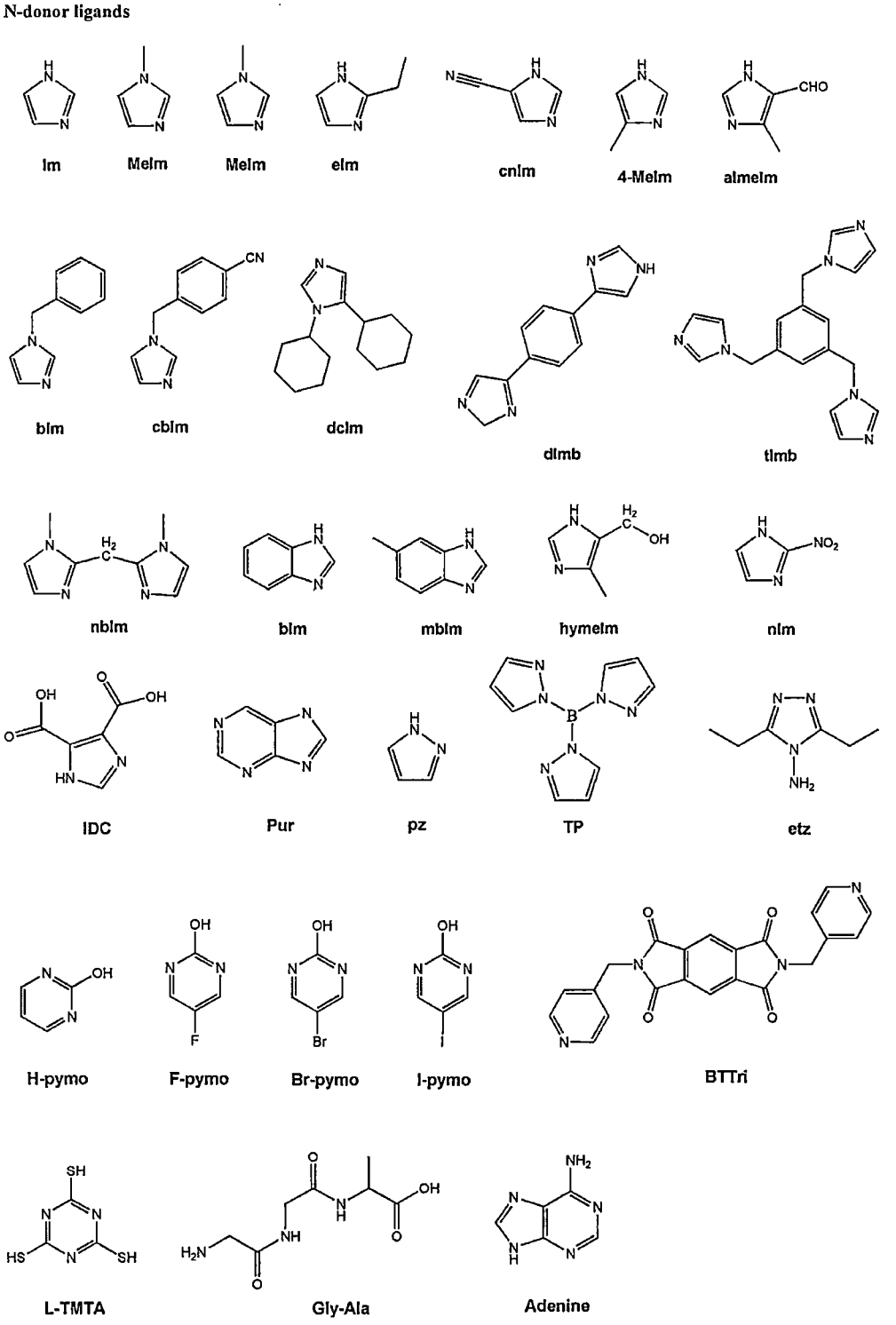

Fig. 1.6 Some N-donor linkers employed in the syntheses of MOFs characterized for CO_2 adsorption (Summarized from Refs. 10,11,12,14,18,25 and references therein)

capturing MOFs is nonetheless surprisingly very few. The other polycarboxylates besides the dicarboxylates include tri-, tetra-, hexa- and octacarboxylates. In addition to the polycarboxylate linkers, the N-donor linkers (Fig. 1.6) have also been used in the derivation of the frameworks; *e.g.*, Co(BDP) (41.3% at 40 bar; BDP = 1,4-benzenedipyrazolate) [40], $H_3[(Cu_4Cl)_3(BTTri)_8]$ (Cu-BTTri; 42.8% at 40 bar; BTTri = 1,3,5-benzenetristriazolate) [40], $Zn(MeIm)_2$ (nZif-8; 35.0% at 30 bar; MeIm = 2-methylimidazole) [41], $Zn(F\text{-}pymo)_2$ (26.0% at 28 bar and 273 *K*; F-pymo = 5-fluoropyrimidin-2-olate) [42], $Zn(Gly\text{-}Ala)_2$ (19.0% at 15 bar and 273 *K*; Gly-Ala = glycylalanine) [43], $H_3[(Cu_4Cl)_3(BTTri)_8]$ (14.3% at 1 bar and 293 K; BTTri = 1,3,5-tri(1H-1,2,3-triazol-4-yl)benzene) [44]. Limitation and the less success in the use of the N-donor ligands may be noted.

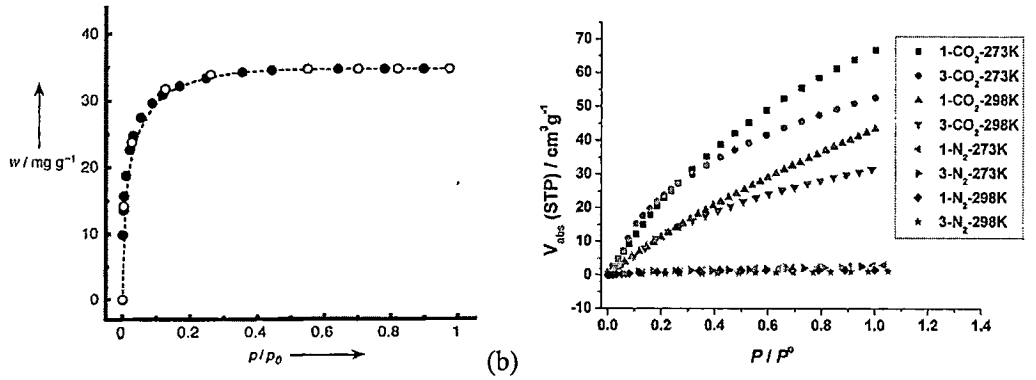

Fig. 1.7 (a) Sorption and desorption isotherms of $Tb(BDC)NO_3$ [49], and (b) $[Ln_2(TPO)_2(HCOO)]\cdot(Me_2NH_2)\cdot(DMF)_4\cdot(H_2O)_6$ (Ln = Y(1) and Eu(3)) [50]

1.4 Literature survey on lanthanide MOFs (LOFs) as carbon dioxide capture materials

Due to the feasibility in adopting large coordination number varying from 3 to 12, the lanthanide metal ions dominated by the trivalent state (Ln^{III}) exhibit diverse coordination geometries and behavior governed mostly by the coordinating ligands [45,46]. Such characteristic of the Ln^{III} makes the design and synthesis of the metal-organic framework to be very unpredictable and challenging; especially in the case where permanent porosity is required [47]. This is particularly the issue as most of the porous frameworks collapse after the removal of the extraframework species located in the framework voids. Compared to the transition metal MOFs, the porous frameworks made up of the Ln^{III} are not yet prevailing and remaining a challenge [47].

The first lanthanide MOF exhibiting permanent porosity even upon solvent removal are the extended frameworks of Tb^{III}; the microporous $Tb_2(BDC)_3$ [48] and $Tb(BDC)NO_3$ [49], both of which are reported to possess accessible metal sites. The $Tb(BDC)NO_3$ is thermally stable up to 320 °C and exhibits zeolite-like sorption behavior toward carbon dioxide (Fig. 1.7) [49]. Since

then, there has not any reports on the exceptional uptake of carbon dioxide by lanthanide MOFs, and reports on the studies of these materials for the carbon dioxide capture applications to date are extremely rare and are listed as follows. Two isostructural microporous $[Ln_2(TPO)_2(HCOO)]\cdot(Me_2NH_2)\cdot(DMF)_4\cdot(H_2O)_6$ (Ln = Y and Eu; H_3TPO = tris-(4-carboxylphenyl)phosphineoxide; DMF = N,N-dimethylformamide) shows preferential adsorption of carbon dioxide over nitrogen (Fig. 1.7), and the carbon dioxide uptakes of 25.58% (Y) and 18.42% (Eu) at 20 bar and 273 *K* [50]. The honeycomb-type channel containing $\{[Tb(FDA)_{1.5}(DMF)]\cdot DMF\}_n$ (H_2FDA = furan-2,5-dicarboxylic acid) framework was reported to show significant selective sorption of carbon dioxide over nitrogen and methane and guest dependent luminescence behavior [51]. The carbon dioxide uptake was reported to be 61 $cm^3\cdot g^{-1}$ measured at 1 bar and 273 *K* [51]. The synergistic effect of the exposed open metal sites and proximal highly localized charge density toward materials with enhanced carbon dioxide sorption energetics was proposed for a series of lanthanide MOF with **fcu** topology, synthesized using linear fluorinated/nonfluorinated, homo/heterofunctional ligands [52]. Two isostructural $[Ln_2(pam)_3(DMF)_2(H_2O)_2]\cdot nDMF$ (Ln = Gd and Dy; H_2pam = 4,4′-methylenebis[3-hydroxy-2-naphthalenecarboxylic acid) were reported last year to show selectivity toward carbon dioxide sorption over other gases (Fig. 1.8) and to exhibit high methanol vapor uptake [53].

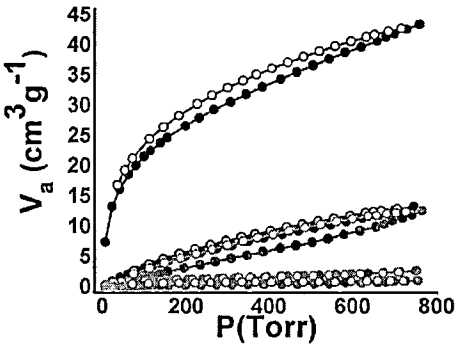

Fig. 1.8 Carbon dioxide and nitrogen adsorption isotherms observed for $[Gd_2(pam)_3(DMF)_2(H_2O)_2]\cdot$ nDMF (blue, 195 K; black, 273 K; and red, 298 K for CO_2 and magenta 273 K, yellow 298 K for N_2) (closed and open symbols represent adsorption and desorption branches) [53]

Research works relating to carbon dioxide capture by lanthanide MOFs has gain rather an attention this year, reflected *via* the exceptional increase in number of publications in year 2015 [54-56]. The enhancement of carbon dioxide capture capacity and selectivity by framework flexibility and

therefore guest-induced structural transformation (Fig. 1.9) of $[Sm(HL)(DMA)_2]$ (H_4L = 5,5′-(2,3,5,6-tetramethyl-1,4-phenylene)bis(methylene)bis(azanediyl) diisophthalic acid) has illustrated the striking feature for further framework design [54].

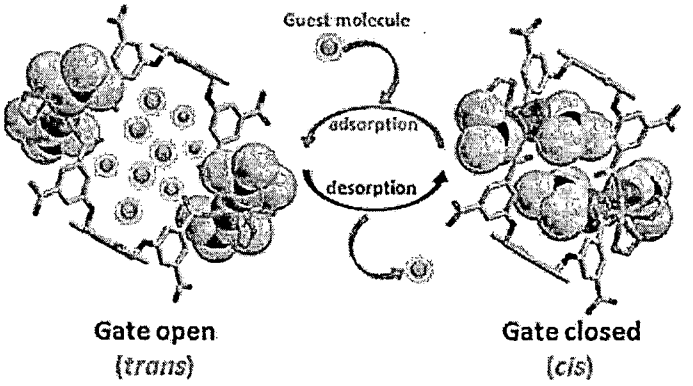

Fig. 1.9 Depiction of carbon dioixde induced structural transformation in $[Sm(HL)(DMA)_2]$ framework [54]

1.5 Research project objective

The primary objective of the research is to design and synthesize new lanthanide coordination polymers/metal organic frameworks for use in carbon dioxide capture application. To achieve the desired objective, two strategies have been adopted in the design and synthesis of new lanthanide CPs and lanthanide MOFs, *i.e.* (i) the generation of coordinative unsaturated or open metal sites by using lanthanide as nodes and (ii) the introduction of framework flexibility without disrupting their hydrothermal stability by using mixed rigid/flexible dicarboxylate linkers.

1.6 Structure of the project report

Aiming at carbon dioxide capture application based on lanthanides and dicarboxylate linkers, several series of lanthanide CPs of both porous (MOFs) and dense frameworks have been synthesized. Not only the carbon dioxide capturing property, temperature dependent photoluminescence of the yielded frameworks has become significantly intriguing leading to an extension of the project to include the ratiometric photoluminescent temperature sensing.

The content of this report is classified according to the chemical and physical properties of the yielded lanthanide CPs and/or lanthanide MOFs.

Chapter 2

- $[La_2(NO_2\text{-}BDC)_3(H_2O)_4]$
- $[Ln(L)_{0.5}(NO_2\text{-}BDC)(H_2O)]\cdot 3H_2O$, Ln=Eu, Tb, Dy, Ho; L=$BDC^{2-}$, $BDC^{2-}/NO_2\text{-}BDC^{2-}$
- $[Tm(NO_2\text{-}BDC)_{1.5}(H_2O)]\cdot H_2O$

Chapter 3

- $[Ln_2(BDC)_3(DMF)_2(H_2O)_2]_n$, Ln = Gd, Eu, Tb; H_2BDC = benzene-1,4-dicarboxylic acid; DMF = dimethylformamide
- $[Ln_xGd_{2-x}(BDC)_3(DMF)_2(H_2O)_2]_n$ Ln = Eu, Tb

Chapter 4

- $[Ln(pdc)(H_2O)_4]_3\cdot 3Cl$, Ln = Pr, Nd, Sm, Eu, Gd,
- $[Ln(pdc)(Hpdc)(H_2O)_2]\cdot 3H_2O$, Ln = Pr, Nd, Sm
- $[Ln(pdc)(H_2O)_4]_3\cdot 3Cl$, Ln = Sm, Eu

Chapter 5

- $[Nd_2(ad)(phth)_2(H_2O)_4]$
- $[Ln(ad)_{0.5}(phth)(H_2O)_2]$, Ln = Eu, Gd, Tb, Dy, Er, Tm, Eu/Tb

Chapter 6

- $[Ln(bdc)_{0.5}(phth)(H_2O)_2]$, Ln = Eu, Tb, Ho, Er, Tm, Gd, Eu/Tb

It should also note that numbering of the reported complexes are restricted for each chapter since there are too many new complexes. The consecutive numbering of all complexes is believed to cause confusion for the readers.

REFERENCES

[1] C. McGlade, P. Ekins, *Nature* **517** (7533) (2015) 187-190.

[2] J. Hansen, R. Ruedy, M. Sato, K. Lo, *Rev. Geophys.* **48**(4) (2010) RG4004.

[3] S. Khan (ed.), *Fossil Fuel and the Environment*, InTeO, 2012.

[4] A. Yamasaki, *J. Chem. Eng. Jpn.* **36**(4) (2003) 361e75.

[5] S.A. Rackley (ed.), *Carbon Capture and Storage*, Butterworth-heinemann/Elsevier, Burington, 2010.

[6] I. Dincer, A. Hepbasli, A. Midilli, T.H. Karakoc (eds.), *Global Warming*, Springer Science, LLC, 2010.

[7] International Energy Agency (IEA), *CO_2 Emission from Fuel Combustion Highlights*, 2014 ed., OECD/IEA, 2014.

[8] H. Yang, Z. Xu, M. Fan, R. Gupta, R.B. Slimane, A.E. Bland, I. Wright, *J. Environ. Sci.* **20** (2008) 14-27.

[9] J.D. Figueroa, T. Fout, S. Plasynski, H. McIlvried, R.D. Srivastava, *Inter. J. Greenh. Gas Control* **2** (2008) 9-20.

[10] K. Sumida, D.L. Rogow, J.A. Mason, T.M. McDonald, E.D. Bloch, Z.R. Herm, T.-H. Bae, J. R. Long, *Chem. Rev.* **112** (2012) 724-781.

[11] R. Sabouni, H. Kazemine, S. Rohani, *Environ. Sci. Pollut. Res.* **21** (2014) 5427-5449.

[12] J. Liu, P.K. Thallapally, B.P. McGrail, D.R. Brown, J. Liu, *Chem. Soc. Rev.* **41** (2012) 2308-2322.

[13] A.R. Milward, O.M. Yaghi, *J. Am. Chem. Soc.* **127** (2005) 17998-17999.

[14] S. Ma, H.-C. Zhou, *Chem. Commun.* **46** (2010) 44-53.

[15] M.J. Rosseinsky, *Micropor. Mesopor. Mater.* **73** (2004) 15-30.

[16] S.R. Batten, N.R. Champness, X.-M. Chen, J. Garcia-Martinez, S. Kitagawa, L. Ohrstrom, M. O'Keeffe, M.P. Suh, J. Reedijk, *Cryst. Eng. Comm.* **14** (2012) 3001-3004.

[17] D.J. Collins, H.-C. Zhou, *J. Mater. Chem.* **17** (2007) 3154-3156.

[18] F. Rouquerol, J. Rouquerol, K. Sing (eds.), *Adsorption by Powders and Porous Solids: Principles, Methodology and Applications*, Academic Press, Cornwall, 1999.

[19] M. Songolzadeh , M.T. Ravanchi , M. Soleimani, *WASET* **6**(10) (2012) 213-220.

[20] E.F. da Silva, H.F. Svendsen, *Inter. J. Greenh. Gas Control* **1** (2007) 151-157.

[21] G.F. Versteeg, L.A.J. Van Dijck, W.P.M. Van Swaaij, *Chem. Eng. Comm.* **144**(1) (1996) 113-158.

[22] G. Sartori, D.W. Savage, *Ind. Eng. Chem. Fund.* **22**(2) (1983) 239-249.

[23] A.B. Rao, E.S. Rubin, *Environ. Sci. Tehnol.* **36** (2002) 4467-4475.

[24] M.T. Ho, G.W. Allinson, D.E. Wiley, *Ind. Eng. Chem. Res.* **47**(14) (2008) 4883-4890.

[25] Y. Liu, Z.U. Wang, H.-C. Zhou, *Greenhouse Sci. Technol.* **2** (2012) 239-259.

[26] S. Choi, J.H. Drese, C.W. Jones, *ChemSusChem.* **2**(9) (2009) 796-854.

[27] M. Sevilla, A.B. Fuertes, *J. Colloid Interface Sci.* **366**(1) (2012) 147-154.

[28] J.L.C. Rowsell, O.M. Yaghi, *Micropor. Mesopor. Mater.* **73** (2004) 3-14.

[29] S. Kitagawa, R. Kitaura, S. Noro, *Angew. Chem. Ind. Ed.* **43** (2004) 2334-2375.

[30] R.J. Kuppler, D.J. Timmons, Q.-R. Fang, J.-R. Li, T.A. Makal, M.D. Young, D. Yuan, D. Zhao, W. Zhuang, H.-C. Zhou, *Coord. Chem. Rev.* **253** (2009) 3042-3066.

[31] M. Eddaoudi, D.B. Moler, H. Li, B. Chen, T.M. Reineke, M. O'Keeffe, O.M. Yaghi, *Acc. Chem. Res.* **34**(4) (2001) 319-330.

[32] H. Li, M. Eddaoudi, T.L. Groy, O.M. Yaghi, *J. Am. Chem. Soc.* **120**(33) (1998) 8571-8572.

[33] S. Cavenati, C.A. Grande, A.E. Rodrigues, *J. Chem. Eng. Data* **49** (2004) 1095-1101.

[34] S. Himeno, T. Komatsu, S. Fujita, *J. Chem. Eng. Data* 50 (2005) 369-376.

[35] H. Furukawa, N. Ko, Y.B. Go, N. Aratani, S.B. Choi, E. Choi, A.O. Yazaydin, R.Q. Snurr, M. O'Keeffe, O.M. Yaghi, *Science* **329** (2010) 424-428.

[36] O.K. Farha, A.O. Yazaydin, I. Eryazici, C.D. Malliakas, B.G. Nauser, M.G. Kanatzidis, S.T. Nguyen, R.Q. Snurr, J.T. Hupp, *Nat. Chem.* **2**(11) (2010) 944-948.

[37] M. Xue, Y. Liu, R.M. Schaffino, X. Xiang, X. Zhao, G.-S. Zhu, S.-L. Qiu, B. Chen, *Inorg. Chem.* **48**(11) (2009) 4649-4651.

[38] Q.O. Yazaydin, R.Q. Snurr, T.-H. Park, K. Koh, J. Liu, M.D. LeVan, A.I. Benin, P. Jakubczak, M. Lanuza, D.B. Galloway, J.L. Low, R.R. Willis, *J. Am. Chem. Soc.* **131** (2009) 18198-18199.

[39] A.O. Yazaydin, A.I. Benin, S.A. Faheem, P. Jakubczak, J.L. Low, R.R. Willis, R.Q. Snurr, *Chem. Mater.* **21**(8) (2009) 1425-1430.

[40] Z.R. Herm, J.A. Sweisher, B. Smit, R. Krishna, J.R. Long, *J. Am. Chem. Soc.* **133**(15) (2011) 5664-5667.

[41] S.K. Nune, P.K. Thallapally, A. Dohnalkova, C. Wang, J. Liu, G.J. Exahos, *Chem. Commun.* **46** (2010) 4878-4880.

[42] S. Galli, N. Masciocchi, G. Tagliabue, A. Sironi, J.A.R. Navarro, J.M. Salas, L. Mendez-Linan, M. Domingo, M. Perez-Mendoza, E. Barea, *Chem.-Eur. J.* **14**(32) (2008) 9890-9901.

[43] J. Rabone, Y.-F. Yue, S.Y. Chong, K.C. Stylianou, J. Basca, D. Bradshaw, G.R. Darling, N.G. Berry, Y.Z. Khimyak, A.Y. Ganin, P. Wiper, J.B. Claridge, M.J. Rosseinsky, *Science* **329**(5995) (2010) 1053-1057.

[44] T.M. McDonald, D.M. D'Alessandro, R. Krishna, J.R. Long, *Chem. Sci.* **2** (2011) 2022-2028.

[45] J.-C.G. Bunzil, *J. Coord. Chem.* **67**(23-24) (2014) 3706-3733.

[46] S. Cotton, *Lanthanide and Actinide Chemistry*, John Wiley & Sons, Ltd., Chichester, 2006.

[47] S. Roy, A. Chakraborty, T.K. Maji, *Coord. Chem. Rev.* **273-274** (2014) 139-164.

[48] T.M. Reineke, M. Eddaoudi, M. Fehr, D. Kelley, O.M. Yaghi, *J. Am. Chem. Soc.* **121**(8) (1999) 1651-1657.

[49] T.M. Reineke, M. Eddaoudi, M. O'Keeffe, O.M. Yaghi, *Angew. Chem. Int. Ed.* **38**(17) (1999) 2590-2593.

[50] Z.-J. Lin, Z. Yang, T.-F. Liu, Y.-B. Huang, R. Cao, *Inorg. Chem.* **51** (2012) 1813-1820.

[51] H. Li, W. Shi, K. Zhao, Z. Niu, H. Li, P. Cheng, *Chem. Eur. J.* **19** (2013) 3358-3365.

[52] D.-X. Xu, A.J. Cairns, Y. Belmabkhout, L. Wojtas, Y. Liu, M.H. Alkordi, M. Eddaoudi, *J. Am. Chem. Soc.* **135** (2013) 7660-7667.

[53] S. Biswas, H.S. Jena, S. Goswami, S. Sanda, S. Konar, *Cryst. Growth Des.* **14** (2014) 1287-1295.

[54] C. Wang, L. Li, J.G. Bell, X. Lv, S. Tang, X. Zhao, K.M. Thomas, *Chem. Mater.* **27** (2015) 1502-1516.

[55] T. Araki, A. Kondo, K. Maeda, *Chem. Eur. J.* **21** (2015) 6257-6264.

[56] Y. Zu, Y. Wang, P. Liu, C. Xia, Y. Wu, X. Lu, J. Xia, *Dalton Trans.* **44** (2015) 1955-1961.

CHAPTER 2

Carbon Dioxide Capture Capacity of Lanthanide benzene-1,4- dicarboxylates

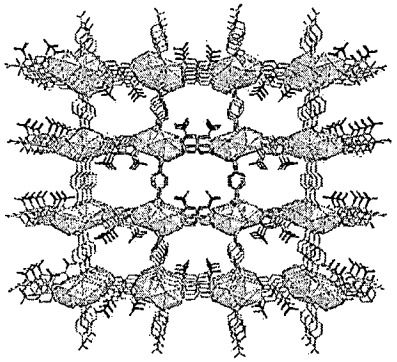

- Six new lanthanide metal organic frameworks were synthesized using mixed ligands of benzene-1,4-dicarboxylic acid and the *in situ* generated 2-nitro-benzene-1,4-dicarboxylic acid.
- Influences of the lanthanides on porosity of the frameworks and topologies are illustrated.
- Four of the six complexes are microporous exhibiting significant stability and remarkable sorption capacities for carbon dioxide and hydrogen.

In this chapter, six new lanthanide coordination frameworks designed and synthesized using benzene-1,4-dicarboxylate (BDC^{2-}) and 2-nitro-benzene-1,4-dicarboxylate (NO_2-BDC^{2-}) is reported. These two ligands were selected as the linkers because of their tendency to generate microporous frameworks which was reported to be suitable for carbon dioxide capture [1,2]. *In situ* nitration was employed to introduce the nitro group to BDC^{2-} and therefore to generate the multivariate frameworks comprising both BDC^{2-} and NO_2-BDC^{2-} linkers. The inclusion of the nitro group was intended to increase the interaction of the framework and carbon dioxide [3]. Four of the six reported complexes are microporous with accessible voids, extraordinary stability and significant gas capture capacities. The photoluminescence properties of the complexes have also been investigated.

2.1 Hydrothermal crystal growth and *in situ* ligand synthesis

Following our interest in extending the use of lanthanide ions in fabricating new microporous frameworks [4], six new complexes, *i.e.* $[La_2(NO_2\text{-}BDC)_3(H_2O)_4]$ **(1)** $[Ln(L)_{0.5}(NO_2\text{-}BDC)(H_2O)]\cdot 3H_2O$ where Ln = Eu (**2**), Tb (**3**), Dy (**4**) and Ho (**5**), and L = BDC^{2-} or BDC^{2-}/NO_2-BDC^{2-}}, and $[Tm(NO_2\text{-}BDC)_{1.5}(H_2O)]\cdot H_2O$ (**6**), have been synthesized.* Colors of the crystals were in good agreement with characteristic colors of the corresponding lanthanide ions. The crystals showed a yellow tint which is consistent with the presence of NO_2-BDC^{2-} derived *in situ* under strong acidic hydrothermal conditions [4,5]. The existence of NO_2-BDC^{2-} is also revealed *via* the characteristic υ(C-N) and υ(N-O) in the IR spectra of all complexes (Table 2.1). To the best of our knowledge, these lanthanide coordination polymers can be regarded as one of the very few multivariate lanthanide coordination polymers yielded by using the *in situ* ligand synthesis strategy. It should be however noted that the formation of nitrosamines may be possible under the employed condition according to the previous literature reporting on the formation of these powerful carcinogens under similar synthesis condition [5].

Single crystal data of **1** and **6** were collected on a Bruker APEX-II CCD diffractometer and a Stoe IPDS2 image plate diffractometer, respectively, whereas those of **2-5** were collected on a Bruker D8 QUEST CMOS diffractometer. The machines were operated using Mo *K*α radiation (λ = 0.71073 Å) at 298(2) *K* for **1-5** and 150(2) *K* for **6**. Data reduction and an adsorption correction of **1-5** were performed with the SAINT [6] and SADABS [7] software packages, whilst that of **6**

*The solution of the corresponding Ln_2O_3 was first prepared by dissolving the Ln_2O_3 (1.70 mmol) in 1.00 mL of concentrated HNO_3 aqueous solution. Each solution was then mixed with 10.0 mL of an aqueous solution containing H_2BDC (4.0 mmol) and DABCO (4.0 mmol) with vigorous stirring. The Ln_2O_3 : HNO_3 : H_2BDC : DABCO : H_2O mole ratio of every reaction was 1.70 : 5.16 : 4.00 : 4.00 : 556. The reactions were performed using a 23.0 mL Teflon lined hydrothermal autoclave under an autogenous pressure generated at 180 °C for 24 h, and afforded a few crystals as the solid products.

was done using the Tompa method [8]. The structures were solved by direct methods implemented within SHELXS-86 [9] and full-matrix least squares refinements were carried out on F^2 for all data with the program SHELXL-97 [9] *via* either the WinGX [10] or the OLEX2 [11] program interfaces. Crystallographic and refinement data are summarized in Table 2.2.

Table 2.1 IR Spectral band assignments for **1-6**

Band assignment	1	2	3	4	5	6
υ(O–H)	3430(m,br)	3413(m,br)	3472(m,br)	3488(m,br)	3472(m,br)	3480(m,br)
	3087(w)	3087(w)	3413(w)	3422(w)	3422(w)	3413(w)
υ(C–H); aromatic	2911(w)	2911(w)	3087(w)	-	-	3095(w)
	2852(w)	-	2920(w)	2928(w)	2920(w)	-
υ_{asym}(C–O)	1581(vs)	1589(vs)	1581(vs)	1615(vs)	1615(vs)	1615(vs)
υ(N–O)	1531(vs)	1531(vs)	1539(vs)	1539(vs)	1539(vs)	1523(vs)
υ_{sym}(C–O)	1497(s)	1497(s)	1497(s)	1455(s)	1431(s)	1489(s)
	1422(s)	1422(s)	1414(s)	1422(s)	1380(s)	1405(s)
	1372(s)	-	1372(s)	1372(s)	1347(s)	-
δ(O–H); in plane	1347(m)	1347(m)	1339(m)	-	-	1339(m)
δ(C-H); aromatic	1238(w)	1247(w)	1255(w)	1264(w)	1264(w)	1247(w)
δ(C–C); *p*-	1171(w)	1171(w)	1156(w)	1171(w)	1171(w)	1171(w)
substituent on	1121(w)	1131(w)	1126(w)	1111(w)	1131(w)	1137(w)
benzene ring	1062(w)	1061(w)	1062(w)	1061(w)	1071(w)	1062(w)
	1022(w)	1021(w)	1022(w)	-	1011(w)	-
υ(C–N)	861(m)	930(m)	929(m)	870(m)	930(m)	929(m)
δ(C–H); aromatic,	831(m)	830(m)	861(m)	840(m)	870(m)	837(m)
in plane	791(m)	789(m)	781(m)	789(m)	779(m)	803(m)
	751(m)	749(m)	-	649(m)	-	778(m)
δ(C–H); aromatic,	600(w)	608(w)	600(w)	618(w)	608(w)	708(w)
out of plane	529(w)	528(w)	529(w)	528(w)	528(w)	678(w)
υ(Ln–O)	489(w)	488(w)	479(w)	468(w)	488(w)	467(w)

2.2 Crystal structures of 1-6

$[La_2(NO_2\text{-}BDC)_3(H_2O)_4]$ (1). Complex **1** crystallizes in the triclinic space group $P\bar{1}$ with two unique lanthanum ions in the asymmetric unit (Fig. 2.1a). The two distinct lanthanum ions are similarly eight-fold coordinated by eight oxygen atoms from the carboxylates of six NO_2-BDC^{2-} and two coordinated water molecules, and form a distorted square-face bicapped trigonal prismatic unit, *TPRS*-{LaO_8}, alike. All of the NO_2-BDC^{2-} function as the tetradentate linkers using the μ_4-η^1:η^1:η^1:η^1 coordination mode, leading to the formation of the three-dimensional [$La_2(NO_2$-$BDC)_3(H_2O)_4$] framework. The structure of **1** is a dense framework without any void according to calculations using PLATON [12] and can be viewed as being composed of two-dimensional puckered layers spreading in the *ac* plane which are further pillared by the organic ligands in the direction of *b* (Fig. 2.1b). The framework can be simplified to the uninodal 6-connected **pcu** α-Po net with $\{4^{12}.6^3\}$ point symbol using the *TPRS*-{LaO_8} units as nodes and the NO_2-BDC^{2-} as linker (Fig. 2.1c). The framework of **1** is governed mainly by very strong O–H···O hydrogen bonding interactions involving every coordinated water molecule and the nitro groups of NO_2-BDC^{2-} (Table

Table 2.2 Crystallographic data and structure refinement summary of **1-6**

	1	**2**	**3**	**4**	**5**	**6**
CCDC						
Empirical formula	$La_2C_{24}H_{18}N_2O_{20}$	$EuC_{12}H_{13}NO_{12}$	$TbC_{12}H_{13}NO_{12}$	$DyC_{12}H_{13}NO_{12}$	$HoC_{12}H_{13}NO_{12}$	$TmC_{12}H_{8.5}N_{1.5}O_{11}$
Formula weight	924.16	507.14	514.10	519.69	522.12	514.60
Temperature/K	293(2)	273.15	273.15	273.15	273.15	150(2)
Crystal system	Triclinic	Orthorhombic	Orthorhombic	Orthorhombic	Orthorhombic	Monoclinic
Space group	$P\bar{1}$	*Pbca*	*Pbca*	*Pbca*	*Pbca*	*C2/c*
a/Å	9.7849(5)	6.8849(2)	6.8451(9)	21.6689(3)	6.7919(3)	16.5383(13)
b/Å	10.9160(6)	21.8286(7)	21.731(3)	22.8825(10)	21.6514(11)	11.2800(13)
c/Å	15.6249(8)	23.0388(7)	22.936(3)	6.8125(11)	22.8375(10)	15.2694(15)
α/°	82.299(2)	90	90	90	90	90
β/°	77.197(2)	90	90	90	90	90.350(7)
γ/°	63.398(2)	90	90	90	90	90
Volume/Å^3	1453.99(13)	3462.45(18)	3411.7(9)	3377.9(6)	3358.3(3)	2848.5(5)
Z	2	8	8	8	8	8
ρ_{calc}mg/mm^3	2.111	1.946	2.002	2.044	2.065	2.3997
μ/mm^{-1}	2.995	3.685	4.209	4.488	4.777	6.299
F(000)	884.0	1944	1960	1984.0	1992.0	1950.8
Crystal size/mm^3	0.8×0.6×0.5	0.2×0.18×0.16	0.2×0.18×0.16	0.4×0.2×0.2	0.4×0.2×0.2	0.45×0.42×0.25
Radiation	Mo K_α ($\lambda = 0.71073$)	Mo K_α ($\lambda = 0.71073$)	Mo K_α ($\lambda = 0.71073$)	Mo K_α ($\lambda = 0.71073$)	Mo K_α ($\lambda = 0.71073$)	Mo K_α ($\lambda = 0.71073$)
Data/restraints/parameters	9378/0/422	4300/0/242	4785/0/253	5868/0/233	4174/0/233	3127/0/228
Goodness-of-fit	1.058	1.079	1.155	1.114	1.147	0.859
$R(F^2)$, R_w [I≥2σ (I)]	0.0423, 0.1153	0.0415, 0.1147	0.0389, 0.1082	0.0446, 0.1089	0.0518, 0.1189	0.0252, 0.0578
$R(F^2)$, R_w (all data)	0.0565, 0.1260	0.0544, 0.1218	0.0448, 0.1113	0.0562, 0.1143	0.0625, 0.1241	0.0351, 0.0592

2.3). The hydrogen bonding interactions are in good agreement with the apparent disorder in the structure of **1** and additionally result in an arrangement of the organic ligand that prohibits any π-π interaction.

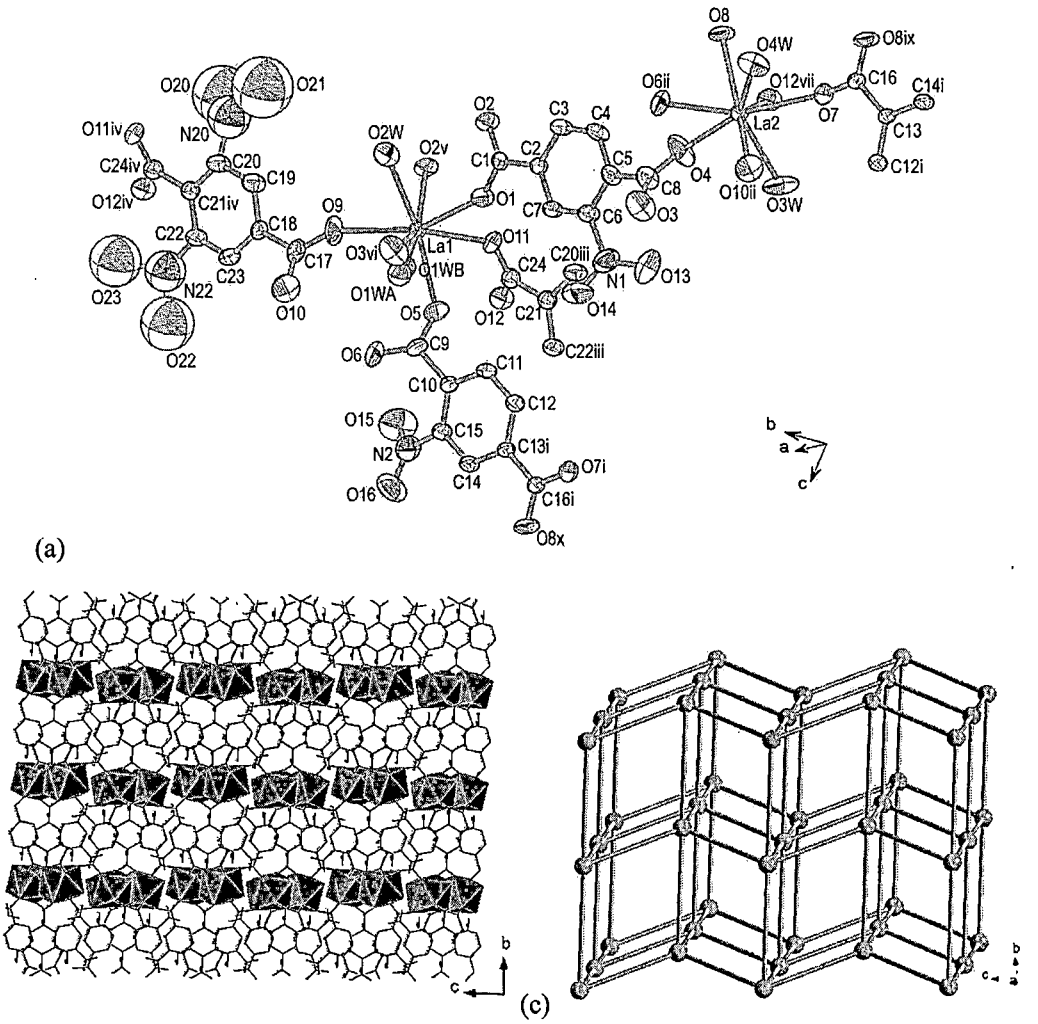

Fig. 2.1 Views of (a) an extended asymmetric unit drawn as 50% thermal ellipsoids, (b) the three-dimensional framework, and (c) the simplified **pcu** α-Po topology of **1**. Symmetry operations: (i) 2-*x*, -1-*y*, 1-*z* (ii) 2-*x*, -*y*, 1-*z* (iii) *x*, -1+*y*, *z* (iv) *x*, 1+*y*, *z* (v) 1-*x*, 1-*y*, 1-*z* (vi) 2-*x*, -*y*, 1-*z* (vii) 1-*x*, -*y*, 1-*z* (viii) 1-*x*, 2-*y*, 2-*z* (ix) 2-*x*, -1-*y*, -*z* (x) *x*, *y*, 1+*z*.

$[Ln(L)_{0.5}(NO_2\text{-}BDC)(H_2O)]\cdot 3H_2O$ {Ln = Eu (2), Tb (3), Dy (4) and Ho (5); L = BDC^{2-} or $BDC^{2-}/NO_2\text{-}BDC^{2-}$}. Complexes **2-5** are isostructural and crystallize in the same orthorhombic space group *Pbca* (Table 2.1). The unit cell parameters of **2-5** are in good agreement with those of $[Ln(NO_2\text{-}BDC)(L)_{0.5}(H_2O)]\cdot 3H_2O$ (Ln = Pr, Nd, Sm and Gd; L = BDC^{2-} or $BDC^{2-}/NO_2\text{-}BDC^{2-}$) [4],

with a descending tendency across the series attributed to the lanthanide contraction. The asymmetric units of **2-5** are similar comprising only one unique lanthanide metal ion which exhibits the same nine-fold coordination of the square-face capped square antiprismatic geometry, *SAPRS*-{LaO_9}, as exemplified in Fig. 2.2. Two modes of coordination including the μ_4-η^1:η^1:η^2:η^2 and μ_4-η^1:η^1:η^1:η^1 are adopted by the ligands upon the coordination leading to the formation of the one-dimensional {Ln(μ_3-OCO)$_4$(μ_2-OCO)$_2$(η^1,η^1-OCO)(OH_2)} chains extending along the direction of *a* (Fig. 2.3a). These chains are further linked by the ligands to form a three-dimensional framework which can be simplified to the four-connected uninodal **NbO** net (Fig. 2.3b).

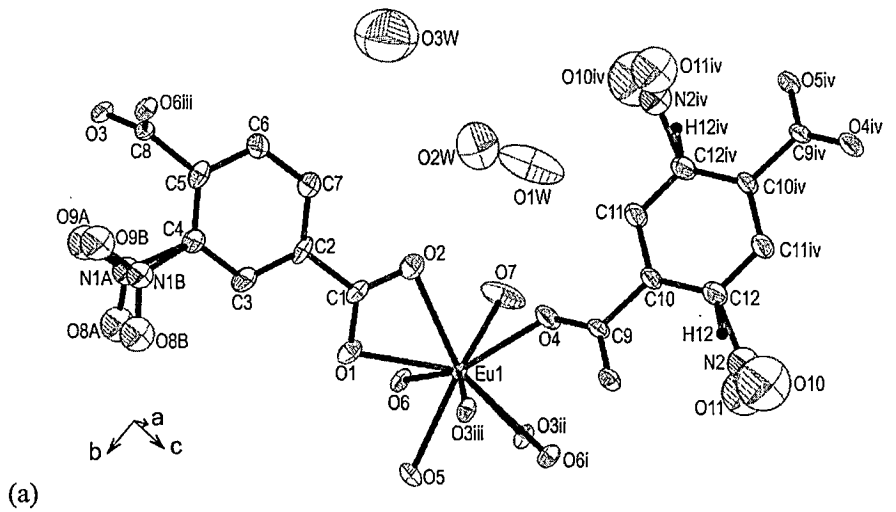

Fig. 2.2 Views of the extended asymmetric units of (a) **2** and (b) **4** both of which are drawn as 50% thermal ellipsoids. Symmetry operations for **2:** (i) 0.5+*x*, 0.5-*y*, 1-*z* (ii) *x*, 0.5-*y*, 0.5+*z* (iii) 0.5+*x*, *y*, 0.5-*z* (iv)1-*x*, -*y*, 1-*z*. For **3**: (i) 1.5-*x*, 1-*y*, -0.5+*z* (ii) 1.5-*x*, 0.5+*y*, *z* (iii) *x*, 0.5-*y*, -0.5+*z* (iv) 1.5-*x*, 1-*y*, 0.5+*z* (v) *x*, 0.5-*y*, 0.5+*z* (vi) 1-*x*, 1-*y*, 2-*z*.

The framework includes the one-dimensional rectangular channel extending in the same direction as the $\{Eu(\mu_3\text{-}OCO)_4(\mu_2\text{-}OCO)_2(\eta^1,\eta^1\text{-}OCO)(OH_2)\}$ chains, housing the unbound water molecules. In the same fashion to $[Ln(NO_2\text{-}BDC)(L)_{0.5}(H_2O)]\cdot 3H_2O$ [4], these unbound water molecules are organized as the edge-shared pentagons by strong hydrogen bonding interactions(Table 2.3). Besides the hydrogen bonding interactions, there are π-π interactions between the adjacent organic ligands. The distances and angles between the centroids of the two aromatic rings, range from 4.022 Å and 78.7° in **2** (Eu^{III}) to 3.951 Å and 78.0 ° in **5** (Ho^{III}). The effective sizes of the channel openings of **2-5** are similar (4×8 $Å^2$) which is also similar to those of $[Ln(NO_2\text{-}BDC)(L)_{0.5}(H_2O)]\cdot 3H_2O$ [4]. If the unbound water molecules are excluded, the solvent accessible void volumes of 895.7 $Å^3$ (**2**; 25.87 %), 848.7 $Å^3$ (**3**; 24.88%), 825.4 $Å^3$ (**4**; 24.40%), 809.0 $Å^3$ (**5**; 24.10%) could be calculated.

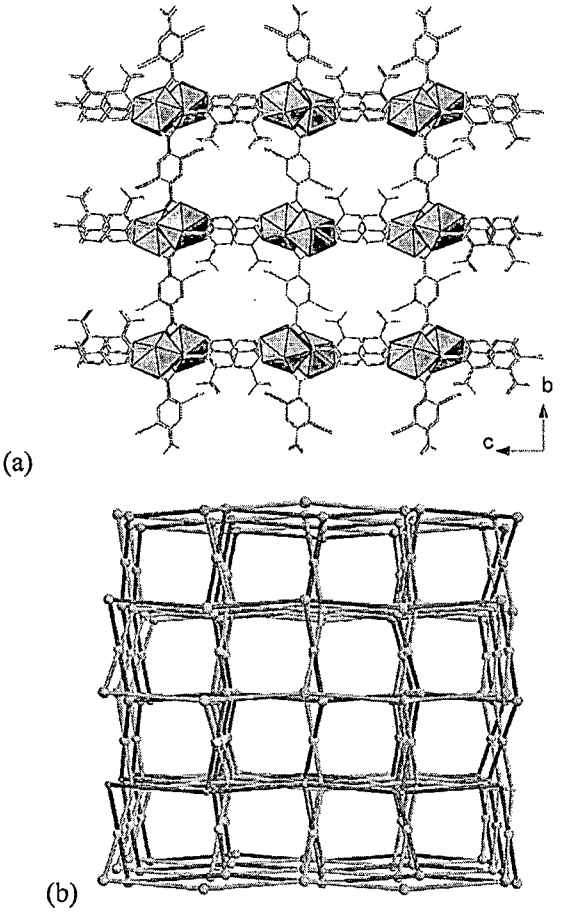

Fig. 2.3 Illustrations showing (a) the three-dimensional framework and (b) the simplified **NbO** topology of **2** (as a representative of **2-5**).

Table 2.3 Lists of hydrogen bonding distances (d, Å) and angles (∠, °) in **1-6***

D–H···A	d (D–H···A)	∠ D–H···A	D–H···A	d (D–H···A)	∠ D–H···A
1[a]			**2**[b]		
O4w–H4wB···O12i	3.281(7)	143	O7···O1w	2.786(11)	-
O4w–H4wB···O7ii	2.993(7)	111	O9B···O6iii	2.971(11)	-
O3w–H3wB···O14iii	2.776(8)	137	O1w···O2w	2.852(15)	-
O2w–H2wA···O2	3.067(7)	115	O1w···O3wi	2.993(19)	-
O2w–H2wB···O13iv	2.989(12)	163	O1w···O8Bii	3.145(17)	-
C3–H3···O1wBv	3.498(10)	167	O2w···O2	2.870(10)	-
O9···O1wA	2.809(14)	-	O2w···O3w	2.987(17)	-
O9···O1wB	3.045(13)	-	O2w···O3wi	2.993(19)	-
3[c]			**4**[d]		
O7···O1wi	2.786(10)	-	O7···O1w	2.787(10)	-
O1w···O2w	2.957(17)	-	O9A···O6	3.007(11)	-
O1w···O3wii	2.832(14)	-	O1w···O2w	2.929(13)	-
O1w···O9Biii	3.118(17)	-	O1w···O3wi	2.901(16)	-
O2w···O3w	2.840(16)	-	O1w···O8Aii	3.098(19)	-
O2w···O3wiv	2.974(16)	-	O1w···O9Bii	3.193(12)	-
O8A···O1wv	3.098(19)	-	O2w···O3w	2.992(15)	-
O9B···O1wv	3.193(12)	-	O2w···O3wiii	2.806(15)	-
5[e]			**6**[f]		
O7···O1wie	2.778(15)	-	C3–H3···O8i	3.265(15)	151
O9B···O1wii	3.112(25)	-	C6–H6···O9ii	2.858(13)	101
O8A···O1wii	3.198(19)	-	C7–H7···O6iii	3.219(7)	140
O1w···O2w	2.924(25)	-	C11–H11···O8	2.288(13)	138
O1w···O3wiii	2.821(19)	-	C11–H11···O9	2.328(14)	132
O3w···O2w	2.827(24)	-	O1w···O2w	2.647(7)	-

* Potential hydrogen bonding interactions are provided in cases where hydrogen atoms were not assigned with precision due to limitations crystallographically.

[a](i) 1+*x*,-1+*y*,-1+*z* (ii) 2-*x*, -1-*y*, -*z* (iii) 2-*x*, -1-*y*, -1-*z* (iv) *x*, 1+*y*, *z* (v) 1-*x*, 1-*y*, 1-*z*

[b](i) -0.5+*x*, *y*, 0.5-*z* (ii) -*x*, -0.5+*y*, 0.5-*z* (iii) 0.5+*x*, *y*, 0.5-*z*

[c](i) 0.5+*x*, 1.5-*y*, 1-*z* (ii) 1+*x*, *y*, *z* (iii) 0.5-*x*, -0.5+*y*, *z* (iv) 0.5+*x*, *y*, 0.5-*z* (v) 0.5+*x*, 0.5-*y*, 1-*z*

[d](i) *x*, 0.5-*y*, -0.5+*z* (ii) -0.5+*x*, 0.5-*y*, 1-*z* (iii) *x*, 0.5-*y*, 0.5+*z*

[e](i) -0.5+*x*, 0.5-*y*, 1-*z* (ii) 1.5-*x*, -0.5+*y*, *z* (iii) 1+*x*, *y*, *z* (iv) -0.5+*x*, *y*, 0.5-*z*

[f](i) 3/2-*x*, 1/2+*y*, 3/2-*z* (ii) 2-*x*, *y*, 3/2-*z* (iii) 3/2-*x*, -1/2+*y*, 3/2-*z* (iv) x, 2-*y*, -0.5+*z*

$[Tm(NO_2\text{-}BDC)_{1.5}(H_2O)]\cdot H_2O$ (6). Complex **6** crystallizes in the monoclinic *C2/c* space group comprising only one unique thulium ion which is eight-fold coordinated in a distorted square-face bicapped trigonal prismatic geometry, *TPRS*-{TmO_8} (Fig. 2.4a). Every two *TPRS*-{TmO_8} motifs are linked by four carboxyl bridges, *i.e.* $2\times\mu_2\text{-}\eta^1\text{:}\eta^1$ (O10–C14–O10 and O7–C9–O7) and $2\times\mu_2\text{-}\eta^2\text{:}\eta^1$ (O5–C8–O6), to form an edge-shared {Tm_2O_{12}} dimer (Fig. 2.4b). These dimers are then connected by the NO_2-BDC^{2-} ligands through $\mu_4\text{-}\eta^1\text{:}\eta^1\text{:}\eta^1\text{:}\eta^1$ and $\mu_4\text{-}\eta^2\text{:}\eta^1\text{:}\eta^1\text{:}\eta^1$ modes of coordination establishing the three-dimensional framework. There are rectangular channels extending along the direction of *b* of the framework housing the water of crystallization. The crystallizing water molecule is in close proximity to both the coordinating water and the carboxylate oxygen atoms rendering a strong O–H···O hydrogen bonding interactions (Table 2.3). The framework structure of **6** is further stabilized by the other extensive weak interactions, including the weak C–H···O hydrogen bonding and the aromatic π-π parallel-displaced interactions. The distance and angle between the centroids of the two aromatic rings of two adjacent NO_2-BDC^{2-} are 3.929 Å and 82.5 °, respectively. The framework of **6** notably contains negligible solvent accessible void. If the edge-shared {Tm_2O_{12}} dimer is regarded as node with the organic ligand as a linker, the framework of **6** can be intriguingly simplified to the same uninodal **pcu** α-Po net as that of **1** (Fig. 2.4c), although degrees of puckering of the two nets are different. According to the literature, the structure of **6** is isostructural to those of the recently reported $[Ln_2(NO_2\text{-}BDC)_3(H_2O)_2]\cdot 2(H_2O)$ (Ln = Sm, Eu, Gd, Tb, Er) which were synthesized directly using the NO_2-H_2BDC ligand under hydrothermal and slow evaporation conditions [13].

Intriguingly, the eight-fold coordination as found for the unoccupied *f* orbital in lanthanum ion (**1**) and the smallest thulium ion (**6**) results in similar dense frameworks with negligible void and the same **pcu** α-Po topology. This is however not the case for $[Ln_2(NO_2\text{-}BDC)_3(H_2O)_2]\cdot 2(H_2O)$ (Ln = Sm, Eu, Gd, Tb, Er), where the NO_2-H_2BDC was used as the sole linker during the synthesis [13]. This implies the influence of the NO_2-BDC^{2-} linker in regulating the construction of such a dense framework which may be due to the steric nitro group on the linker, and the crucial role of the BDC^{2-} linker in providing genuine microporosity to the derived frameworks.

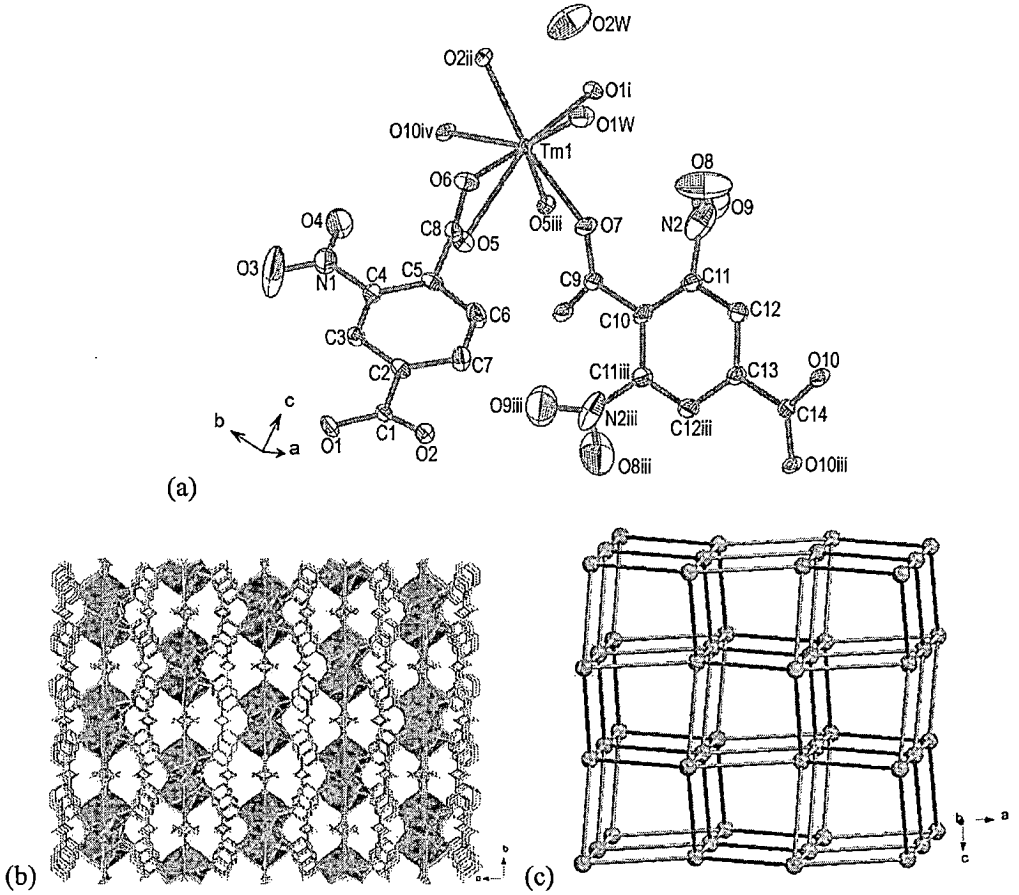

Fig. 2.4 Views of (a) an extended asymmetric unit drawn as 50% thermal ellipsoids, (b) a dense three-dimensional framework, and (c) the simplified **pcu** α-Po topology of **6**. Symmetry operations: (i) 0.5+*x*, 1.5-*y*, 0.5+*z* (ii) 1.5-*x*, 0.5+*y*, 1.5-*z* (iii) 2-*x*, *y*, 1.5-*z* (iv) *x*, 1+*y*, *z*.

2.3 Thermal stability and gas sorption behavior of 2

To investigate gas sorption behavior of the reported microporous complexes, thermal stability of **2** (as a representative of **2-5**) was investigated by thermogravimetric analysis. It is apparent that the complex remains stable up to over 400 °C (Fig. 2.5) despite the two successive losses of both the unbound and the coordinating water molecules (RT-180 °C; exp. 10.0%, calcd. 10.5%). Nonetheless, such losses resulted in the vanishing of the long-range order in the *c* direction revealed by the disappearance of the (0 0 *l*) reflections in the PXRD pattern. The importance of the hydrogen bonded water molecules which are organized in the framework void in regulating the framework is therefore illustrated. The persistence of the *h*00 and 0*k*0 reflections with appreciable intensities, on the other hand, suggests the retention of the framework crystallinity in the other two

directions. A slight shift of the (0 2 0) diffraction peak to lower 2θ for the heat-treated samples implies the modest alteration of the framework structure after the losses of the water molecules. Stability of the framework and the retention of the framework microporosity after the removal of the water molecules were confirmed by the classical type I sorption isotherm of the nitrogen gas collected at 77 *K* (Fig. 2.6a). The surface area of 543 $m^2 \cdot g^{-1}$ could be calculated based on the BET model with an average pore size of 1.2 nm.

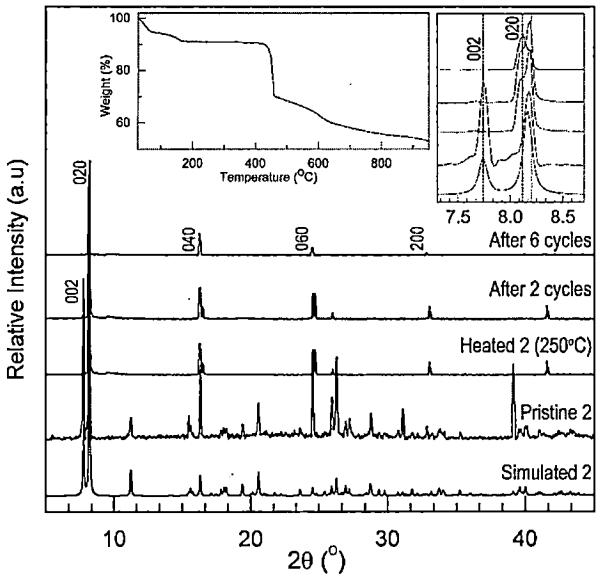

Fig. 2.5 The PXRD pattern of the pristine sample of **2** compared with the pattern simulated from single crystal data and those of the treated samples with the enlargement of the low 2θ area and the thermogravimetric curve in the insets.

The sample exhibited similar adsorption behavior for carbon dioxide gas (Fig. 2.6b). The sudden uptake of the gas signifies the interactions of the gas molecule with the unoccupied coordination sites on the europium ions generated by the removal of the coordinated water. The maximum gravimetric capacity of approximately 19 wt%, which is equivalent to 95 $cm^3 \cdot g^{-1}$ or 4.2 $mmol \cdot g^{-1}$, was achieved at extremely low pressure of less than 10 kPa or 0.1 bar. This value is much higher than those reported for zeolitic materials [14], and comparable to some recently reported metal organic frameworks under similar measuring temperatures and pressures such as $[(Ni_2L^2)(bptc)] \cdot 6H_2O \cdot 3DEF$, $[(Ni_2L^4)(bptc)] \cdot 14H_2O$ ($bptc^{4-}$ = 1,1′-biphenyl-3,3′,5,5′-tetracarboxylate, DEF = *N*,*N*-diethylformamide) [15], and $[Co_{2.5}(btc)(Hbtc)_{0.5}(atz)(CH_3CN)(H_2O)] \cdot H_2O$ (H_3btc = 1,3,5-benzenetricarboxylic acid, atz = 3-amino-1,2,4-triazole) [16]. In addition to the interactions to the exposed europium ions, the

interactions between the polar nitro groups on the NO_2-BDC^{2-} linker and the carbon dioxide molecule [16-18] should also contribute to the significant uptake capacity in **2**. Intriguingly, this capacity was retained even after six cycles of sorption/desorption experiments with the intact framework crystallinity revealed by both the powder (Fig. 2.5) and single crystal X-ray diffraction experiments. A single crystal that had been used for six cycles of gas sorption was exposed to air for a period of a few weeks and then examined by single crystal X-ray diffraction. This demonstrated that the same network present in the pristine sample is retained. The structure refinement of this crystal (data to 56.5° 2θ for Mo radiation) converged with $R = 4.53\%$ and $wR(F^2) = 7.13\%$. The stability of the framework and therefore recyclability of the material is one of the most desired properties for the storage applications [19].

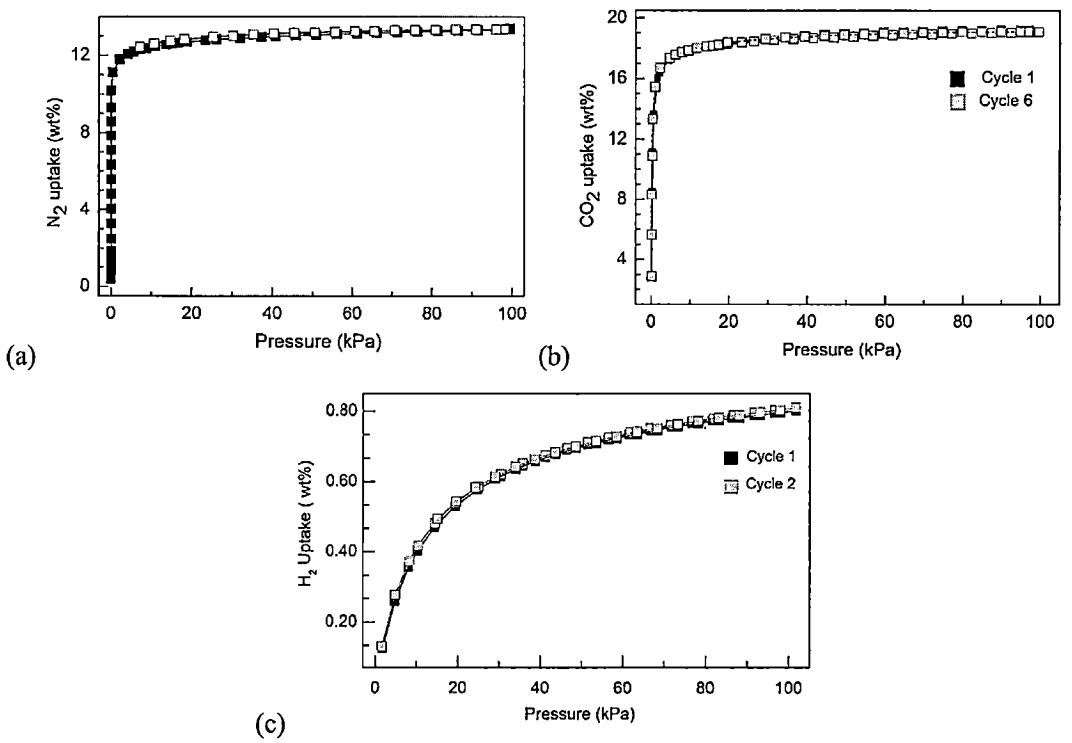

Fig. 2.6 Gas sorption/desorption isotherms of (a) nitrogen (b) carbon dioxide and (c) hydrogen gases.

Rather than an abrupt increase in gravimetric adsorption like that observed for the nitrogen and carbon dioxide gases, the uptake of the hydrogen gas by **2** gradually occurred over a range of pressures before reaching approximately 0.80 wt% at 1 bar, which is equivalent to 79 $cm^3 \cdot g^{-1}$ or 4 $mmol \cdot g^{-1}$ (Fig. 2.6c). This gravimetric sorption capacity is comparable to those reported for the best

zeolite ZSM-5 [20] and the series of Co-INA, CO-FINA and IRMOF [21]. The rather small gravimetric capacities observed for **2** attributes partially to relatively heavy framework compared to the light weight of the hydrogen gas. The gradual increase in the sorption with increasing pressure at low temperatures is notably characteristic of the physisorption process in the microporous solids [22], which is reported to be potential for the pressure swing adsorption processes [23]. Regarding the structure of **2**, the sorption of the hydrogen gas should occur through the interactions with the electron rich phenyl rings of both the BDC^{2-} and NO_2-BDC^{2-} linkers [24].

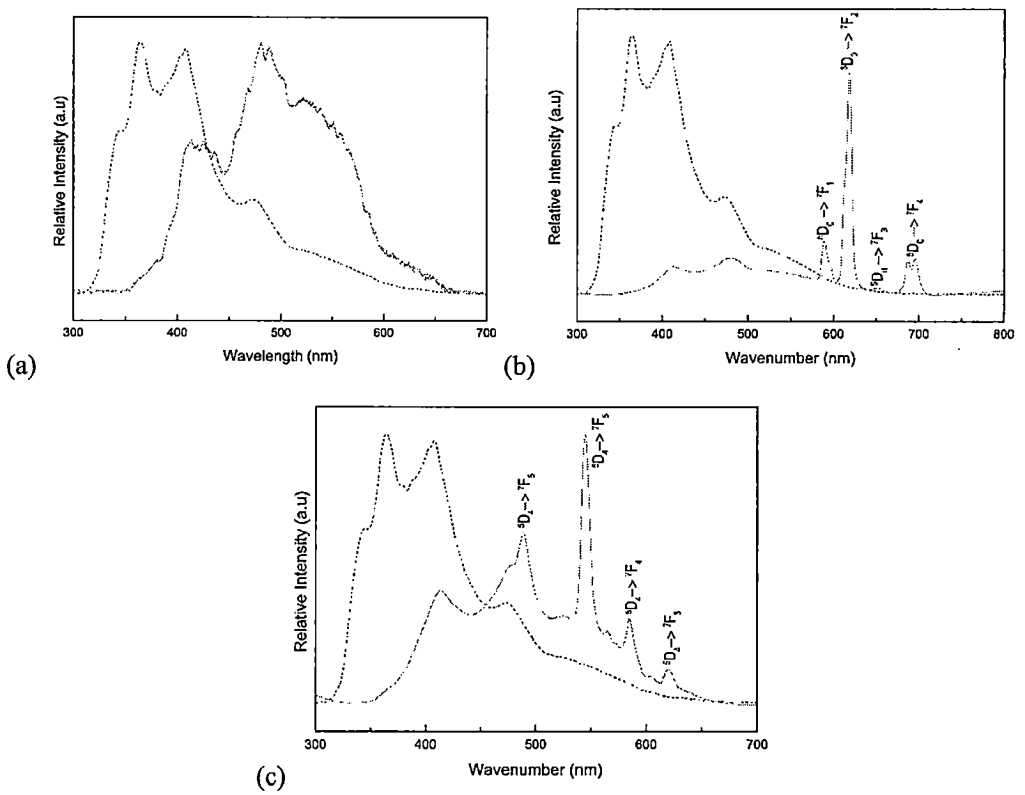

Fig. 2.7 Photoluminescence spectra (solid lines) of (a) **1** (as a representative of **1** and **4-6**) (b) **2**, and (c) **3**, compared with those of the H_2BDC (dotted lines).

2.4 Photoluminescence properties of 1-6

The NO_2-BDC^{2-} ligand has been reported previously as a poor sensitizer in $[Ln(NO_2\text{-}BDC)(L)_{0.5}(H_2O)]\cdot 3H_2O$ [4] and the closely relevant $[Ln_2(NTA)_3(OH_2)_2](H_2O)_2$ (Ln = Sm, Eu, Gd, Tb, Er and H_2NTA = 2-nitroterephthalic acid) [13], which is also true for the complexes reported here. Upon the excitation at 255 nm, similar broad bands covering almost the entire region of the visible light derived from the intra-ligand charge transfer (ILCT) transitions is present, as

exemplified in Fig. 2.7. Characteristic emissions of the europium (**2**; $^5D_0 \rightarrow {}^7F_J$, J = 1, 2, 3, 4) and terbium (**3**; $^5D_4 \rightarrow {}^7F_J$, J = 3, 4, 5, 6) can, nonetheless, be observed. These emission bands are significantly less intense relative to other europium and terbium complexes which agree with the poor sensitizing role of the NO_2-BDC^{2-} ligand. The relatively high intensity of the $^5D_0 \rightarrow {}^7F_2$ band in the spectrum of complex **2** can be attributed to the absence of the inversion center at the europium ion crystallographic site [13].

2.5 Conclusion

By employing the H_2BDC ligand and the *in situ* nitration reaction, six new lanthanide metal organic complexes have been synthesized; $[La_2(NO_2\text{-}BDC)_3(H_2O)_4]$ (**1**) $[Ln(L)_{0.5}(NO_2\text{-}BDC)(H_2O)]\cdot 3H_2O$ (Ln = Eu (**2**), Tb (**3**), Dy (**4**) and Ho (**5**); L=BDC^{2-} or $BDC^{2-}/NO_2\text{-}BDC^{2-}$) and $[Tm(NO_2\text{-}BDC)_{1.5}(H_2O)]\cdot H_2O$ (**6**). Complexes **1** and **6** are can be simplified to the same topology of **pcu** α-Po net despite the different framework structures, and the isostructural frameworks of **2-5** can be simplified to the **NbO** net. Whilst the frameworks of **1** and **6** contained negligible void, those of **2-5** are microporous in nature with similar void opening of 4×8 $Å^2$ and solvent accessible void volumes varying in a range of 809.0-895.7 $Å^3$. Complex **2** (as a representative of **2-5**) exhibits exceptional stability upon the loss of all the water in the structure and also the heat treatment. After the loss of the water, the BET surface area of 543 $m^2 \cdot g^{-1}$ and an average pore size of 1.2 nm can be calculated for **2**, which shows significant adsorption capacities for both carbon dioxide (95 $cm^3 \cdot g^{-1}$ or 4.2 $mmol \cdot g^{-1}$) and hydrogen gases (79 $cm^3 \cdot g^{-1}$ or 4 $mmol \cdot g^{-1}$). The framework shows high stability even after six cycles of sorption/desorption experiments. The poor sensitizing ability of the NO_2-BDC^{2-} ligand has been illustrated.

REFERENCES

[1] Li, H.; Eddaoudi, M.; Groy, T.L.; Yaghi, O.M. *J. Am. Chem. Soc.* 1998, *120*(33), 8571-8572.

[2] Eddaoudi, M.; Li, H.; Reineke, T.; Fehr, M.; Kelley, D.; Groy, T.L.; Yaghi, O.M. *Top. Catal.* 1999, 9, 105-111.

[3] Maity, D.K.; Halder, A.; Bhattacharya, B.; Das, A.; Ghoshal, D. *Cryst. Growth Des.* 2016, *16*, 1162-1167.

[4] Panyarat, K.; Prior, T.J.; Rujiwatra, A. *Polyhedron* **2014**, *81*, 74-80.

[5] Xiao, H.-P.; Zhu, L.-G. *Inorg. Chem. Commun.* **2006**, *9*, 1125-1128.

[6] Bruker, SAINT, Bruker AXS Inc., Madison, Wisconsin, USA, 2007.

[7] Krause, L.; Herbst-Irmer, R.; Sheldrick, G.M.; Stalke, D. J. *Appl. Crystallogr.* **2015**, *48*, 3-10.

[8] de Meulenaer, J.; Tompa, H. *Acta Crystallogr.* **1965**, *19*, 1014.

[9] Sheldrick, G.M. *Acta Crystallogr.* **2008**, A*64*(112), 112-122.

[10] Farrugia, L.J. *J. Appl. Crystallogr.* **1999**, *32*, 837-838.

[11] Dolomanov, O.V.; Bourhis, L.J.; Gildea, R.J.; Howard, J.A.K.; Puschmann, H. *J. Appl. Crystallogr.* **2009**, *42*, 339-341.

[12] Spek A.L. (1980-2014). PLATON. Version 191114. Utrecht University, Padualaan 8, 3584 CH Utrecht, The Netherlands.

[13] Smith, J.A.; Wilmot, M.A.S.; Carter, K.P.; Cahill, C.L.; Loughe, A.J.; Knee, C.S. *New J. Chem.* **2016**, *40*, 7338-7349.

[14] Sabouni, R.; Kazemian, H.; Rohani, S. *Environ. Sci. Pollut. Res.* **2014**, *21*, 5427-5449.

[15] Choi, H.-S.; Suh, M.P. *Angew. Chem. Int. Ed.* **2009**, *48*, 6865-6869.

[16] Liu, B.; Zhao, R.; Yue, K.; Shi, J.; Yu, Y.; Wang, Y. *Dalton Trans.* **2013**, *42*, 13990-13996.

[17] Zhang, Z.; Yao, Z.-Z.; Xiang, S.; Chen, B. *Energy Environ. Sci.* **2014**, *7*, 2868-2899.

[18] Kapelewski, M.T.; Geier, S.J.; Hudson, M.R.; Stück, D.; Mason, J.A.; Nelson, J.N.; Xiao, D.J.; Hulvey, Z.; Gilmour, E.; FitzGerald, S.A.; Gordon, M.H.; Brown, C.M.; Long, J.R. *J. Am. Chem. Soc.* **2014**,*136*,12119-12129.

[19] Furukawa, H.; Cordova, K.E.; O'Keeffe, M.; Yaghi, O.M. *Science* **2013**, *341*, 1230444.

[20] Phan, A.; Doonan, C.; Romo, F.J.U.; Knobler, C.B.; O'Keeffe, M.; Yaghi, O.M. *Acc. Chem. Res.* **2010**, *43*(9), 58-67.

[21] Pachfule, P.; Chen, Y.; Jiang, J.; Banerjee, R. *Chem. Eur. J.* **2012**, *18*, 688-694.

[22] Thommes, M.; Kaneko, K.; Neimark, A.V.; Olivier, J.P.; Reinoso, F.R.; Rouquerol, J.; Sing, K.S.W. *Pure Appl. Chem.* **2015**, *87*, 1051-1069.

[23] Silva, B.; Solomon, I.; Ribeiro, A.M.; Lee, U.H.; Hwang, Y.K.; Chang, J.-S.; Loureiro, J.M.; Rodrigues, A.E. *Sep. Purif. Technol.* **2013**, *118*, 744-756.

[24] Collins, D.J.; Zhou, H.-C. *J. Mater. Chem.* **2007**, *17*, 3154-3160.

CHAPTER 3

Colorimetric Ratiometric Temperature Sensing by Lanthanide benzene-1,4- dicarboxylates

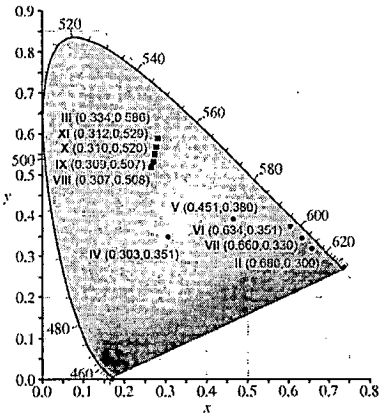

- New opportunity to develop high performance temperature sensors based on lanthanide coordination polymers using colorimetric analysis
- Ratiometric parameters were developed based on temperature dependent emitting colors (white to pinkish red) of Eu^{III}-loaded Gd^{III} complex
- Excellent performance in temperature measurements with respect to both sRGB and CIE XYZ systems over 303-348 *K*

In this chapter, the temperature dependent photoluminescent behavior in term of colorimetry of Eu^{III}- and Tb^{III}-loaded Gd^{III} complexes, *i.e.* $[Ln_xGd_{2-x}(BDC)_3(DMF)_2(H_2O)_2]_n$ (Ln = Eu^{III}, Tb^{III}), is reported. Discussion with respect to the corresponding monometallic $[Ln_2(BDC)_3(DMF)_2(H_2O)_2]_n$ (Ln = Eu^{III}, Gd^{III}, Tb^{III}) is also included. The attempts to apply colorimetric analysis with temperature dependent photoluminescent colors of $[Eu_xGd_{2-x}(BDC)_3(DMF)_2(H_2O)_2]_n$ is described with reference to two color matching systems, *e.g.* CIE XYZ and sRGB, from which the temperature sensing performance have been evaluated.

3.1 Hydrothermal synthesis and characterization

A series of monometallic $[Ln_2(BDC)_3(DMF)_2(H_2O)_2]_n$ (Ln = Gd^{III} (**I**), Eu^{III} (**II**), Tb^{III} (**III**) H_2BDC = benzene-1,4-dicarboxylic acid; DMF = dimethylformamide) and the lanthanide luminophores-loaded $[Ln_xGd_{2-x}(BDC)_3(DMF)_2(H_2O)_2]_n$ (Ln = Eu^{III} (**IV-VII**) and Tb^{III} (**VIII-XI**) were synthesized for use in photoluminescent study.* According to the PXRD data (Fig. 3.1), the monometallic **I-III** and the Eu^{III}- (**IV-VII**) and Tb^{III}-loaded (**VIII-XI**) samples are isostructural with $[Ln_2(BDC)_3(DMF)_2(H_2O)_2]_n$ (Ln = Gd^{III}, Tb^{III}) [1]. Due to the trace amounts of Eu^{III} and Tb^{III} in **IV-VII** and **VIII-XI** prohibiting the precise contents to be determined by available techniques, their existence was conclusive from the characteristic emissions of Eu^{III} and Tb^{III} in the corresponding photoluminescent spectra. Photoluminescent studies of these complexes using the samples yielded from different batches of the synthesis confirmedly provided repeatable results.

3.2 Temperature dependent emitting colors of I-III, IV-VII and VIII-XI

According to literature [2-4], the triplet state energy of BDC^{2-} is in an appropriate range to sensitize the intraconfigurational *f-f* emissions of both Eu^{III} and Tb^{III}, which are otherwise forbidden. With reference to the emission spectrum of **I** (Gd^{III}), where the sensitization is nonviable

*To synthesize colorless crystals of **I**, $Gd(NO_3)_3{\cdot}5H_2O$ (180 mg, 0.413 mmol) and H_2BDC (144 mg, 0.867 mmol) was first dissolved in a mixed solvent prepared from 3.00 mL each of deionized water and DMF. The solution was then sealed in a 10 mL glass bottle and kept at 80 °C for 6 h. After cooling down to room temperature, crystals of **7** were collected by filtration. The same procedure was adopted for the synthesis of **II** and **III**, but replacing $Gd(NO_3)_3{\cdot}5H_2O$ with $Eu(NO_3)_3{\cdot}6H_2O$ (**II**: 35.0 mg, 0.0785 mmol) and $Tb(NO_3)_3{\cdot}6H_2O$ (**III**; 22.6 mg, 0.0499 mmol). The Eu^{III}-loaded Gd^{III} complexes were prepared by first dissolving $Gd(NO_3)_3{\cdot}5H_2O$ (180 mg, 0.413 mmol) in 1 mL of an aqueous $Eu(NO_3)_3{\cdot}6H_2O$ solution contained in a 15 mL glass bottle. The 1 mL aliquot of $Eu(NO_3)_3{\cdot}6H_2O$ solution was prepared by diluting the concentrated $Eu(NO_3)_3{\cdot}6H_2O$ solution (0.0785 mmol·mL^{-1}) to varied concentrations (μmol·mL^{-1}): **IV** 0.785, **V** 1.57, **VI** 3.14, **VII** 6.28. A 9 mL of H_2BDC (144 mg, 0.867 mmol) in DMF was then added into each aliquot of the prepared lanthanide solution, which was then tightly closed and kept at 80 °C for 6 h. The Tb^{III}-loaded Gd^{III} complexes were prepared under similar synthesis conditions as **IX-VII** but diluting $Tb(NO_3)_3{\cdot}6H_2O$ solution (0.0499 mmol·mL^{-1}) to varied concentrations (μmol·mL^{-1}): **VIII** 0.499, **IX** 1.00, **X** 2.00, **XI** 3.99, instead of $Eu(NO_3)_3{\cdot}6H_2O$ solution.

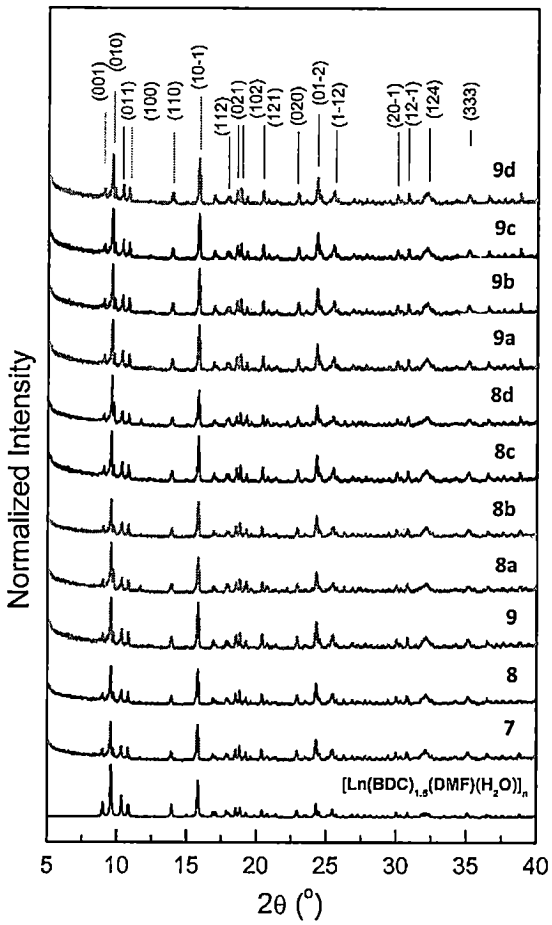

Fig. 3.1 PXRD patterns of **I-XI** compared with the simulated pattern of $[Gd^{III}_2(BDC)_3(DMF)_2(H_2O)_2]_n$ (CCDC NO. 949513)

(Fig. 3.2), the triplet state energy of BDC^{2-} could be estimated, *i.e.* 23 809 cm^{-1} (420 nm). With the excitation at 337 nm, the sensitization of **II** (Eu^{III}) and **III** (Tb^{III}) was exceptionally effective manifesting through the intense red Eu^{III}:$^5D_0 \rightarrow {}^7F_J$ (J=1-4) and green Tb^{III}:$^5D_4 \rightarrow {}^7F_J$ (J=6-3) emission. A broad and intense feature attributing to the ligand-centered $\pi^* \rightarrow \pi$ emission as found in spectrum of **I** was absent confirming the effective energy transfer from BDC^{2-} to both Eu^{III} and Tb^{III}. The heating of **II** and **III** from 303 *K* to 393 *K* apparently did not cause any significant change in their emitting colors although the falling of Eu^{III}:$^5D_0 \rightarrow {}^7F_J$ (J=1-4) and Tb^{III}:$^5D_4 \rightarrow {}^7F_J$ (J=6-3) emission intensities were apparent. Peak splitting was particularly observed for the Tb^{III}:$^5D_4 \rightarrow {}^7F_J$ (J=6-3) emissions at 393 *K* which should be due to the thermally quenching of the $^5D_4$ [5].

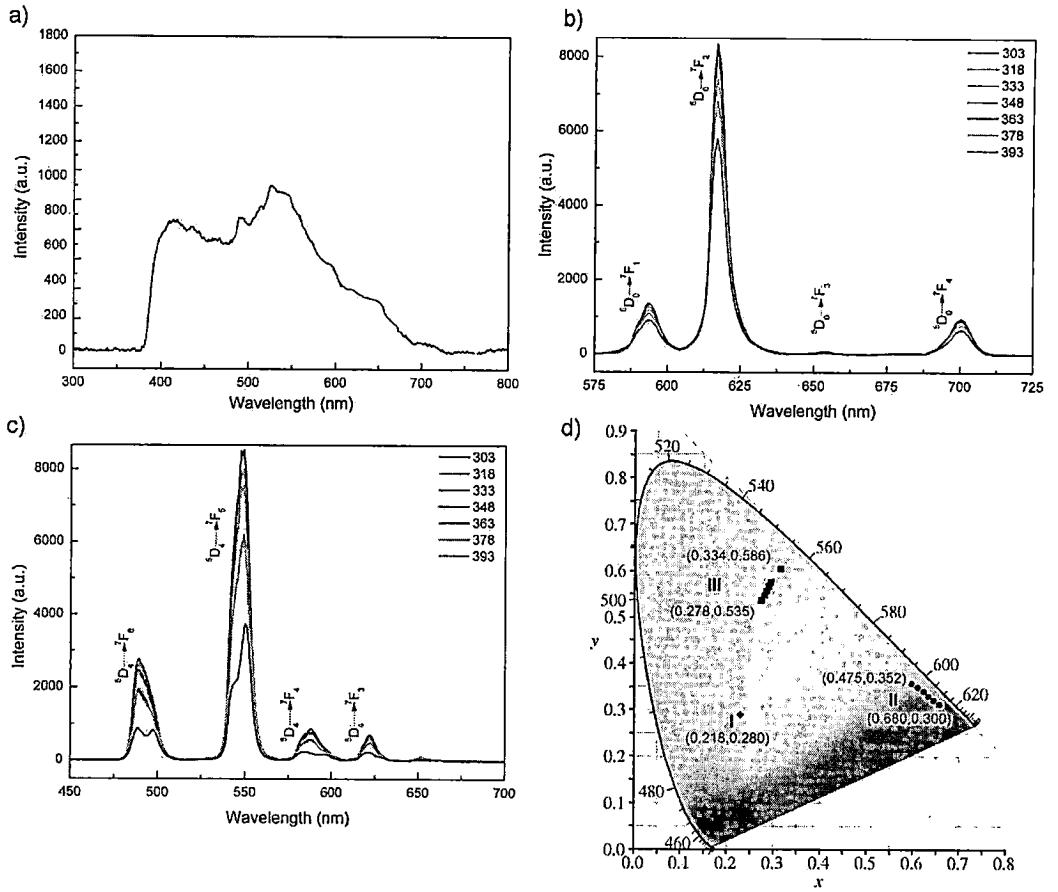

Fig. 3.2 Emission spectra of (a) **I** collected at room temperature, and (b) **II** and (c) **III** collected at different temperatures with (d) the corresponding coordinates in CIE colorimetric diagram (◆ = **I**, ● = **II**, ■ = **III**)

Regarding the emitting color of the Eu^{III}-loaded Gd^{III} complexes at room temperature (Fig. 3.3), shades of the red color apparently depended on the Eu^{III} content. The increased Eu^{III} contents (from **IV** to **VII**) evidently instigated significant change in the emission colors of the complexes, traversing from white (**IV**: 0.303, 0.351) to red (**V**: 0.660, 0.330) which is close to the color of the monometallic **II** (0.680, 0.300). This is consistent with their emitting spectra in which almost all Eu^{III}:$^5D_0 \rightarrow {}^7F_J$ emissions were pronounced in the spectra of **VI** and **VII**, whereas only the Eu^{III}:$^5D_0 \rightarrow {}^7F_J$ (J=1, 2) could be observed for **IV** and **V**.

On the other hand, the increased Tb^{III} contents (from **VIII** to **XI**) did not induced any practical change in the emitting colors, all of which were yellowish green corresponding to the CIE coordinates ranging from (0.307, 0.508) for **VIII** to (0.310, 0.529) for **XI**. To the naked eye, the

apparent color of **VIII-XI** was almost identical to the color of **III** (0.334,0.586). The insignificant alteration in green color of **VIII-XI** may ascribe to the exceptionally effective sensitization of Tb^{III} by BDC^{2-}, which is more effective than the Eu^{III} case, leading to a dominating green color even with trace amounts of Tb^{III} in the complexes. This feature is well consistent with an energy gap between the triplet state energy of BDC^{2-} and the accepting level of Tb^{III} ($^5D_4$) which is more appropriate than that of the Eu^{III} ($^5D_0$).

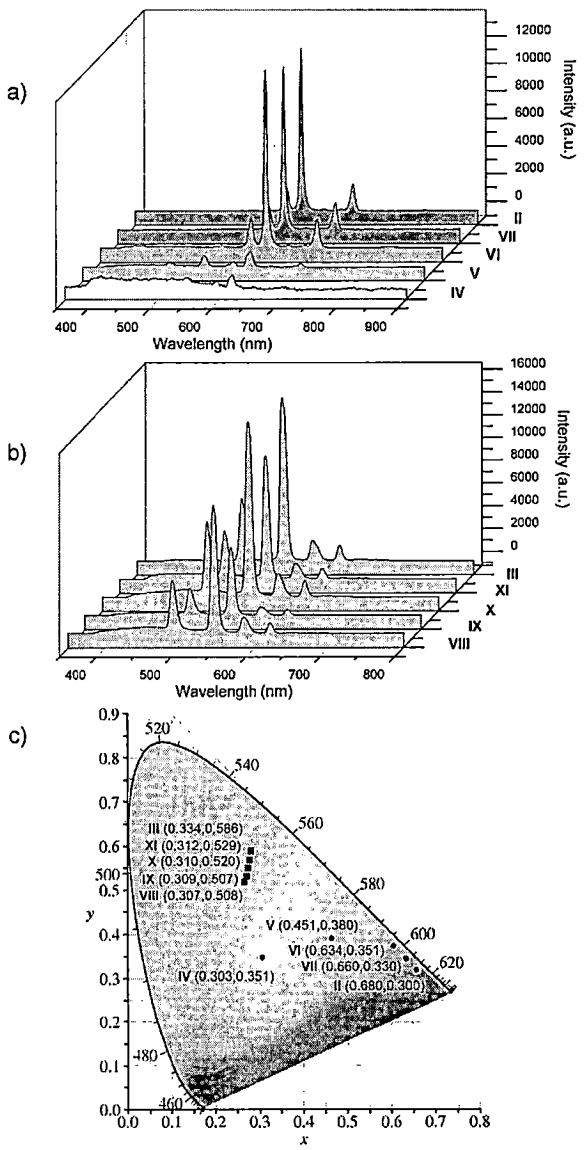

Fig. 3.3 Emission spectra of (a) **II, IV-VII**, and (b) **III, VIII-XI** collected at room temperature with (c) the corresponding coordinates in the CIE colorimetric diagram (● = **II, IV-VII**, ■ = **III, VIII-XI**)

3.3 Colorimetric-ratiometric temperature dependence of IV

Owing to the white emitting color at room temperature of **IV**, it was chosen for further colorimetric analysis. The thermally-induced color change in **IV** was distinctly visible despite the poor Eu^{III}:$^5D_0 \rightarrow {}^7F_J$ emissions (Fig. 3.4). Upon the heating from 303 to 393 *K*, the emitting color of **IV** gradually changed from white (0.315, 0.359) at 303 *K* to reddish pink (0.446, 0.291) at 393 *K*. The change was noticeably reversible upon successive heating and cooling cycles. The thermally-induced non-radiative decay apparently imparted drastic effect on the ligand-centered $\pi^* \rightarrow \pi$ emission revealed *via* the substantial deterioration of the corresponding emission band. Although similar influence was explicit for the Eu^{III}:$^5D_0 \rightarrow {}^7F_J$ emissions, the reduction in intensities was relatively insignificant.

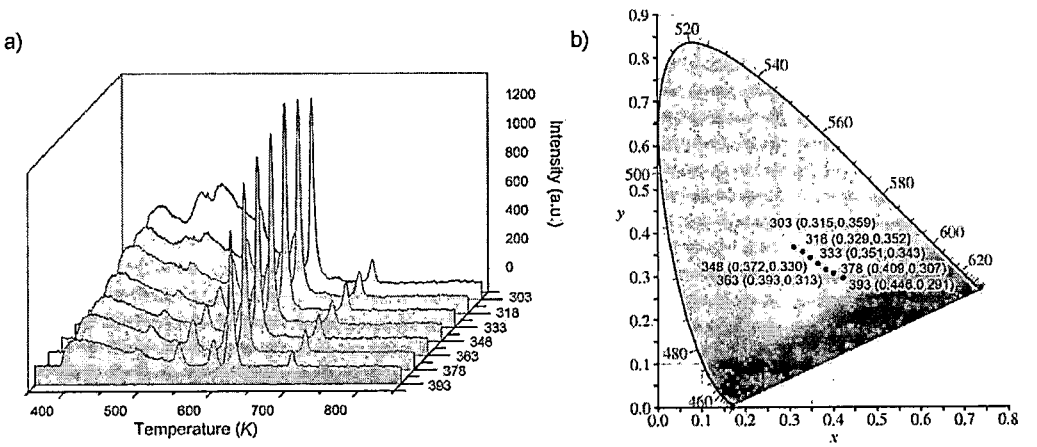

Fig. 3.4 (a) Emission spectra of **IV** collected at different temperatures with (b) the corresponding coordinates (*x*,*y*) in CIE colorimetric diagram

Within the CIE XYZ color matching systems, the colorimetric coordinates (*x*,*y*) of temperature dependent emitting colors of IV were noticeably aligned with a uniform tendency and a regular gap between each coordinate. From the plots of the temperature dependent *x* and *y* (Fig. 3.5), a diversion in temperature dependencies of the two parameters was vivid and a linear correlation could intriguingly be established: $R^2(x)$ =0.994, $R^2(y)$ = 0.976. With reference to these *x* and *y* parameters, linear correlation of *x*/*y* and *x*/(*x*+*y*) ratios with temperatures were examined from which a better correlation was yielded for the *x*/(*x*+*y*) ratio. The temperature dependent *x*/(*x*+*y*) ratio was therefore adopted for the calculation of the ratiometric Δ. Disparity in temperature readouts from the expected values despite the high precision at temperatures ≥ 363 *K* was however observed, which should attribute to the deviation of *y* parameter from linearity. The working temperature range was therefore truncated to 303-348 *K*, from which an excellent linear correlation

(R^2 = 0.997) could be achieved. Over ten successive measurements at three temperatures, the measurements provided satisfying repeatability (R) and temperature resolution (δT) in term of standard deviation (SD) of the readouts although there were few data points departed from the expected values. Based on these data the relative sensitivities (Sr) of the measurements were calculated showing the descending tendency with the increasing temperature providing the maximum (Sm) and the minimum values of 0.579 %·K^{-1} (303 K) and 0.494 %·K^{-1} (348 K), respectively.

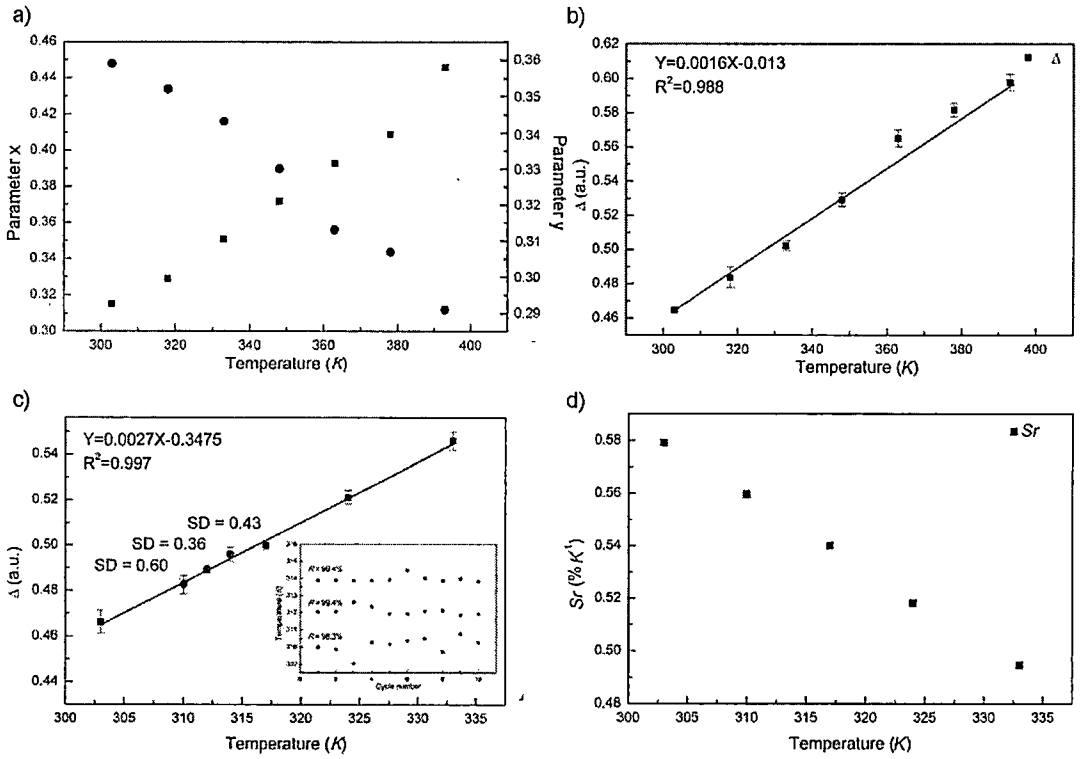

Fig. 3.5 (a) Diverse temperature dependencies of x (●) and y (■) of **IV**, with the corresponding Δ calculated from $x/(x+y)$ over (b) 302-393 K and (c) 303-333 K, the average temperature readouts of ten successive readings (inset; R > 99%), and (d) the corresponding Sr

Since the emitting colors of **IV** are within the human eye perception [1], the CIE coordinates x and y were converted to the R and G parameters of the sRGB color matching system using nix™ Color Sensor software package. Exceptional linear correlation (R^2 = 0.999) was achieved for the temperature dependent ratiometric Δ over the same temperature range if the R/(R+G) ratio was employed (Fig. 3.6). On the basis of R and G parameters, the temperature measuring performance of **IV** was also evaluated, revealing improved SD (δT) and R for the ten

successive measurements compared with the CIE XYZ case. In a similar fashion to the measurements based on the $x/(x+y)$ ratio, the *Sr* of the measurements based on the R/(R+G) ratio also declined with the rising of temperature. Considerable enhancement of the maximum and the minimum relative sensitivity, *i.e.* 1.12 $\%\cdot K^{-1}$ (303 *K*) and 0.839 $\%\cdot K^{-1}$ (348 *K*), were however revealed. Irrespective of the color matching systems, colorimetric analysis was therefore viable as a new strategy in founding the ratiometric Δ parameters from which a high performance ratiometric temperature sensing was achieved.

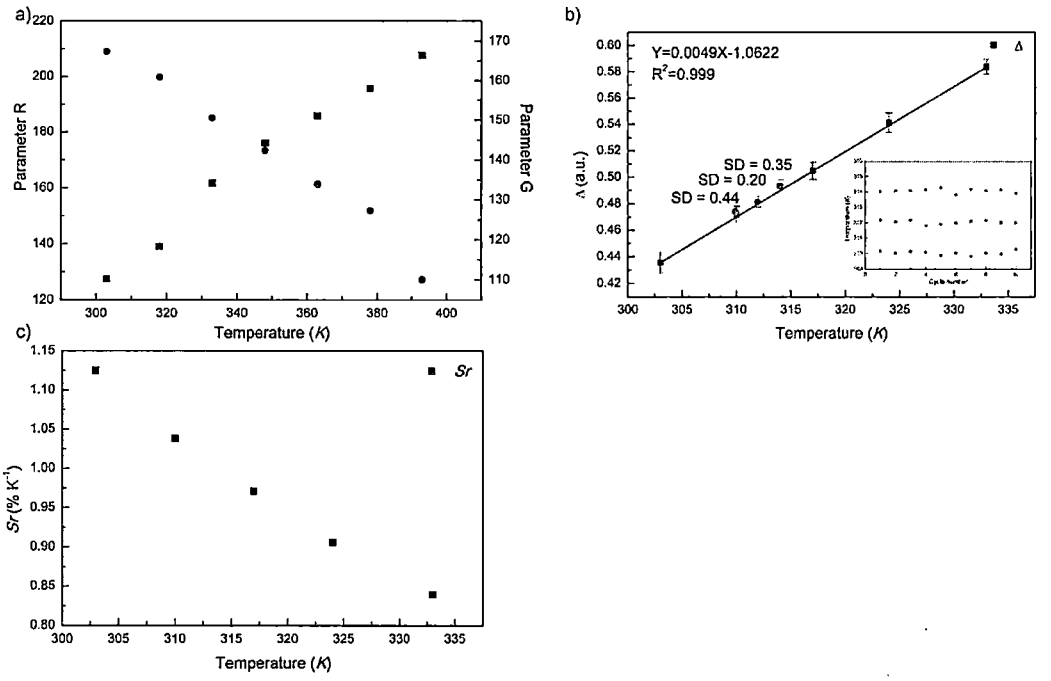

Fig. 3.6(a) Diverse temperature dependencies of R (●) and G (■) of **IV**, with (b) the corresponding Δ calculated from R/(R+G) over 303-333 *K* and the average temperature readouts of ten successive readings (inset; $R > 99\%$), and (c) the corresponding *Sr*

3.4 Conclusion

In view of ratiometric temperature sensing, colorimetric analysis was introduced as a new and effective strategy for the establishment of reliable ratiometric Δ parameter with reference to **8a** exhibiting temperature dependent emitting colors. Irrespective of the employed color matching systems, *i.e.* sRGB and CIE XYZ, exceptional performance specified by a linear correlation of the ratiometric Δ calculated from either $x/(x+y)$ or R/(R+G) could be derived over the 303-348 *K* range, from which exceptional δT, *R* and maximum *Sr* could be achieved. As the reported working

temperature range covers biological temperatures, a new opportunity in the development of high performance sensor for physiological temperature measurements is revealed for lanthanide coordination polymers.

REFERENCES

[1] Smith, T.; Guild, J. *Transac. Opt. Soc.* **1931**, *33*(3), 73-134.

[2] Decadt, R.; Hecke, K.V.; Depla, D.; Leus, K.; Weinberger, D.; Driessche, I.V.; Der Voort, P.V.; Deun, R.V.N. *Inorg. Chem.* **2012**, *51*(21), 11623-11634.

[3] Grishko, A.Y.; Utochnikova, V.V.; Averin, A.A.; Mironov, A.V.; Kuzmina, N.P. *Eur. J. Inorg. Chem.* **2015**, *10*, 1660-1664.

[4] Yang, X.-P.; Jones, R.A.; Rivers, J.H.; Laia, R.P.-J. *Dalton Trans.* **2007**, *35*, 3936-3942.

[5] Yamashita, T.; Ohishi, Y. *J. Appl. Phys.* **2007**, *102*,123107.

CHAPTER 4

Structural Variation and Preference in Lanthanide pyridine-2,6-dicarboxylates

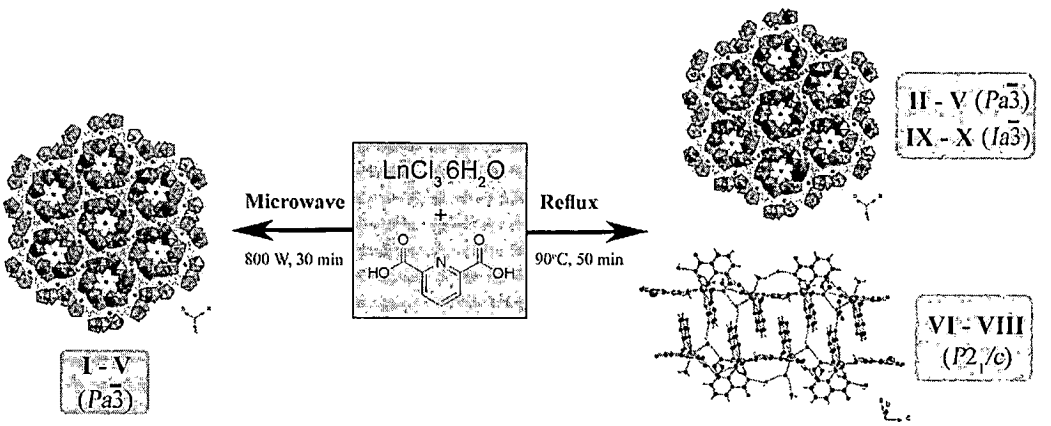

$[Ln(pdc)(H_2O)_4]_3 \cdot 3Cl$ Ln = Pr (**I**), Nd (**II**), Sm (**III**), Eu (**IV**), Gd (**V**)

$[Ln(pdc)(Hpdc)(H_2O)_2] \cdot 3H_2O$ Ln = Pr (**VI**), Nd (**VII**), Sm (**VIII**)

$[Ln(pdc)(H_2O)_4]_3 \cdot 3Cl$ Ln = Sm (**IX**), Eu (**X**)

Due to the hard acid nature of the trivalent lanthanide ions, different types of multicarboxylic acids including pyridine-2,6-dicarboxylic acid (H_2pdc) have been explored as organic linkers in the fabrication of novel lanthanide frameworks [1-11]. In solid state structures, the H_2pdc ligand may be present in the partially deprotonated ($Hpdc^-$) or the fully deprotonated (pdc^{2-}) forms. According to the survey on the lanthanide-H_2pdc coordination polymers submitted to the Cambridge Structure Database [12], the H_2pdc ligand almost always adopts, nonetheless, the fully deprotonated form, and twelve modes of coordination are found with few typical preferences (Scheme 4.1). The chelation of the ligand upon the coordination seems to be usual. The solid state structures of these lanthanide based coordination polymers intriguingly exhibit proclivity to be either one- or three-dimensional depending on subtle alteration in the synthesis and the structures. The template effect of the chloride anion in the formation of the three-dimensional $[Ln(pdc)(H_2O)_4]_3 \cdot 3Cl$, for example, was investigated compared with the formation of the one-dimensional $[Ln(pdc)(Hpdc)(H_2O)_2] \cdot 3H_2O$ [10,13-16].

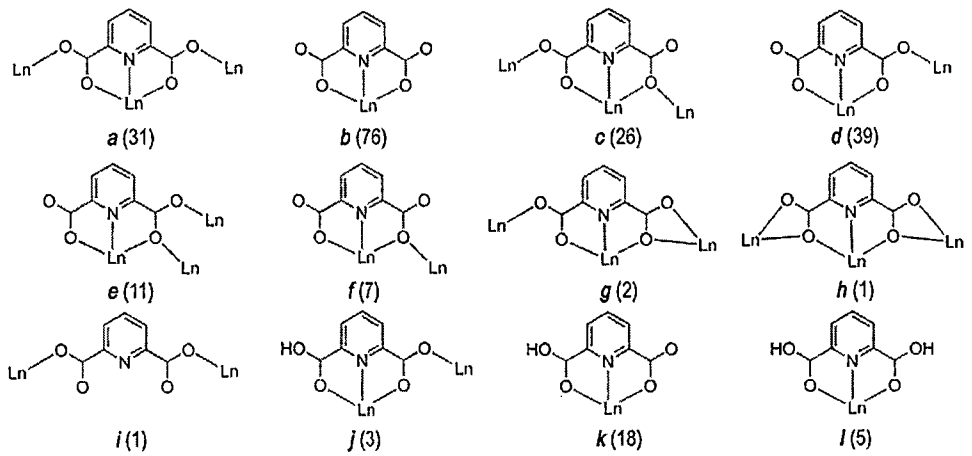

Scheme 4.1 Diagrammatic depiction of twelve coordination modes adopted by the H_2pdc ligand in lanthanide based coordination polymers deposited to the CSD. Frequencies of occurring are shown in brackets.

Based on these information, ten new lanthanide coordination polymers have been designed and synthesized using the H_2pdc ligand. The influences of two heating techniques with different heating mechanism and kinetics, namely the conventional heating under reflux and the dielectric microwave heating, on the final structures have been investigated. The synthesized structures can be classified to three different groups according to their structural symmetries (Scheme 4.2); (i) the cubic $Pa\bar{3}$ structures of $[Ln(pdc)(H_2O)_4]_3 \cdot 3Cl$ where Ln = Pr (**I**), Nd (**II**), Sm (**III**), Eu (**IV**), and

Gd (**V**), (ii) the monoclinic $P2_1/c$ structures of $[Ln(pdc)(Hpdc)(H_2O)_2]\cdot 3H_2O$ where Ln = Pr (**VI**), Nd (**VII**), and Sm (**VIII**), and (iii) the cubic $Ia\bar{3}$ structures of $[Ln(pdc)(H_2O)_4]_3\cdot 3Cl$ where Ln = Sm (**IX**), and Eu (**X**). Structural differences and preferences are rationalized and discussed. Thermogravimetric and photoluminescence properties of selected complexes are included.

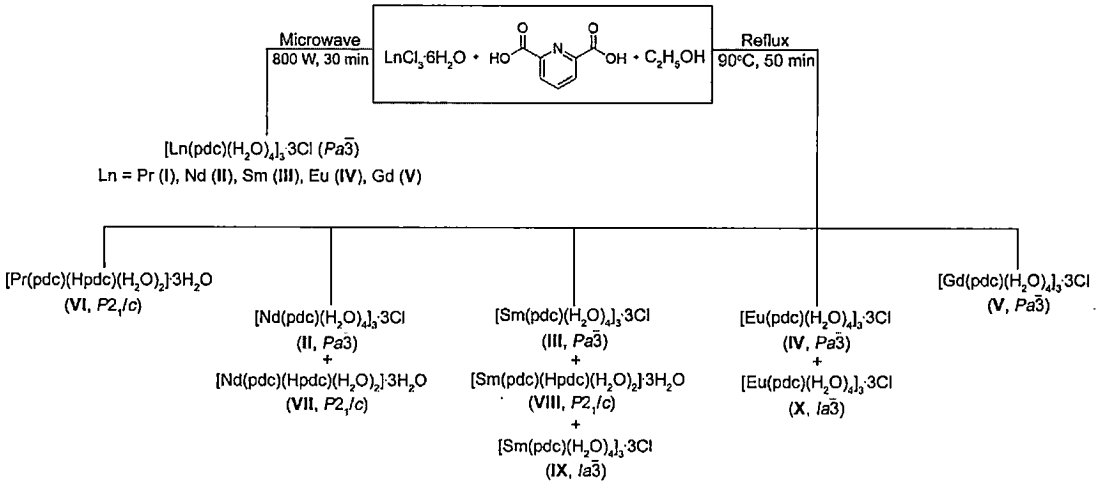

Scheme 4.2 Diagrammatic presentation summarizing the syntheses and the yielded complexes.*

4.1 Influences of heating techniques on crystal structures

Despite the different heating techniques, clear solutions of colors characteristic to the corresponding lanthanide ions were yielded alike. Crystals as the sole products appeared after the solvents evaporated in few days. Under an optical microscope, the two different heating techniques provided crystals of similar habits although qualities and sizes of these crystals varied. There was not any significant correlation between the heating techniques and qualities of the yielded crystals.

*The mixtures of the 1 : 1 : 128 for the $LnCl_3\cdot 6H_2O$: H_2pdc : ethanol mole ratio were employed for every reaction. **Microwave syntheses.** $LnCl_3\cdot 6H_2O$ (0.100 mmol) and H_2pdc (0.100 mmol) were dissolved in 10.00 mL of ethanol using a Teflon vessel. After the vessel was sealed and placed in the household microwave oven (Samsung MS23F301E), the reaction was conducted at 800 W for 30 min and left to cool down to room temperature. The crystals were obtained after the ethanol solvent evaporated in few days. It has been revealed by the PXRD and the single crystal X-ray diffraction that crystals of $[Ln(pdc)(H_2O)_4]_3\cdot 3Cl$ {$Pa\bar{3}$; Ln = Pr (**I**), Nd (**II**), Sm (**III**), Eu (**IV**) and Gd (**V**)} were obtained. There are nonetheless few diffraction peaks in the collected PXRD patterns which could not be indexed suggesting the existence of other crystalline phases. The attempts to find crystals of other structures beside **I-V** were however not successful, and further characterization was therefore not performed. **Heating under reflux.** Rather than the use of the microwave heating, the reaction mixtures were heated at 90°C under reflux for 50 min and left to cool down to room temperature. Crystals of similar habits to those obtained from the microwave syntheses were obtained after the evaporation of the ethanol solvent in few days. The PXRD and the single crystal X-ray diffraction indicated the yielding of five more distinct crystals; $[Ln(pdc)(Hpdc)(H_2O)_2]\cdot 3H_2O$ {$P2_1/c$; Ln = Pr (**VI**), Nd (**VII**), Sm (**VIII**)} and $[Ln(pdc)(H_2O)_4]_3\cdot 3Cl$ {$Ia\bar{3}$; Ln = Sm (**IX**), Eu (**X**)}.

The PXRD patterns collected on the ground crystals (Fig. 4.1) and the single crystal data however suggest the acquiring of ten different structures among which seven structures are new (Scheme 4.2). The microwave heating apparently led to the formation of the isostructural cubic complexes **I-V** ($Pa\bar{3}$), which is also isostructural to the previously reported $[La(pdc)(H_2O)_4]_3 \cdot 3Cl$ [3]. There are however few mismatched diffraction peaks between the collected PXRD patterns and the patterns simulated from the single crystal data. These unidentified peaks appear at closely similar 2θ in every pattern. The existence of the other crystalline structure can therefore be concluded, although the attempt to find single crystals of the other structures beside **I-V** was not successful.

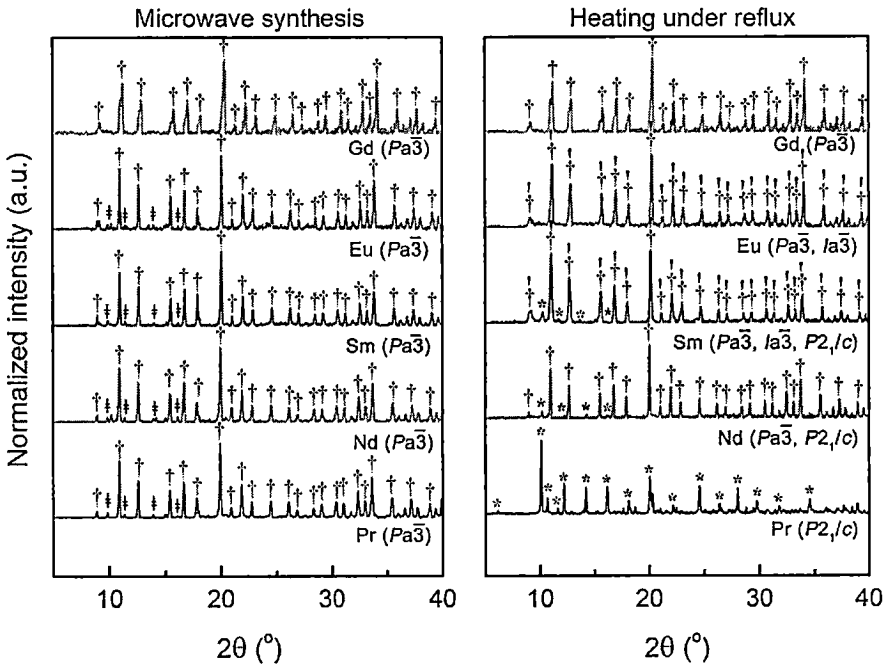

Fig. 4.1 Experimental PXRD patterns collected on bulk solids obtained from the microwave synthesis (left) and the conventional heating (right). Symbols: † = $Pa\bar{3}$, ˡ = $Ia\bar{3}$, * = $P2_1/c$, ǂ = unknown.

The heating under reflux, on the other hand, led to the formation of different structures which can be classified into three groups of isostructural crystals: (i) the monoclinic $P2_1/c$ structures **VI** (Pr), **VII** (Nd) and **VIII** (Sm), (ii) the cubic $Ia\bar{3}$ structures **IX** (Sm) and **X** (Eu), and (iii) the cubic $Pa\bar{3}$ structures **II** (Nd), **III** (Sm), **IV** (Eu) and **V** (Gd). Few observations are noteworthy. First, there is a tendency in crystal symmetry alteration across the lanthanide series. The crystal symmetry increases from the pure monoclinic $P2_1/c$ in Pr (**VI**) to the mixtures of the monoclinic $P2_1/c$ and

the cubic $Pa\bar{3}$ and $Ia\bar{3}$ in Nd (**II**+**VII**) and Sm (**III**+**VIII**+**IX**), to the mixed cubic $Pa\bar{3}$ and $Ia\bar{3}$ in Eu (**IV**+**X**), and to the pure cubic $Pa\bar{3}$ in Gd (**V**). Second, the cubic $Ia\bar{3}$ structures **IX** (Sm) and **X** (Eu) are the supramolecular isomers of the cubic $Pa\bar{3}$ structures **III** (Sm) and **IV** (Eu). Third, only the monoclinic $P2_1/c$ (**VI**; Pr) and the cubic $Pa\bar{3}$ (**V**; Gd) structures can be yielded as pure phases if the heating under reflux was applied. Forth, the cubic structures are more favorable than the monoclinic independent of the heating techniques with the exception of praseodymium complexes.

The fact that the crystals were grown after the evaporation of the ethanol solvent in every case suggests the nucleation process to be critical in determining the final structures. Since the nucleation process is kinetically controlled [17,18], the cubic $Pa\bar{3}$ structures are therefore favored kinetically. The conventional heating, which generally provides thermodynamically favorable structures, however, results in structures of different symmetries and supramolecular assemblies. These structures should therefore be comparatively favored from the thermodynamic point of view, although the $Pa\bar{3}$ structures should be the most favorable structures from both kinetic and thermodynamic viewpoints manifested in the yielding of these structures from every synthesis except the praseodymium case (**VI**).

An apparent tendency in the changing of the crystal structures across the reported lanthanide series when the conventional heating was employed can be due to the differences in numbers of the coordinating organic ligands and water molecules the latter of which depends on the hydration enthalpies of the lanthanide metal ions. With the lowest hydration preference, only two water molecules are included in the coordination sphere of the praseodymium ion (**VI**). Number of the coordinating water molecules in the more favorable cubic structures of the heavier lanthanide ions with larger hydration energies are four. In addition, the praseodymium ion of relatively large ionic radius can accommodate more organic ligands compared with the smaller lanthanide metal ions. This is well reflected in the Ln^{III} : pdc^{2-}/$Hpdc^{-}$: H_2O_{ligand} ratios; 1 : 2 : 2 (**VI**-**VIII**) compared with 1 : 1 : 4 (**I**-**V**, **IX** and **X**). The larger number of the coordinating water molecules in the latter group should also attribute to the coordination requirement of the lanthanide ions. Similar structural variation of the cubic $Pa\bar{3}$ and the monoclinic $P2_1/c$ was notably reported for $[La(pdc)(H_2O)_4]_3 \cdot 3Cl$ [3]. The change was however induced by the removal of the chloride anions from the cubic $Pa\bar{3}$ $[La(pdc)(H_2O)_4]_3 \cdot 3Cl$ structure using $AgBF_4$ which led to the formation of the monoclinic $P2_1/c$ ladder-like $[La(pdc)(Hpdc)(H_2O)_2] \cdot 3H_2O$ [3].

4.2 Crystal structures description

Crystallographic data of **I**-**V** were collected at 296(2) *K* using a Bruker D8 QUEST CMOS diffractometer equipped with graphite-monochromated Mo K_α radiation ($\lambda = 0.71073$ Å), and those

of **VI-X** were collected using a Bruker D8 Venture diffractometer (Photon CMOS detector) equipped with a micro focus sealed tube X-ray source with graphite monochromatic Mo K_α radiation (λ = 0.71073 Å). Empirical absorption corrections were applied to all data using the SADABS program [13]. Every structure was solved by direct methods within the SHELXS program [14] and refined on F^2 by the full-matrix least squares technique using the SHELXL program [14] *via* the Olex2 interface [15].

In order to take the contribution of the disordered chloride anions into account in the cases of **I-V**, the SQUEEZE option provided in the program PLATON [19] was implemented with every structure after two chloride anions were located. Numbers of electrons per unit cell to be found in the framework accessible voids were determined, and numbers of equivalent chloride anions were calculated: 10 (**I** and **IV**), 9 (**II** and **III**) and 7 (**V**) chlorides per unit cell leading to the addition of one chloride per formula. Similar treatment was also required for **VI-X.** In the cases of **VI** and **VII**, numbers of equivalent water molecules were calculated: 10 (**VI**) and 5 (**VII**) crystallized water molecules per unit cell. These values led to the approximation of one crystallized water per formula. In the cases of **VIII** and **X**, 9 chlorides per unit cell was calculated leading to one additional chloride per formula. The application of SQUEEZE on these structures resulted in significant improvement in the *R* and *Rw* values. There is additional site disordering at the chloride anion in every structures possessing the chloride as guest anions. Appreciable improvement in the final residual electron density maxima and minima was achieved after the treatment of such. The crystallographic and refinement data of **I-X** are summarized in Table 4.1.

The cubic $Pa\bar{3}$ $[Ln(pdc)(H_2O)_4]_3{\cdot}3Cl$ (I-V). Complexes **I-V** are revealed to be isostructural with the previously reported lanthanum complex, $[La(pdc)(H_2O)_4]_3{\cdot}3Cl$ [3]. According to the results from the SQUEEZE calculations after the assignment of two well defined chloride anions, the general formula of $[Ln(pdc)(H_2O)_4]_3{\cdot}3Cl$ can be deduced. The presence of the three unbound chlorides in the formula is in good accordance with the tri-positive charges of the $[Ln(pdc)(H_2O)_4]_3^{3+}$ framework. Complexes **I-V** crystallize in the same cubic $Pa\bar{3}$ space group with cell parameters *a* and *V* descending from **I** (Pr) to **V** (Gd) consistent with the lanthanide contraction. The asymmetric units of **I-V** are alike, comprising one unique lanthanide ion, a fully deprotonated pdc^{2-} ligand, four coordinated water molecules, and two unbound chloride anions. The other chloride anion has been treated as a diffuse contribution to the overall scattering without specific atom position by SQUEEZE. One of the well-defined chloride anions in every structure, except **III**, shows additional disorder over two crystallographic sites, with different site occupancy Cl2A : Cl2B ratios; 0.932 : 0.068 (**I**), 0.605 : 0.395 (**II**), 0.582 : 0.418 (**IV**), and 0.719 : 0.281 (**V**). Atom Cl2 in structure **III** shows similar disorder but over three crystallographic sites with site occupancy

Table 4.1 Crystallographic data and refinement details for **I-V**

	I	II	III	IV	V
CCDC No.	1448352	1448353	1448354	1494337	1494338
Formula[a]	$C_{21}H_{33}N_3O_{24}Cl_3Pr_3$	$C_{21}H_{33}N_3O_{24}Cl_3Nd_3$	$C_{21}H_{33}N_3O_{24}Cl_3Sm_3$	$C_{21}H_{33}N_3O_{24}Cl_3Eu_3$	$C_{21}H_{33}N_3O_{24}Cl_3Gd_3$
Formula weight[a]	1240.57	1250.57	1268.93	1273.74	1289.60
Temperature (K)	296(2)	296(2)	296(2)	296(2)	296(2)
Crystal system	Cubic	Cubic	Cubic	Cubic	Cubic
Space group	$Pa\bar{3}$ (No. 205)	$Pa\bar{3}$ (No. 205)	$Pa\bar{3}$ (No. 205)	$Pa\bar{3}$ (No. 205)	$Pa\bar{3}$ (No. 205)
a (Å)	19.9853(3)	19.9091(6)	19.8330(3)	19.8085(6)	19.7822(6)
V (Å)3	7982.4(4)	7891.4(4)	7801.3(4)	7772.4(4)	7741.5(4)
Z	8	8	8	8	8
F(000)	4664	4688	4736	4760	4784
ρ (mg·m^{-3})	2.006	2.046	2.100	2.121	2.152
μ (mm^{-1})	3.824	4.112	4.682	5.008	5.307
Data/Restraints/Parameters	4283/6/168	3268/0/168	3966/12/170	2997/0/168	2953/0/168
GOOF	1.104	1.153	1.098	1.187	1.199
Before SQUEEZE					
R_1 (I=2σ(I))[b]	0.0490	0.0470	0.0569	0.0598	0.0404
wR_2 (all data)[b]	0.1419	0.1433	0.1701	0.1542	0.1116
After SQUEEZE					
R_1 (I=2σ(I))[b]	0.0383	0.0293	0.0389	0.0555	0.0325
wR_2 (all data)[b]	0.0686	0.0627	0.0739	0.0703	0.0565

[a]Include one chlorine atom approximated using SQUEEZE. [b]$R_1 = \Sigma||F_o|-|F_c||/|F_o|$, $wR_2 = [\Sigma w(F_o^2-F_c^2)^2/\Sigma w(F_o^2)_2]^{1/2}$.

Table 4.1 Crystallographic data and refinement details for **VI-X** (continued)

	VI	**VII**	**VIII**	**IX**	**X**
CCDC No.	1494339	1494340	1491342	1494341	1494343
Formula[a]	$C_{14}H_{14}N_2O_{12}Pr$	$C_{14}H_{14}N_2O_{12}Nd$	$C_{14}H_{19}N_2O_{14}Sm$	$C_{21}H_{33}Cl_2N_3O_{24}Sm_3$	$C_{21}H_{33}Cl_2N_3O_{24}Eu_3$
Formula weight[a]	543.18	546.51	589.66	1233.48	1238.28
Temperature (*K*)	298(2)	298(2)	273(2)	298(2)	298(2)
Crystal system	monoclinic	monoclinic	monoclinic	cubic	cubic
Space group	$P2_1/c$ (No. 14)	$P2_1/c$ (No. 14)	$P2_1/c$ (No. 14)	$Ia\bar{3}$ (No. 206)	$Ia\bar{3}$ (No. 206)
a (Å)	14.785(3)	14.810(3)	13.9892(5)	19.8346(9)	19.8027(10)
b (Å)	10.9727(18)	11.064(2)	11.2046(3)	-	-
c (Å)	12.936(2)	12.944(3)	12.8312(3)	-	-
α (°)	90.00	90.00(3)	90.00	90.00	90.00
β (°)	100.256(6)	100.23(3)	102.314(2)	90.00	90.00
γ (°)	90.00	90.00(3)	90.00	90.00	90.00
V (Å)^3	2065.0(6)	2087.4(7)	1964.93(10)	7803.2(6)	7765.6(7)
Z	4	4	4	8	8
F(000)	1068.0	1072.0	1164.0	4736.0	4760.0
ρ (mg·m^{-3})	1.747	1.739	1.993	2.100	2.118
μ (mm^{-1})	2.421	2.548	3.067	4.681	5.013
Data/Restraints/Parameters	9145/0/270	7906/0/270	4897/0/294	2841/0/88	3670/2/88
GOOF	1.049	1.038	1.096	1.194	1.177
Before SQUEEZE					
R_1 (I=2σ(I))[b]	0.1407	0.1924	0.0467	0.0720	0.1050
wR_2 (all data)[b]	0.2963	0.2369	0.0799	0.1488	0.1506
After SQUEEZE					
R_1 (I=2σ(I))[b]	0.0836	0.0719	0.0339	0.0532	0.0649
wR_2 (all data)[b]	0.2346	0.1762	0.0799	0.1075	0.1089

Cl2A : Cl2B : Cl2C ratio of 0.55 : 0.40 : 0.05. The attempt to exclude Cl2B and Cl2C from the refinement of **I** and **III**, respectively, resulted in injudiciously elongated ellipsoids of the corresponding Cl2A and Cl2B.

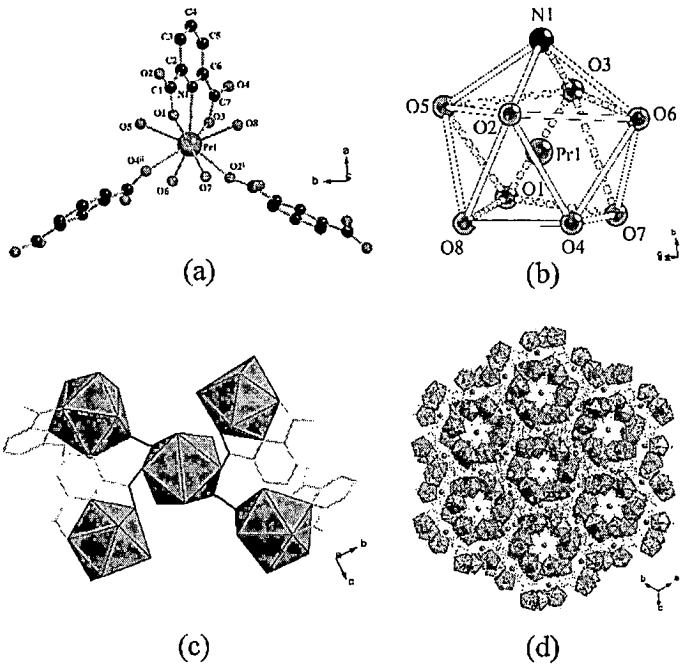

Fig. 4.2 Illustrations showing (a) an extended asymmetric unit, (b) the *SAPRS*-{LnO_8N} unit, (c) the linkage of these units, and (d) the infinite tubular structure of **I** (as representative of **I-V**, **IX-X**).

The Ln ion in **I-V** is nine-fold coordinated to three pdc^{2-} ligands through the pyridyl N1 and the carboxyl O1-O4 atoms and the water O5-O8 atoms (Fig. 4.2a). The Ln–O and Ln–N bond distances of the structures **I-V** are in good agreement with those of $[La(pdc)(H_2O)_4]_3 \cdot 3Cl$ [3] and consistent with the lanthanide contraction. The bond valence sum calculations based on these bond distances affirm the trivalent state of the lanthanide ions. The nine coordinated atoms delineate the square-face monocapped antiprism coordination geometry, *SAPRS*-{LnO_8N} (Fig. 4.2b), with the pdc^{2-} ligand using two μ_2-η^1:η^1 carboxyl groups and the pyridyl N atom in coordination (mode *a* in Scheme 4.1, Fig. 4.2c). The coordination as described results in almost complete co-planarity between the carboxyl groups and the central pyridyl ring.

The infinite frameworks of **I-V** are built up of the discrete *SAPRS*-{LnO_8N} units, each of which is linked to four adjacent units *via* three pdc^{2-} linkers. The linkages of the *SAPRS*-{LnO_8N} units result in the formation of four discrete one-dimensional channels extending in four <1 1 1>

Table 4.2 List of hydrogen bonding distances (D···A, Å) and angles (∠D–H···A,°) for **I-X**

I[a]			**II**[b]		
D–H···A	D···A	∠D–H···A	D–H···A	D···A	∠D–H···A
O5–H5A···O2^{i}	3.171(8)	145	O5–H5A···O3^{i}	2.931(2)	147
O5–H5A···O3^{ii}	2.874(7)	132	O5–H5B···Cl2A^{ii}	3.084(8)	140
O5–H5B···Cl2A	3.141(2)	82	O5–H5B···Cl2B	3.281(7)	122
O5–H5B···Cl2B	3.142(2)	111	O6–H6B···O3^{i}	2.687(7)	151
O6–H6A···O1^{iii}	2.640(1)	160	O7–H7B···O1^{iii}	2.650(7)	154
O8–H8B···Cl1	3.113(1)	131	O8–H8B···Cl1	3.120(4)	97
			O8–H8B···Cl2A	3.481(3)	127
III[c]			**IV**[d]		
D–H···A	D···A	∠D–H···A	D–H···A	D···A	∠D–H···A
O5–H5A···Cl2A	3.260(7)	132	O5–H5B···Cl1	3.136(5)	134
O5–H5A···Cl2B^{i}	3.055(6)	133	O6–H6A···O3^{i}	2.689(2)	153
O5–H5B···O3^{ii}	2.941(4)	144	O7–H7B···O1^{ii}	2.637(3)	160
O6–H6A···O1^{iii}	2.638(7)	157	O8–H8A···Cl2A^{iii}	3.053(8)	133
O7–H7B···O3^{ii}	2.675(5)	138	O8–H8A···Cl2B	3.242(9)	136
O8–H8A···Cl2C	2.750(3)	85	O8–H8B···O3^{i}	2.929(1)	140
O8–H8B···Cl1	3.131(5)	119			
V[e]			**VI**[f]		
D–H···A	D···A	∠D–H···A	D-H···A	D···A	∠D-H···A
O5–H5A···Cl2A	3.476(3)	149	O9-H9A···O14^{i}	2.8236	153
O5–H5B···Cl1	3.123(8)	145	O9-H9B···O13^{ii}	2.6504	111
O6–H6B···O1^{i}	2.634(8)	161	O10-H10A···O3^{iii}	2.7788	142
O7–H7B···O3^{ii}	2.681(9)	158	O10-H10B···O7^{iv}	2.7773	147
O8–H8A···O3^{ii}	2.902(3)	151	O13-H13A···O6	2.7464	149
O8–H8B···Cl2A^{iii}	3.106(8)	139	O13-H13B···O14	2.9051	156
O8–H8B···Cl2B	3.271(9)	124	O14-H14A···O5	2.9373	170
			O14-H14B···O6^{ii}	2.8732	139
VII[g]			**VIII**[h]		
D-H···A	D···A	∠D-H···A	D-H···A	D···A	∠D-H···A
O9-H9A···O11^{i}	2.7091	118	O9-H9A···O12^{i}	2.7143	126
O9-H9B···O12^{ii}	2.8173	158	O9-H9B···O11^{ii}	2.7526	143
O10-H10A···O2^{iii}	2.7894	103	O10-H10A···O1^{iii}	2.7176	129
O10-H10B···O6^{iv}	2.7690	163	O10-H10B···O7^{iv}	2.7216	142
O11-H11A···O8	2.7384	142	O11-H11A···O6^{i}	2.8759	161
O11-H11B···O12	2.9132	141	O11-H11B···O9^{iv}	2.7526	167
O12-H12A···O5	3.2154	166	O12-H12A···O6	2.6866	172
O12-H12A···O7	2.9505	113	O12-H12B···O11	2.9041	145
O12-H12B···O8^{i}	2.9189	165	O13-H13A···O12	3.0075	132
			O14-H14A···O13^{v}	2.7926	103
			O14-H14B···O13^{v}	2.7926	100
IX[i]			**X**[j]		
D-H···A	D···A	∠D-H···A	D-H···A	D···A	∠D-H···A
O3-H3A···O1^{i}	3.0782	118	O3-H3A···O1^{i}	3.0821	109
O3-H3B···Cl1B	3.1946	142	O3-H3B···Cl1B^{ii}	3.1894	150
O4-H4A···O1^{i}	2.6478	135	O4-H4B···O1^{iii}	2.6539	151

[a] Symmetry codes: (i) = -0.5+*x*, 0.5-*y*, 1-*z*; (ii) = 0.5-*x*, 0.5+*y*, *z*; (iii) = -0.5+*x*, *y*, 0.5-*z*

[b] Symmetry codes: (i) = 0.5-*x*, 0.5+*y*, *z*; (ii) = 0.5+*x*, *y*, 0.5-*z*; (iii) = -0.5+*x*, *y*, 0.5-*z*

[c] Symmetry codes: (i) = 0.5+*x*, *y*, 0.5-*z*; (ii) = 0.5-*x*, 0.5+*y*, *z*; (iii) = -0.5+*x*, *y*, 0.5-*z*

[d] Symmetry codes: (i) = 0.5-*x*, 0.5+*y*, *z*; (ii) = -0.5+*x*, *y*, 0.5-*z*; (iii) = 0.5+*x*, *y*, 0.5-*z*

[e] Symmetry codes: (i) = *x*, 0.5-*y*, -0.5+*z*; (ii) = 0.5+*x*, *y*, 0.5-*z*; (iii) = *x*, 0.5-*y*, 0.5+*z*

[f] Symmetry codes: (i) = *x*, 1/2 -*y*, -1/2+*z*; (ii) = -*x*, -1/2+*y*, 1/2-*z*; (iii) = 1-*x*, 1/2+*y*, 1/2-*z*; (iv) = *x*, 1/2-*y*, 1/2+*z*.

[g] Symmetry codes: (i) = -*x*, -1/2+*y*, 1/2-*z*; (ii) = *x*, 1/2-*y*, -1/2+*z*; (iii) = 1-*x*, 1/2+*y*, 1/2-*z*; (iv) = *x*, 1/2-*y*, 1/2+*z*.

[h] Symmetry codes: (i) = -*x*, -1/2+*y*, 1/2-*z*; (ii) = *x*, 1/2-*y*, -1/2+*z*; (iii) = 1-*x*, 1/2+*y*, 1/2-*z*; (iv) = *x*, 1/2-*y*, 1/2+*z*; (v) = 1-*x*, 1-*y*, 1-*z*.

[i] Symmetry codes: (i) = 2/1-*x*,2/1 -*y*, 2/1-*z*.

[j] Symmetry codes: (i) = *x*,2/1 -*y*, -2/1+*z*; (ii) = *x*, -*y*, 1/2-*z*; (iii) = 1/2-*x*, 1/2-*y*, 1/2-*z*.

directions along the 3-fold rotoinversion axes (Fig. 4.2d). The openings of these channels range from 2.96(1) Å to 3.35(3) Å. The interior of these channels is decorated with the coordinated water molecules and therefore hydrophilic in nature. Inside these channels, there are the unbound chloride anions some of which are transfixed by the O–H···O and O–H···Cl hydrogen bonding interactions (Table 4.2) and some are diffused with high degree of freedom. These channels can therefore be viewed as a micro-container of the chloride aqueous solution. The entire hydrogen donor atoms are intriguingly of the coordinated water molecules. The involvement of every chloride anions including the disordering chlorides in the hydrogen bonding interactions can account for the apparent site disorder of the anions.

The cubic $Ia\bar{3}$ [Ln(pdc)$(H_2O)_4]_3$·3Cl (IX, X). Complexes **IX** (Sm) and **X** (Eu) are isostructural and revealed to be the supramolecular isomers of **III** (Sm) and **IV** (Eu), respectively. The asymmetric units of **IX** and **X** are closely similar to the corresponding isomers comprising one unique lanthanide ion, half a molecule of the fully deprotonated pdc^{2-} ligand, two coordinated water molecules and one chloride anion which shows disorder over two crystallographic sites. The occupancy ratios of Cl1A:Cl1B in both structures are closely similar, *i.e.* 0.256(11):0.744(1) (**IX**) and 0.262(9):0.738(9) (**X**). Since **IX** and **X** are the isomers of **III** and **IV**, the coordination environment about the lanthanide ion and mode of coordination adopted by the pdc^{2-} ligand are principally identical (Fig. 4.3a). If the arrangement and the linkage of the *SAPRS*-{LnO_8N} units in these structures are considered carefully, the *SAPRS*-{LnO_8N} units in **IX** and **X** are however not exactly the same as those found in **III** and **IV**, but being their enantiomers (Fig. 3b). Whilst the spatial arrangement of the ligands about the lanthanide ion in the cubic $Pa\bar{3}$ structures (**III** and **IV**) can be defined as the Λ stereoisomer, the configuration in the $Ia\bar{3}$ structures (**IX** and **X**) are the enantiomeric counterpart, Δ. Despite the existence of these stereoisomeric building motifs, the packings of these building motifs in the crystal structures according to the operations about the inversion center and the mirror planes result in achiral cubic frameworks. The cubic $Pa\bar{3}$ structures are apparently favored both thermodynamically and kinetically over the cubic $Ia\bar{3}$ structures which exist only in the samarium (**IX**) and europium (**X**) cases.

The formation of channels in the $Ia\bar{3}$ structures is similar to those of the cubic $Pa\bar{3}$ structures. The unbound chloride anions are positioned approximately along the 3-fold rotoinversion axes. The hydrogen bonding interactions observed in the cubic $Ia\bar{3}$ structures are also closely similar to the cubic $Pa\bar{3}$ counterparts (Table 4.2), involving every water molecules as the hydrogen bonding donors and the unbound chloride anions as the acceptors. The alignments of

chlorides governed by these hydrogen bonding interactions can therefore be the key factor driving the formation of the tubular structures in these cubic $Pa\bar{3}$ and $Ia\bar{3}$ structures alike.

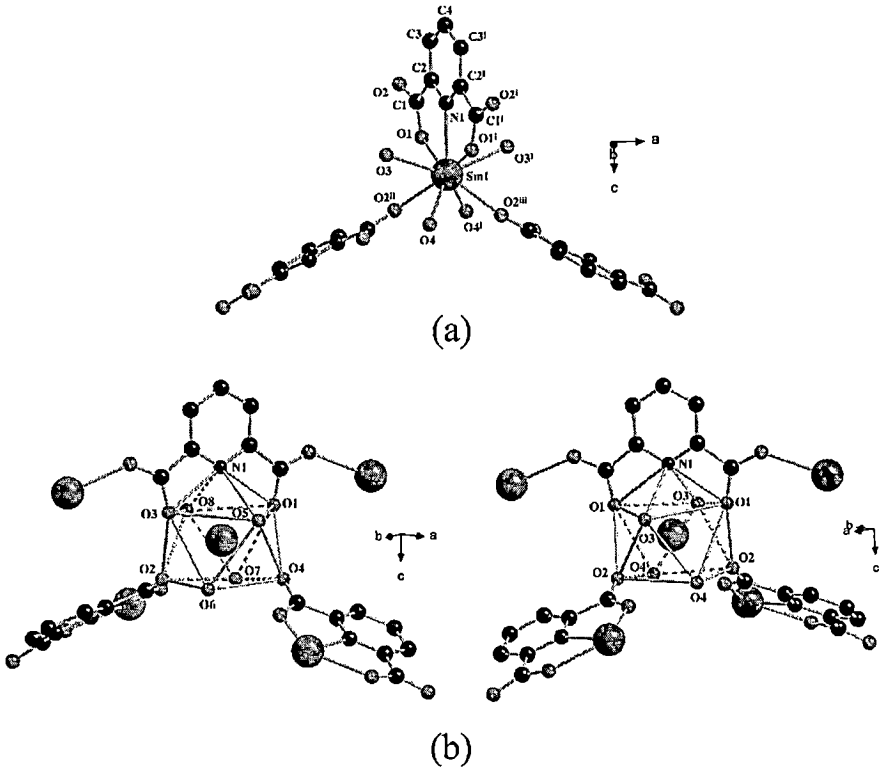

Fig. 4.3 Views of (a) an extended asymmetric unit of **IX**, and (b) the enantiomeric Λ (**III, IV**) and Δ (**IX, X**) configurations.

The monoclinic $P2_1/c$]Ln)pdc()Hpdc()H_2O($_2$[·3H_2O)VI-VIII(. As the heating under reflux was employed, the lower symmetry structures of the monoclinic $P2_1/c$ space group have been synthesized. Pure monoclinic structure could even be afforded in the case of praseodymium complex (**VI**), although the cubic structures are favored for the other lanthanides. These $P2_1/c$ structures have been previously reported as can be yielded also by hydrothermal technique [6,7]. The asymmetric units of **VI-VIII** are bulky, comprising one unique lanthanide ion, a whole molecule each of the partially deprotonated $Hpdc^-$ and the completely deprotonated pdc^{2-}, two coordinated water molecules, two unbound water molecules. Contrary to the cubic structures, the monoclinic structures include the partially deprotonated $Hpdc^-$ ligand and less coordinated water molecules (Fig. 4.4a). Although the coordination about the lanthanide ion in **VI-VIII** are the same

nine-fold *SAPRS*-9 as those of the cubic structures, they are however highly distorted (Fig. 4.4b). The distorted *SAPRS*-9 unit of the monoclinic structures is delineated with two fully deprotonated pdc^{2-} through the pyridyl N2 and the carboxylate O5, O7 and O8, and one mono-deprotonatd $Hpdc^-$ through the pyridyl N1 and the carboxyl O1 and O3. Here, two different modes of coordination, namely modes *a* and *b* (Scheme 4.1), are adopted by the pdc^{2-} ligand, whereas mode *k* is adopted by the $Hpdc^-$. Two water O atoms (O9 and O10) complete the coordination requirement and therefore the formation of the *SAPRS*-$\{LnO_7N_2\}$ structural building unit. Atoms O1 and N1 of the $Hpdc^-$ ligand seem to be the major contribution to the distortion in the *SAPRS*-$\{LnO_7N_2\}$ unit, which on the other hand accounts for the less proclivity for the $P2_1/c$ structures to be yielded.

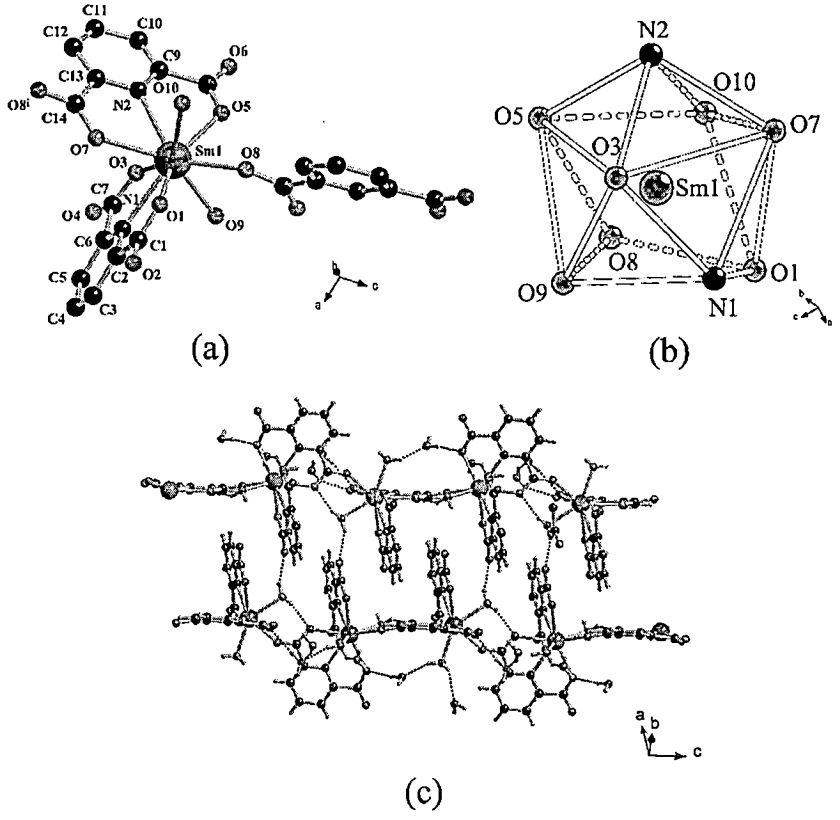

Fig. 4.4 Illustrations of (a) an extended asymmetric unit, (b) the *SAPRS*-$\{LnO_7N_2\}$ unit, and (c) the infinite ladder-like structure of **VIII** (as a representative of **VI-VIII**).

The discrete *SAPRS*-$\{LnO_7N_2\}$ units are bridged by the pdc^{2-} ligands to form an infinite one-dimensional $[Ln(pdc)(Hpdc)(H_2O)_2]$ chain extending along the direction of *c* (Fig. 4.4c). As the $Hpdc^-$ is arranged in an anti-parallel fashion to the pdc^{2-}, the derived chain is puckered rather than linear. Compared to the cubic structures reported in this work, the presence of the $Hpdc^-$ ligand

forbids the linkage of the adjacent lanthanide ions to form higher dimensional coordination framework. These chains are bundled up into a dense assembly by the hydrogen bonding interactions between the coordinating and the unbound water molecules (Table 4.2) The hydrophobic pyridyl rings of these chains are aligned leading to the ladder-like assemblies extending in the direction of *c*. According to the statistics on the structures submitted to the CSD [12], the chelating $Hpdc^-$ ligand tends to give the ladder-like structures in both the monoclinic $P2_1/c$ and $P2_1/a$ space groups [8,12,16,20,21]. There is however no π-π interaction in structures **VI-VIII**. The supramolecular assemblies of these $[Ln(pdc)(Hpdc)(H_2O)_2]$ chains into two-dimensional collugated layer extending in the *ab* plan, and to the three-dimensional assembly are directed solely by the hydrogen bonding interactions.

Topology of the cubic structures. Despite the different sets of symmetry operations and the Bravais translation adopted by the $Pa\bar{3}$ and the $Ia\bar{3}$ structures, the derived framework topologies of both cubic structures are identical. The cubic $Pa\bar{3}$ and $Ia\bar{3}$ frameworks can be simplified to two interpenetrated uninodal **lcs** and **pcu** nets (Fig. 4.5) [22]. If the hydrogen bonding interactions between the coordinating water molecules and the unbound chloride anions are disregarded and only the *SAPRS*-$\{PrO_8N\}$ unit is taken as node, a uninodal 4-connected **lcs** net with $\{6^6\}$ point symbol is derived. If only the $\{Cl_2(H_2O)_6\}$ motif is, on the other hand, taken as node, the other uninodal 6-connected **pcu** net with $\{4^{12}.6^3\}$ point symbol is obtained. The interpenetration of the **lcs** and **pcu** nets then establishes the networks in **I-V** and **IX-X**.

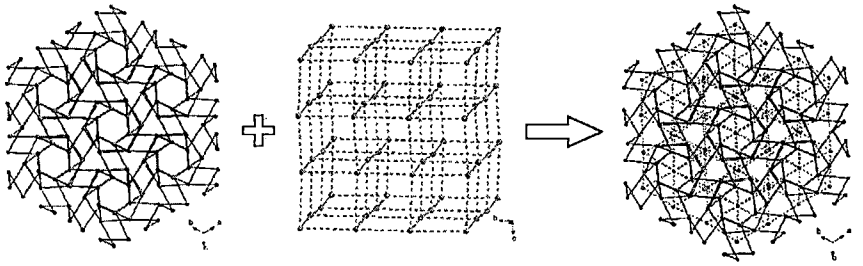

Fig. 4.5 The interpenetrated uninodal **lcs** and **pcu** nets of the cubic structures **I-V** and **IX-X**.

4.3 Thermogravimetric behaviors of V and VI

Due to the fact that only complexes **V** ($Pa\bar{3}$; Gd) and **VI** ($P2_1/c$; Pr) could be obtained with high purity, thermogravimetric behavior of the two complexes were studied revealing similar weight loss patterns (Fig. 4.6). The first weight loss in both complexes readily occurred under the flow of nitrogen gas attributing to the liberation of the water molecules; calc. = 16.76%, exp. = 17.4% for **V** and calc. = 16.02%, exp. = 17.2% for **VI**. After the loss of the water molecules, the

weight loss gradually proceeded in both cases although the process was extremely slow in the case of **V**. The gradual loss led to the collapse of most of the long range order in both frameworks revealed by the PXRD results, suggesting the successive loss of the other compartments of the frameworks. The second abrupt drops of weights were yet apparent for both complexes during the heat treatment occurring at higher temperature in the case of **V** (*ca.* 470 °C) compared to that of **VI** (*ca.* 360 °C). This is consistent with the higher stability of the three-dimensional framework in **V** in relative to the one-dimensional structure in **VI**. The gradual weight loss was then occurred again for both complexes leading to the corresponding cubic lanthanide oxides.

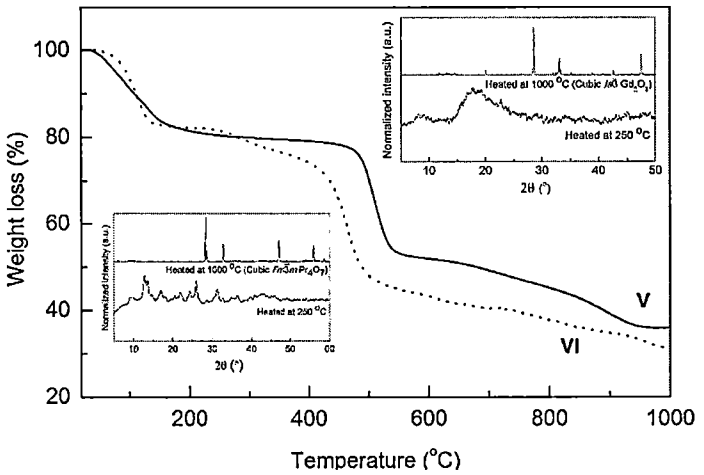

Fig. 4.6 Thermogravimetric curves of **V** (solid line) and **VI** (dotted line) with the PXRD patterns of the heated samples shown in the insets.

4.4 Photoluminescence properties of VI-X

Due to the purity limitation of the samples yielded from the microwave synthesis, the photoluminescence spectra of only the samples yielded from the conventional heating of which every phase could be identified were collected (Fig. 4.7). The free H_2pdc exhibits a broad feature with multiple maxima covering almost an entire visible region which can be ascribed to the pyridyl ring π^*-π emission [23,24]. Different degrees of deprotonation has been reported to negligibly affect the energy of the triplet state of the ligand [23]. Apparently the ligand is a moderately good sensitizer for the reported complexes, especially those of the europium ion (**IV**+**X**) of which the intense characteristic emissions incited from the transitions from the first excited $^5D_0$ state to the ground multiplets ^7F_J (J=0-4) are vivid. The efficiency of the energy transfer process from the ligand to the europium can also be enhanced by the increased molecular rigidity of the ligand after coordination and the singlet pathway of the energy transfer [25-27]. In the case of praseodymium

(VI), neodymium (II+VII) and samarium ions (III+VIII+IX), differences between the triplet state of the ligand and the first excited states of the metal ions result in poor energy transfer and therefore only weak emissions can be observed [23]. Large numbers of the excited states in praseodymium (VI) and neodymium (II+VII) may additionally render energy loss through the non-radiative pathways [28]. In comparison to the spectrum of the free H_2pdc, an emission band at 300 nm in the spectra of these samples may attribute to the ligand centered π^*-π emission promoted by the greater molecular rigidity upon the coordination to the metal centers [29]. The photoluminescence spectrum of the gadolinium complex (V) was notably not collected. The remarkably high energies of the excited states of gadolinium ion owing to the exceptional stability of the half-filled *f*-shell are known to prevent energy transfer from any known ligands, which consequently causes any *f-f* transition to be unachievable [30,31].

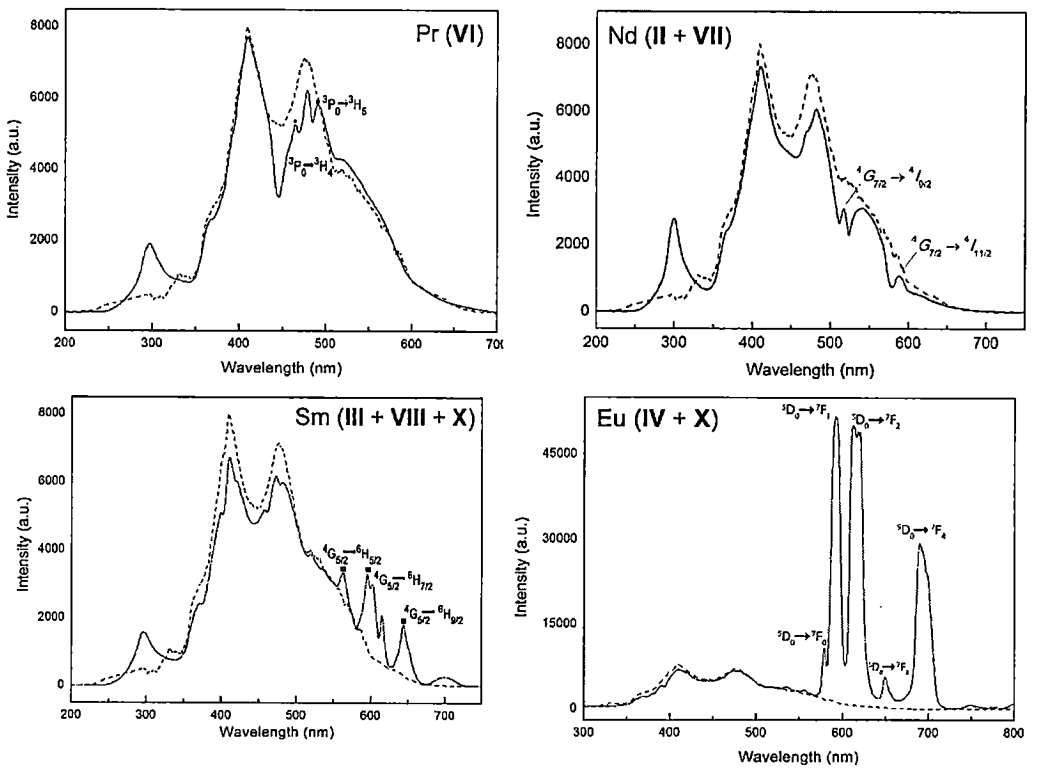

Fig. 4.7 Photoluminescence spectra of the synthesized samples (solid line) compared with that of the free H_2pdc ligand (dashed line).

4.5 Conclusion

In summary, we reported the variation and preference in crystal structures of the lanthanide-H_2pdc complexes synthesized by two different heating techniques, namely the

conventional and the microwave heating. The microwave heating provides the kinetically favorable cubic $Pa\bar{3}$ structures **I-V**, while the conventional heating results in the formation of three groups of isostructural crystals: (i) the monoclinic $P2_1/c$ structures **VI-VIII**, (ii) the cubic $Ia\bar{3}$ structures **IX** and **X**, and (iii) the cubic $Pa\bar{3}$ structures **II**, **III** and **V**. The $Pa\bar{3}$ complexes **I-V** exhibit the tubular structures built up of the *SAPRS*-{LnO_8N} units leading to the formation of four discrete one-dimensional channels extending in four <1 1 1> directions. Inside the channels, the chloride ions are transfixed by coordinating water molecules through hydrogen bonding interactions. The $Ia\bar{3}$ complexes **IX** and **X** which are the supramolecular isomers of **III** and **IV**, respectively, consist of the Δ stereoisomeric *SAPRS*-{LnO_8N} units, while the configuration in **III** and **IV** are the enantiomeric counterpart, Λ. Owing to the close similarity between the cubic $Ia\bar{3}$ and $Pa\bar{3}$ structures, their frameworks can be simplified to two interpenetrating uninodal **lcs** and **pcu** nets alike. In the case of the $P2_1/c$ complexes **VI-VIII**, they are different from the other complexes becasuse of the existence of the $Hpdc^-$ ligand which leads to the construction of highly distorted *SAPRS*-{LnO_7N_2} units. The linkage of these discrete *SAPRS*-{LnO_7N_2} units resulting in the formation of the infinite one-dimensional [Ln(pdc)(Hpdc)$(H_2O)_2$] chains which are further assembled solely by the hydrogen bonding interactions to two- and three-dimensional framework. The title complexes showed moderate thermal stabilities. The photoluminescence study reveraled the modest ability of the coordinated organic ligand in sensitizing the characteristic emissions of the lanthanide ions.

REFERENCES

[1] Zhang, J.; Zheng, B.; Zhao, T.; Li, G.; Huo, Q.; Liu, Y. *Cryst. Growth Des.* **2014**, *14*, 2394-2400.

[2] Li, M.; Li, D.; O'Keeffe, M.; Yaghi, O. M. *Chem. Rev.* **2014**, *114*, 1343-1370.

[3] Ghosh, S. K.; Bharadwaj, P. K. *Inorg. Chem.* **2005**, *44*, 3156-3161.

[4] Ghosh, S. K.; Bharadwaj, P. K. *Inorg. Chem.* **2004**, *43*, 2293-2298.

[5] Gao, H.-L.; Yi, L.; Zhao, B.; Zhao, X.-Q.; Cheng, P.; Liao, D.-Z.; Yan, S.-P. *Inorg. Chem.* **2006**, *45*, 5980-5988.

[6] Ghosh, S. K.; Bharadwaj, P. K. *Inorg. Chem.* **2003**, *42*, 8250-8254.

[7] Liu, S.-H.; Meng, Q.-J.; Li, Y.-Z. *Acta Crystallogr.* **2005**, E*61*, m1111-m1113.

[8] Hao, L.-J.; Yu, T.-L. *Acta Crystallogr.* **2007**, E*63*, m1967-m1967.

[9] Zhao, B.; Yi, L.; Dai, Y.; Chen, X.-Y.; Cheng, P.; Liao, D.-Z.; Yan, S.-P.; Jiang, Z.-H. *Inorg. Chem.* **2005**, *44*, 911-920.

[10] Starynowicz, P. *Acta Crystallogr.* **1992**, C*48*, 1428-1430.

[11] Liu, Y.-R.; Yang, T.; Li, L.; Liu, J.-M.; Su, C.-Y. *Aust. J. Chem.* **2009**, *62*, 1667-1674.

[12] Groom, C. R.; Bruno, I. J.; Lightfoot, M. P.; Ward, S. C. *Acta Crystallogr.* **2016**, B*72*, 171-179.

[13] Sheldrick, G. M. *SADABS*, University of Göttingen: Germany, **1996**.

[14] Sheldrick, G. *Acta Crystallogr.* **2008**, A*64*, 112-122.

[15] Dolomanov, O. V.; Bourhis, L. J.; Gildea, R. J.; Howard, J. A. K.; Puschmann, H. *J. Appl. Crystallogr.* **2009**, *42*, 339-341.

[16] Ramezanipour, F.; Aghabozorg, H.; Shokrollahi, A.; Shamsipur, M.; Stoeckli-Evans, H.; Soleimannejad, J.; Sheshmani, S. *J. Mol. Struct.* **2005**, *779*, 77-86.

[17] Jhung, S. H.; Jin, T.; Hwang, Y. K.; Chang, J.-S. *Chem. Eur. J.* **2007**, *13*, 4410-4417.

[18] Rodiguez-Horzedo, Nair; Murphy, D. *J. Pharm. Sci.* **1999**, *88*, 651-660.

[19] Spek, A. *J. Appl. Crystallogr.* **2003**, *36*, 7-13.

[20] Wang, P.; Fan, R.-Q.; Liu, X.-R.; Yang, Y.-L.; Zhou, G.-P. *J. Inorg. Organomet. Polym. Mater.* **2012**, *22*, 744-755.

[21] Zou, J.-P.; Wen, Z.-H.; Peng, Q.; Zeng, G.-S.; Xing, Q.-J.; Chen, M.-H. *J. Coord. Chem.* **2009**, *62*, 3324-3331.

[22] Blatov, V. A.; Shevchenko, A. P.; Proserpio, D. M. *Cryst. Growth Des.* **2014**, *14*, 3576-3586.

[23] Massaro, R. D.; Blaisten-Barojas, E. *Comput. Theor. Chem.* **2011**, *977*, 148-156.

[24] Hameka, H. F.; Jensen, J. O.; Jensen, J. L.; Merrow, C. N.; Vlahacos, C. P. *J. Mol. Struct. THEOCHEM* **1996**, *365*, 131-141.

[25] Rao, X.; Huang, Q.; Yang, X.; Cui, Y.; Yang, Y.; Wu, C.; Chen, B.; Qian, G. *J. Mater. Chem.* **2012**, *22*, 3210-3214.

[26] Yang, C.; Fu, L.-M.; Wang, Y.; Zhang, J.-P.; Wong, W.-T.; Ai, X.-C., Qiao, Y.-F.; Zou, B.-S.; Gui, L.-L. *Angew. Chem. Int. Ed.* **2004**, *43*, 5010-5013.

[27] Garcia-Torres, J.; Bosch-Jimenez, P.; Torralba-Calleja, E.; Kennedy, M.; Ahmed, H. Doran, J.; Gutierrez-Tauste, D.; Bautista, L.; Della Pirriera, M. *J. Photochem. Photobiol.*, **2014**, A*283*, 8-16.

[28] Cui, Y.; Chen, B.; Qian, G. *Coord. Chem. Rev.* **2014**, *273–274*, 76-86.

[29] Wang, P.; Fan, R.-Q.; Liu, X.-R.; Yang, Y.-L.; Zhou, G.-P. *J. Inorg. Organomet. Polym. Mater.* **2012**, *22*, 744-755.

[30] Vogler, A.; Kunkely, H. *Inorg. Chim. Acta* **2006**, *359*, 4130-4138.

[31] Strasser, A.; Vogler, A. *Inorg. Chim. Acta* **2004**, *357*, 2345-2348.

CHAPTER 5

Ratiometric Temperature Sensing by Lanthanide Coordination Polymers of Adipate/Phthalate

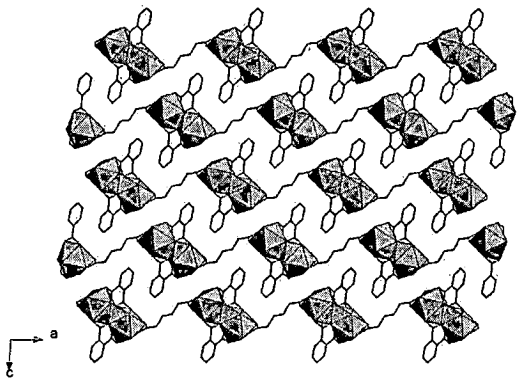

New lanthanide coordination polymers of mixed phthalate and adipate of $[Nd_2(ad)(phth)_2(H_2O)_4]$ and $[Ln(ad)_{0.5}(phth)(H_2O)_2]$ were synthesized and characterized, the latter of which show excellent potential in ratiometric luminescence thermometry: working temperature range = 303-423 *K*, maximum $S_r = 1.21\ \%\cdot K^{-1}$ (303 *K*), and excellent temperature resolution (S.D. < 2 *K*) and repeatability ($R \geq 98\%$).

Designing of lanthanide coordination polymers for use as ratiometric luminescent thermometers in biological and higher temperature ranges is of great challenge, and bimetallic Tb^{III}/Eu^{III} coordination networks are seemingly eligible choices. According to the antenna and the recently developed band models [1,2], scrupulous choices of organic antenna with appropriate triplet band energies is a determining factor in effectively promoting the sensitization process and therefore achieving highly luminescence lanthanide complexes. Triplet band energies of organic linkers are generally lower than those of the corresponding molecular states depending on, for example, increased rigidity in ligands' structures upon coordination, interactions with neighbouring structural components, and co-presence of secondary ligand [3,4]. Concentration and type of lanthanide luminophores are also important determinants [1,2].

Based on the use of rigid phthalic acid (H_2phth) with the triplet state energy of 24,770 cm^{-1} and the flexible adipic acid (H_2ad) with molecular freedom to bend or rotate [5,6], $[Nd_2(ad)(phth)_2(H_2O)_4]$ (**I**) and $[Ln(ad)_{0.5}(phth)(H_2O)_2]$ (Ln = Eu (**II**), Gd (**III**), Tb (**IV**), Dy (**V**), Er (**VI**), Tm (**VII**), $0.088Eu^{III}$: $0.912Tb^{III}$ (**VIII**), $0.277Eu^{III}$: $0.723Tb^{III}$ (**IX**) and $0.334Eu^{III}$: $0.666Tb^{III}$ (**X**)) have been synthesized. Single crystal structures, thermal stabilities and luminescence properties of the title complexes are described in this chapter. Ratiometric temperature sensing behaviour of **VIII-X** and key performance parameters of the measurements of **X** are presented.

5.1 Syntheses and crystal structures description

Crystals of **I-X** were synthesized hydrothermally* and characterized by single crystal X-ray diffraction. Crystallographic data of **I-VII** and the temperature dependent data of **II**, **IV** and **VIII** are summarized in Table 5.1and Table 5.2, respectively.†

---

*Ln_2O_3 (0.400 mmol of Ln^{III}) was dissolved in 7.20 M HNO_3(aq). Separately, a solution of H_2phth (0.400 mmol), H_2ad (0.400 mmol) and DABCO (0.400 mmol) was prepared using 7.00 mL of deionized water. The prepared solutions were mixed in a Teflon vessel which was sealed and hydrothermally heated at 120 °C for 24 h.

†Crystallographic data sets of **I**, **III-VII** were collected using a Bruker D8 Venture diffractometer equipped with a micro focus sealed tube X-ray source with graphite monochromatic Mo K_α radiation (λ = 0.71073 Å). Empirical absorption corrections were applied to all data using the SADABS program [7]. Crystallographic data of **II** and **VIII** were collected using a Rigaku FR-E Superbright rotating-anode X-ray source with Mo-target (λ = 0.71075 Å) equipped with a Rigaku RAXIS VII imaging plate as a detector. The intensity data were collected by the ω-scan technique and empirically corrected for absorption. To study temperature dependence in the structures of **II**, **IV** and **VIII**, crystallographic data sets of these samples were collected at 303, 363 and 423 *K* using a Rigaku Mercury 2 CCD detector with the Synchrotron radiation (λ = 0.6997 Å) at the BL02B1 beamline in Spring-8 with the approval of the Japan Synchrotron Radiation Research Institute (JASRI). The intensity data were collected by the ω-scan technique and were proceeded with the Rapid Auto software program. Every structure was solved by direct methods within the SHELXS program and refined on F^2 by the full-matrix least squares technique using the SHELXL program *via* the Olex2 interface [8,9].

According to the PXRD data (Fig. 5.1 and Fig. 5.2), the yielded products from every synthesis were pure phases. Regarding **VIII-X**, their structures can be confirmed to be isostructural to those of **II-VII** based on both single crystal X-ray diffraction data (**VIII**; Table 5.1) and PXRD results (**VIII-X**; Fig. 5.2). If the previously reported complexes are taken into account [10], a series of lanthanide coordination polymers with the same ratio of Ln^{III} : ad^{2-} : $phth^{2-}$: H_2O is noticeably completed manifesting two different structures spanning across the lanthanide contraction from Pr^{III} to Tm^{III}.

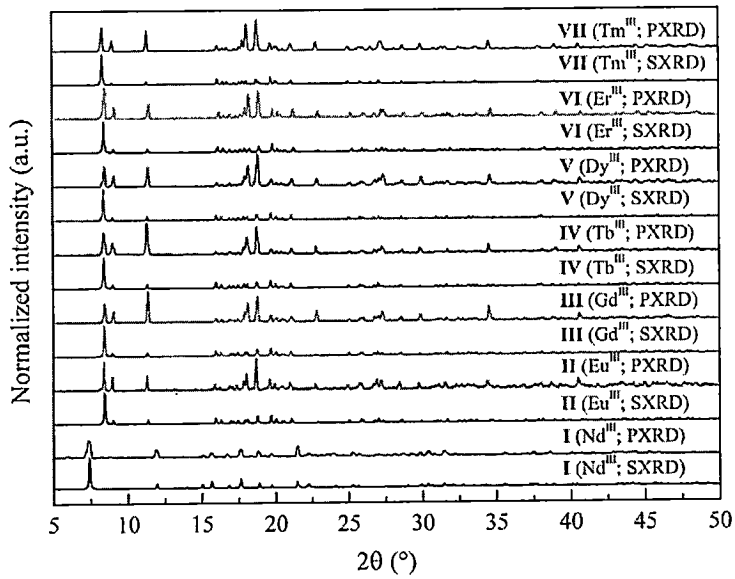

Fig. 5.1 Experimental PXRD patterns of **I-VII** compared with the patterns simulated from the corresponding single crystal data (SXRD).

The structure of $[Nd_2(ad)(phth)_2(H_2O)_4]$ (**I**) is revealed to be isostructural to $[Pr_2(ad)(phth)_2(H_2O)_4]$ [10], which is three-dimensional and non-porous. The asymmetric unit of **I** (Fig. 5.3) is composed of two nine-fold coordinated Nd^{III} ions, a whole molecule of ad^{2-}, two molecules of $phth^{2-}$ and four coordinated water molecules. The coordination about both Nd^{III} ions is alike featuring a distorted tricapped triangular prismatic geometry which is delineated by nine oxygen atoms, *TPRS*-$\{NdO_9\}$, from four $phth^{2-}$, one ad^{2-} and two water molecules. Every two units of *TPRS*-$\{NdO_9\}$ share edge to form a $\{Nd_2O_{16}\}$ dimer each of which is linked to the neighboring dimers by $phth^{2-}$ using μ_4-η^2:η^1:η^1:η^1 mode of coordination leading to the formation of an infinite two-dimensional sheet in the *ab* plane. Both crystallographically

Table 5.1 Crystallographic data and refinement details for **I-VIII**

	II	II	II	IV	IV	VIII	VIII	VIII
Empirical formula	$C_{11}H_{12}O_8Eu$	$C_{11}H_{12}O_8Eu$	$C_{11}H_{12}O_8Eu$	$C_{11}H_{12}O_8Tb$	$C_{11}H_{12}O_8Tb$	$C_{11}H_{12}O_8Eu_{0.09}Tb_{0.91}$	$C_{11}H_{12}O_8Eu_{0.09}Tb_{0.91}$	$C_{11}H_{12}O_8Eu_{0.09}Tb_{0.91}$
Formula weight	424.17	424.17	424.17	431.13	431.13	430.52	430.52	430.52
Temperature (K)	303(2)	363(2)	423(2)	303(2)	423(2)	303(2)	363(2)	423(2)
Crystal system	Monoclinic	Monoclinic	Monoclinic	Monoclinic	Monoclinic	Monoclinic	Monoclinic	Monoclinic
Space group	$P2_1/n$ (No. 11)	$P2_1/n$ (No. 11)	$P2_1/n$ (No. 11)	$P2_1/n$ (No. 11)	$P2_1/n$ (No. 11)	$P2_1/n$ (No. 11)	$P2_1/n$ (No. 11)	$P2_1/n$ (No. 11)
a (Å)	13.3461(12)	13.4045(3)	13.4271(11)	13.3424(9)	13.4478(18)	13.3216(12)	13.3947(3)	13.4320(13)
b (Å)	5.9526(5)	5.9687(1)	5.9705(5)	5.9207(4)	5.9242(8)	5.9193(5)	5.9389(1)	5.9391(6)
c (Å)	15.6205(14)	15.6871(3)	15.7345(13)	15.6055(11)	15.702(2)	15.6002(14)	15.6681(3)	15.7111(15)
β	93.700(7)	93.629(7)	93.581(7)	93.838(7)	93.816(7)	93.901(7)	93.815(7)	93.798(7)
V (Å^3)	1238.37(19)	1252.57(4)	1258.92(18)	1230.01(15)	1248.2(3)	1227.30(19)	1243.63(4)	1250.6(2)
Z	4	4	4	4	4	4	4	4
Density (Mg m^{-3})	2.275	2.249	2.238	2.328	2.294	2.333	2.265	2.253
Abs. coeff. (mm^{-1})	4.928	5.044	4.848	5.592	5.511	5.796	5.080	5.048
F(000)	820	820	820	828	828	828	820	820
Data/restraints/parameters	2824/0/183	2859/0/183	2866/0/183	2813/0/183	2847/0/183	2822/0/183	2842/0/183	2864/0/183
Goodness-of-fit on P^2	1.044	1.144	1.057	1.012	0.941	1.047	1.091	1.035
Final Rindices (all data)								
$R1^a$	0.0347	0.0338	0.0408	0.0344	0.0510	0.0339	0.0255	0.0415
$wR2^b$	0.0798	0.0564	0.0859	0.0699	0.0805	0.0691	0.0532	0.0820

$^a R_1 = \Sigma||F_0|-|F_c||/|F_0|$; $^b wR_2 = [\Sigma w(F_0^2-F_c^2)^2/\Sigma w(F_0^2)_2]^{1/2}$

Table 5.2 Crystallographic data and refinement details for **II**, **IV** and **VIII** at various temperatures

	II	**II**	**II**	**IV**	**IV**	**VIII**	**VIII**	**VIII**
Empirical formula	$C_{11}H_{12}O_8Eu$	$C_{11}H_{12}O_8Eu$	$C_{11}H_{12}O_8Eu$	$C_{11}H_{12}O_8Tb$	$C_{11}H_{12}O_8Tb$	$C_{11}H_{12}O_8Eu_{0.09}Tb_{0.91}$	$C_{11}H_{12}O_8Eu_{0.09}Tb_{0.91}$	$C_{11}H_{12}O_8Eu_{0.09}Tb_{0.91}$
Formula weight	424.17	424.17	424.17	431.13	431.13	430.52	430.52	430.52
Temperature (K)	303(2)	363(2)	423(2)	303(2)	423(2)	303(2)	363(2)	423(2)
Crystal system	Monoclinic	Monoclinic	Monoclinic	Monoclinic	Monoclinic	Monoclinic	Monoclinic	Monoclinic
Space group	$P2_1/n$ (No. 11)	$P2_1/n$ (No. 11)	$P2_1/n$ (No. 11)	$P2_1/n$ (No. 11)	$P2_1/n$ (No. 11)	$P2_1/n$ (No. 11)	$P2_1/n$ (No. 11)	$P2_1/n$ (No. 11)
a (Å)	13.3461(12)	13.4045(3)	13.4271(11)	13.3424(9)	13.4478(18)	13.3216(12)	13.3947(3)	13.4320(13)
b (Å)	5.9526(5)	5.9687(1)	5.9705(5)	5.9207(4)	5.9242(8)	5.9193(5)	5.9389(1)	5.9391(6)
c (Å)	15.6205(14)	15.6871(3)	15.7345(13)	15.6055(11)	15.702(2)	15.6002(14)	15.6681(3)	15.7111(15)
β	93.700(7)	93.629(7)	93.581(7)	93.838(7)	93.816(7)	93.901(7)	93.815(7)	93.798(7)
V (Å^3)	1238.37(19)	1252.57(4)	1258.92(18)	1230.01(15)	1248.2(3)	1227.30(19)	1243.63(4)	1250.6(2)
Z	4	4	4	4	4	4	4	4
Density (Mg m^{-3})	2.275	2.249	2.238	2.328	2.294	2.333	2.265	2.253
Abs. coeff. (mm^{-1})	4.928	5.044	4.848	5.592	5.511	5.796	5.080	5.048
F(000)	820	820	820	828	828	828	820	820
Data/restraints/parameters	2824/0/183	2859/0/183	2866/0/183	2813/0/183	2847/0/183	2822/0/183	2842/0/183	2864/0/183
Goodness-of-fit on P^2	1.044	1.144	1.057	1.012	0.941	1.047	1.091	1.035
Final Rindices (all data)								
$R1^a$	0.0347	0.0338	0.0408	0.0344	0.0510	0.0339	0.0255	0.0415
$wR2^b$	0.0798	0.0564	0.0859	0.0699	0.0805	0.0691	0.0532	0.0820

^{a} $R_1 = \Sigma||F_0|-|F_c||/|F_0|$; ^{b} $wR_2 = [\Sigma w(F_0^2-F_c^2)^2/\Sigma w(F_0^2)_2]^{1/2}$

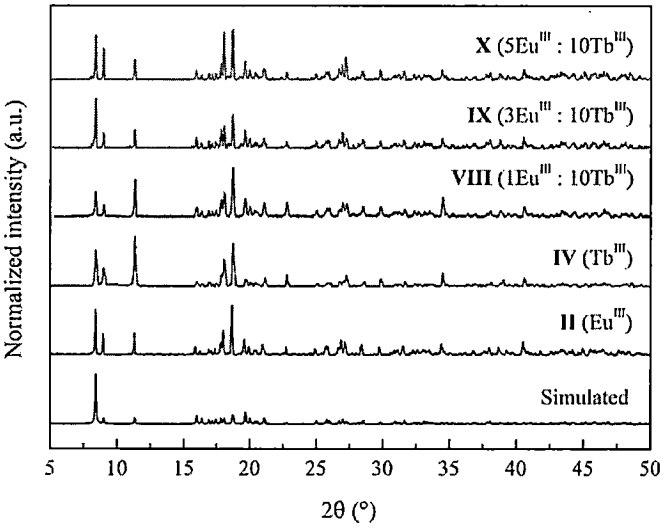

Fig. 5.2 Experimental PXRD patterns of **VIII-X** compared with those of **II**, **IV** and the simulated pattern of **II** (as a representative of **II** and **IV**).

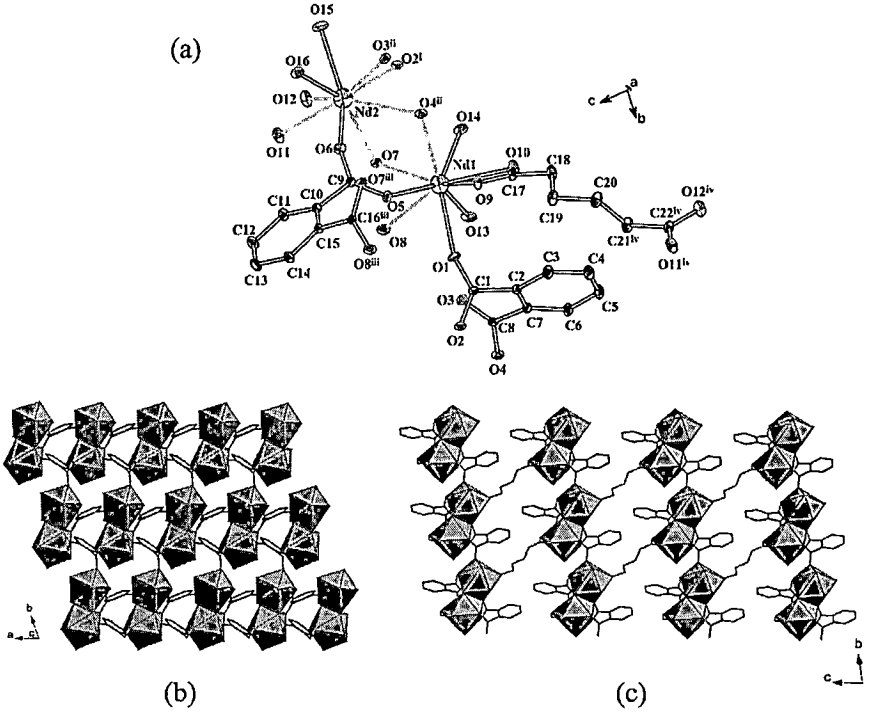

Fig. 5.3 Illustrations of (a) the extended asymmetric unit drawn using 50% thermal ellipsoids with hydrogen atoms omitted, and the fabrication of (b) the two-dimensional and (c) the three-dimensional structures in **I**. Symmetry codes: (i) 1+*x*, -1+*y*, *z*; (ii) *x*, -1+*y*, *z*; (iii) -1+*x*, *y*, *z*; (iv) -1+*x*, 1+*y*, -1+*z*; (v) 1+*x*, *y*, *z*.

independent $phth^{2-}$ ligands adopt the same μ_4-η^2:η^1:η^1:η^1 mode of coordination (Fig. 5.4), which can be found only in **I** and the isostructural $[Pr_2(ad)(phth)_2(H_2O)_4]$ [10]. These sheets are then transfixed into three-dimensional framework by ad^{2-} *via* the μ_2-η^1:η^1:η^1:η^1 mode of coordination.

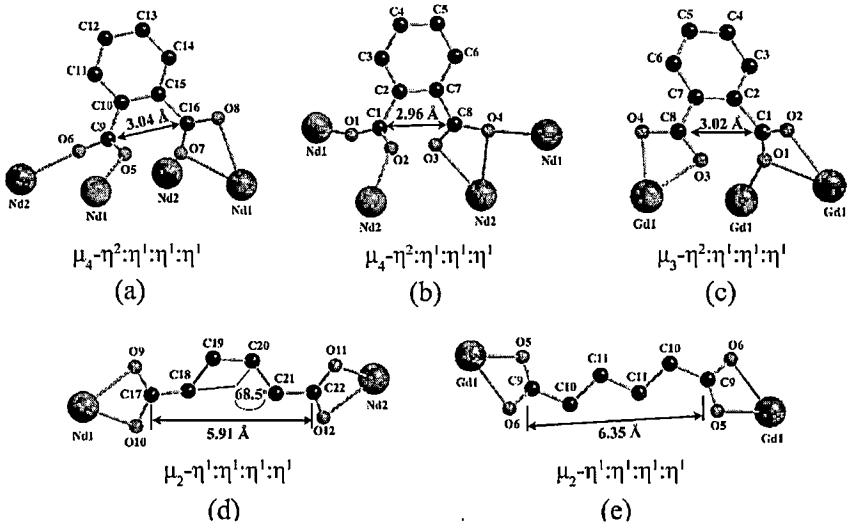

Fig. 5.4 Modes of coordination adopted by $phth^{2-}$ (a-c) and ad^{2-} (d-e) ligands.

Contrary to the three-dimensional framework of **I**, **II-VII** feature two-dimensional framework. The asymmetric units of every complex are similar, composing of one unique Ln^{III} ion which is nine-fold coordinated to a whole molecule of $phth^{2-}$, half a molecule of ad^{2-}, and two coordinated water molecules (Fig. 5.5). The coordination about the Ln^{III} ion in **II-VII** is intriguingly the same as that of **I**, *i.e. TPRS*-$\{LnO_9\}$. The nine oxygen atoms of the *TPRS*-$\{LnO_9\}$ unit in **II-VII** are however contributed from one ad^{2-}, two water molecules and three $phth^{2-}$ which is different from **I** of which four $phth^{2-}$ are included. This can be well accounted for by the lanthanide contraction.

Rather than the μ_4-η^2:η^1:η^1:η^1 bridging mode found in **I**, the $phth^{2-}$ in **II-VII** exhibits the μ_3-η^2:η^1:η^1:η^1 mode which is also very rare for the lanthanide coordination polymers (Fig. 5.4). This mode of coordination leads however to the formation of the edge-shared $\{Ln_2O_{16}\}$ dimer, which is linked to the adjacent dimers to form an infinite one-dimensional chain along *b* axis (Fig. 5.5). The established chains are further linked by ad^{2-} of which the aliphatic chain conforms in an *anti-anti-anti* fashion leading to the formation of two-dimensional puckered sheet in the *ab* plane. Conformation of the ad^{2-}aliphatic chain in **I** and **II-VII** are notably different (Fig. 5.4). The constructed sheets are stacked in the *c* direction and interlocked by weak π-π interactions between the phenyl rings of $phth^{2-}$. The centroid-to-centroid distances and the angles between the two phenyl

rings for the π-π interactions in **II-VII** are distributed in narrow ranges of 4.78-4.80 Å and 66.84-68.21°, respectively. Noticeably, there is not any hydrogen bonding interaction found in these complexes.

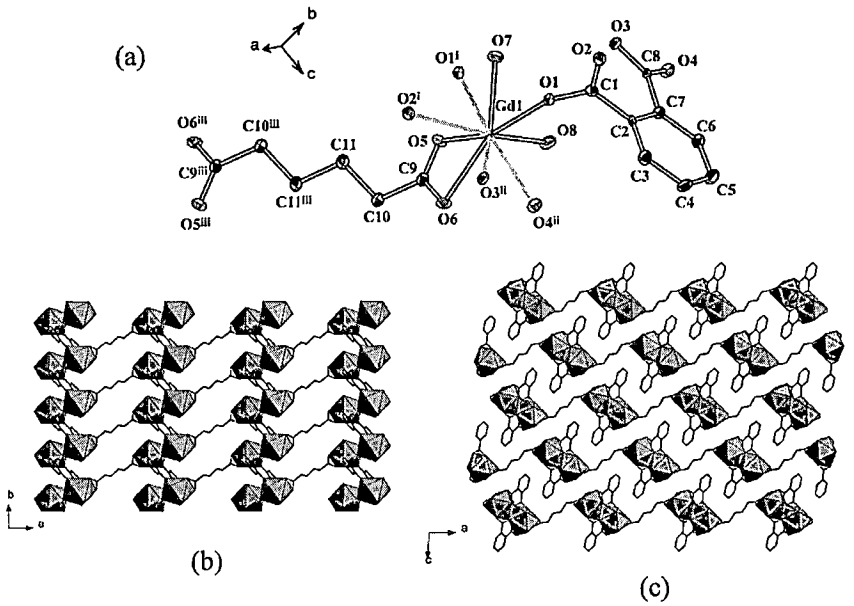

Fig. 5.5 Illustrations of (a) the extended asymmetric unit drawn using 50% thermal ellipsoids with hydrogen atoms omitted, and the fabrication of (b) the two-dimensional structure and (c) the supramolecular packing in **III** (as a representative of **II-VII**).

5.2 Room temperature photoluminescence behavior of I-VII

Upon the excitation at 255 nm (Fig. 5.6), H_2phth displays a broad emission band with multiple maxima covering almost the entire spectrum attributing to $\pi^* \rightarrow \pi$ of the phenyl ring [11]. The $phth^{2-}$ centered emission remains vivid in the spectra of **I** and **V-VII** although the change in spectral profiles and the red shift are significant which should be imparted from the increased molecular rigidity upon coordination [12]. According to the band model [9], the accumulation of these ligands in the frameworks can also be a significant cause. A distinct display of the ligand centered emission suggests nonetheless the poor energy transfer from $phth^{2-}$ to Nd^{III} (**I**), Dy^{III} (**V**), Er^{III} (**VI**) and Tm^{III} (**VII**). Characteristic emissions corresponding to $^4F_{9/2} \rightarrow {}^6H_J$ (J = 15/2, 13/2, 11/2) of Dy^{III} (**V**) are nevertheless visible [7].

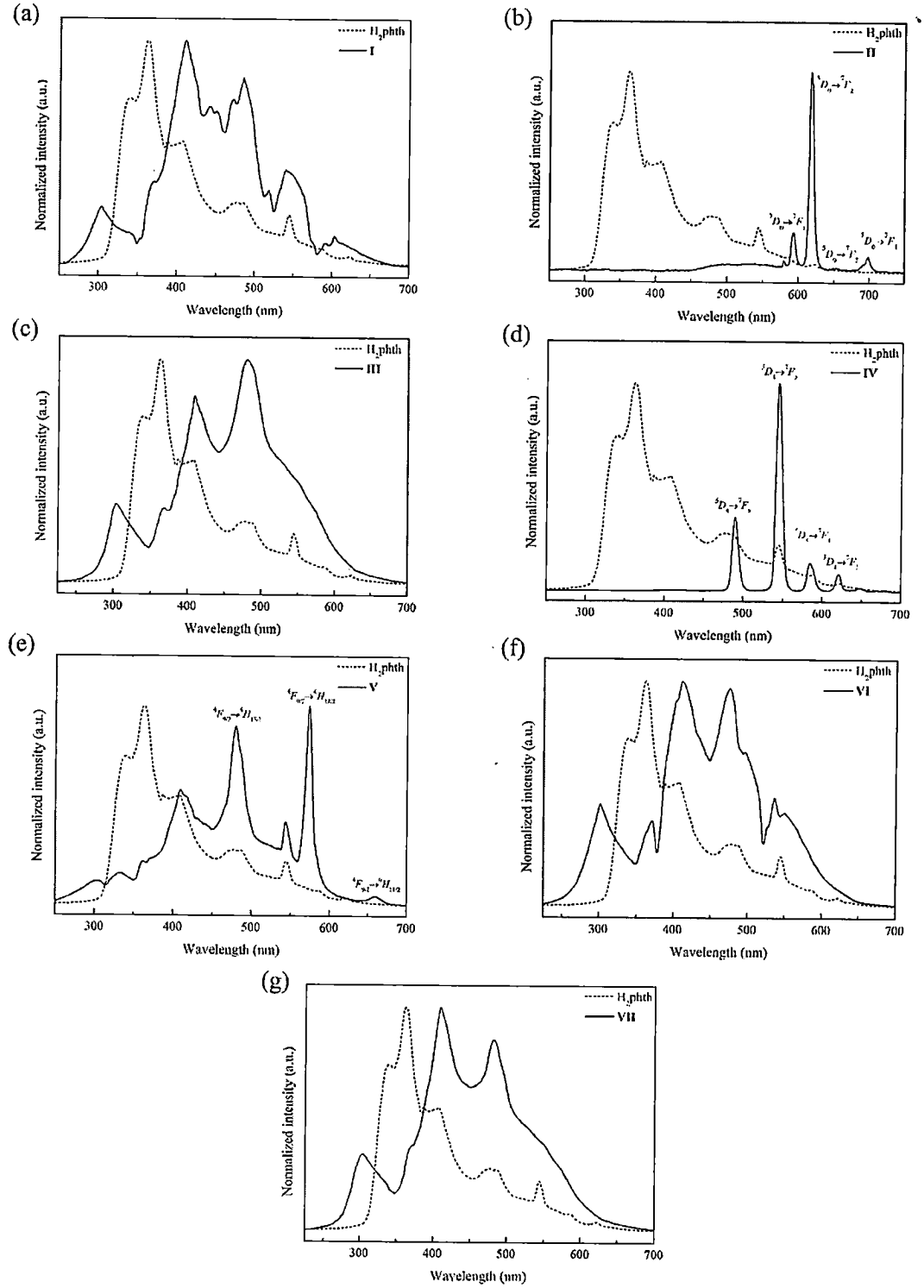

Fig. 5.6 Emission spectra (solid line) of (a) **I** (b) **II** (c) **III** (d) **IV** (e) **V** (f) **VI** and (g) **VII** compared with that of H_2phth pro-ligand (dash line)

In contrast to **I** and **V-VII**, $phth^{2-}$ can effectively sensitize the emission in Eu^{III} (**II**) and Tb^{III} (**IV**) even at room temperature, reflected *via* the complete silence of the $phth^{2-}$ centered emission. The characteristic $^5D_0 \rightarrow {}^7F_J$ (J = 1-4) emissions of Eu^{III} are, as planned, distinct in the spectrum of **II** with the most intense $^5D_0 \rightarrow {}^7F_2$ red emission centered at 618 nm. The characteristic $^5D_4 \rightarrow {}^7F_J$ (J = 6-3) emissions of Tb^{III} are also explicit in the spectrum of **IV** with the most intense $^5D_4 \rightarrow {}^7F_5$ green emission centered at 544 nm [14]. Since the lowest excited state energy of Gd^{III} is much higher than the lowest triplet band energy of any ligand, it is therefore common to estimate the triplet band energy of the organic antennae from the measurement of Gd^{III} complexes [9,20]. Based on the emission at 480 nm in the spectrum of **III**, the triplet band energy of 20,833 cm^{-1} can be estimated for $phth^{2-}$, which is in a suitable energy range to promote the sensitization of both Eu^{III} (**II**) and Tb^{III} (**IV**) according to Latva's empirical rule [1].

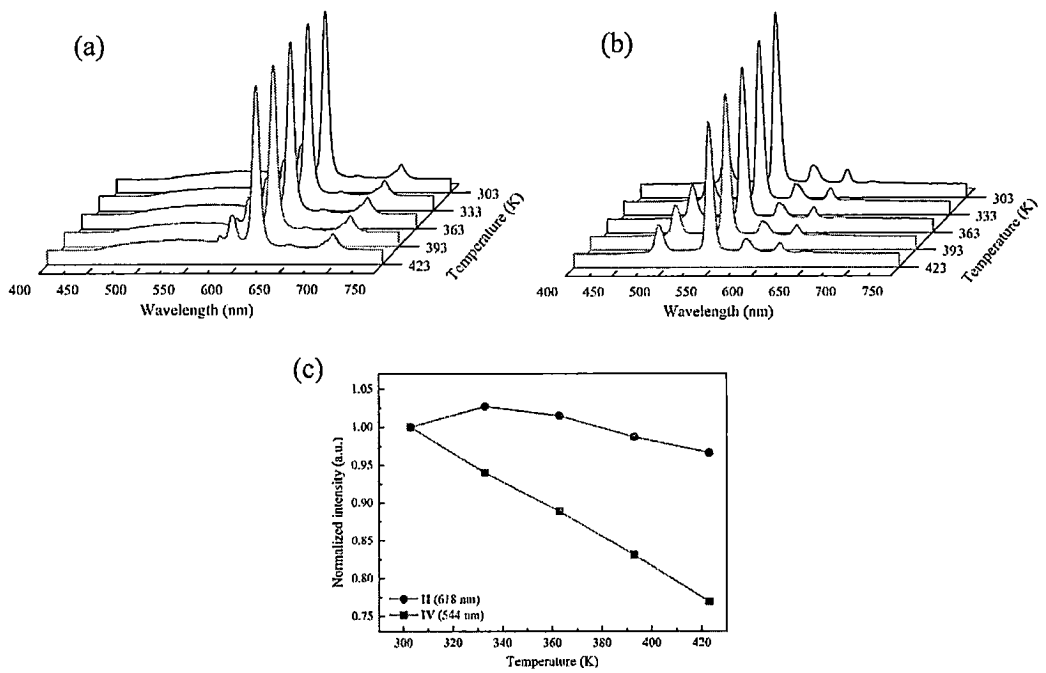

Fig. 5.7 Emission spectra of (a) **II** and (b) **IV** recorded between 303-423 *K* excited at 365 nm, and (c) temperature dependent intensity of the emissions at 618 nm (for **II**) and 544 nm (for **IV**).

5.3 Temperature dependent photoluminescence behavior of II, IV and VIII-X

The temperature dependent emission spectra of **II** and **IV** were collected in term of intensity from 303 to 423 *K* (Fig. 5.7). With increasing temperature, intensity of the most intense $^5D_4 \rightarrow {}^7F_5$ (Tb^{III}; **IV**) emission centering at 544 nm dropped approximately 23% whilst that of $^5D_0 \rightarrow {}^7F_2$ (Eu^{III}; **II**) emission centering at 618 nm negligibly changed. The reduction in intensity in the

case of **IV** is commonly explained by thermal activated non-radiative decay [21,22]. Intriguingly, the effect of thermal vibration of the coordinated water molecules about the Eu^{III} in **II** is silent. This should be due to the fact that these coordinated water molecules are transfixed in the frameworks and have limited freedom in vibration which is different from the molecular cases [19]. The intact of the coordinated water molecules in **II** and **IV** upon the heating has been confirmed by the single crystal data collected at the BL02B1 beamline in Spring-8 (Table 5.2). This agrees well with thermogravimetric data (Fig. 5.8) revealing no weight lost up to approximately 473 *K* (200 °C). The enlargement in the unit cell parameters and volumes of every complex is nonetheless apparent (Fig. 5.9).

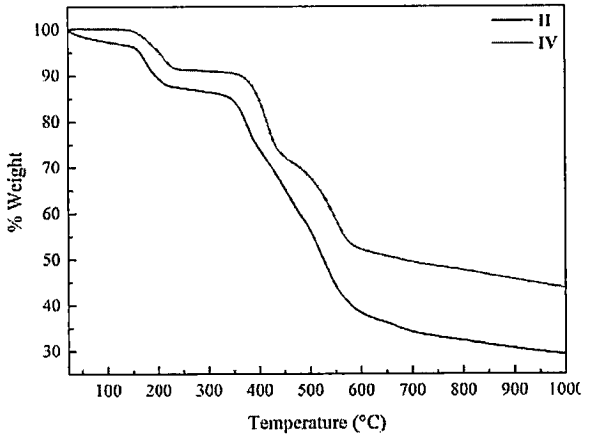

Fig. 5.8 TGA of **II** and **IV**.

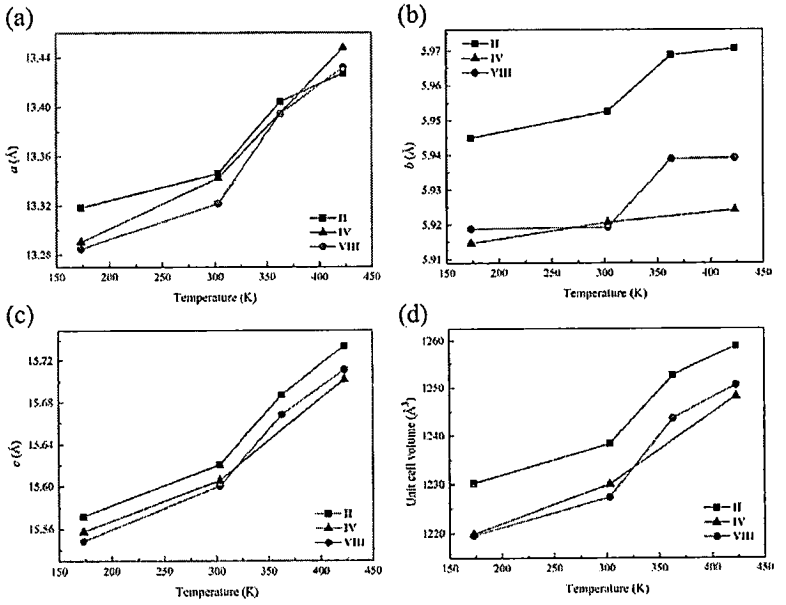

Fig. 5.9 Temperature dependence of unit cell parameters in **II**, **IV** and **VIII**.

The apparently different behavior in temperature dependent emission between **II** (Eu^{III}) and **IV** (Tb^{III}) brought about the investigation of **VIII-X** if they could exhibit temperature dependent ratiometric photoluminescence behavior [18,23,24]. The remaining of the coordinated water molecules in **VIII** (as a representative of **VIII-X**) was similarly affirmed by the single crystal data (Table 5.2) and the thermogravimetric analysis (Fig. 5.8). Although the temperature dependent PL spectra of **VIII-X** look rather similar at first glance, they are significantly different. In the case of **VIII** ($1Eu^{III}$: $10Tb^{III}$; Fig. 5.10), intensity of the $^5D_4 \rightarrow {}^7F_5$ (Tb^{III}) emission decreased approximately 37% from 303 *K* to 423 *K* which is more drastic than that observed in **IV** (23%). The intensity of $^5D_0 \rightarrow {}^7F_2$ (Eu^{III}) emission however negligibly increased and successively diminished at temperatures higher than 365 *K*. Based on the intensity ratio of $^5D_4 \rightarrow {}^7F_5$ (Tb^{III}) and $^5D_0 \rightarrow {}^7F_2$ (Eu^{III}), the thermometric parameter (Δ) have been calculated revealing temperature dependent linear correlation of Δ in a temperature range of 303-393 *K* ($R^2 = 0.993$). To evaluate the performance of **VIII** for use as a ratiometric photoluminescent thermometer, the relative sensitivity (S_r) which is defined as [3,4,25]

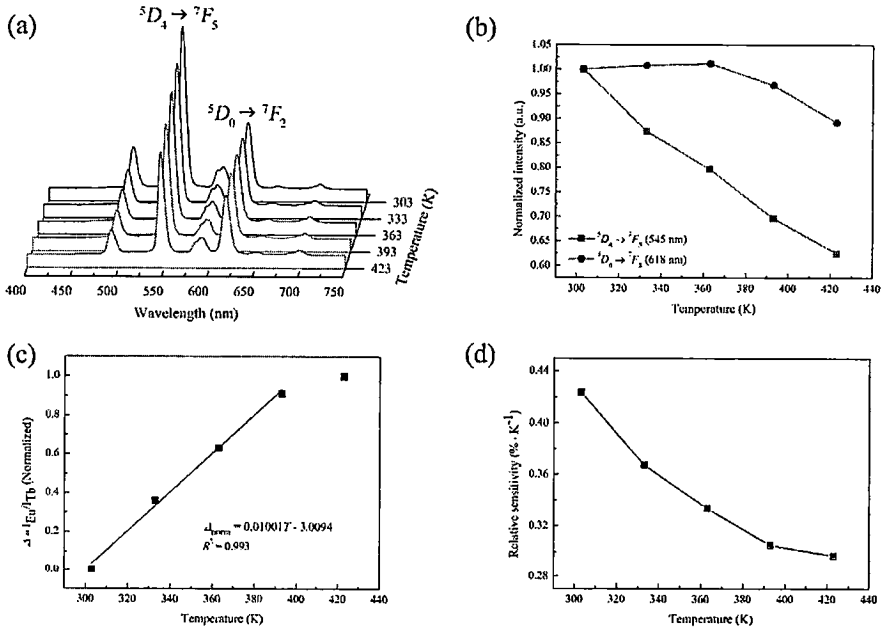

Fig. 5.10 (a) Emission spectra of **VIII** excited at 365 nm with (b) the temperature-dependent normalized emission intensity of the $^5D_4 \rightarrow {}^7F_5$ and $^5D_0 \rightarrow {}^7F_2$, (c) temperature dependent Δ and linearly fitted curve, and (d) temperature dependent S_r.

$$S_r = \frac{\partial \Delta / \partial T}{\Delta} \quad (1)$$

were calculated revealing the maximum S_r value of 0.42 %·K^{-1} at 303 K.

As the ratio of Eu^{III} was increased, *i.e.* $3Eu^{III}$: $10Tb^{III}$ (**IX**; Fig. 5.11) and $5Eu^{III}$: $10Tb^{III}$ (**X**; Fig. 5.12), the temperature dependent linear correlation of Δ was improved to cover the whole range of the experimented temperatures (303-423 K) with excellent fit to linearity; $R^2 = 0.996$ (**IX**) and 0.998 (**X**). This temperature range intriguingly overlaps with physiological temperature range (298-328 K). The improvement of the maximum S_r values is also evident. Whilst the S_r for **IX** brings off the maximum and minimum values of 0.59 %·K^{-1} at 303 K and 0.34 %·K^{-1} at 423 K, respectively, those for **X** is 1.21 %·K^{-1} at 303 K and 0.49 %·K^{-1} at 423 K, respectively. The maximum S_r value of **X** is intriguingly almost twice that of $Eu_{0.37}Tb_{0.63}$-BTC at similar temperature and corresponding temperature range (0.68 %·K^{-1} at 313 K, 313-473 K) [25]. Reports on S_r of over 1.2 %·K^{-1} at temperatures over 300 K are rare particularly for the physiological and higher temperature range [3]. According to the PXRD results (Fig. 5.13), stability of **VIII-X** over several

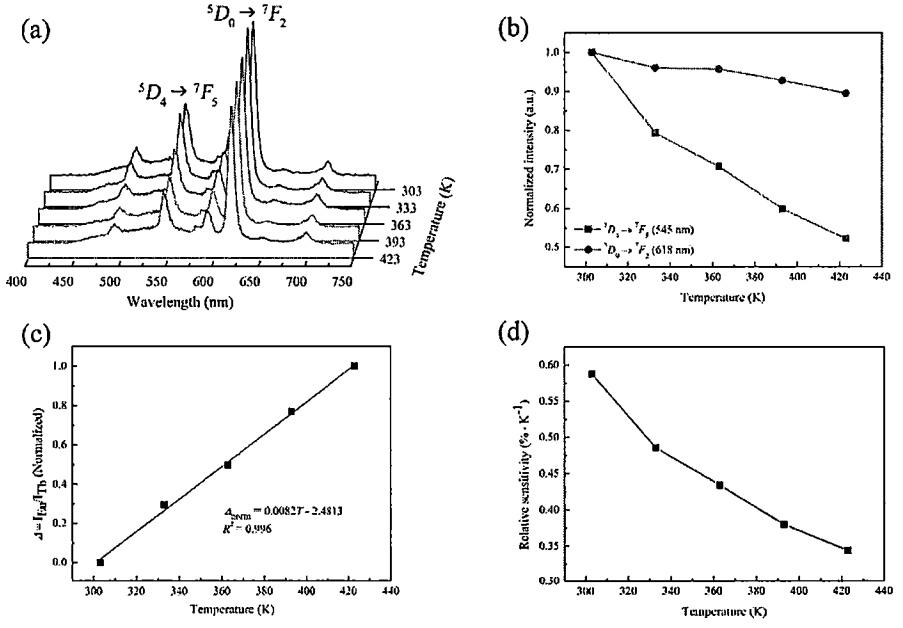

Fig. 5.11 (a) Emission spectra of **IX** excited at 365 nm with (b) the temperature-dependent normalized emission intensity of the $^5D_4 \rightarrow {}^7F_5$ and $^5D_0 \rightarrow {}^7F_2$, (c) temperature dependent Δ and linearly fitted curve, and (d) temperature dependent S_r.

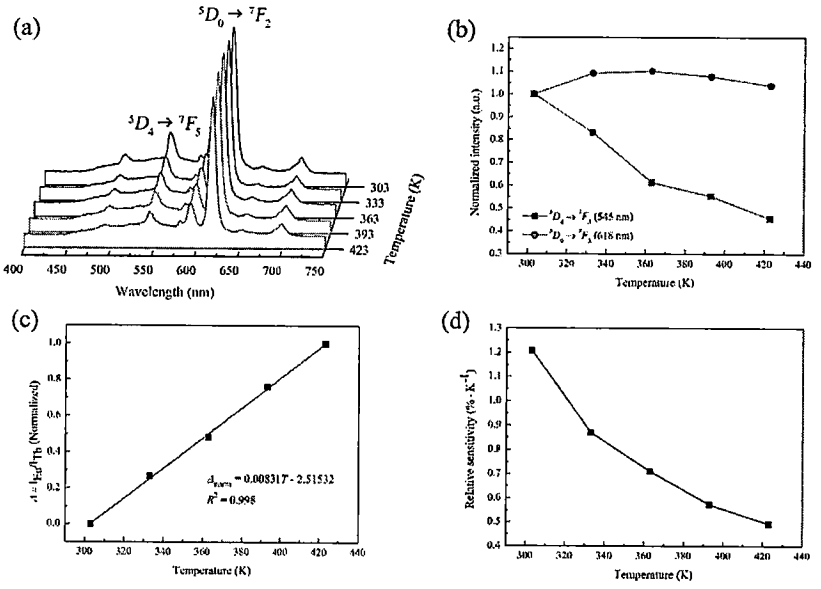

Fig. 5.12 (a) Emission spectra of **X** excited at 365 nm with (b) the temperature-dependent normalized emission intensity of the $^5D_4 \rightarrow {}^7F_5$ and $^5D_0 \rightarrow {}^7F_2$, (c) temperature dependent Δ and linearly fitted curve, and (d) temperature dependent S_r.

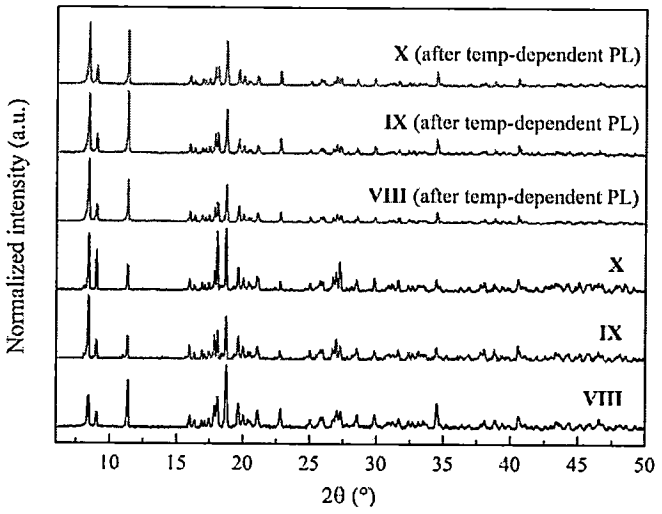

Fig. 5.13 PXRD patterns of **VIII-X** after several cycles of temperature dependent photoluminescent measurements compared to those of the pristine samples.

multiple cycles of heating and cooling during the temperature dependent photoluminescence experiments as well as few months of storage under ambient condition has been confirmed to be significant.

With the increasing ratio of Eu^{III}, the intensity of the $^5D_4 \rightarrow {}^7F_5$)Tb^{III}(emission notably declined to a greater extent: 23%)**IV**(, 37%)**VIII**(, 48%)**IX**(and 54%)X(, indicating the energy transfer from Tb^{III} to Eu^{III} in these lanthanide coordination polymers [18,26,27]. This is consistent with the room temperature lifetime measurement results (Table 5.3), revealing the shorter lifetimes for the $^5D_4 \rightarrow {}^7F_5$)Tb^{III}(transition with the increasing Eu^{III} ratio. The longer lifetimes were consistently apparent for the $^5D_0 \rightarrow {}^7F_2$)Eu^{III}(emission in **VIII-X** compared to that of **II** although the alteration tendency was not apparent. The efficiency of the energy transfer)η_{ET}(from Tb^{III} to Eu^{III} in **VIII-X** were also estimated [28];

$$\eta_{ET} = \frac{\tau_1^{-1} - \tau_0^{-1}}{\tau_1^{-1}} \qquad (2)$$

where τ_1 and τ_0 are the lifetimes of the $^5D_4 \rightarrow {}^7F_5$)Tb^{III}(emission with and without the acceptor)Eu^{III}(, respectively. In a similar manner, the η_{ET} was improved with the increasing ratio of the Eu^{III} acceptor)Table 5.3(, which is consistent with the tendency reported for other materials; $La_{2.85-x}GaGe_5O_{16}$:0.15Tb^{III}, xEu^{III})x = 0, 0.05, 0.07, 0.10 and 0.20([29], and)$Tb_{1-x}Eu_x(_2Mo_3O_{12}$)x = 0, 0.1, 0.4, 0.6, 0.8 and 1([30]. Reports on the dependence of η_{ET} on the acceptor concentration are however scarce.

Table 5.3 List of photoluminescence lifetimes and energy transfer efficiencies (η_{ET}) at room temperature for **II**, **IV** and **VIII-X**

	Lifetimes (ms)		η_{ET} (%)
	544 nm	618 nm	
$[Eu(ad)_{0.5}(phth)(H_2O)_2]$ (**II**)	-	0.441	-
$[Tb(ad)_{0.5}(phth)(H_2O)_2]$ (**IV**)	1.21	-	-
$[Ln(ad)_{0.5}(phth)(H_2O)_2]$ (Ln =1Eu^{III} : 10Tb^{III} ; **VIII**)	1.04	0.816	14.05
$[Ln(ad)_{0.5}(phth)(H_2O)_2]$ (Ln =3Eu^{III} : 10Tb^{III} ; **IX**)	0.834	0.613	31.07
$[Ln(ad)_{0.5}(phth)(H_2O)_2]$ (Ln =5Eu^{III} : 10Tb^{III} ; **X**)	0.795	0.555	41.65

To investigate the performance of **X** in better details, the values of temperature resolution (δT) in term of standard deviation of the temperature read out, and repeatability of the measurement (R) were additionally determined;

$$R = 1 - \frac{\max(|\Delta_c - \Delta_i|)}{\Delta} \qquad (3)$$

when Δ_c is thermometric parameter calculated from calibration curve and Δ_i refers to value of individual measurement [3]. Based on ten consecutive temperatures read out at two different temperatures (Fig. 5.14), both the R and δT values are exceptional. The potential of **X** as a high performance ratiometric luminescent thermometer is therefore illustrated.

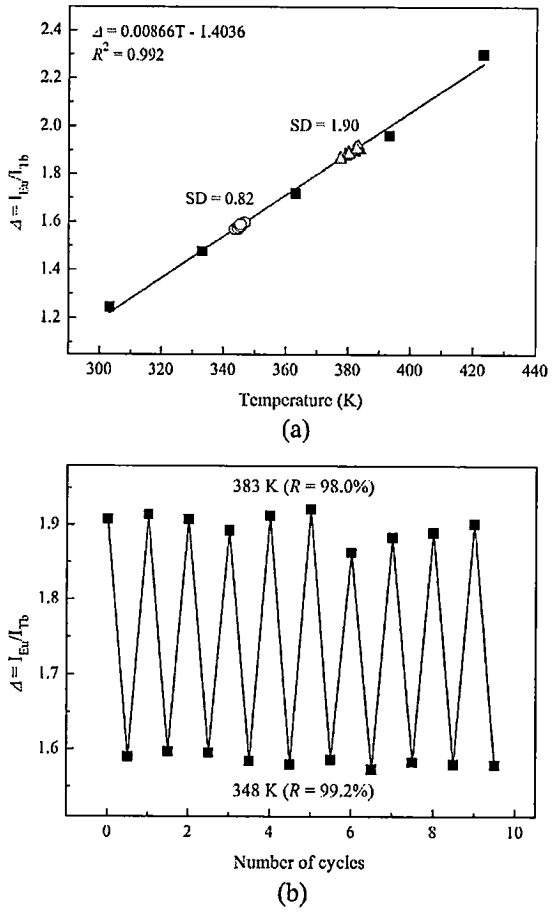

Fig. 5.14 (a) Calibration curve and (b) repeatability for temperature measurement of **X**.

5.4 Conclusion

In summary, the three-dimensional $[Nd_2(ad)(phth)_2(H_2O)_4]$ (**I**) and the two-dimensional $[Ln(ad)_{0.5}(phth)(H_2O)_2]$ (**II-VII**) have been constructed based on the mix ligands approach. Every LnCP shows exceptional thermal stability without any liberation of the coordinated water molecules up to approximately 473 K (200 °C), although cell expansion is manifested. The effective sensitization of Eu^{III} and Tb^{III} in **II**, **IV** and **VIII-X** by $phth^{2-}$ has evidently been illustrated and in good correspondence with the triplet band energy of $phth^{2-}$ estimated from the Gd^{III} complex (**III**).

Complexes **VIII-X** exhibit temperature dependent ratiometric photoluminescence behavior rendered by the energy transfer process from Tb^{III} to Eu^{III}. Linear temperature dependence of Δ in the range of 303-423 K with the maximum S_r of 1.21%·K^{-1} (at 303 K) and excellent R and δT has been determined for **X**. In addition to temperature, efficiency of the Tb^{III}-to-Eu^{III} energy transfer process as illustrated through the lifetime measurements depend, also, on the mole ratio of Eu^{III} : Tb^{III} in the frameworks. If framework structures and composition are considered as matrix which is well acknowledged as an important determinant governing photoluminescence behavior of lanthanide complexes [31,32], the mixed ligand approach such as the work reported here would be worthwhile for further investigation. Use of mixed ligands with varying degree of sensitization in facile synthesis of new lanthanide coordination polymers are currently studied by our group.

REFERENCES

(1) Latva, M.; Takalo, H.; Mukkala, V. -M.; Matachescu, C.; Rodríguez-Ubis, J. C.; Kankare, J. *J. Lumin.* **1997**, *7*, 149-169.

(2) Einkauf, J. D.; Clark, J. M.; Paulive, A.; Tanner, G. P.; de Lill, D. T. *Inorg. Chem.* **2017**, *56*, 5544-5552.

(3) Rocha, J.; Brites, C. D. S.; Carlos, L. D. *Chem. Eur. J.* **2016**, *22*, 14782-14795.

(4) Cui, Y.; Zhu, F.; Chen, B.; Qian, G. *Chem. Commun.* **2015**, *51*, 7420-7431.

(5) Ruan, L.; Wang, H.; Hao, Y.; Zhou, H.; Liu, X.; Xu, B. *J. Lumin.* **2007**, *122-123*, 467-470.

(6) Kim; Suh, M.; Jung, D.-Y. *Inorg. Chem.* **2004**, *43*, 245-250.

(7) Sheldrick, G. M. University of Göttingen: Germany, 1996.

(8) Sheldrick, G. *Acta Crystallogr. Sect. A: Found. Crystallogr.* **2008**, *64*, 112-122.

(9) Dolomanov, O. V.; Bourhis, L. J.; Gildea, R. J.; Howard, J. A. K.; Puschmann, H. *J. Appl. Crystallogr.* **2009**, *42*, 339-341.

(10) Wang, Z.; Xing, Y.-H.; Wang, C.-G.; Sun, L.-X.; Zhang, J.; Ge, M.-F.; Niu, S.-Y. *CrystEngComm* **2010**, *12*, 762-773.

(11) Yan, B.; Xu, B. *Spectrochim. Acta, Part A* **2005**, *62*, 269-275.

(12) Xu, B.; Yan, B. *Spectrosc. Lett.* **2006**, *39*, 237-248.

(13) Sahu, I. P.; Bisen, D. P.; Brahme, N.; Tamrakar, R. K.; Shrivastava, R. *J. Mater. Sci. - Mater. Electron.* **2015**, *26*, 8824-8839.

(14) Ramya, A. R.; Varughese, S.; Reddy, M. L. P. *Dalton Trans.* **2014**, *43*, 10940-10946.

(15) Strasser, A.; Vogler, A. *Inorg. Chim. Acta* **2004**, *357*, 2345-2348.

(16) Ramya, A. R.; Sharma, D.; Natarajan, S.; Reddy, M. L. P. *Inorg. Chem.* **2012**, *51*, 8818-8826.

(17) Peng, H.; Stich, M. I. J.; Yu, J.; Sun, L.-n.; Fischer, L. H.; Wolfbeis, O. S. *Adv. Mater.* **2010**, *22*, 716-719.

(18) Yang, Y.; Chen, L.; Jiang, F.; Yu, M.; Wan, X.; Zhang, B.; Hong, M. *J. Mater. Chem. C* **2017**, *5*, 1981-1989.

(19) Wang, X.-d.; Wolfbeis, O. S.; Meier, R. J. *Chem. Soc. Rev.* **2013**, *42*, 7834-7869.

(20) Hou, K.-L.; Bai, F.-Y.; Xing, Y.-H.; Wang, J.-L.; Shi, Z. *CrystEngComm* **2011**, *13*, 3884-3894.

(21) Feng, X.; Zhao, J.; Liu, B.; Wang, L.; Ng, S.; Zhang, G.; Wang, J.; Shi, X.; Liu, Y. *Cryst. Growth Des.* **2010**, *10*, 1399-1408.

(22) Hou, K.-L.; Bai, F.-Y.; Xing, Y.-H.; Wang, J.-L.; Shi, Z. *Inorg. Chim. Acta* **2011**, *365*, 269-276.

(23) Wang, K.-M.; Du, L.; Ma, Y.-L.; Zhao, J.-S.; Wang, Q.; Yan, T.; Zhao, Q.-H. *CrystEngComm* **2016**, *18*, 2690-2700.

(24) An, R.; Zhao, H.; Hu, H.-M.; Wang, X.; Yang, M.-L.; Xue, G. *Inorg. Chem.* **2016**, *55*, 871-876.

(25) Rodrigues, M.; Piñol, R.; Antorrena, G.; Brites, C. D. S.; Silva, N. J. O.; Murillo, J. L.; Cases, R.; Díez, I.; Palacio, F.; Torras, N.; Plaza, J. A.; Pérez-García, L.; Carlos, L. D.; Millán, A. *Adv. Funct. Mater.* **2016**, *26*, 200-209.

(26) Wang, H.; Zhao, D.; Cui, Y.; Yang, Y.; Qian, G. *J. Solid State Chem.* **2017**, *246*, 341-345.

(27) Wei, Y.; Sa, R.; Li, Q.; Wu, K. *Dalton Trans.* **2015**, *44*, 3067-3074.

(28) Zhao, D.; Rao, X.; Yu, J.; Cui, Y.; Yang, Y.; Qian, G. *Inorg. Chem.* **2015**, *54*, 11193-11199.

(29) Zhou, J.; Xia, Z. *J. Mater. Chem. C* **2014**, *2*, 6978-6984.

(30) Baur, F.; Glocker, F.; Justel, T. *J. Mater. Chem. C* **2015**, *3*, 2054-2064.

(31) Gavriluta, A.; Fix, T.; Nonat, A.; Slaoui, A.; Guillemoles, J. -F.; Charbonniere, L. J. *J. Mater. Chem. A* **2017**, *5*, 14031-14040.

(32) Binnemans, K. *Chem. Rev.* **2009**, *109*, 4283-4374.

CHAPTER 6

Ratiometric Temperature Sensing by Lanthanide Coordination Polymers of Benzene-1,4-dicarboxylate/Phthalate

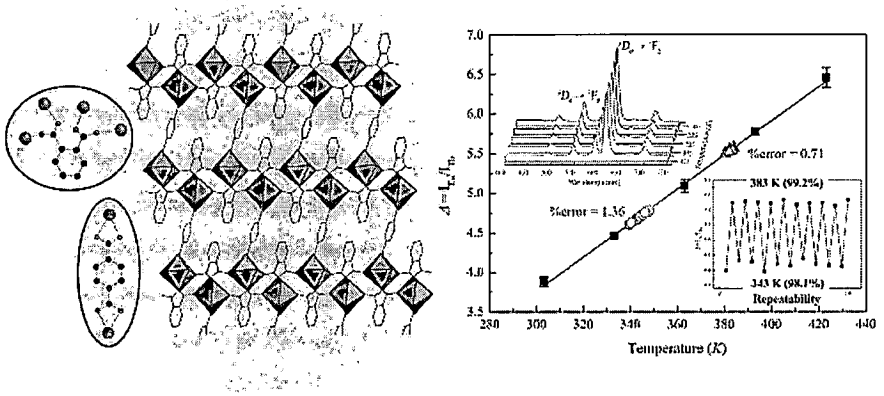

- Two-dimensional polymorphism in lanthanide coordination network
- Effect of mixed-benzenedicarboxylate antennae on ratiometric temperature sensing

In this chapter, the synthesis* and characterization of the monometallic $[Ln(bdc)_{0.5}(phth)(H_2O)_2]$ (bdc^{2-} = 1,4-benzenedicarboxylate; Ln = Eu^{III} (**I**), Tb^{III} (**II**), Ho^{III} (**III**), Er^{III} (**IV**), Tm^{III} (**V**), Gd^{III} (**IX**)) and the bimetallic $[Ln(bdc)_{0.5}(phth)(H_2O)_2]$ (Ln = $1.10Eu^{III}$: $10.0Tb^{III}$ (**VI**), $2.99Eu^{III}$: $10.0Tb^{III}$ (**VII**), $4.84Eu^{III}$: $10.0Tb^{III}$ (**VIII**)), are reported. Single crystal structures of **I-V** were determined revealing the closely relevant framework structures to $[Ln(ad)_{0.5}(phth)(H_2O)_2]$ [1]. Details on structural relation of the two series of LnCPs are discussed. Temperature dependent photoluminescent behavior of the titled complexes, and the influences of mixed antennae on the Tb^{III}-to-Eu^{III} energy transfer and consequently the ratiometric temperature-sensing performance are described.

6.1 Crystal Structure Description of I-V

The crystal structures of **I-V** are revealed to be isostructural with $[Gd(bdc)_{0.5}(phth)(H_2O)_2]$ and $[Dy(bdc)_{0.5}(phth)(H_2O)_2]$ yielded from different synthesis approach [2], featuring a non-porous three-dimensional framework. More importantly, **I-V** exhibit significant correlation with $[Ln(ad)_{0.5}(phth)(H_2O)_2]$ (Ln = Eu, Gd, Tb, Dy, Er and Tm; H_2ad = adipic acid) in views of both structure and photoluminescent property [1].

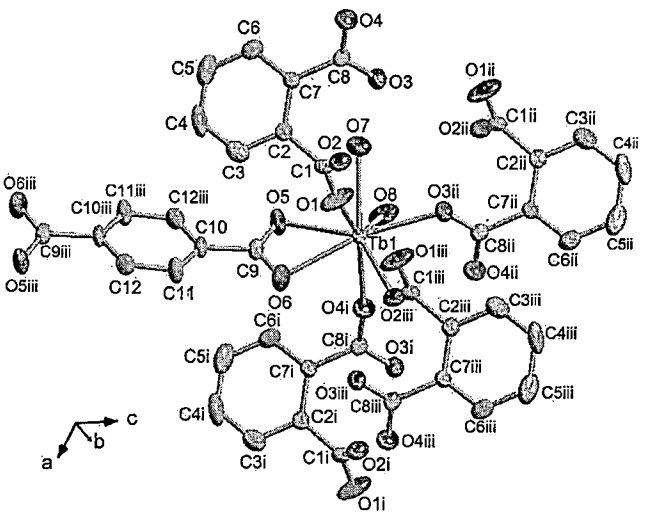

Fig. 6.1 An extended asymmetric unit of **II** as a representative of **I-VIII**, drawn using 70% thermal ellipsoids with H atoms omitted. Symmetry codes: (i) 1+x, 1+y, z (ii) 1-x, 1-y, 2-z (iii) 2-x, 1-y, 1-z.

*Solution **A**: Ln_2O_3 (0.400 mmol) was dissolved in 1.00 mL of HNO_3 solution (7.20 mol·L^{-1}). **B**: H_2phth (0.400 mmol), H_2bdc (0.400 mmol) and DABCO (0.400 mmol) were dissolved in 7.00 mL of deionized water. Solutions **A** and **B** were mixed in a 25 mL Teflon lined hydrothermal reactor and made up to 10.00 mL by deionized water. After carefully sealed, the reaction was carried out under autogenous pressure generated at 180 °C for 24 h.

Crystallographic data sets of **I-V** were collected at 293(2) *K* using a Rigaku XtaLAB SuperNova Diffractometer† and the crystallographic and refinement data for **I-V** are summarized in Table 6.1. The asymmetric units of **I-V** are alike comprising an eight-fold coordinated Ln^{III} bearing a distorted dodecahedral geometry, denoted as *DD*-{TbO_8}, of which the eight oxygen atoms are from four equivalent $phth^{2-}$, one bdc^{2-} and two water molecules (Fig. 6.1). Due to the μ_4-η^1:η^1:η^1:η^1 coordination mode adopted by $phth^{2-}$, each *DD*-{TbO_8} unit exists as a discreet moiety and is linked to the other eight equivalents through 8×{OCO} bridges of four surrounding $phth^{2-}$ to form a two-dimensional [Ln(phth)$(H_2O)_2$] sheet in the *ab* plane (Fig. 6.2). The derived sheet can be characterized as a uninodal 4-connected **sql/Shubnikov** with {$4^4.6^2$} point symbol.

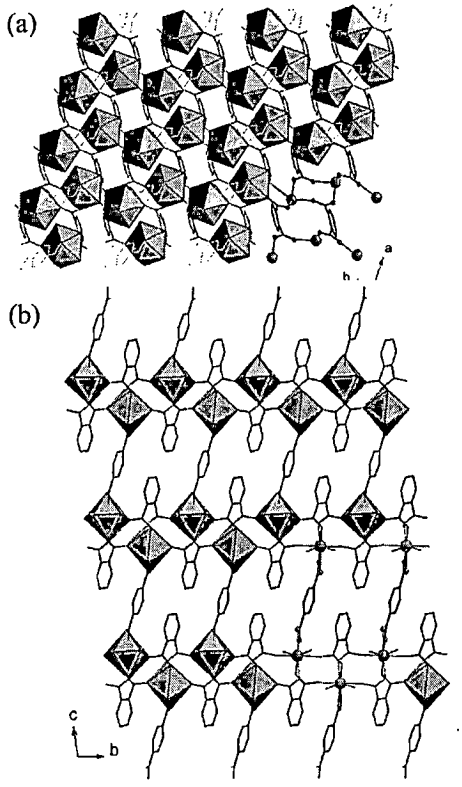

Fig. 6.2 Depictions of (a) two-dimensional and (b) three-dimensional framework structures of **II** and coordination modes adopted by the occluded ligands. H atoms are omitted for clarity.

†The diffractometer was equipped with a single micro-focus sealed X-ray tube (Mo K_α, $\lambda = 0.71073$ Å) and a Hypix Hybrid Pixel Array detector. Data collection and reduction were performed using CrysAlisPro 1.171.39.46, and empirical absorption corrections were applied to all data sets using spherical harmonics, implemented in SCALE3 ABSPACK scaling algorithm [3]. The structures were solved by intrinsic phasing methods within the SHELXT program [4] and refined on F^2 by the full-matrix least squares technique using the SHELXL program [4] *via* the Olex2 interface [5].

Table 6.1 Crystallographic and refinement details of **I-V**

	I	**II**	**III**	**IV**	**V**
CCDC No.	1871926	1871927	1871928	1871929	1871930
Empirical formula	$C_{12}H_{10}O_8Eu$	$C_{12}H_{10}O_8Tb$	$C_{12}H_{10}O_8Ho$	$C_{12}H_{10}O_8Er$	$C_{12}H_{10}O_8Tm$
Formula weight	434.16	441.12	447.13	449.46	451.13
Crystal color	Colorless	Colorless	Pink/orange	Pale pink	Colorless
Temperature)*K*(	293)2(	293)2(	293)2(	293(2)	293)2(
Crystal system	Triclinic	Triclinic	Triclinic	Triclinic	Triclinic
Space group	$P\bar{1}$)No. 2(	$P\bar{1}$)No. 2(	$P\bar{1}$)No. 2(	$P\bar{1}$)No. 2(	$P\bar{1}$)No. 2(
a)Å(	6.1203)2(	6.1106)1(	6.1086)1(	6.1089)1(	6.1060)1(
b)Å(	8.8435)4(	8.8120)1(	8.7916)1(	8.7835)1(	8.7537)1(
c)Å(	12.9577)6(	12.8911)2(	12.8634)2(	12.8533)2(	12.8332)2(
α (°)	94.933)3(	94.902(1)	95.117(1)	78.447(1)	78.324(1)
β (°)	99.053)3(	99.170)1(	99.100)1(	80.964)1(	80.976(1)
γ (°)	109.493)3(	109.803(2)	110.154(1)	69.654(1)	69.728(1)
V)Å^3(	645.63)5(	637.439(18)	632.619(17)	630.671)17(	627.319)17(
Z	2	2	2	2	2
Density)Mg·m^{-3}(	2.233	2.298	2.347	2.367	2.388
μ)mm^{-1}(	4.896	5.586	6.293	6.693	7.111
F)000(	418	422	426	428	430
Data/Restraints/Parameters	2766/0/192	2756/0/192	2728/0/192	2723/0/192	2730/0/192
S	1.006	1.059	1.066	1.067	1.012
$R_1{}^a/wR_2{}^b$	0.0438/0.0964	0.0302/0.0615	0.0282/0.0614	0.0255/0.0468	0.0281/0.0502

$^a R_1 = \Sigma||F_0|-|F_c||/|F_0|$; $^b wR_2 = [\Sigma w(F_0^2-F_c^2)^2/\Sigma w(F_0^2)_2]^{1/2}$

The completely deprotonated phth^{2-} discernibly tends to provide two-dimensional framework structure of which the architecture is diversified by the adopted coordination mode (Fig. 6.3). Whilst the μ_4-η^1:η^1:η^1:η^1 mode of phth^{2-} leads to a discrete *DD*-{LnO_8} unit as found in **I-V**, the μ_3-η^2:η^1:η^1:η^1 mode in [Ln(ad)$_{0.5}$(phth)(H_2O)$_2$] renders an edge-sharing dimer built up of two *TPRS*-{LnO_9} units [1]. Despite the differences in the primary structure-building units, *i.e.* a discrete *DD*-{LnO_8} and a dimer of two *TPRS*-{LnO_9}, and the three-dimensional framework topology between **I-V** and [Ln(ad)$_{0.5}$(phth)(H_2O)$_2$], chemical composition of the derived sheets of both series is identical, *i.e.* [Ln(phth)(H_2O)$_2$]. The [Ln(phth)(H_2O)$_2$] sheet in **I-V** can therefore be regarded as a polymorph of the [Ln(phth)(H_2O)$_2$] sheet in [Ln(ad)$_{0.5}$(phth)(H_2O)$_2$], which is

evidently induced by different coordination modes of $phth^{2-}$. This type of polymorphism which is accounted for by versatile coordination modes of the bridging ligand is markedly atypical for lanthanide coordination polymers.

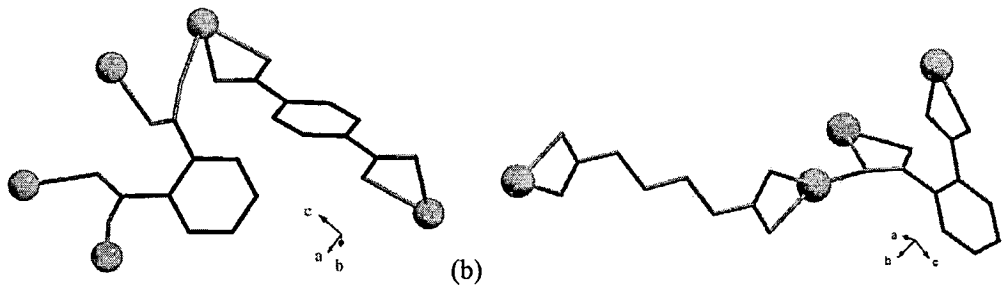

Fig. 6.3 Coordination modes of $phth^{2-}$ and bdc^{2-} in (a) **I-V**, compared with those in $[Ln(ad)_{0.5}(phth)(H_2O)_2]$ [1].

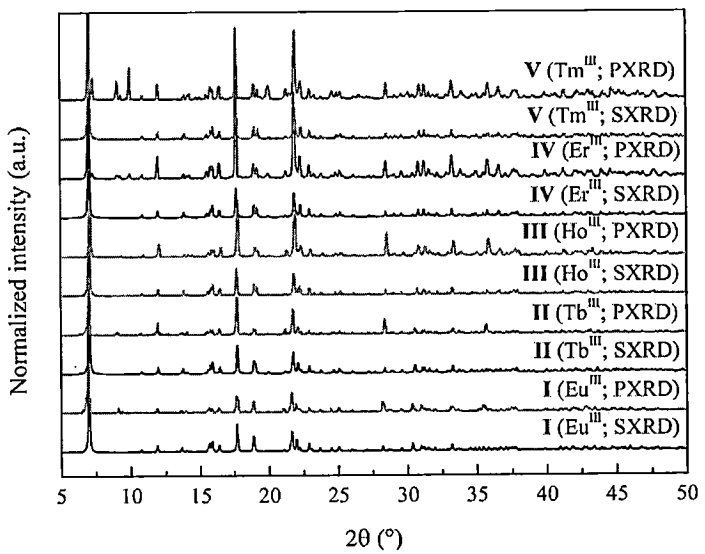

Fig. 6.4 PXRD patterns collected from powder samples yielded from the synthesis, compared with the patterns simulated from the corresponding single crystal data.

The $[Ln(phth)(H_2O)_2]$ sheets in structures **I-V** are collectively pillared by bdc^{2-} in *c* direction through the chelating μ_2-η^1:η^1:η^1:η^1 mode, giving rise to the three-dimensional $[Ln(bdc)_{0.5}(phth)(H_2O)_2]$ (Fig. 6.2). Compared with $[Ln(ad)_{0.5}(phth)(H_2O)_2]$ [1], role of the longer and more flexible ad^{2-} resembles that of the relatively rigid and short bdc^{2-}, *i.e.* being a pillar connecting the polymorphic $[Ln(phth)(H_2O)_2]$ sheets. The two linear bridging bdc^{2-} and ad^{2-} intriguingly adopt the same chelating μ_2-η^1:η^1:η^1:η^1 mode of coordination, although the shorter

bdc^{2-} instigates the non-porosity in **I-V**. This is an explicit evidence for the introduction of porosity in pillared layered structures of LnCPs by the pillaring ligands. According to the PXRD (Fig. 6.4), structures of **I-V** deduced from single crystal data were confirmed to be appropriate representatives of the synthesized samples all of which could be yielded as pure phases.

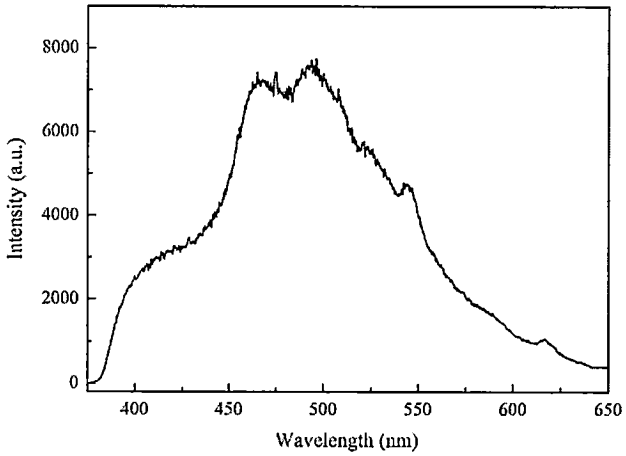

Fig. 6.5 Room temperature photoluminescent spectrum of $[Gd(bdc)_{0.5}(phth)(H_2O)_2]$ (**IX**).

6.2 Sensitization Efficiency of Co-existing $phth^{2-}$ and bdc^{2-}

Upon the excitation at 337 nm, the emission spectra of **III-V** were dominated by a broad feature of the ligand-centered $\pi^*\rightarrow\pi$ emissions (Fig. 6.5). The strong and intense $Eu^{III}:{}^5D_0\rightarrow{}^7F_J$ (J=1-4) (**I**) and $Tb^{III}:{}^5D_4\rightarrow{}^7F_J$ (J=6-3) (**II**) emissions were, on the other hand, explicit without any trait of the $\pi^*\rightarrow\pi$ emissions. Since both $phth^{2-}$ and bdc^{2-} are well acknowledged for being effective antennae with respect to both Eu^{III} and Tb^{III} [6], the co-existence of both antennae should therefore ensure the effective sensitization in **I** and **II**.

According to an antenna model, the primary factor governing effective sensitization is an appropriate energy gap between the triplet state of the organic antenna and the accepting levels of Ln^{III}, *e.g.* $\Delta\{E(^3T)\text{-}E(Eu^{III}:{}^5D_J)\}$ (J = 0-2) and $\Delta\{E(^3T)\text{-}E(Tb^{III}:{}^5D_J)\}$ (J = 3, 4) [7,8]. The $E(^3T)$ of an antenna transfixed in coordination framework however differs from that of the corresponding molecular state and depends on its local environment in the framework. To estimate the $E(^3T)$ of $phth^{2-}$ and bdc^{2-} in the titled complexes, $[Gd(bdc)_{0.5}(phth)(H_2O)_2]$ (**IX**) was synthesized using the same synthesis procedure as that of **I-V**. Its photoluminescence spectrum was collected (Fig. 6.6). With reference to two emissions at 415 and 466 nm, the $E(^3T)$ of 24,096 and 21,459 cm^{-1} could be estimated for $phth^{2-}$ and bdc^{2-}, both of which are consistent with the previously reported values: 23,810 cm^{-1} from $[Gd_2(phth)_2(H_2O)_2]$ [9], 23,256 cm^{-1} from $[Gd_2(bdc)_2(H_2O)_2]$ [9], 22,220 cm^{-1}

from $[Gd_2(phth)_3(H_2O)_3]$ and $[Gd_2(bdc)_3(DEF)_2(EtOH)_2]\cdot 2DEF$ [10]. Contribution of structural diversity to discrepancy of $E(^3T)$ is clearly displayed. In comparison with the primary accepting levels of Eu^{III} (^5D_J, J= 0-2) and Tb^{III} ($^5D_4$),[20] $phth^{2-}$ and bdc^{2-} should be able to facilitate the *f-f* emissions in both **I** and **II**.

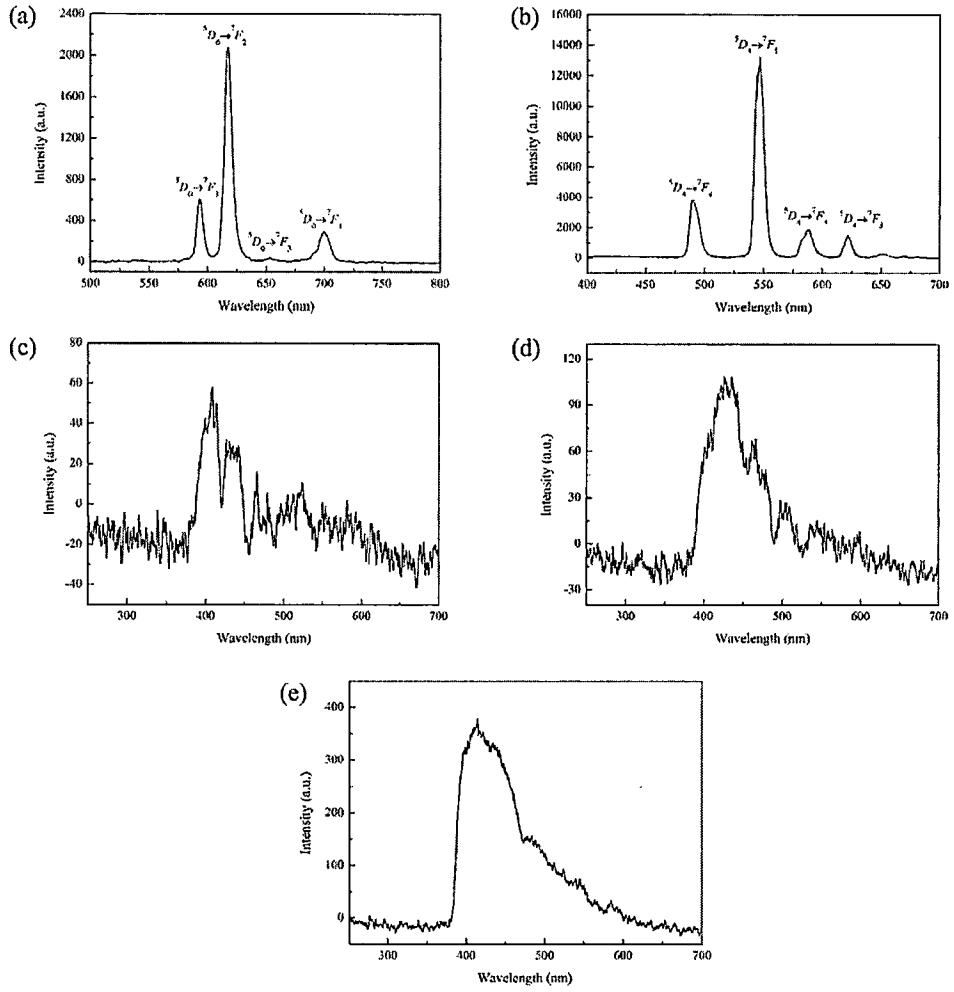

Fig. 6.6 Emission spectra of (a) **I** (b) **II** (c) **III** (d) **IV** and (e) **V**.

6.3 Temperature-dependent Photoluminescence of I, II, VI-VIII

Upon the heating of **I** and **II** from 303 to 423 *K* (Fig. 6.7), intensity of both the red Eu^{III}:$^5D_0 \rightarrow {}^7F_2$ (617 nm, **I**) and the green Tb^{III}:$^5D_4 \rightarrow {}^7F_5$ (547 nm, **II**) emissions significantly declined, indicating the gravity of the thermally-induced non-radiative decay in both complexes. According to an antenna model and the Latva proposal [6,7], a reduction in intensity of Tb^{III}:$^5D_4 \rightarrow {}^7F_5$ (**II**) should attribute to the energy-back transfer owing to a small $\Delta\{E(^3T,bdc^{2-})$-$E(Tb^{III}:{}^5D_4)\}$. Intensity declining in the Eu^{III}:$^5D_0 \rightarrow {}^7F_2$ (**I**) case may however ascribe to a large

$\Delta\{E(^3T,phth^{2-})-E(Eu^{III}:^5D_0)\}$ which detracts the sensitization and allows intra-ligand non-radiative decay.

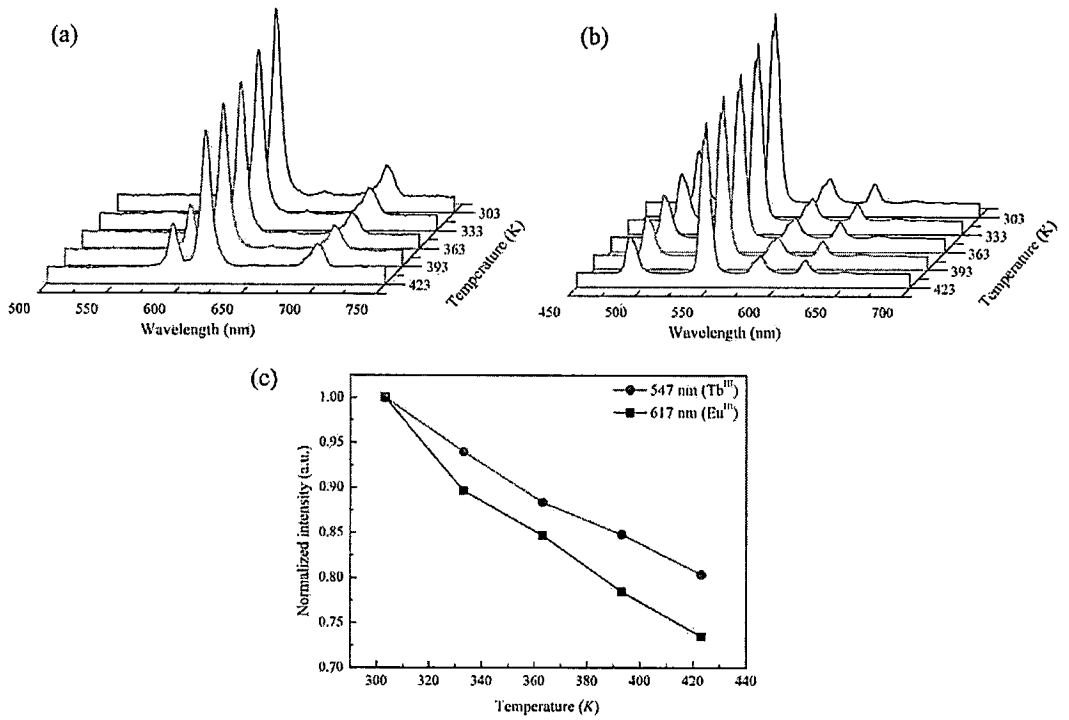

Fig. 6.7 Temperature dependent emission spectra of (a) **I** and (b) **II**, with (c) the corresponding temperature dependent intensities of $Eu^{III}:^5D_0 \rightarrow ^7F_2$ (617 nm, **I**) and $Tb^{III}:^5D_4 \rightarrow ^7F_5$ (547 nm, **II**).

To appraise the Tb^{III}-to-Eu^{III} energy transfer, the bimetallic $[Tb^{III}_xEu^{III}_{1-x}(bdc)_{0.5}(phth)(H_2O)_2]$ (**VI-VIII**) were synthesized. Structures of **VI-VIII** were ensured to be isostructural with **I** and **II** by PXRD (Fig. 6.8). According to EDXA microanalysis (Fig. 6.9), the Eu^{III}-to-Tb^{III} mole ratios are $1.10Eu^{III}$-to-$10.0Tb^{III}$ (**VI**), $2.99Eu^{III}$-to-$10.0Tb^{III}$ (**VII**) and $4.84Eu^{III}$-to-$10.0Tb^{III}$ (**VIII**). In accordance with these results, the following formulas can be concluded; $[Eu_{0.100}Tb_{0.900}(ad)_{0.5}(phth)(H_2O)_2]$ (**VI**), $[Eu_{0.230}Tb_{0.770}(ad)_{0.5}(phth)(H_2O)_2]$ (**VII**) and $[Eu_{0.330}Tb_{0.670}(ad)_{0.5}(phth)(H_2O)_2]$ (**VIII**). Based upon intensities of the red $Eu^{III}:^5D_0 \rightarrow ^7F_2$ and the green $Tb^{III}:^5D_4 \rightarrow ^7F_5$ emissions, the grievous effect of heating on photoluminescent properties of the **VI-VIII** were displayed (Fig. 6.10). The declining intensity of the green emission was markedly more substantial than the red emission, which is contrary to the **I-II** cases. The heating effect became successively more drastic with the rising content of Eu^{III}, *i.e.* from 34% (**VI**) to 49% (**VII**) and 51% (**VIII**). A reduction of the red emission of **VI** containing the lowest Eu^{III} content was less than 10% compared with approximately 20% in the cases of **VII** and **VIII**. These results manifest

the Tb^{III}-to-Eu^{III} energy transfer in **VI-VIII**, and the dependence of the process efficiency on the concentration of Eu^{III}, which is an acceptor.

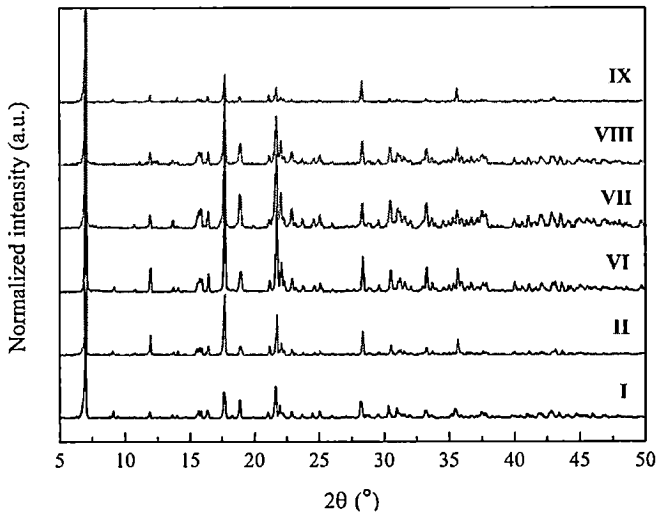

Fig. 6.8 PXRD patterns of **VI-IX** compared with those of **I** and **II**.

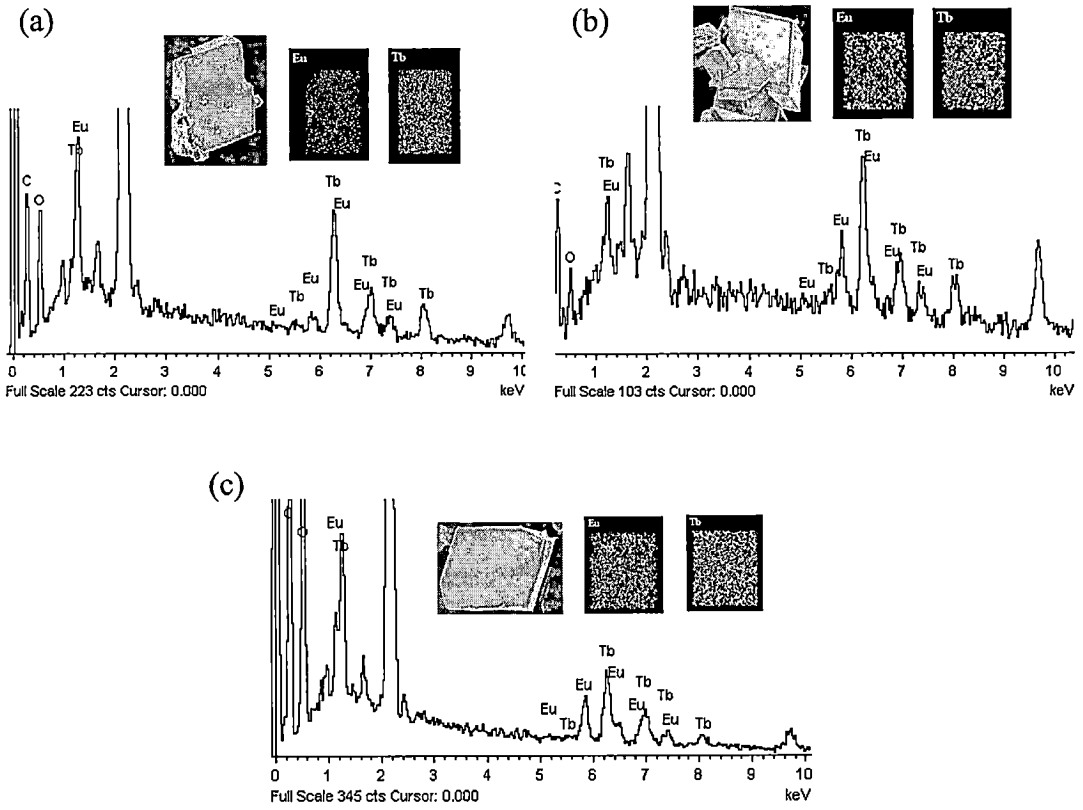

Fig. 6.9 EDXA spectra of (a) **VI**, (b) **VII**, and (c) **VIII** with the corresponding scanning electron micrograph and elemental mappings.

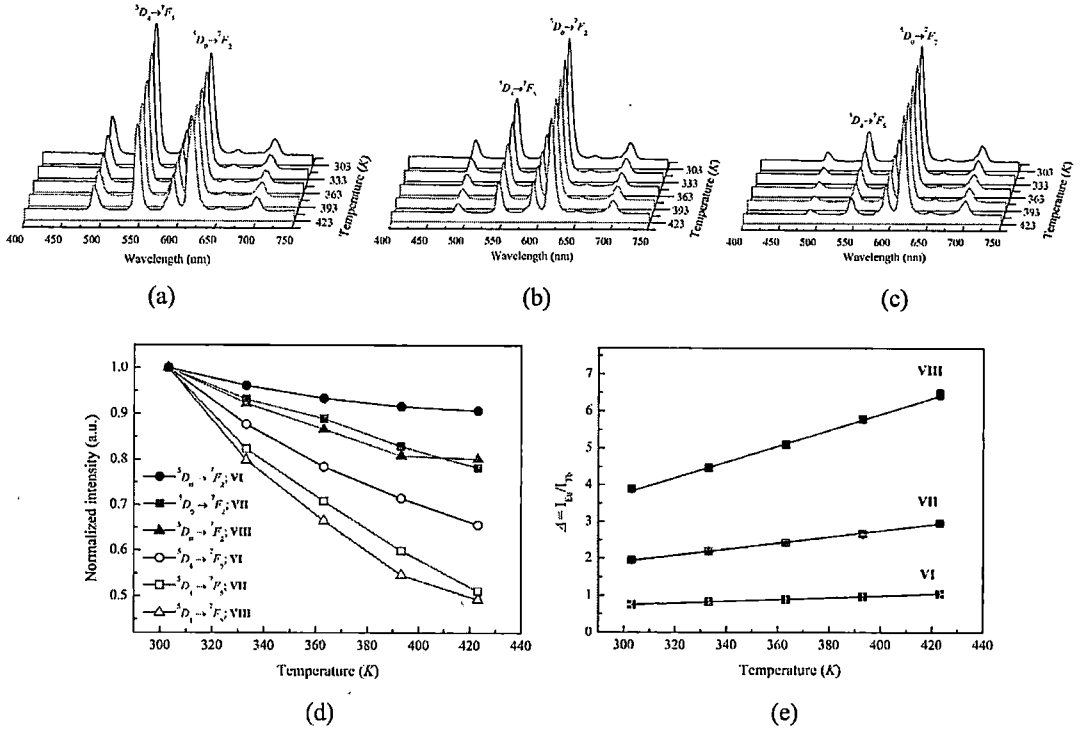

Fig. 6.10 Temperature dependent emission spectra of (a) **VI** (b) **VII** and (c) **VIII**, with the corresponding (d) temperature dependent intensities, and (e) the calculated Δ parameters.

6.4 Ratiometric Temperature Sensing Potentiality of VI-VIII

Since the enlarged divergence in temperature dependent characters as found in intensity change of **VI-VIII** is a common indicator of sensitivity in ratiometric thermometry [10], thermometric parameters (Δ) were thus calculated from intensity ratio of the red Eu^{III}:$^5D_0 \rightarrow {}^7F_2$ and the green Tb^{III}: $^5D_4 \rightarrow {}^7F_5$ emissions (I_{Eu}/I_{Tb}). An excellent linear correlation has been revealed for the temperature dependent Δ over the 303-423 K for **VI-VIII** (Fig. 6.11). This correlation can be reproduced with exceptional standard deviations. To evaluate performance of **VI-VIII** in temperature sensing, the relative sensitivity (S_r; $\%{\cdot}K^{-1}$) were determined, showing the reverse temperature-dependence with the maximal and the minimal S_r at 303 and 423 K, respectively; 0.32-0.23 $\%{\cdot}K^{-1}$ (**VI**), 0.42-0.28 $\%{\cdot}K^{-1}$ (**VII**), and 0.55-0.33 $\%{\cdot}K^{-1}$ (**VIII**). The highest S_r was achieved for **VIII** containing the highest content of Eu^{III}, which is an acceptor in the Tb^{III}-to-Eu^{III} energy transfer process. The S_r of **VI-VIII** were however poorer than those of the closely relevant $[Ln(ad)_{0.5}(phth)(H_2O)_2]$ containing only the $phth^{2-}$ antenna [1]. A nullifying affect imparted from the co-existing of bdc^{2-} and $phth^{2-}$ possessing different triplet state energies is therefore revealed.

Accordingly, a small $\Delta\{E(^3T,bdc^{2-})\text{-}E(Tb^{III}:^5D_4)\}$ in **II** leads to a critical energy-back transfer manifested through a declining of the emission intensity, despite the presence of $phth^{2-}$. These results imply the sensitization process between each antenna and the Ln^{III} to be independent.

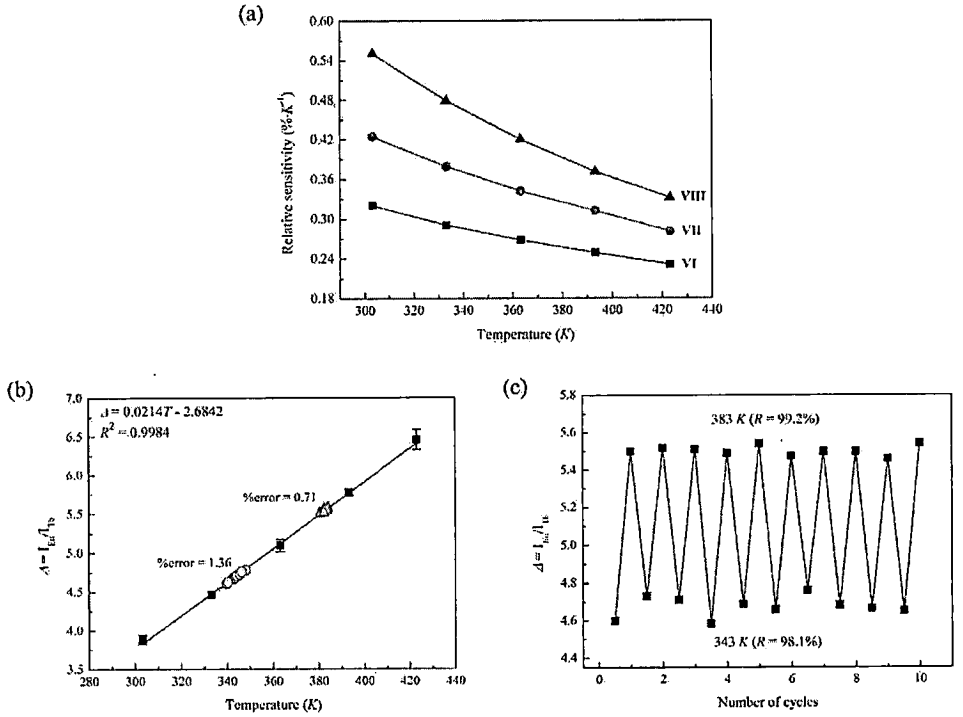

Fig. 6.11 Depiction of (a) the temperature dependent Δ parameters of **VI-VIII**, and the sensing performance of **VIII** in terms of (b) S_r of **VI-VIII**, (c) δT, and (d) R based on ten successive measurements.

Table 6.2 Photoluminescent τ (ms) and η_{ET} (%) at room temperature for **I, II** and **VI-VIII**

	$\tau(Tb^{III}:{}^5D_4\rightarrow{}^7F_5)$	$\tau(Eu^{III}:{}^5D_0\rightarrow{}^7F_2)$	η_{ET}
I,]Eu)bdc$_{(0.5)}$phth()$H_2O_{(2}$[	-	0.256	-
II,]Tb)bdc$_{(0.5)}$phth()$H_2O_{(2}$[	1.17	-	-
VI,]$Eu_{0.100}Tb_{0.900}$)bdc$_{(0.5)}$phth()$H_2O_{(2}$[	0.533	0.524	54.5
VII,]$Eu_{0.230}Tb_{0.770}$)bdc$_{(0.5)}$phth()$H_2O_{(2}$[	0.308	0.383	73.6
VIII,]$Eu_{0.330}Tb_{0.670}$)bdc$_{(0.5)}$phth()$H_2O_{(2}$[	0.222	0.389	81.0

With reference to ten successive measurements at two different temperatures (343 and 383 *K*), the values of temperature resolution (δT) in term of percentage deviation of the temperature read outs (%) and repeatability of the measurement (R) were determined. An excellent δT of 1.36% at 343 *K* and 0.71% at 383 *K* with R >98% were achieved for **VIII**. Noticeably, better sensing

performance was noticeably yielded at higher temperature. The room temperature lifetimes (τ) were also determined from the Eu^{III}:$^5D_0 \rightarrow {}^7F_2$ (τ_{Eu}) and the Tb^{III}:$^5D_4 \rightarrow {}^7F_5$ (τ_{Tb}) emissions (Table 6.2), showing the truncated τ_{Tb} and the extended τ_{Eu} in **VI- VIII** compared with the corresponding values of **I** and **II**. The Tb^{III}-to-Eu^{III} energy transfer efficiencies (η_{ET}) in **VI-VIII** were calculated, displaying the successive enhancement in η_{ET} from **VI** to **VIII** of which approximately 81% efficiency was revealed. These results are in excellent agreement with aforementioned tendencies. In accordance with the yielded data, the crucial influence of the Tb^{III}-to-Eu^{III} energy transfer of which the efficiency depends on the Eu^{III} content can therefore be concluded. The promotion of the divergence in temperature dependent intensities of the two emitters and the enhanced S_r can also be accounted for. The improved η_{ET} would result in a greater loss in Tb^{III}:$^5D_4 \rightarrow {}^7F_5$ (τ_{Tb}) intensity but a gaining in Eu^{III}:$^5D_0 \rightarrow {}^7F_2$ (τ_{Eu}) intensity leading to their divergent temperature dependency. The S_r which is one of the practical parameters determining the sensing performance is consequently enhanced. This finding is consistent with previous reports on the association between the enhancement of η_{ET} and the Eu^{III} acceptor content and the evidence for the importance of the Tb^{III}-to-Eu^{III} energy transfer to the improvement of S_r which is notably rare [1,11,12].

6.5 Conclusion

Based on a series of monometallic and bimetallic $[Ln(bdc)_{0.5}(phth)(H_2O)_2]$ of which the structures are intimately relevant to $[Ln(ad)_{0.5}(phth)(H_2O)_2]$ [1], the influences of mixed bdc^{2-} and $phth^{2-}$ antennae on temperature dependent photoluminescent behaviour and temperature sensing performance were studied. Despite being effective antennae, the co-existence of $phth^{2-}$ and bdc^{2-} evidently resulted in poorer S_r compared with $[Ln(ad)_{0.5}(phth)(H_2O)_2]$ containing only $phth^{2-}$, over the same working temperature range of 303-423 *K*. The energy gap between the $E(^3T)$ of each antenna and the accepting levels of each Ln^{III} need to be separately considered. The crucial influence of the Tb^{III}-to-Eu^{III} energy transfer on S_r and its dependency on the content of Eu^{III} have been displayed. With reference to **VIII** as a representative of $[Ln(bdc)_{0.5}(phth)(H_2O)_2]$, the maximum S_r of $0.55\%{\cdot}K^{-1}$ was revealed at 303 *K* before deteriorating to $0.33\ \%{\cdot}K^{-1}$ at 423 *K*. The δT of 1.36% and 0.71% were however yielded at 343 and 383 *K*, respectively, with $R > 98\%$, indicating the characteristic temperature resolution and precision of the measurements.

REFERENCES

(1) Chuasaard, T.; Ngamjarurojana, A.; Surinwong, S.; Konno, T.; Bureekaew, S.; Rujiwatra, A. *Inorg. Chem.* **2018**, *57*, 2620-2630.

(2) Thirumurugan, A.; Natarajan, S. *Eur. J. Inorg. Chem.* **2004**, *2004*, 762-770.

(3) Rigaku Oxford Diffraction, *CrysAlisPRO Software System*, versions 1.171.39.46 (**2018**), Rigaku Corporation, Oxford, UK.

(4) Sheldrick, G. *Acta Cryst. A* **2015**, *71*, 3-8.

(5) Dolomanov, O. V.; Bourhis, L. J.; Gildea, R. J.; Howard, J. A. K.; Puschmann, H. *J. Appl. Crystallogr.* **2009**, *42*, 339-341.

(6) Einkauf, J.D.; Clark, J.M.; Paulive, A.; Tanner, G.P.; de Lill, D.T.A. *Inorg. Chem.* **2017**, *56*, 5544-5552.

(7) Latva, M.; Takalo, H.; Mukkala, V.-M.; Matachescu, C.; Rodríguez-Ubis, J. C.; Kankare, J. *J. Lumin.* **1997**, *75*, 149-169.

(8) Bünzli, J.-C. G. In *Handbook on the Physics and Chemistry of Rare Earths*; Bünzli, J.-C. G., Pecharsky, V. K., Ed.; Elsevier: 2016; Vol. 50, pp 141-176.

(9) Hilder, M.; Junk, P.C.; Kynast, U.H.; Lezhnina, M.M. *J. Photochem. Photobiol.* **2009**, *202*, 10-20.

(10) Cheng, Y.; Gao, Y.; Lin, H.; Huang, F.; Wang, Y. *J. Mater. Chem. C* **2018**, *6*, 7462-7478.

(11) Zhou, J.; Xia, Z. *J. Mater. Chem. C* **2014**, *2*, 6978-6984.

(12) Baur, F.; Glocker, F.; Jüstel, T. *J. Mater. Chem. C* **2015**, *3*, 2054-2064.

APPENDICES

List of Publications

No.	Article Title	Journal Matrix		
		Quartile	JIF	Citation
1	T. Chuasaard, K. Panyarat, P. Rodlamul, K. Chainok, S. Yimklan, **A. Rujiwatra***, Structural Variation and Preference in Lanthanide-pyridine-2,6-dicarboxylate Coordination Polymers, *Crystal Growth & Design* **17** (2017) 1045-1054.	Q1	3.972	5
2	K. Panyarat, S. Surinwong, T.J. Prior, T. Konno, **A. Rujiwatra***, Crystal Structure and Gas Adsorption Behavior of New Lanthanide-benzene-1,4-dicarboxylate Frameworks, *Microporous Mesoporous Materials* **251** (2017) 155-164.	Q1	3.649	5
3	T. Chuasaard, A. Ngamjarurojana, S. Surinwong, T. Konno, S. Bureekaew, **A. Rujiwatra***, Lanthanide Coordination Polymers of Mixed Phthalate/Adipate for Ratiometric Temperature Sensing in the Upper-Intermediate Temperature Range, *Inorganic Chemistry* **57** (2018) 2620-2630.	Q1	4.700	9
4	K. Panyarat, A. Ngamjarurojana, A. Rujiwatra*, Colorimetric Analysis: A New Strategy to Improve Ratiometric Temperature Sensing Performance of Lanthanide Benzenedicarboxylates, *Journal of Photochemistry and Photobiology A – Chemistry*, Accepted.	Q2	2.891	-
5	T. Chuasaard, A. Ngamjarurojana, T. Konno, **A. Rujiwatra***, Influences of Mixed Antennae on Ratiometric Thermometry of Lanthanide Benzenedicarboxylates, *Inorganic Chemistry*, Submitted (as of March 22, 2019).	Q1	4.700	-

Microporous and Mesoporous Materials 251 (2017) 155–164

Contents lists available at ScienceDirect

Microporous and Mesoporous Materials

journal homepage: www.elsevier.com/locate/micromeso

Crystal structures and gas adsorption behavior of new lanthanide-benzene-1,4-dicarboxylate frameworks

Kitt Panyarat [a, b], Sireenart Surinwong [c], Timothy J. Prior [d], Takumi Konno [c], Apinpus Rujiwatra [a, *]

[a] Department of Chemistry, Faculty of Science, Chiang Mai University, Chiang Mai 50200 Thailand
[b] Graduate School, Chiang Mai University, Chiang Mai 50200, Thailand
[c] Department of Chemistry, Graduate School of Science, Osaka University, Toyonaka, Osaka 560-0043, Japan
[d] Chemistry, The University of Hull, Cottingham Road, Hull HU6 7RX, UK

ARTICLE INFO

Article history:
Received 21 November 2016
Received in revised form
2 May 2017
Accepted 1 June 2017
Available online 3 June 2017

Keywords:
Metal organic framework
Lanthanide
Benzenedicarboxylate
Gas adsorption
Crystal structure

ABSTRACT

Six new lanthanide metal organic complexes, *i.e.* $[La_2(NO_2\text{-}BDC)_3(H_2O)_4]$ (**1**) $[Ln(L)_{0.5}(NO_2\text{-}BDC)(H_2O)]\cdot 3H_2O$ (Ln = Eu (**2**), Tb (**3**), Dy (**4**) and Ho (**5**); L = BDC^{2-} or $BDC^{2-}/NO_2\text{-}BDC^{2-}$) and $[Tm(NO_2\text{-}BDC)_{1.5}(H_2O)]\cdot H_2O$ (**6**), have been synthesized using mixed ligands of benzene-1,4-dicarboxylic acid (H_2BDC) and the *in situ* generated 2-nitro-benzene-1,4-dicarboxylic acid ($NO_2\text{-}BDC^{2-}$). Single crystal structures and topologies of the complexes are presented based on the single crystal X-ray diffraction and spectroscopic data. Whilst the structures of **1** and **6** contain negligible voids, the frameworks of **2**–**5** are microporous in nature and stable upon the removal of all the water molecules from the structures and thermal treatment to over 400 °C. Based on the study of **2**, significant adsorption capacities for carbon dioxide (95 $cm^3\cdot g^{-1}$ or 4.2 $mmol\cdot g^{-1}$) and hydrogen (79 $cm^3\cdot g^{-1}$ or 4 $mmol\cdot g^{-1}$), as well as the remarkable stability of the framework upon the sorption/desorption experiments are revealed.

1. Introduction

Environmental impact caused by the emission of greenhouse gases has become a major global concern which therefore demands technologies to control the emission of such gases especially carbon dioxide which is reported to be the primary culprit for the rising of global temperature [1,2]. Despite extensive research on the capture of carbon dioxide in the last two decades, none of the existing technologies have fulfilled the target performance criteria; for example, large capture capacity, high selectivity, optimal affinity and high stability under capture and regeneration conditions [3–5]. Among the capturing techniques under investigation at the present, solid sorbent materials and metal organic frameworks (MOFs) draw an immense interest as the most promising candidates. This is due to their unprecedentedly high active surface area, remarkably large void volume, structural and chemical robustness, and potential to be tailor-made, up-scaled and made into membranes [4,6–8]. Since the first report of [Zn(BDC)]·(DMF) (H_2O) (BDC = benzene-1,4-dicarboxylate and DMF = N,N′-dimethylformamide) with promising carbon dioxide capture capacity [9], several series of new MOFs with encouraging performance have been reported. Strategies to enhance the capture capacities and selectivity such as the generation of unsaturated or open metal sites, the fabrication of flexible interpenetrating frameworks, and the installation of desired functionalities on the organic linkers have been proposed [4,10,11]. Regarding the open metal sites, lanthanide metal ions are deemed to be judicious choices as they tend to include small solvent molecules in their coordination sphere which can be removed to generate open metal sites without framework disruption. In addition, there is a tendency for lanthanide metal ions to provide robust frameworks of high dimensionality with adjustable pore characteristics. The study of lanthanide MOFs for carbon dioxide capture has thus far been limited with only few examples reported; $Tb_2(BDC)_3$ [12], $Tb(BDC)NO_3$ [13] and $[Ln_2(TPO)_2(HCOO)]\cdot(Me_2NH_2)\cdot(DMF)_4\cdot(H2O)_6$ (Ln = Y and Eu, H_3TPO = tris-(4-carboxylphenyl)phosphineoxide, DMF = N,N-dimethylformamide) [14].

Here, a series of six new lanthanide MOFs have been designed and synthesized using $NO_2\text{-}BDC^{2-}$ and BDC^{2-} as the primary

* Corresponding author.
E-mail address: apinpus.rujiwatra@cmu.ac.th (A. Rujiwatra).

http://dx.doi.org/10.1016/j.micromeso.2017.06.003
1387-1811/

linkers because of its tendency to generate microporous frameworks which was reported to be suitable for carbon dioxide capture [9,15]. *In situ* nitration was employed to introduce the nitro group to BDC^{2-} and therefore to generate the multivariate frameworks comprising both BDC^{2-} and NO_2-BDC^{2-} linkers. The inclusion of the nitro group was intended to increase the interaction of the framework and carbon dioxide [16]. Four of the six reported complexes are microporous with accessible voids, extraordinary stability and significant gas capture capacities. The photoluminescence properties of the complexes have also been investigated.

2. Experimental

2.1. Materials and methods

All chemicals were obtained commercially and used without further purification; La_2O_3 (99.9%, Merck), Eu_2O_3 (99.9%, Merck), Tb_2O_3 (99.9%, Merck), Dy_2O_3 (99.9%, Fluka), Ho_2O_3 (99%, Prolabo), Er_2O_3 (99%, Fluka), Tm_2O_3 (99%, Merck), HNO_3 (≥90%, Sigma-Aldrich), benzene-1,4-dicarboxylic acid (H_2BDC; $C_8H_6O_4$, 97%, BDH), and 1,4-diazabicyclo [2.2.2]octane (DABCO; $C_6H_{12}N_2$, 98%, Sigma-Aldrich).

Infrared (IR) spectra were recorded using a Bruker Tensor 27 FT-IR instrument and KBr discs (98.5%, BDH). Thermogravimetric analyses were conducted on a Perkin Elmer Pyris Diamond TG/DTA using a heating rate of 10 °C·min^{-1} from room temperature to 1000 °C in a nitrogen gas flow. Powder X-ray diffraction (PXRD) experiments were conducted using a Bruker D8 Advance X-ray diffractometer operated with Ni filtered Cu *Kα* radiation (λ = 1.5418 Å, 48 kV, 30 mA). The gas sorption experiments were performed using a BELSORP-mini II instrument in a range of 0–1 bar pressures. Ultra-pure research grade nitrogen, hydrogen and carbon dioxide gases were used. The samples were heated at 250 °C for 2 h under vacuum before the measurements which were performed at 77 *K* for the nitrogen and hydrogen and at 195 *K* for the carbon dioxide. Photoluminescence spectra were collected at room temperature using an Avantes Multichannel spectrometer with the Ocean Optics LED 255 nm excitation source.

2.2. Hydrothermal syntheses of 1–6

To synthesize $[La_2(NO_2\text{-}BDC)_3(H_2O)_4]$ (**1**) $[Ln(L)_{0.5}(NO_2\text{-}BDC)(H_2O)]\cdot 3H_2O$ {Ln = Eu (**2**), Tb (**3**), Dy (**4**) and Ho (**5**); L = BDC^{2-} or $BDC^{2-}/NO_2\text{-}BDC^{2-}$} and $[Tm(NO_2\text{-}BDC)_{1.5}(H_2O)]\cdot H_2O$ (**6**), the solution of the corresponding Ln_2O_3 was first prepared by dissolving the Ln_2O_3 (1.70 mmol) in 1.00 mL of concentrated HNO_3 aqueous solution. Each solution was then mixed with 10.0 mL of an aqueous solution containing H_2BDC (4.0 mmol) and DABCO (4.0 mmol) with vigorous stirring. The Ln_2O_3: HNO_3: H_2BDC: DABCO: H_2O mole ratio of every reaction was 1.70: 5.16: 4.00: 4.00: 556. The reactions were performed using a 23.0 mL Teflon lined hydrothermal autoclave under an autogenous pressure generated at 180 °C for 24 h, and afforded a few crystals as the solid products.

2.3. X-ray crystallography

Diffraction data of **1** and **6** were collected on a Bruker APEX-II CCD diffractometer and a Stoe IPDS2 image plate diffractometer, respectively, whereas those of **2–5** were collected on a Bruker D8 QUEST CMOS diffractometer. The machines were operated using Mo *Kα* radiation (λ = 0.71073 Å) at 298 (2) *K* for **1–5** and 150 (2) *K* for **6**. Data reduction and an adsorption correction of **1–5** were performed with the SAINT [17] and SADABS [18] software packages, whilst that of **6** was done using the Tompa method [19]. The structures were solved by direct methods implemented within SHELXS-86 [20] and full-matrix least squares refinements were carried out on F^2 for all data with the program SHELXL-97 [20] *via* either the WinGX [21] or the OLEX2 [22] program interfaces. Non-hydrogen atoms were refined anisotropically, and the hydrogen atoms on the organic ligands were located at ideal geometrical positions using a riding model. No hydrogen atoms were assigned on the unbound water molecules. Crystallographic and refinement data are summarized in Table 1.

Table 1
Crystallographic data and structure refinement summary of **1–6**.

	1	2	3	4	5	6
CCDC	1517770	1517767	1517771	1517766	1517768	1517769
Chemical formula	$La_2C_{24}H_{14}N_3O_{22}$	$EuC_{12}H_{4.69}N_{1.31}O_{12.62}$	$TbC_{12}H_{4.68}N_{1.32}O_{12.64}$	$DyC_{12}H_5NO_{12}$	$HoC_{12}H_7NO_{12}$	$TmC_{12}H_4N_{1.5}O_{11}$
Formula weight	974.20	521.09	528.50	517.67	520.10	514.10
Temperature/*K*	293 (2)	273.15	273.15	273.15	273.15	150 (2)
Crystal system	Triclinic	Orthorhombic	Orthorhombic	Orthorhombic	Orthorhombic	Monoclinic
Space group	$P\bar{1}$	*Pbca*	*Pbca*	*Pbca*	*Pbca*	*C2/c*
a/Å	9.7849 (5)	6.8849 (2)	6.8451 (9)	21.6689 (3)	6.7919 (3)	16.5383 (13)
b/Å	10.9160 (6)	21.8286 (7)	21.731 (3)	22.8825 (10)	21.6514 (11)	11.2800 (13)
c/Å	15.6249 (8)	23.0388 (7)	22.936 (3)	6.8125 (11)	22.8375 (10)	15.2694 (15)
α/°	82.299 (2)	90	90	90	90	90
β/°	77.197 (2)	90	90	90	90	90.350 (7)
γ/°	63.398 (2)	90	90	90	90	90
Volume/Å^3	1453.99 (13)	3462.45 (18)	3411.7 (9)	3377.9 (6)	3358.3 (3)	2848.5 (5)
Z	2	8	8	8	8	8
ρ_{calc}mg/mm^3	2.225	1.999	2.058	2.036	2.057	2.398
μ/mm^{-1}	3.001	3.685	4.215	4.488	4.777	6.299
F(000)	917.0	1998.0	2016.0	1968.0	1976.0	1948.0
Crystal size/mm^3	0.08 × 0.06 × 0.05	0.18 × 0.14 × 0.12	0.2 × 0.16 × 0.14	0.4 × 0.2 × 0.2	0.4 × 0.2 × 0.2	0.45 × 0.42 × 0.25
Radiation	Mo K_α (λ = 0.71073)	Mo K_α (λ = 0.71073)	Mo K_α (λ = 0.71073)	Mo K_α (λ = 0.71073)	Mo K_α (λ = 0.71073)	Mo K_α (λ = 0.71073)
Data/restraints/parameters	9378/7/450	4295/1/244	4780/1/244	5906/0/232	4174/0/232	3127/1/258
Goodness-of-fit	1.087	1.089	1.159	1.120	1.130	0.913
R (F^2), R_w [$I \geq 2\sigma$ (I)]	0.0398, 0.1040	0.0389, 0.0913	0.0377, 0.0882	0.0445, 0.1090	0.0519, 0.1209	0.0254, 0.0577
R (F^2), R_w (all data)	0.0540, 0.1137	0.0519, 0.0969	0.0438, 0.0908	0.0561, 0.1143	0.0626, 0.1263	0.0355, 0.0589

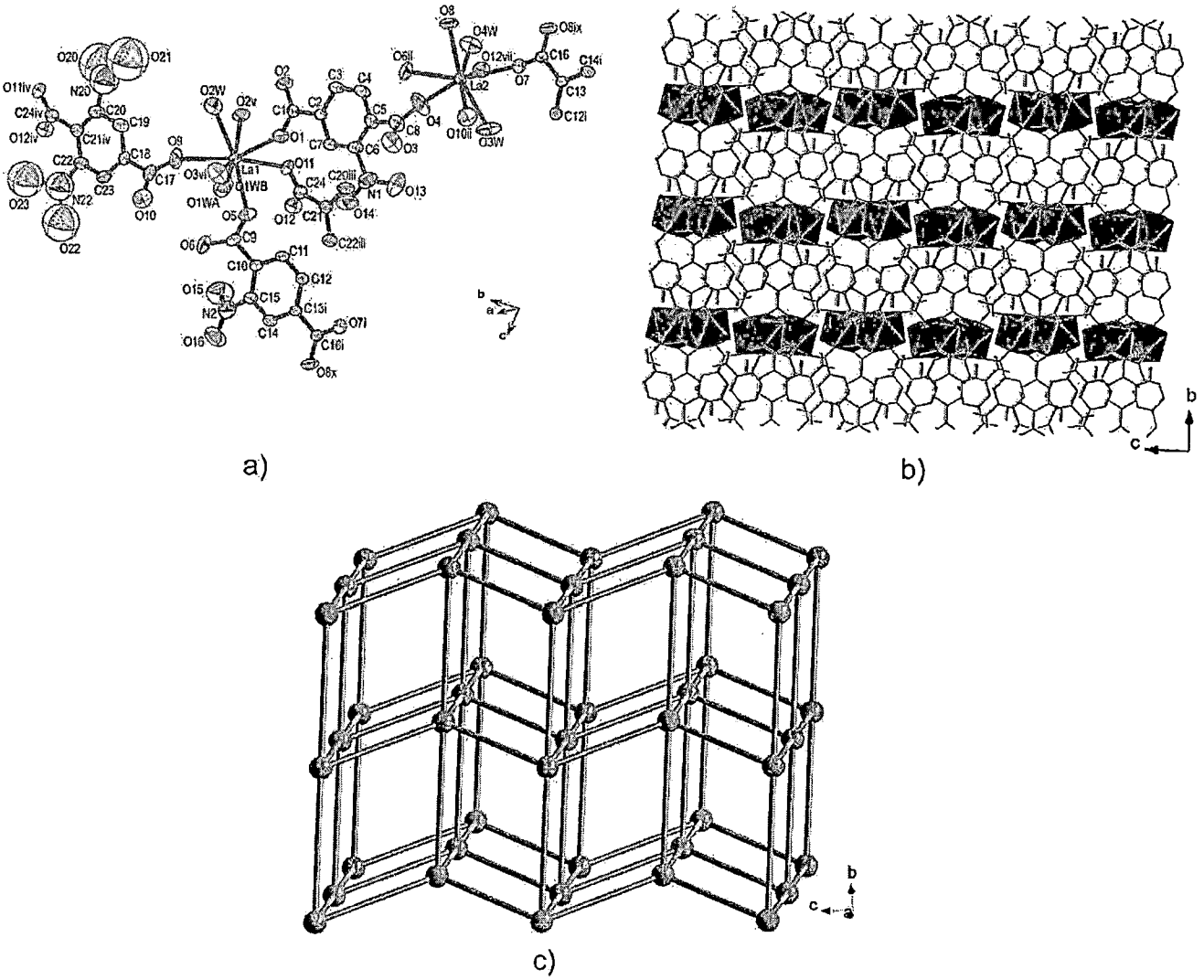

Fig. 1. Views of (a) an extended asymmetric unit drawn as 50% thermal ellipsoids, (b) the three-dimensional framework, and (c) the simplified **pcu** α-Po topology of **1**. Symmetry operations: (i) 2-x, -1-y, 1-z (ii) 2-x, -y, 1-z (iii) x, −1+y, z (iv) x, 1 + y, z (v) 1-x, 1-y, 1-z (vi) 2-x, -y, 1-z (vii) 1-x, -y, 1-z (viii) 1-x, 2-y, 2-z (ix) 2-x, -1-y, -z (x) x, y, 1 + z.

Table 2
Summary of hydrogen bonding distances (d, Å) and angles (∠,°) observed in **1–6**.

D–H···A	d (D–H···A)	∠D–H···A	D–H···A	d (D–H···A)	∠D–H···A
1[a]			**2**[b]		
O4w–H4wA···O15i	2.996 (4)	143	O7···O1w	2.774 (9)	–
O4w–H4wB···O7ii	3.003 (1)	146	O1w···O2w	2.820 (13)	–
O3w–H3wA···O11iii	3.001 (3)	160	O2w···O3w	2.956 (13)	–
O3w–H3wB···O13iv	3.416 (9)	162	O2w···O3wi	2.855 (15)	–
O3w–H3wB···O14iv	2.781 (0)	115	O1wii···O3w	2.986 (15)	–
O2w–H2wA···O2	3.077 (0)	148	O2w···O2	2.882 (9)	–
O2w–H2wB···O13v	2.991 (7)	146	C12···O5iii	2.820 (4)	–
3[c]			**4**[d]		
O7i···O1w	2.778 (8)	–	O7···O1w	2.788 (10)	–
O2···O3wi	2.875 (7)	–	O1wi···O9Aii	3.208 (13)	–
O2w···O3wii	2.954 (13)	–	O1wii···O3w	2.909 (16)	–
O1w···O3w	2.952 (13)	–	O3wii···O2w	2.993 (15)	–
O10···O2w	3.132 (26)	–	O2w···O3w	2.806 (15)	–
O1w···O2w	2.952 (13)	–	O1w···O2w	2.828 (13)	–
O2wiii···O9Biv	3.370 (14)	–	C12···O5	2.788 (7)	–

(*continued on next page*)

Table 2 (*continued*)

D–H···A	d (D–H···A)	∠D–H···A	D–H···A	d (D–H···A)	∠D–H···A
1[a]			**2**[b]		
5[c]			**6**[f]		
O7···O1wi	2.778 (15)	–	C3–H3···O8i	3.265 (15)	151
O9Bi···O1wii	3.112 (25)	–	C6–H6···O9ii	2.858 (13)	101
O1wii···O3wiii	2.813 (19)	–	C7–H7···O6iii	3.219 (7)	140
O2wiv···O3wiii	2.827 (24)	–	O9···O2wiv	3.661 (13)	–
O3wiii···O9Av	2.784 (9)	–	O1w···O8	2.984 (7)	–
O3w···O2w	2.967 (24)	–	O1w···O2w	2.647 (7)	–
C12···O4	2.784 (9)	–	O2···O2wv	2.856 (7)	–

[a] (i) −1+*x*, −1+*y*, −1+*z* (ii) *x*, *y*, 1 + *z* (iii) 1-*x*, 2-*y*, 1-*z* (iv) -*x*, 3-*y*, 1-*z* (v) *x*, 1 + *y*, *z*.
[b] (i) 0.5 + *x*, *y*, 0.5-*z* (ii) −0.5 + *x*, *y*, 0.5-*z* (iii) 0.5 + *x*, 0.5 + *y*, -*z* (iv) 0.5-*x*, 0.5 + *y*, *z*.
[c] (i) −0.5 + *x*, 1.5-*y*, 1-*z* (ii) 0.5 + *x*, *y*, 0.5-*z* (iii) 0.5-*x*, 1-*y*, 0.5 + *z* (iv) *x*, 1.5-*y*, 0.5 + *z*.
[d] (i) −0.5 + *x*, *y*, 0.5-*z* (ii) *x*, 0.5-*y*, −0.5 + *z*.
[e] (i) −0.5 + *x*, 0.5-*y*, 1-*z* (ii) 1-*x*, 1-*y*, 1-*z* (iii) -*x*, 1-*y*, 1-*z* (iv) 0.5-*x*, 1-*y*, 0.5 + *z* (v) 0.5-*x*, 0.5 + *y*, *z*.
[f] (i) 3/2-*x*, 1/2 + *y*, 3/2-*z* (ii) 2-*x*, *y*, 3/2-*z* (iii) 3/2-*x*, −1/2 + *y*, 3/2-*z* (iv) x, 2-*y*, −0.5 + *z*.

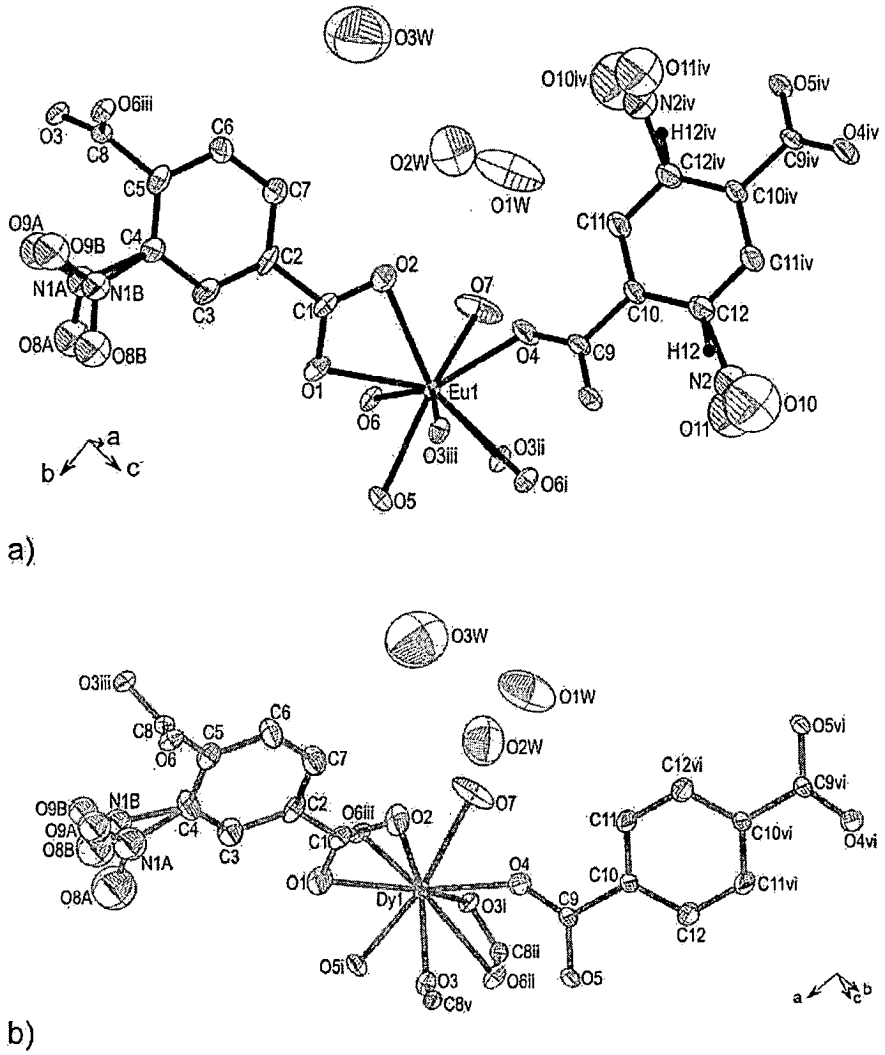

Fig. 2. Views of the extended asymmetric units of (a) **2** and (b) **4** both of which are drawn as 50% thermal ellipsoids. Symmetry operations for **2:** (i) 0.5 + *x*, 0.5-*y*, 1-*z* (ii) *x*, 0.5-*y*, 0.5 + *z* (iii) 0.5 + *x*, *y*, 0.5-*z* (iv)1-*x*, -*y*, 1-*z*. For **3**: (i) 1.5-*x*, 1-*y*, −0.5 + *z* (ii) 1.5-*x*, 0.5 + *y*, *z* (iii) *x*, 0.5-*y*, −0.5 + *z* (iv) 1.5-*x*, 1-*y*, 0.5 + *z* (v) *x*, 0.5-*y*, 0.5 + *z* (vi) 1-*x*, 1-*y*, 2-*z*.

3. Results and discussion

3.1. Hydrothermal crystal growth and in situ ligand synthesis

Following our interest in extending the use of lanthanide ions in fabricating new microporous frameworks [23], six new complexes have been synthesized. The colors of the crystals are in good agreement with the characteristic colors of the corresponding lanthanide ions. The crystals showed a tint of yellow color which is consistent with the presence of the nitrated BDC^{2-} (NO_2-BDC^{2-}) derived *in situ* under strong acidic hydrothermal conditions [23,24]. The existence of NO_2-BDC^{2-} is confirmed by characteristic υ(C-N) and υ(N-O) in the IR spectra of all complexes (see Appendix). To the best of our knowledge, these lanthanide MOFs can be regarded as one of the very few multivariate lanthanide MOFs yielded by using the *in situ* ligand synthesis strategy. It should be however noted that the formation of nitrosamines may be possible under the employed condition according to the previous literature reporting on the formation of these powerful carcinogens under similar synthesis condition [25].

The employment of the *in situ* nitration in the synthesis results nonetheless in pronounced disorder in the structures of the synthesized complexes. In the cases of **1** and **6** in which there are two NO_2-BDC^{2-} in the asymmetric unit, the nitro group on one of the NO_2-BDC^{2-} ligands in both structures shows disorder over two sites with approximately equal occupancies of 50%. Similar site disorder is also observed in the structures of **3** and **5** which are isostructural to **2** and **4**. The disorder in structures **2** and **4** is however more complicated and similar to those observed in [Ln (NO_2-BDC) $(L)_{0.5}(H_2O)]\cdot 3H_2O$ (Ln = Pr, Nd, Sm and Gd, and L = BDC^{2-} or BDC^{2-}/NO_2-BDC^{2-}) [23]. In addition to site disorder at the nitro group of one of the NO_2-BDC^{2-} ligands, there are two types of crystallographic disorder, including site and substitutional disorder, at the nitro group of the other ligand. This suggests the co-existence of both BDC^{2-} and NO_2-BDC^{2-} of which the nitro group on the NO_2-BDC^{2-} shows additional site disorder over two crystallographic sites with equal site occupancy. The BDC^{2-}-to-NO_2-BDC^{2-} ratios in both structures are intriguingly similar of approximately 0.7: 0.3. Given the synthetic conditions the variable degree of nitration is not unexpected.

Despite the addition of DABCO in the reaction, the absence of DABCO in the title structures should be noted. The attempts to synthesize the title complexes without the addition of DABCO were however unsuccessful, suggesting the crucial role of this organic base in the synthesis. Acid-base reaction between H_2BDC and DABCO can be assumed [26]. The deprotonation of the carboxyl groups of H_2BDC by such acid-base reaction should generate free carboxylate groups on the organic ligands to coordinate lanthanide metal ions.

3.2. Crystal structures of 1–6

$[La_2(NO_2\text{-}BDC)_3(H_2O)_4]$ (1). Complex **1** crystallizes in the triclinic space group $P\bar{1}$ with two unique lanthanum ions in the asymmetric unit (Fig. 1a). The two distinct lanthanum ions are similarly eight-fold coordinated by eight oxygen atoms from the carboxylates of six NO_2-BDC^{2-} and two coordinated water molecules, and form a distorted square-face bicapped trigonal prismatic unit, *TPRS*-{LaO_8}, alike. All of the NO_2-BDC^{2-} function as the tetradentate linkers using the μ_4-η^1:η^1:η^1:η^1 coordination mode, leading to the formation of the three-dimensional [La_2(NO_2-$BDC)_3(H_2O)_4$] framework. The framework of **1** is a dense framework without any void according to calculations using PLATON [27], and can be viewed as being composed of two-dimensional puckered layers spreading in the *ac* plane which are further pillared by the organic ligands in the direction of *b* (Fig. 1b). The framework can be simplified to the uninodal 6-connected **pcu** α-Po net with $\{4^{12}.6^3\}$ point symbol using the *TPRS*-{LaO_8} units as nodes and the NO_2-BDC^{2-} as linker (Fig. 1c). The framework of **1** is governed mainly by very strong O–H···O hydrogen bonding interactions involving every coordinated water molecules and the nitro groups of NO_2-BDC^{2-} (Table 2). The hydrogen bonding interactions are in good agreement with the apparent disorder in the structure of **1** and additionally result in an arrangement of the organic ligand that prohibits any π-π interaction.

$[Ln(L)_{0.5}(NO_2\text{-}BDC)\ (H_2O)]\cdot 3H_2O$ {Ln = Eu (2), Tb (3), Dy (4) and Ho (5); L = BDC^{2-} or BDC^{2-}/NO_2-BDC^{2-}}. Complexes **2–5** are isostructural and crystallize in the same orthorhombic space group *Pbca* (Table 1). The unit cell parameters of **2–5** are in good agreement with those of [Ln (NO_2-BDC) $(L)_{0.5}(H_2O)]\cdot 3H_2O$ (Ln = Pr, Nd, Sm and Gd; L = BDC^{2-} or BDC^{2-}/NO_2-BDC^{2-}) [23], with a descending tendency across the series attributed to the lanthanide

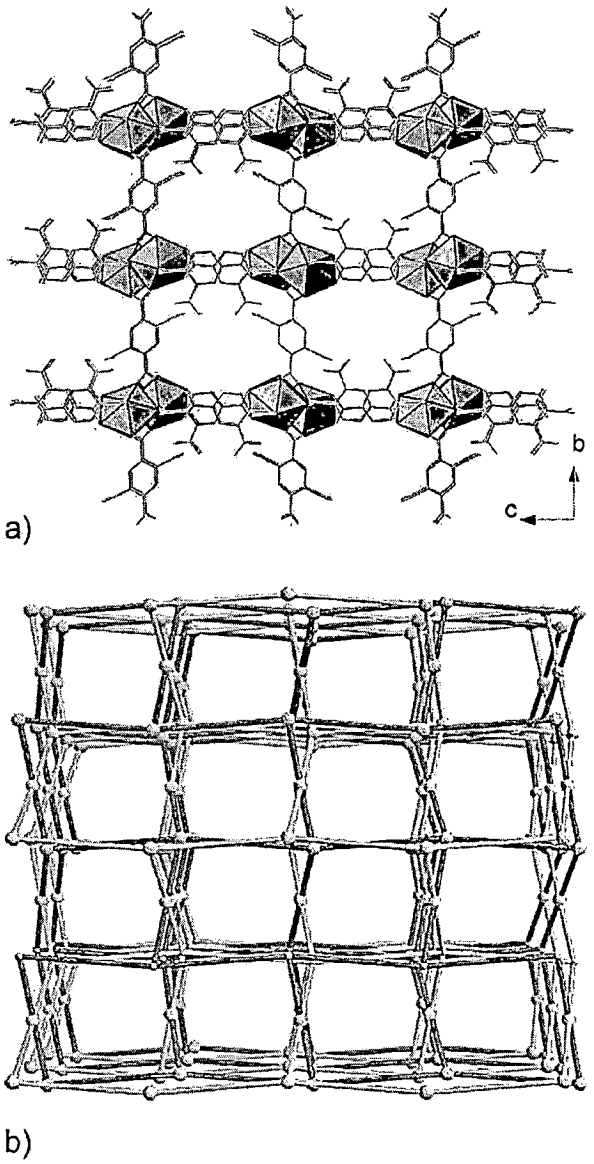

Fig. 3. Illustrations showing (a) the three-dimensional framework and (b) the simplified **NbO** topology of **2** (as a representative of **2–5**).

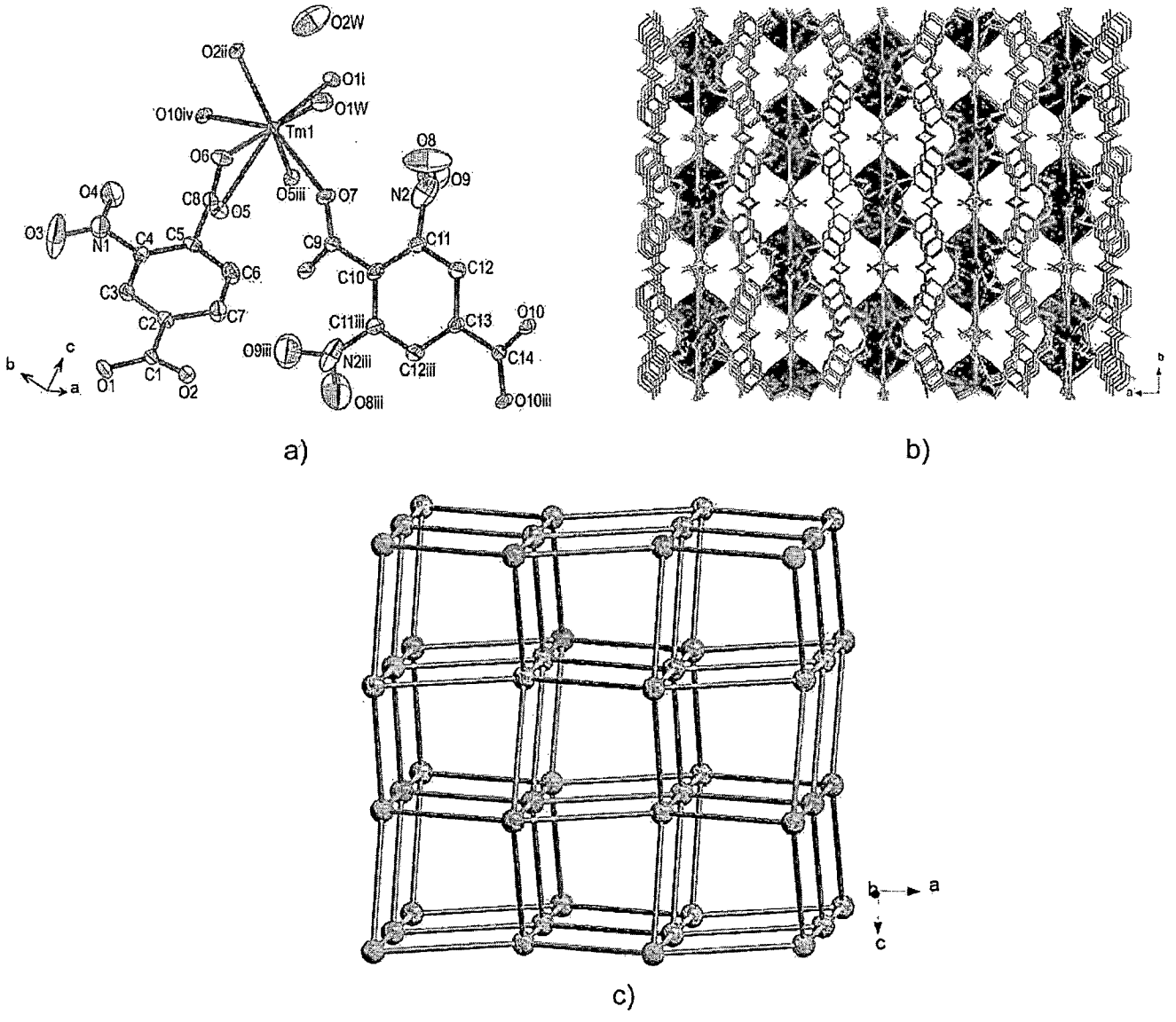

Fig. 4. Views of (a) an extended asymmetric unit drawn as 50% thermal ellipsoids, (b) a dense three-dimensional framework, and (c) the simplified **pcu** α-Po topology of **6**. Symmetry operations: (i) 0.5 + *x*, 1.5-*y*, 0.5 + *z* (ii) 1.5-*x*, 0.5 + *y*, 1.5-*z* (iii) 2-*x*, *y*, 1.5-*z* (iv) *x*, 1 + *y*, *z*.

contraction. The asymmetric units of **2–5** are similar comprising only one unique lanthanide metal ion which exhibits the same nine-fold coordination of the square-face capped square antiprismatic geometry, *SAPRS*-{LaO_9}, as exemplified in Fig. 2. Two modes of coordination including the μ_4-η^1:η^1:η^2:η^2 and μ_4-η^1:η^1:η^1:η^1 are adopted by the ligands upon the coordination leading to the formation of the one-dimensional {Ln (μ_3-OCO)$_4$ (μ_2-OCO)$_2$ (η^1,η^1-OCO) (OH_2)} chains extending along the direction of *a* (Fig. 3a). These chains are further linked by the ligands to form a three-dimensional framework which can be simplified to the four-connected uninodal **NbO** net (Fig. 3b).

The framework includes the one-dimensional rectangular channel extending in the same direction as the {Eu (μ_3-OCO)$_4$ (μ_2-OCO)$_2$ (η^1,η^1-OCO) (OH_2)} chains, housing the unbound water molecules. In the same fashion to [Ln (NO_2-BDC) $(L)_{0.5}(H_2O)$]·$3H_2O$ [23], these unbound water molecules are organized as the edge-shared pentagons by strong hydrogen bonding interactions (Table 2). Besides the hydrogen bonding interactions, there are π-π interactions between the adjacent organic ligands. The distances and angles between the centroids of the two aromatic rings, range from 4.022 Å and 78.7° in **2** (Eu) to 3.951 Å and 78.0° in **5** (Ho). The effective sizes of the channel openings of **2–5** are similar (4 × 8 $Å^2$) which is also similar to those of [Ln (NO_2-BDC) $(L)_{0.5}(H_2O)$]·$3H_2O$ [23]. If the unbound water molecules are excluded, the solvent accessible void volumes of 895.7 $Å^3$ (**2**; 25.87%), 848.7 $Å^3$ (**3**; 24.88%), 825.4 $Å^3$ (**4**; 24.40%), 809.0 $Å^3$ (**5**; 24.10%) could be calculated. The slight decrease of these values across the lanthanide series are in good agreement with the lanthanide contraction.

[Tm(NO$_2$-BDC)$_{1.5}$(H$_2$O)]·H$_2$O (6). Complex **6** crystallizes in the monoclinic *C*2/*c* space group comprising only one unique thulium ion which is eight-fold coordinated in a distorted square-face bicapped trigonal prismatic geometry, *TPRS*-{TmO$_8$} (Fig. 4a). Every two *TPRS*-{TmO$_8$} motifs are linked by four carboxyl bridges, *i.e.* 2 × μ_2-η^1:η^1 (O10–C14–O10 and O7–C9–O7) and 2 × μ_2-η^2:η^1 (O5–C8–O6), to form an edge-shared {Tm$_2$O$_{12}$} dimer (Fig. 4b). These dimers are then connected by the NO$_2$-BDC^{2-} ligands through μ_4-η^1:η^1:η^1:η^1 and μ_4-η^2:η^1:η^1:η^1 modes of coordination establishing the three-dimensional framework. There are rectangular channels extending along the direction of *b* of the framework housing the water of crystallization. The crystallizing water molecule is in close proximity to both the coordinating water and the carboxylate oxygen atoms rendering a strong O–H···O hydrogen bonding interactions (Table 2). The framework structure of **6** is further stabilized by the other extensive weak interactions, including the weak C–H···O hydrogen bonding and the aromatic π-π parallel-displaced interactions. The distance and angle between the centroids of the two aromatic rings of two adjacent NO$_2$-BDC^{2-} are 3.929 Å and 82.5°, respectively. The framework of **6** notably contains negligible solvent accessible void. If the edge-shared {Tm$_2$O$_{12}$} dimer is regarded as node with the organic ligand as a linker, the framework of **6** can be intriguingly simplified to the same uninodal **pcu** α-Po net as that of **1** (Fig. 4c), although degrees of puckering of the two nets are different. According to the literature, the structure of **6** is isostructural to those of the recently reported [Ln$_2$(NO$_2$-BDC)$_3$(H$_2$O)$_2$]·2(H$_2$O) (Ln = Sm, Eu, Gd, Tb, Er) which were synthesized directly using the NO$_2$-H$_2$BDC ligand under hydrothermal and slow evaporation conditions [28].

Intriguingly, the eight-fold coordination as found for the unoccupied *f* orbital in lanthanum ion (**1**) and the smallest thulium ion (**6**) results in similar dense frameworks with negligible void and the same **pcu** α-Po topology. This is however not the case for [Ln$_2$(NO$_2$-BDC)$_3$(H$_2$O)$_2$]·2(H$_2$O) (Ln = Sm, Eu, Gd, Tb, Er), where the NO$_2$-H$_2$BDC was used as the sole linker during the synthesis [28]. This implies the influence of the NO$_2$-BDC^{2-} linker in regulating the construction of such a dense framework which may be due to the steric nitro group on the linker, and the crucial role of the BDC^{2-} linker in providing genuine microporosity to the derived frameworks.

3.3. Thermal stability and gas sorption behavior of 2

To investigate gas sorption behavior of the reported microporous complexes, thermal stability of **2** (as a representative of **2**–**5**) was investigated by thermogravimetric analysis. It is apparent that the complex remains stable up to over 400 °C (Fig. 5) despite the two successive losses of both the unbound and the coordinating water molecules (RT-180 °C; exp. 10.0%, calcd. 10.5%). Nonetheless, such losses resulted in the vanishing of the long-range order in the *c* direction revealed by the disappearance of the (0 0 *l*) reflections in

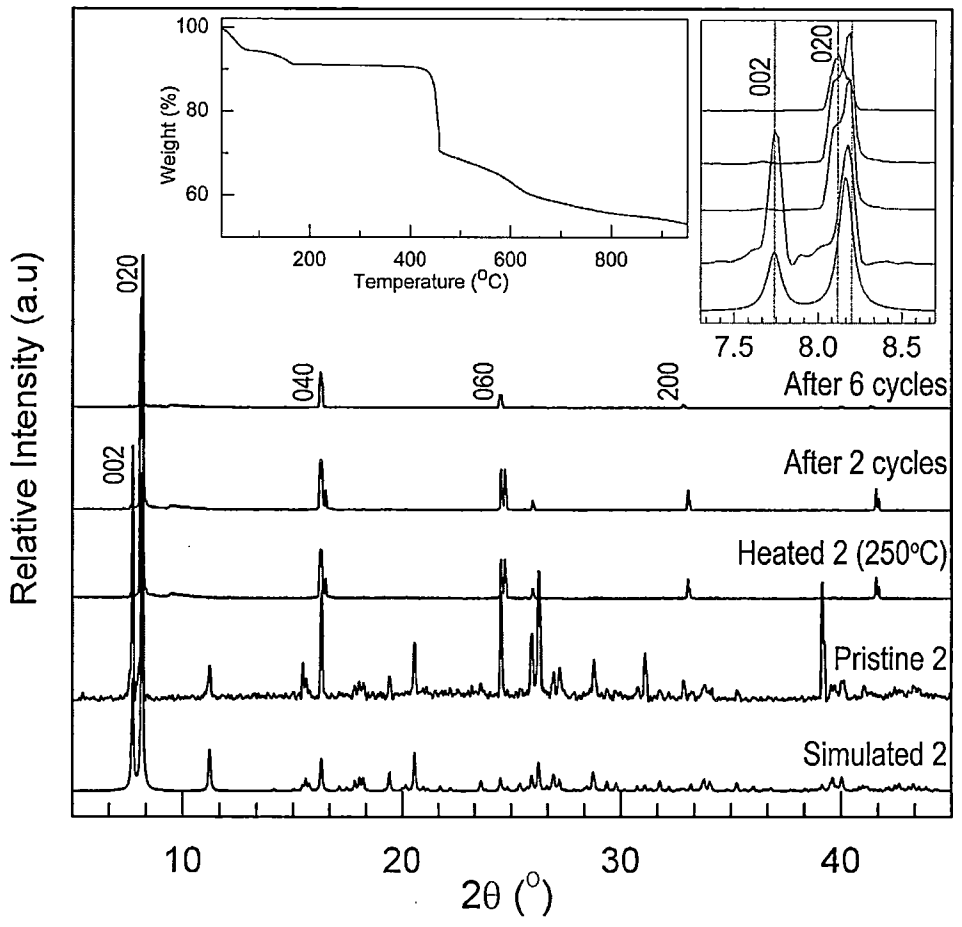

Fig. 5. The PXRD pattern of the pristine sample of **2** compared with the pattern simulated from single crystal data and those of the treated samples with the enlargement of the low 2θ area and the thermogravimetric curve in the insets.

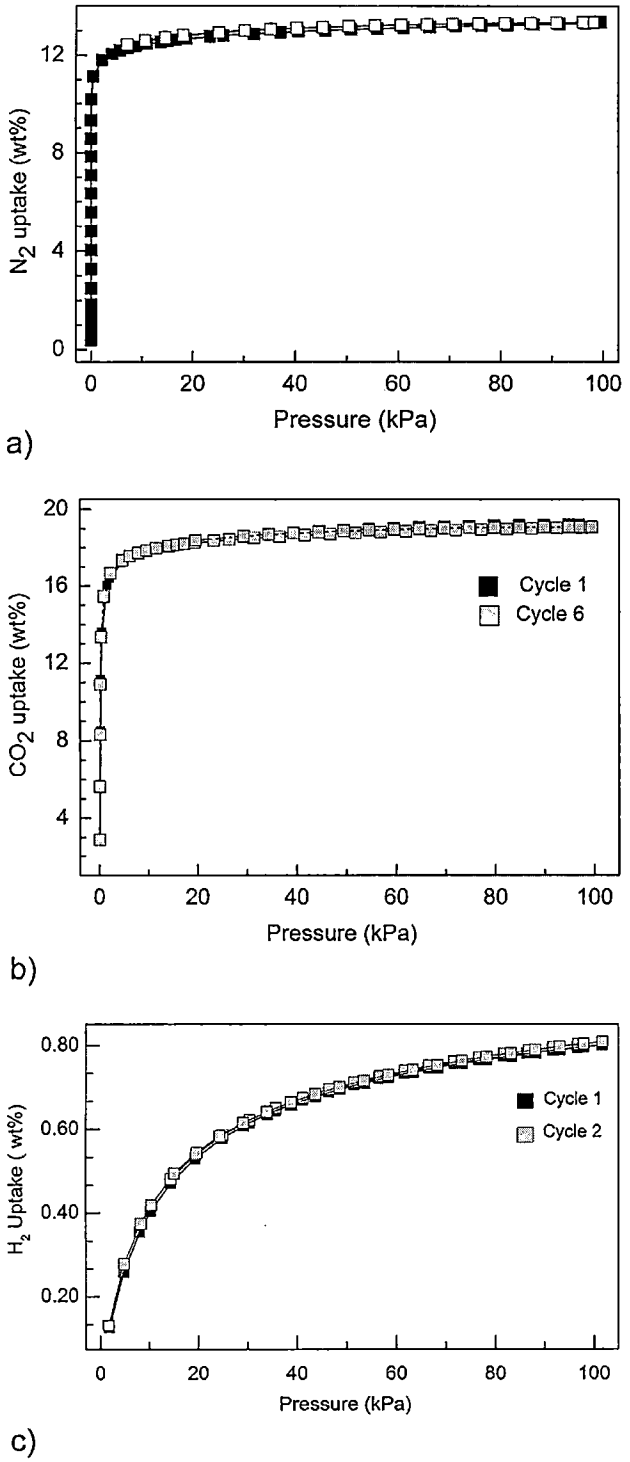

Fig. 6. Gas sorption/desorption isotherms of (a) nitrogen (b) carbon dioxide and (c) hydrogen gases.

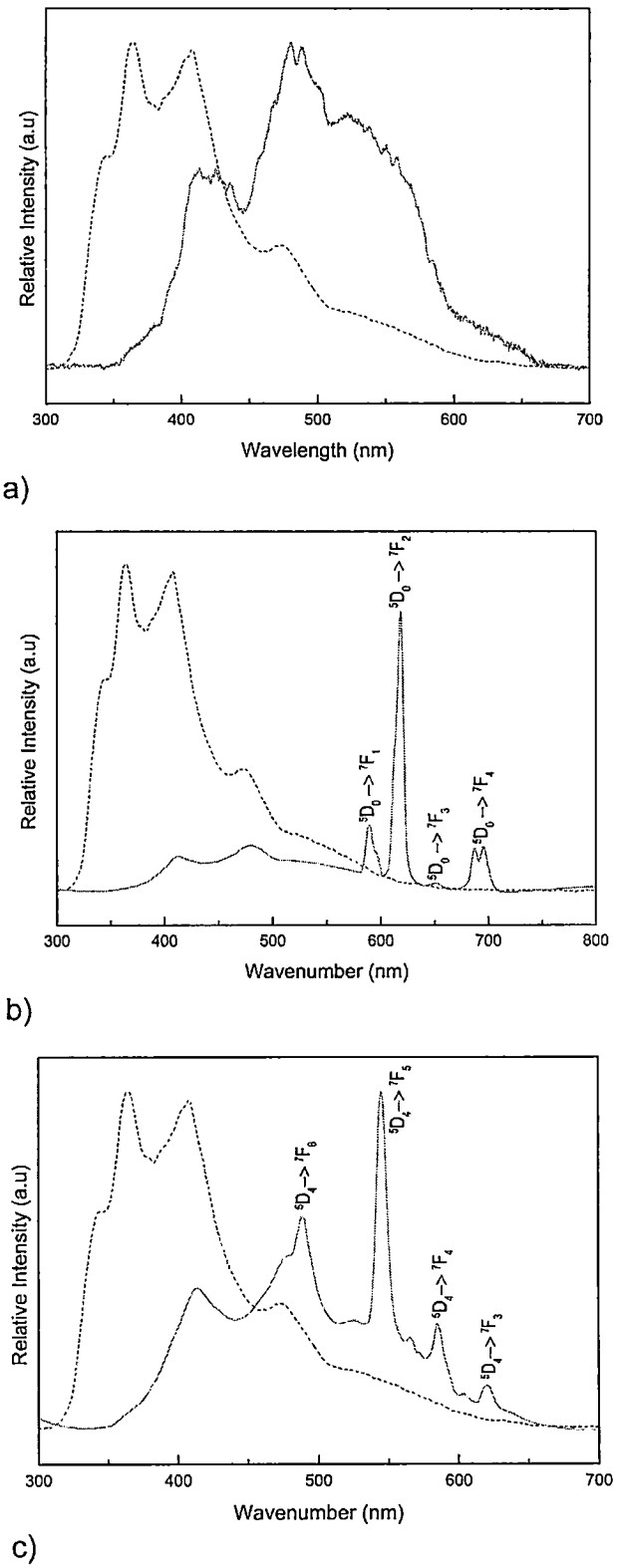

Fig. 7. Photoluminescence spectra (solid lines) of (a) **1** (as a representative of **1** and **4–6**) (b) **2**, and (c) **3**, compared with those of the H_2BDC (dotted lines).

the PXRD pattern. The importance of the hydrogen bonded water molecules which are organized in the framework void in regulating the framework is therefore illustrated. The persistence of the *h*00 and 0*k*0 reflections with appreciable intensities, on the other hand, suggests the retention of the framework crystallinity in the other two directions. A slight shift of the (0 2 0) diffraction peak to lower 2θ for the heat-treated samples implies the modest alteration of the framework structure after the losses of the water molecules.

Stability of the framework and the retention of the framework microporosity after the removal of the water molecules were confirmed by the classical type I sorption isotherm of the nitrogen gas collected at 77 *K* (Fig. 6a). The surface area of 543 $m^2 \cdot g^{-1}$ could be calculated based on the BET model with an average pore size of 1.2 nm.

The sample exhibited similar adsorption behavior for carbon dioxide gas (Fig. 6b). The sudden uptake of the gas signifies the interactions of the gas molecule with the unoccupied coordination sites on the europium ions generated by the removal of the coordinated water. The maximum gravimetric capacity of approximately 19 wt%, which is equivalent to 95 $cm^3 \cdot g^{-1}$ or 4.2 $mmol \cdot g^{-1}$, was achieved at extremely low pressure of less than 10 kPa or 0.1 bar. This value is much higher than those reported for zeolitic materials [3], and comparable to some recently reported MOFs under similar measuring temperatures and pressures such as $[(Ni_2L^2)\ (bptc)] \cdot 6H_2O \cdot 3DEF$, $[(Ni_2L^4)\ (bptc)] \cdot 14H_2O$ ($bptc^{4-}$ = 1,1′-biphenyl-3,3′,5,5′-tetracarboxylate, DEF = *N,N*-diethylformamide) [29], and $[Co_{2.5}\ (btc)\ (Hbtc)_{0.5}\ (atz)\ (CH_3CN)\ (H_2O)] \cdot H_2O$ (H_3btc = 1,3,5-benzenetricarboxylic acid, atz = 3-amino-1,2,4-triazole) [30]. In addition to the interactions to the exposed europium ions, the interactions between the polar nitro groups on the NO_2-BDC^{2-} linker and the carbon dioxide molecule [30–32] should also contribute to the significant uptake capacity in **2**. Intriguingly, this capacity was retained even after six cycles of sorption/desorption experiments with the intact framework crystallinity revealed by both the powder (Fig. 5) and single crystal X-ray diffraction experiments. A single crystal that had been used for six cycles of gas sorption was exposed to air for a period of a few weeks and then examined by single crystal X-ray diffraction. This demonstrated that the same network present in the pristine sample is retained. The structure refinement of this crystal (data to 56.5° 2θ for Mo radiation) converged with R = 4.53% and $wR(F^2)$ = 7.13%. The stability of the framework and therefore recyclability of the material is one of the most desired properties for the storage applications [33].

Rather than an abrupt increase in gravimetric adsorption like that observed for the nitrogen and carbon dioxide gases, the uptake of the hydrogen gas by **2** gradually occurred over a range of pressures before reaching approximately 0.80 wt% at 1 bar, which is equivalent to 79 $cm^3 \cdot g^{-1}$ or 4 $mmol \cdot g^{-1}$ (Fig. 6c). This gravimetric sorption capacity is comparable to those reported for the best zeolite ZSM-5 [34] and the series of Co-INA, CO-FINA and IRMOF [35]. The rather small gravimetric capacities observed for **2** attributes partially to relatively heavy framework compared to the light weight of the hydrogen gas. The gradual increase in the sorption with increasing pressure at low temperatures is notably characteristic of the physisorption process in the microporous solids [36], which is reported to be potential for the pressure swing adsorption processes [37]. Regarding the structure of **2**, the sorption of the hydrogen gas should occur through the interactions with the electron rich phenyl rings of both the BDC^{2-} and NO_2-BDC^{2-} linkers [38].

3.4. Photoluminescence properties of 1–6

The NO_2-BDC^{2-} ligand has been reported previously as a poor sensitizer in $[Ln\ (NO_2\text{-}BDC)\ (L)_{0.5}(H_2O)] \cdot 3H_2O$ [23] and the closely relevant $[Ln_2(NTA)_3(OH_2)_2](H_2O)_2$ (Ln = Sm, Eu, Gd, Tb, Er and H_2NTA = 2-nitroterephthalic acid) [28], which is also true for the complexes reported here. Upon the excitation at 255 nm, similar broad bands covering almost the entire region of the visible light derived from the intra-ligand charge transfer (ILCT) transitions is present, as exemplified in Fig. 7. Characteristic emissions of the europium (**2**; $^5D_0 \rightarrow {}^7F_J$, J = 1, 2, 3, 4) and terbium (**3**; $^5D_4 \rightarrow {}^7F_J$, J = 3, 4, 5, 6) can, nonetheless, be observed. These emission bands are significantly less intense relative to other europium and terbium complexes which agree with the poor sensitizing role of the NO_2-BDC^{2-} ligand. The relatively high intensity of the $^5D_0 \rightarrow {}^7F_2$ band in the spectrum of complex **2** can be attributed to the absence of the inversion center at the europium ion crystallographic site [28].

4. Conclusions

By employing the H_2BDC ligand and the *in situ* nitration reaction, six new lanthanide metal organic complexes have been synthesized; $[La_2(NO_2\text{-}BDC)_3(H_2O)_4]$ (**1**) $[Ln(L)_{0.5}(NO_2\text{-}BDC)\ (H_2O)] \cdot 3H_2O$ (Ln = Eu (**2**), Tb (**3**), Dy (**4**) and Ho (**5**); L = BDC^{2-} or BDC^{2-}/NO_2-BDC^{2-}) and $[Tm(NO_2\text{-}BDC)_{1.5}(H_2O)] \cdot H_2O$ (**6**). Complexes **1** and **6** are can be simplified to the same topology of **pcu** α-Po net despite the different framework structures, and the isostructural frameworks of **2–5** can be simplified to the **NbO** net. Whilst the frameworks of **1** and **6** contained negligible void, those of **2–5** are microporous in nature with similar void opening of 4 × 8 $Å^2$ and solvent accessible void volumes varying in a range of 809.0–895.7 $Å^3$. Complex **2** (as a representative of **2–5**) exhibits exceptional stability upon the loss of all the water in the structure and also the heat treatment. After the loss of the water, the BET surface area of 543 $m^2 \cdot g^{-1}$ and an average pore size of 1.2 nm can be calculated for **2**, which shows significant adsorption capacities for both carbon dioxide (95 $cm^3 \cdot g^{-1}$ or 4.2 $mmol \cdot g^{-1}$) and hydrogen gases (79 $cm^3 \cdot g^{-1}$ or 4 $mmol \cdot g^{-1}$). The framework shows high stability even after six cycles of sorption/desorption experiments. The poor sensitizing ability of the NO_2-BDC^{2-} ligand has been illustrated.

Acknowledgements

The work is co-funded by the Thailand Research Fund (RSA5980026) and Chiang Mai University. K. Panyarat thanks to the Science Achievement Scholarship of Thailand for the Ph.D. scholarships.

Appendix A. Supplementary data

Supplementary data related to this article can be found at http://dx.doi.org/10.1016/j.micromeso.2017.06.003.

References

[1] H. Yang, Z. Xu, M. Fan, R. Gupta, R.B. Slimane, A.E. Bland, I. Wright, J. Environ. Sci. 20 (2008) 14–27.
[2] J.D. Figueroa, T. Fout, S. Plasynski, H. McIlvried, R.D. Srivastava, Inter. J. Greenh. Gas. Control 2 (2008) 9–20.
[3] R. Sabouni, H. Kazemian, S. Rohani, Environ. Sci. Pollut. Res. 21 (2014) 5427–5449.
[4] K. Sumida, D.L. Rogow, J.A. Mason, T.M. McDonald, E.D. Bloch, Z.R. Herm, T.-H. Bae, J.R. Long, Chem. Rev. 112 (2012) 724–781.
[5] M.T. Ho, G.W. Allinson, D.E. Wiley, Ind. Eng. Chem. Res. 47 (14) (2008) 4883–4890.
[6] M. Eddaoudi, D.B. Moler, H. Li, B. Chen, T.M. Reineke, M. O'Keeffe, O.M. Yaghi, Acc. Chem. Res. 34 (4) (2001) 319–330.
[7] R.J. Kuppler, D.J. Timmons, Q.-R. Fang, J.-R. Li, T.A. Makal, M.D. Young, D. Yuan, D. Zhao, W. Zhuang, H.-C. Zhou, Coord. Chem. Rev. 253 (2009) 3042–3066.
[8] M.J. Rosseinsky, Micropor. Mesopor. Mater 73 (2004) 15–30.
[9] H. Li, M. Eddaoudi, T.L. Groy, O.M. Yaghi, J. Am. Chem. Soc. 120 (33) (1998) 8571–8572.
[10] J. Liu, P.K. Thallapally, B.P. McGrail, D.R. Brown, J. Liu, Chem. Soc. Rev. 41 (2012) 2308–2322.
[11] D. Andirova, C.F. Cogswell, Y. Lei, S. Choi, Micropor. Mesopor. Mater 219 (2016) 276–305.
[12] T.M. Reineke, M. Eddaoudi, M. Fehr, D. Kelley, O.M. Yaghi, J. Am. Chem. Soc. 121 (8) (1999) 1651–1657.
[13] T.M. Reineke, M. Eddaoudi, M. O'Keeffe, O.M. Yaghi, Angew. Chem. Int. Ed. 38 (17) (1999) 2590–2593.

[14] Z.-J. Lin, Z. Yang, T.-F. Liu, Y.-B. Huang, R. Cao, Inorg. Chem. 51 (2012) 1813–1820.
[15] M. Eddaoudi, H. Li, T. Reineke, M. Fehr, D. Kelley, T.L. Groy, O.M. Yaghi, Top. Catal. 9 (1999) 105–111.
[16] D.K. Maity, A. Halder, B. Bhattacharya, A. Das, D. Ghoshal, Cryst. Growth Des. 16 (2016) 1162–1167.
[17] Bruker, SAINT, Bruker AXS Inc., Madison, Wisconsin, USA, 2007.
[18] L. Krause, R. Herbst-Irmer, G.M. Sheldrick, D. Stalke, J. Appl. Crystallogr. 48 (2015) 3–10.
[19] J. de Meulenaer, H. Tompa, Acta Crystallogr. 19 (1965) 1014.
[20] G.M. Sheldrick, Acta Crystallogr. A64 112 (2008) 112–122.
[21] L.J. Farrugia, J. Appl. Crystallogr. 32 (1999) 837–838.
[22] O.V. Dolomanov, L.J. Bourhis, R.J. Gildea, J.A.K. Howard, H. Puschmann, J. Appl. Crystallogr. 42 (2009) 339–341.
[23] K. Panyarat, T.J. Prior, A. Rujiwatra, Polyhedron 81 (2014) 74–80.
[24] H.-P. Xiao, L.-G. Zhu, Inorg. Chem. Commun. 9 (2006) 1125–1128.
[25] N.J. Tapp, D.M. Bibby, N.M. Milestone, Zeolites 8 (1988) 157–159.
[26] Z.-S. Yao, K. Yamamoto, H.-L. Cai, K. Takahashi, O. Sato, J. Am. Chem. Soc. 138 (37) (2016) 12005–12008.
[27] A.L. Spek, PLATON, Version 191114, vol. 8, Utrecht University, Padualaan, CH Utrecht, The Netherlands, 1980-2014, p. 3584.
[28] J.A. Smith, M.A.S. Wilmot, K.P. Carter, C.L. Cahill, A.J. Loughe, C.S. Knee, New J. Chem. 40 (2016) 7338–7349.
[29] H.-S. Choi, M.P. Suh, Angew. Chem. Int. Ed. 48 (2009) 6865–6869.
[30] B. Liu, R. Zhao, K. Yue, J. Shi, Y. Yu, Y. Wang, Dalton Trans. 42 (2013) 13990–13996.
[31] Z. Zhang, Z.-Z. Yao, S. Xiang, B. Chen, Energy Environ. Sci. 7 (2014) 2868–2899.
[32] M.T. Kapelewski, S.J. Geier, M.R. Hudson, D. Stück, J.A. Mason, J.N. Nelson, D.J. Xiao, Z. Hulvey, E. Gilmour, S.A. FitzGerald, M.H. Gordon, C.M. Brown, J.R. Long, J. Am. Chem. Soc. 136 (2014) 12119–12129.
[33] H. Furukawa, K.E. Cordova, M. O'Keeffe, O.M. Yaghi, Science 341 (2013) 1230444.
[34] A. Phan, C. Doonan, F.J.U. Romo, C.B. Knobler, M. O'Keeffe, O.M. Yaghi, Acc. Chem. Res. 43 (9) (2010) 58–67.
[35] P. Pachfule, Y. Chen, J. Jiang, R. Banerjee, Chem. Eur. J. 18 (2012) 688–694.
[36] M. Thommes, K. Kaneko, A.V. Neimark, J.P. Olivier, F.R. Reinoso, J. Rouquerol, K.S.W. Sing, Pure Appl. Chem. 87 (2015) 1051–1069.
[37] B. Silva, I. Solomon, A.M. Ribeiro, U.H. Lee, Y.K. Hwang, J.-S. Chang, J.M. Loureiro, A.E. Rodrigues, Sep. Purif. Technol. 118 (2013) 744–756.
[38] D.J. Collins, H.-C. Zhou, J. Mater. Chem. 17 (2007) 3154–3160.

Colorimetric Analysis: A New Strategy to Improve Ratiometric Temperature Sensing Performance of Lanthanide Benzenedicarboxylates

Kitt Panyarat,[a] Athipong Ngamjarurojana,[b] Apinpus Rujiwatra[a,c,*]

[a] Department of Chemistry, Faculty of Science, Chiang Mai University, Chiang Mai, 50200 Thailand

[b] Department of Physics and Materials Science, Chiang Mai University, Chiang Mai, 50200 Thailand

[c] Center of Excellence in Materials Science and Materials Technology, Faculty of Science, Chiang Mai University, Chiang Mai, 50200 Thailand

*To whom the correspondence should be addressed.

Department of Chemistry, Faculty of Science,

Chiang Mai University,

Chiang Mai,

50200 Thailand

E-mail: apinpus.rujiwatra@cmu.ac.th

apinpus.rujiwatra@gmail.com

Colorimetric Analysis: A New Strategy to Improve Ratiometric Temperature Sensing Performance of Lanthanide Benzenedicarboxylates

Kitt Panyarat,[a] Athipong Ngamjarurojana,[b] Apinpus Rujiwatra[a,c,*]

[a] Department of Chemistry, Faculty of Science, Chiang Mai University, Chiang Mai, 50200 Thailand

[b] Department of Physics and Materials Science, Chiang Mai University, Chiang Mai, 50200 Thailand

[c] Center of Excellence in Materials Science and Materials Technology, Faculty of Science, Chiang Mai University, Chiang Mai, 50200 Thailand

Abstract

A series of monometallic $[Ln_2(BDC)_3(DMF)_2(H_2O)_2]_n$ (Ln = Eu^{III}, Gd^{III}, Tb^{III}; H_2BDC = benzene-1,4-dicarboxylic acid; DMF = dimethylformamide) and the lanthanide luminophores-loaded $[Ln_xGd_{2-x}(BDC)_3(DMF)_2(H_2O)_2]_n$ (Ln = Eu^{III} and Tb^{III}) were synthesized and used in photoluminescent study. The dependence of emitting colors of $[Ln_xGd_{2-x}(BDC)_3(DMF)_2(H_2O)_2]_n$ on the luminophore contents is reported and discussed based on the sensitization efficiency of BDC^{2-} antenna. On the basis of an explicit change in the emitting colors of $[Eu_xGd_{2-x}(BDC)_3(DMF)_2(H_2O)_2]_n$, colorimetric analysis has been introduced as a new and effective strategy to establish ratiometric-thermometric parameters. Within the sRGB and CIE XYZ color matching systems, the temperature-dependent ratiometric-thermometric parameters could be derived from both $x/(x+y)$ and $R/(R+G)$ over 303-348 K covering physiological temperatures. Temperature resolution in term of standard deviation of the measurements, repeatability and relative sensitivity of the successive measurements have been evaluated and are reported.

Keywords Lanthanide, Coordination polymer, Thermometry, Colorimetry, Ratiometry

1. Introduction

Through self-assembly and modularity characters of lanthanide coordination polymers (LnCPs), their framework architecture and function can be reasonably tailored despite difficulty raised by the coordination chemistry of the lanthanides (Ln). In concert with the unique photoluminescent properties, LnCPs have introduced new opportunities to a wide range of applications, *e.g.* gas storage and separation [1,2], sensing [3,4], and biomedicine [5]. Amidst the emerging opportunities, application in a non-invasive temperature sensing has gained zealous attention due to the unique characteristics only LnCPs can offer, *e.g.* rapid response, viability in grueling conditions, and excellent temperature and spatial resolution. The implementation of ratiometry or self-reference has in addition encouraged the research in this field. Since the first introduction of [$Eu_{0.0069}Tb_{0.9931}$-DMBDC] (DMBDC = 2,5-dimethoxy-1,4-benzenedicarboxylate) as a potential photoluminescent temperature sensor [6], numerous candidates have been reported [7-10].

Thermometric parameter (Δ) which is fundamental in temperature sensing can be derived from any temperature dependent responses. Regarding the LnCPs, the ratiometric Δ has been thus far calculated solely from intensity ratio of two luminophores which are mostly Eu^{III} and Tb^{III} co-existing in the same framework structure [10,11]. The enhancement of sensing performance has been concentrated entirely on the tailored modification of structural building modules, particularly the antenna and therefore the triplet state energy. Recently, a multifunction fit has been proposed as an alternative strategy for data analysis, leading to a substantial improvement in accuracy of the detection [12].

Colorimetry, which is a technique based on the dependence of the sensing probe's color on the target analyte, has been widely employed in both biosensing and chemical sensing based primarily on spectroscopic data [13-15]. Since every spectral data contains colorimetric information which can be described using various color matching systems, *e.g.* sRGB which is

the common working space in digital photography and CIE XYZ which has been established by the International Commission on Illumination as a standard to scientifically define light colors [16-18]. Based on the CIE XYZ values, the colorimetric parameters x and y can be derived and used in defining light colors irrespective of its luminance [16]. Since they are directly related to spectral data, both parameters can, in principle, be the basis for the derivation of the ratiometric Δ parameter.

Here, the temperature dependent photoluminescent behavior in term of colorimetry of Eu^{III}- and Tb^{III}-loaded Gd^{III} complexes, *i.e.* $[Eu_xGd_{2-x}(BDC)_3(DMF)_2(H_2O)_2]_n$ (**IV-VII**) and $[Tb_xGd_{2-x}(BDC)_3(DMF)_2(H_2O)_2]_n$ (**VIII-XI**), were investigated in relative to the corresponding monometallic $[Ln_2(BDC)_3(DMF)_2(H_2O)_2]_n$ where Ln = Gd^{III} (**I**), Eu^{III} (**II**), Tb^{III} (**III**). Colorimetric analysis was attempted with $[Eu_xGd_{2-x}(BDC)_3(DMF)_2(H_2O)_2]_n$, providing explicit change in emitting colors despite the poor quality spectrum. With reference to two color matching systems, *i.e.* CIE XYZ and sRGB, the temperature sensing performance was evaluated.

2. Experimental

2.1 Materials and Methods

All chemicals were obtained commercially and used as-received; Gd_2O_3 (Sigma-Aldrich, 99.9%), Tb_4O_7 (Sigma Aldrich, 99.9%), Eu_2O_3 (Merck, 99%), benzene-1,4-dicarboxylic acid (H_2BDC; BDH, 65%), HNO_3 (Carlo Erba, 65%), *N*,*N*-dimethylformamide (DMF; Fisher Chemical, 99.98%). The $Ln(NO_3)_3{\cdot}xH_2O$ were prepared by dissolving the corresponding lanthanide oxide in aqueous solution of HNO_3 (7.6 $mol{\cdot}L^{-1}$), from which the $Ln(NO_3)_3{\cdot}xH_2O$ was crystallized. Powder X-ray diffraction (PXRD) patterns were recorded using a Rigaku Mini Flex II X-ray diffractometer (Cu K_α, 40 kV, 15 mA).

Temperature dependent photoluminescent spectra were collected using an ASEQ LR-1T broad range spectrophotometer equipped with a LTB MNL-100 pulsed nitrogen laser excitation source (λ = 337 nm, angle of incidence = 20°). The measurements were conducted on single crystals which were placed on a glass sample holder. The stray light was filtered out using a UV optical band-pass (<400 nm). The temperature controlling compartment was set up using a Dual Digital F/C PID temperature controller furnace Kiln oven, type K thermocouple and a boxcar data acquisition system (ASEQ spectra program version 9.5) provided with ASEQ LR-1T spectrophotometer. The temperature dependent experiments were performed for the 303-393 *K* range, and a DC-3006 cryogenic tank was installed to stabilize the programmed temperatures.

2.2 Hydrothermal Synthesis of I-XI

To synthesize colorless crystals of **I**, $Gd(NO_3)_3{\cdot}5H_2O$ (180 mg, 0.413 mmol) and H_2BDC (144 mg, 0.867 mmol) was first dissolved in a mixed solvent prepared from 3.00 mL each of deionized water and DMF. The solution was then sealed in a 10 mL glass bottle and kept at 80 °C for 6 h. After cooling down to room temperature, crystals of **I** were collected by filtration. The same procedure was adopted for the synthesis of **II** and **III**, but replacing $Gd(NO_3)_3{\cdot}5H_2O$ with $Eu(NO_3)_3{\cdot}6H_2O$ (**II**: 35.0 mg, 0.0785 mmol) and $Tb(NO_3)_3{\cdot}6H_2O$ (**III**; 22.6 mg, 0.0499 mmol).

The Eu^{III}-loaded Gd^{III} complexes were prepared by first dissolving $Gd(NO_3)_3{\cdot}5H_2O$ (180 mg, 0.413 mmol) in 1 mL of an aqueous $Eu(NO_3)_3{\cdot}6H_2O$ solution contained in a 15 mL glass bottle. The 1 mL aliquot of $Eu(NO_3)_3{\cdot}6H_2O$ solution was prepared by diluting the concentrated $Eu(NO_3)_3{\cdot}6H_2O$ solution (0.0785 $mmol{\cdot}mL^{-1}$) to varied concentrations ($\mu mol{\cdot}mL^{-1}$): **IV** 0.785, **V** 1.57, **VI** 3.14, **VII** 6.28. A 9 mL of H_2BDC (144 mg, 0.867 mmol) in DMF was then added into each aliquot of the prepared lanthanide solution, which was then

tightly closed and kept at 80 °C for 6 h. The Tb^{III}-loaded Gd^{III} complexes were prepared under similar synthesis conditions as **IV-VII** but diluting $Tb(NO_3)_3 \cdot 6H_2O$ solution (0.0499 mmol·mL^{-1}) to varied concentrations (μmol·mL^{-1}): **VIII** 0.499, **IX** 1.00, **X** 2.00, **XI** 3.99, instead of $Eu(NO_3)_3 \cdot 6H_2O$ solution.

3. Results and Discussion

According to the PXRD data (Fig. 1), the monometallic **I-III** and the Eu^{III}- and Tb^{III}-loaded **IV-XI** are isostructural with $[Ln_2(BDC)_3(DMF)_2(H_2O)_2]_n$ (Ln = Gd^{III}, Tb^{III}) [16]. Due to the trace amounts of Eu^{III} and Tb^{III} in **IV-VII** and **VIII-XI** prohibiting the precise contents to be determined by available techniques, their existence was conclusive from the characteristic emissions of Eu^{III} and Tb^{III} in the corresponding photoluminescent spectra. Photoluminescent studies of these complexes using the samples yielded from different batches of the synthesis confirmedly provided repeatable results.

3.1 Temperature Dependent Emitting Colors of I-XI

According to references [20-22], the triplet state energy of BDC^{2-} is in an appropriate range to sensitize the intraconfigurational *f-f* emissions of both Eu^{III} and Tb^{III}, which are otherwise forbidden. With reference to the emission spectrum of **I** (Gd^{III}), where the sensitization is nonviable (Fig. 2), the triplet state energy of BDC^{2-} could be estimated, *i.e.* 23 809 cm^{-1} (420 nm). With the excitation at 337 nm, the sensitization of **II** (Eu^{III}) and **III** (Tb^{III}) was exceptionally effective manifesting through the intense red Eu^{III}:$^5D_0 \rightarrow {}^7F_J$ (J=1-4) and green Tb^{III}:$^5D_4 \rightarrow {}^7F_J$ (J=6-3) emission (Fig. 2). A broad and intense feature attributing to the ligand-centered $\pi^* \rightarrow \pi$ emission as found in spectrum of **I** was absent confirming the effective energy transfer from BDC^{2-} to both Eu^{III} and Tb^{III}. The heating of **II** and **III** from 303 *K* to 393 *K* apparently did not cause any significant change in their emitting colors although the falling

of Eu^{III}:$^5D_0 \rightarrow {}^7F_J$ (J=1-4) and Tb^{III}:$^5D_4 \rightarrow {}^7F_J$ (J=6-3) emission intensities were apparent. Peak splitting was particularly observed for the Tb^{III}:$^5D_4 \rightarrow {}^7F_J$ (J=6-3) emissions at 393 K which should be due to the thermally quenching of the $^5D_4$ [23].

Regarding the emitting color of the Eu^{III}-loaded Gd^{III} complexes at room temperature (Fig. 3), shades of the red color apparently depended on the Eu^{III} content. The increased Eu^{III} contents (from **IV** to **VII**) evidently instigated significant change in the emission colors of the complexes, traversing from white (**IV**: 0.303, 0.351) to red (**VII**: 0.660, 0.330) which is close to the color of the monometallic **II** (0.680, 0.300). This is consistent with their emitting spectra in which almost all Eu^{III}:$^5D_0 \rightarrow {}^7F_J$ emissions were pronounced in the spectra of **VI** and **VII**, whereas only the Eu^{III}:$^5D_0 \rightarrow {}^7F_J$ (J =1, 2) could be observed for **IV** and **V**.

On the other hand, the increased Tb^{III} contents (from **VIII** to **XI**) did not induced any practical change in the emitting colors of **VIII-XI**, all of which were yellowish green corresponding to the CIE coordinates ranging from (0.307, 0.508) for **VIII** to (0.310, 0.529) for **XI**. To the naked eye, the apparent color of **VIII-XI** was almost identical to the color of **III** (0.334,0.586). The insignificant alteration in green color of **VIII-XI** may ascribe to the exceptionally effective sensitization of Tb^{III} by BDC^{2-}, which is more effective than the Eu^{III} case, leading to a dominating green color even with trace amounts of Tb^{III} in the complexes. This feature is well consistent with an energy gap between the triplet state energy of BDC^{2-} and the accepting level of Tb^{III} ($^5D_4$) which is more appropriate than that of the Eu^{III} ($^5D_0$).

3.2 Colorimetric-Ratiometric Temperature Dependence of IV

Owing to the white emitting color at room temperature of **IV**, it was chosen for further colorimetric analysis. The thermally-induced color change in **IV** was distinctly visible despite the poor Eu^{III}:$^5D_0 \rightarrow {}^7F_J$ emissions (Fig. 4). Upon the heating from 303 to 393 K, the emitting color of **IV** gradually changed from white (0.315, 0.359) at 303 K to reddish pink (0.446, 0.291)

at 393 *K*. The change was noticeably reversible upon successive heating and cooling cycles. The thermally-induced non-radiative decay apparently imparted drastic effect on the ligand-centered $\pi^*\rightarrow\pi$ emission revealed *via* the substantial deterioration of the corresponding emission band. Although similar influence was explicit for the Eu^{III}:$^5D_0\rightarrow{}^7F_J$ emissions, the reduction in intensities was relatively insignificant.

Within the CIE XYZ color matching systems, the colorimetric coordinates (*x*,*y*) of temperature dependent emitting colors of **IV** were noticeably aligned with a uniform tendency and a regular gap between each coordinate. From the plots of the temperature dependent *x* and *y* (Fig. 5), a diversion in temperature dependencies of the two parameters was vivid and a linear correlation could intriguingly be established: $R^2(x)$ =0.994, $R^2(y)$ = 0.976. With reference to these *x* and *y* parameters, linear correlation of *x*/*y* and *x*/(*x*+*y*) ratios with temperatures were examined from which a better correlation was yielded for the *x*/(*x*+*y*) ratio. The temperature dependent *x*/(*x*+*y*) ratio was therefore adopted for the calculation of the ratiometric Δ. Disparity in temperature readouts from the expected values despite the high precision at temperatures ≥ 363 *K* was however observed, which should attribute to the deviation of *y* parameter from linearity. The working temperature range was therefore truncated to 303-348 *K*, from which an excellent linear correlation (R^2 = 0.997) could be achieved. Over ten successive measurements at three temperatures, the measurements provided satisfying repeatability (*R*) and temperature resolution (δT) in term of standard deviation (SD) of the readouts although there were few data points departed from the expected values. Based on these data the relative sensitivities (*Sr*) of the measurements were calculated showing the descending tendency with the increasing temperature providing the maximum (*Sm*) and the minimum values of 0.579 %·K^{-1} (303 *K*) and 0.494 %·K^{-1} (348 *K*), respectively.

Since the emitting colors of **IV** are within the human eye perception [16], the CIE coordinates *x* and *y* were converted to the R and G parameters of the sRGB color matching

system using nix™ Color Sensor software package. Exceptional linear correlation ($R^2 = 0.999$) was achieved for the temperature dependent ratiometric Δ over the same temperature range if the R/(R+G) ratio was employed (Fig. 6). On the basis of R and G parameters, the temperature measuring performance of **IV** was also evaluated, revealing improved SD (δT) and R for the ten successive measurements compared with the CIE XYZ case. In a similar fashion to the measurements based on the $x/(x+y)$ ratio, the Sr of the measurements based on the R/(R+G) ratio also declined with the rising of temperature. Considerable enhancement of the maximum and the minimum relative sensitivity, *i.e.* 1.12 %·K^{-1} (303 K) and 0.839 %·K^{-1} (348 K), were however revealed. Irrespective of the color matching systems, colorimetric analysis was therefore viable as a new strategy in founding the ratiometric Δ parameters from which a high performance ratiometric temperature sensing was achieved.

4. Conclusions

In view of ratiometric temperature sensing, colorimetric analysis was introduced as a new and effective strategy for the establishment of reliable ratiometric Δ parameter with reference to **IV** exhibiting temperature dependent emitting colors. Irrespective of the employed color matching systems, *i.e.* sRGB and CIE XYZ, exceptional performance specified by a linear correlation of the ratiometric Δ calculated from either $x/(x+y)$ or R/(R+G) could be derived over the 303-348 K range, from which exceptional δT, R and maximum Sr could be achieved. As the reported working temperature range covers biological temperatures, a new opportunity in the development of high performance sensor for physiological temperature measurements is revealed for LnCPs.

Acknowledgements

This work was co-funded by the Thailand Research Fund (RSA5980026) and Chiang Mai University.

References

[1] B. Li, H.-M. Wen, W. Zhou, B. Chen, Porous metal-organic frameworks for gas storage and separation: What, How and Why?, J. Phys. Chem. Lett. 5(20) (2014) 3468-3479.

[2] H. Li, K. Wang, Y. Sun, C.T. Lollar, J. Li, H.-C. Zhou, Recent advances in gas storage and separation using metal-organic frameworks, Mater. Today 21(2) (2018) 108-121.

[3] P. Kumar, A. Deep. K.-H. Kim, Metal organic frameworks for sensing applications, TrAC 73 (2015) 39-53.

[4] B. Yan, Lanthanide-functionalized metal-organic framework hybrid systems to create multiple luminescent centers for chemical sensing, Acc. Chem. Res. 50(11) (2017) 2789-2798.

[5] G. Chedid, A. Yassin, Recent trends in covalent and metal organic frameworks for biomedical applications, Nanomaterials 8(11) (2018) 916.

[6] Y. Cui, H. Xu, Y. Yue, Z. Guo, J. Yu, Z. Chen, J. Gao, Y. Yang, G. Qian, B. Chen, A luminescent mixed-lanthanide metal–organic framework thermometer, J. Am. Chem. Soc. 134 (2012) 3979-3982.

[7] Y. Cui, J. Zhang, H. He, G. Qian, Photonic functional metal-organic frameworks, Chem. Soc. Rev. 47 (2018) 5740-5785.

[8] Y. Cui, F. Zhu, B. Chen, G. Qian, Metal organic frameworks for luminescent thermometry, Chem. Commun. 51 (2015) 7420.

[9] W.P. Lustig, S. Mukherjee, N.D. Rudd, A.V. Desai, J. Li, S.K. Ghosh, Metal-organic frameworks: Functional luminescent and photonic materials for sensing applications, Chem. Soc. Rev. 46 (2017) 3242-3285.

[10] J. Rocha, C.D.S. Brites, L.D. Carlos, Lanthanide organic framework luminescent thermometers, Chem. Eur. J. 22 (2016) 14782-14759.

[11] L. Armelaoa, S. Quici, F. Barigelletti, G. Accorsi, G. Bottaro, M. Cavazzini, E. Tondelloe, Design of luminescent lanthanide complexes: From molecules to highly efficient photo-emitting materials, Coord. Chem. Rev. 254 (2010) 487-505.

[12] L. Li, F. Qin, Y. Zhou, Y. Zheng, H. Zhao, Z. Zhang, Boosting the temperature detection accuracy of luminescent ratiometric thermometry *via* a multifunction fit strategy, J. Phys. Chem. C. 122 (2018) 24246-24525.

[13] O.V. Monogarovaa, K.V. Oskoloka, V.V. Apyaria, Colorimetry in chemical analysis, J. Anal. Chem. 73(11) (2018) 1076-1084.

[14] V.S.A. Piriya, P. Joseph, S.C.G.K. Daniel, S. Lakshmanan, T. Kinoshita, S. Muthusamy, Colorimetric sensors for rapid detection of various analytes, Mater. Sci. Eng. C 78 (2017) 1231-1245.

[15] B. Kaur, N. Kaur, S. Kumar, Colorimetric metal ion sensors - A comprehensive review of the years 2011-2016, Coord. Chem. Rev. 358 (2018) 13-69.

[16] T. Smith, J. Guild, The C.I.E. colorimetric standards and their use, Transactions of the Optical Society. 33(3) (1931) 73-134.

[17] F.-C. Liang, C.-C. Kuo, B.-Y. Chen, C.-J. Cho, C.-C. Hung, W.-C. Chen, R. Borsali, RGB-switchable porous electrospun nanofiber chemoprobe-filter prepared from multifunctional copolymers for versatile sensing of pH and heavy metals, ACS Appl. Mater. Interfaces. 9(19) (2017) 16381-16396.

[18] S.A. L. Johnsen, J. Bollmann, H.W. Lee, Y. Zhou, Accurate representation of interference colors (Michel-Levy chart): From rendering to image color correction, J. Microsc-oxford, 269(3) (2018) 321-337.

[19] H.-J. Zhang, R.-Q. Fan, P. Wang, X.-M. Wang, W. Chen, X.-B. Zheng, K. Li, Y.-L. Yang, Crystal structures and effect of temperature on the luminescence of two lanthanide coordination polymers with twofold interpenetrating pcu topology, J. Inorg. Organomet. Polym. 24(3) (2014) 624-632.

[20] R. Decadt, K.V. Hecke, D. Depla, K. Leus, D. Weinberger, I.V. Driessche, P.V. Der Voort, R.V.N. Deun, Synthesis, crystal structures, and luminescence properties of carboxylate based rare-earth coordination polymers, Inorg. Chem. 51(21) (2012) 11623-11634.

[21] A.Y. Grishko, V.V. Utochnikova, A.A. Averin, A.V. Mironov, N.P. Kuzmina, Unusual luminescence properties of heterometallic REE terephthalates, Eur. J. Inorg. Chem. 10 (2015) 1660-1664.

[22] X.-P. Yang, R.A. Jones, J.H. Rivers, R.P.-J. Laia, Syntheses, structures and luminescent properties of new lanthanide-based coordination polymers based on benzene-1,4-dicarboxylate, Dalton Trans. 35 (2007) 3936-3942.

[23] T. Yamashita, Y. Ohishi, Concentration and temperature effects on the spectroscopic properties of Tb^{3+} doped borosilicate glasses, J. Appl. Phys. 102 (2007) 123107.

LIST OF FIGURES

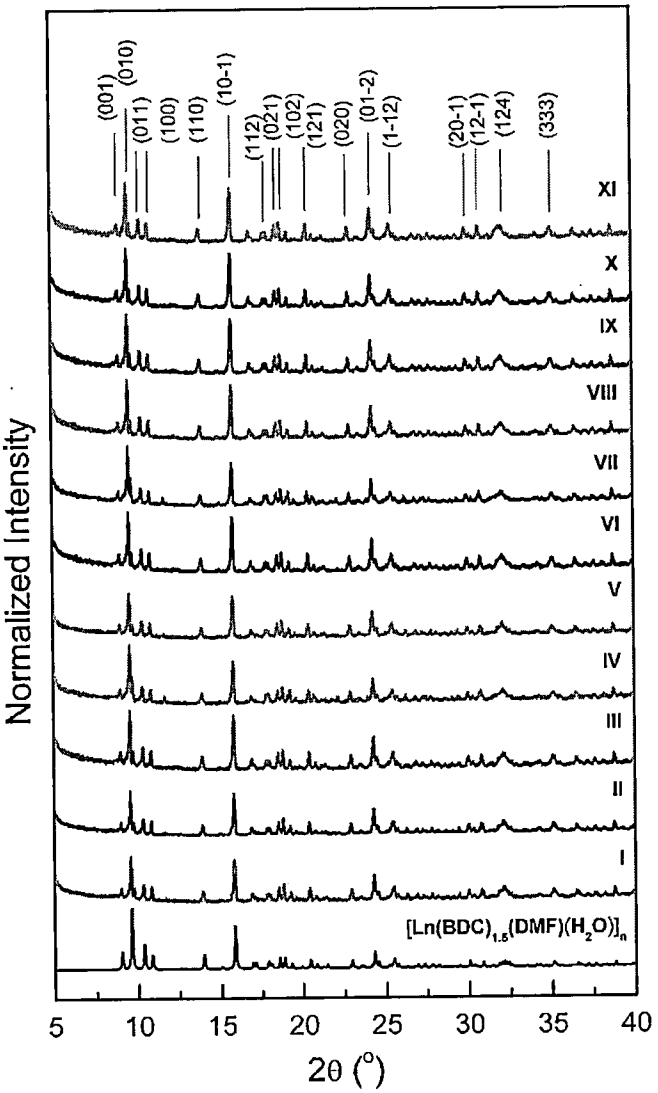

Fig. 1 PXRD patterns of **I-XI** compared with the simulated pattern of $[Gd^{III}_2(BDC)_3(DMF)_2(H_2O)_2]_n$ (CCDC NO. 949513)

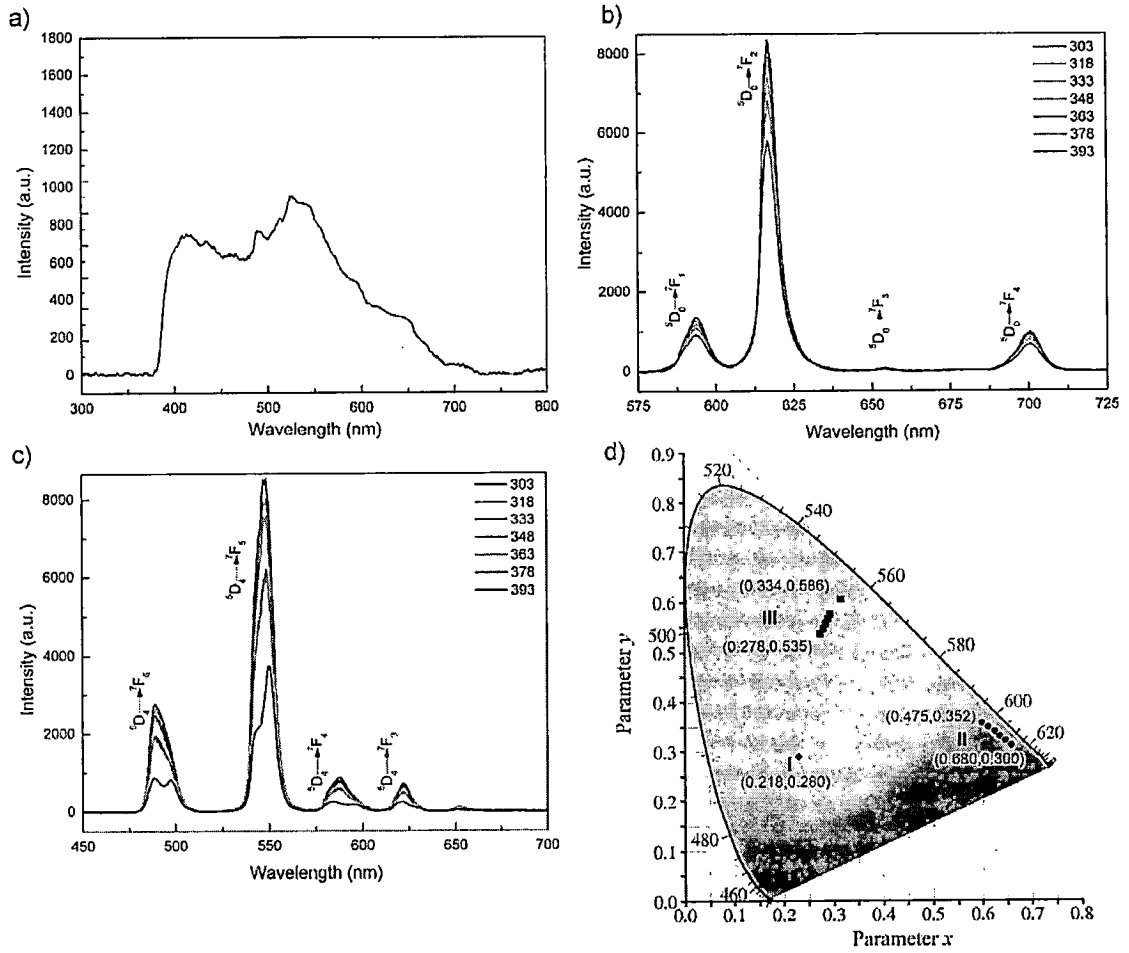

Fig. 2 Emission spectra of (a) **I** collected at room temperature, and (b) **II** and (c) **III** collected at different temperatures with (d) the corresponding coordinates in CIE colorimetric diagram (◆ = **I**, ● = **II**, ■ = **III**)

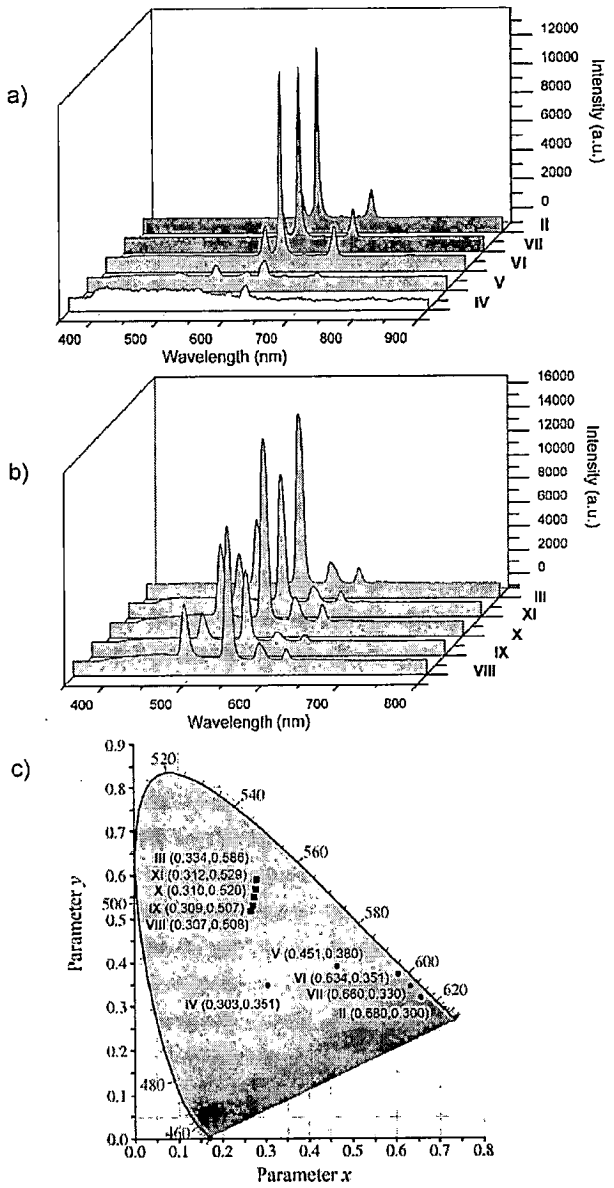

Fig. 3 Emission spectra of (a) **II, IV-VII**, and (b) **III, VIII-XI** collected at room temperature with (c) the corresponding coordinates in the CIE colorimetric diagram (● = **II, IV-VII**, ■ = **III, VIII-XI**)

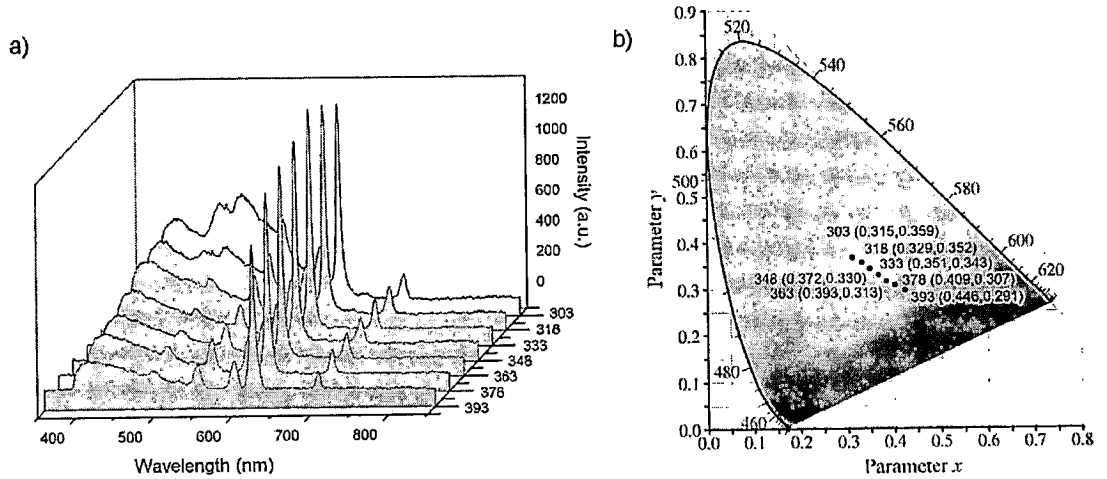

Fig. 4 (a) Emission spectra of **IV** collected at different temperatures with (b) the corresponding coordinates (x,y) in CIE colorimetric diagram

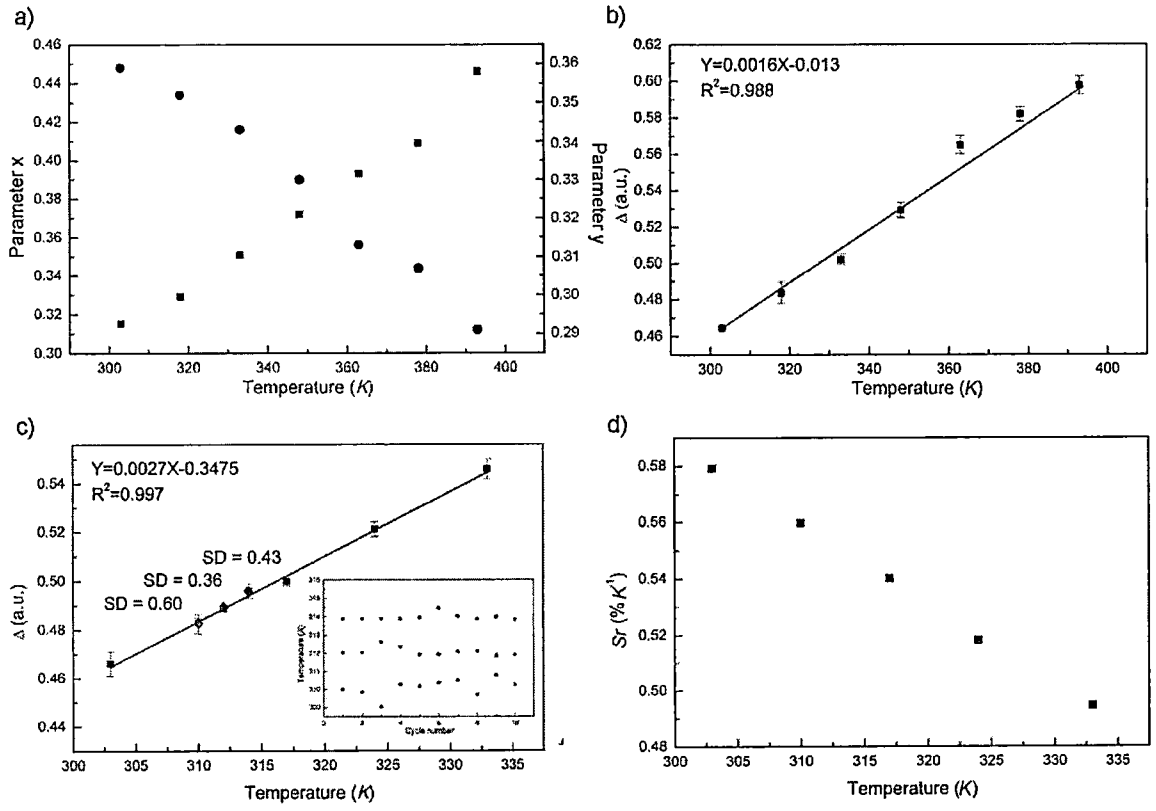

Fig. 5 (a) Diverse temperature dependencies of x (●) and y (■) of **IV**, with the corresponding Δ calculated from $x/(x+y)$ over (b) 302-393 K and (c) 303-348 K, the average temperature readouts of ten successive readings (inset; R > 99%), and (d) the corresponding Sr

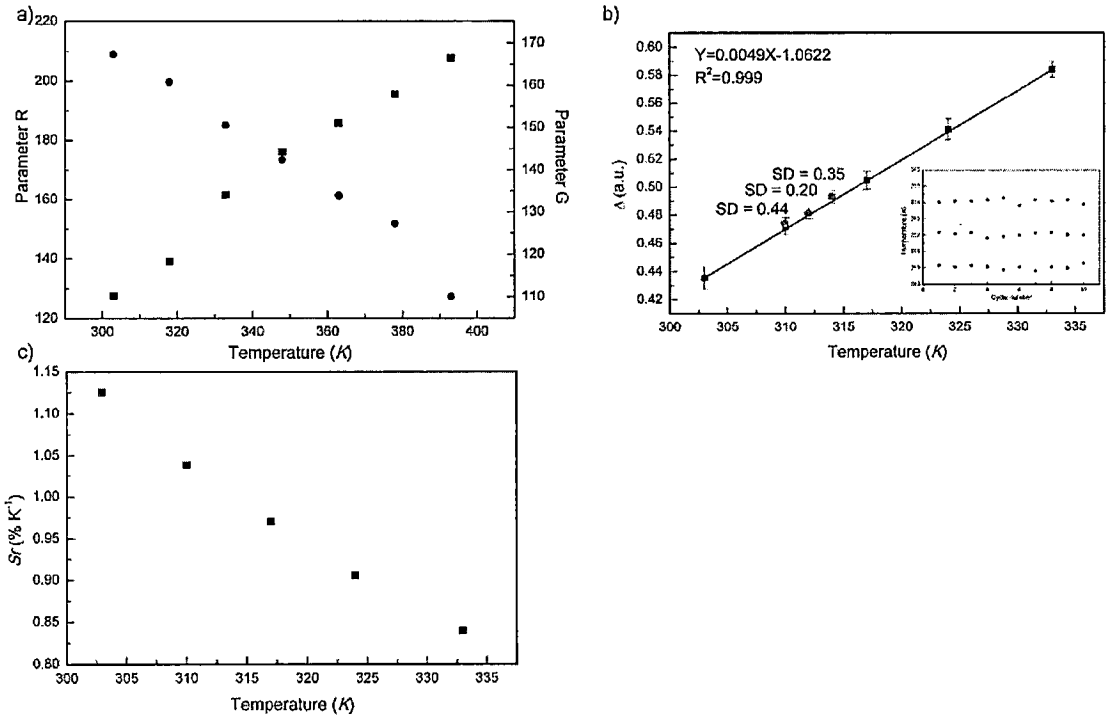

Fig. 6 (a) Diverse temperature dependencies of R (●) and G (■) of **IV**, with (b) the corresponding Δ calculated from R/(R+G) over 303-348 *K* and the average temperature readouts of ten successive readings (inset; $R > 99\%$), and (c) the corresponding *Sr*

CRYSTAL GROWTH & DESIGN

Article

pubs.acs.org/crystal

Structural Variation and Preference in Lanthanide-pyridine-2,6-dicarboxylate Coordination Polymers

Thammanoon Chuasaard,[†] Kitt Panyarat,[†] Pattaraphol Rodlamul,[†] Kittipong Chainok,[‡] Saranphong Yimklan,[†] and Apinpus Rujiwatra*[,†]

[†]Department of Chemistry, Faculty of Science, Chiang Mai University, Chiang Mai 50200, Thailand

[‡]Department of Physics, Faculty of Science and Technology, Thammasat University, Pathum Thani 12120, Thailand

Supporting Information

ABSTRACT: Ten lanthanide coordination polymers were designed and synthesized using pyridine-2,6-dicarboxylic acid (H_2pdc) and two different heating techniques (conventional and microwave): $[Ln(pdc)(H_2O)_4]_3\cdot 3Cl$ {$Pa\bar{3}$; Ln = Pr (I), Nd (II), Sm (III), Eu (IV), and Gd (V)}, $[Ln(pdc)(Hpdc)(H_2O)_2]\cdot 3H_2O$ {$P2_1/c$; Ln = Pr (VI), Nd (VII), and Sm (VIII)} and $[Ln(pdc)(H_2O)_4]_3\cdot 3Cl$ {$Ia\bar{3}$; Ln = Sm (IX), and Eu (X)}. These complexes show variation in structures depending on the heating technique and the lanthanide ions. They can be classified into the cubic $Pa\bar{3}$ (I–V) and $Ia\bar{3}$ (IX, X), and the monoclinic $P2_1/c$ (VI–VIII) complexes. The cubic complexes exhibit supramolecular isomerism and a tubular three-dimensional structure of interpenetrated lcs and pcu net topologies, while the monoclinic complexes are the supramolecular assemblies of the one-dimensional chains. As the cubic $Pa\bar{3}$ structures are favored by the use of the microwave, there is variation in structures as conventional heating was employed, although the cubic $Pa\bar{3}$ structures are still the most favored except for the VI case. The title complexes showed moderate thermal stabilities. The organic ligand is revealed to be a modest sensitizer to initiate the photoluminescence in the title complexes.

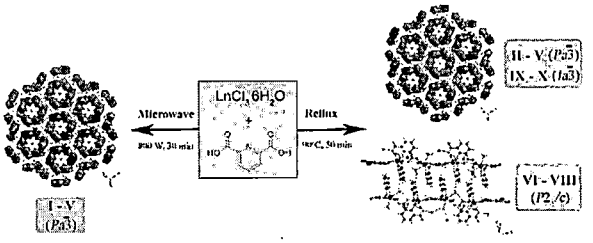

$[Ln(pdc)(H_2O)_4]_3\cdot 3Cl$ Ln = Pr (I), Nd (II), Sm (III), Eu (IV), Gd (V)
$[Ln(pdc)(Hpdc)(H_2O)_2]\cdot 3H_2O$ Ln = Pr (VI), Nd (VII), Sm (VIII)
$[Ln(pdc)(H_2O)_4]_3\cdot 3Cl$ Ln = Sm (IX), Eu (X)

INTRODUCTION

In the last few decades, chemistry of coordination polymers (CPs), which are also known by the more popular name of metal organic frameworks (MOFs) has been investigated intensively and exponentially developed. In addition to the aesthetic beauty and vast diversity in their structures, potential applications such as in gas storage and sepatation, catalysis, magnetism, and sensing are the prime motivations.[1] In constrast to transition metals based CPs, the chemistry of lanthanide based CPs is far less developed despite the inherent properties the lanthanide metal ions can offer.[2] This may be partially due to the coordination chemistry of the lanthanide metal ions which are less predictable compared to the transition metal counterparts. The lanthanide metal ions existing mainly in their trivalent state can adopt variable coordination numbers and geometries. Their similar chemistry and the well acknowledged lanthanide contraction can provide structural diversity and therefore properties upon the subtle alteration in the synthesis.[2−5] In the view of crystal engineering, the design of lanthanide based CPs have therefore been and are still challenging.

Because of the hard acid nature of the trivalent lanthanide ions, different types of multicarboxylic acids including pyridine-2,6-dicarboxylic acid (H_2pdc) have been explored as organic linkers in the fabrication of novel lanthanide frameworks.[6−16] In solid state structures, the H_2pdc ligand may be present in the partially deprotonated ($Hpdc^-$) or the fully deprotonated (pdc^{2-}) forms. According to a survey on the lanthanide-H_2pdc CPs submitted to the Cambridge Structure Database,[17] the H_2pdc ligand almost always adopts, nonetheless, the fully deprotonated form, and 12 modes of coordination are found with few typical preferences (Scheme 1). The chelation of the ligand upon the coordination seems to be usual. The solid state structures of these lanthanide based CPs intriguingly exhibit proclivity to be either one- or three-dimensional depending on the subtle alteration in the synthesis and the structures. The template effect of the chloride anion in the formation of the three-dimensional $[Ln(pdc)(H_2O)_4]_3\cdot 3Cl$, for example, was investigated compared with the formation of the one-dimensional $[Ln(pdc)(Hpdc)(H_2O)_2]\cdot 3H_2O$.[15,18−21]

On the basis of this information, 10 new lanthanide based CPs have been designed and synthesized using the H_2pdc ligand. The influences of two heating techniques with different heating mechanism and kinetics, namely, conventional heating under reflux and dielectric microwave heating, on the final structures have been investigated. The synthesized structures

Received: September 21, 2016
Revised: December 29, 2016
Published: January 23, 2017

DOI: 10.1021/acs.cgd.6b01389
Cryst. Growth Des. 2017, 17, 1045−1054

Scheme 1. Diagrammatic Depiction of 12 Coordination Modes Adopted by the H_2pdc Ligand in Lanthanide Based CPs Deposited to the CSD[17a]

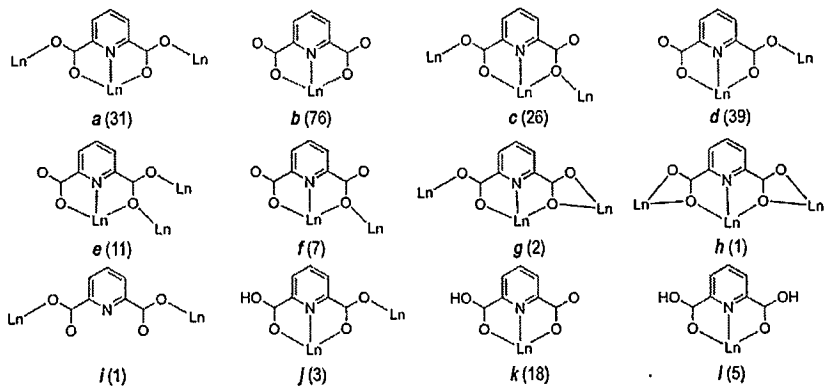

[a]Frequencies of occurring are shown in brackets.

Scheme 2. Diagrammatic Presentation Summarizing the Syntheses and the Yielded Complexes

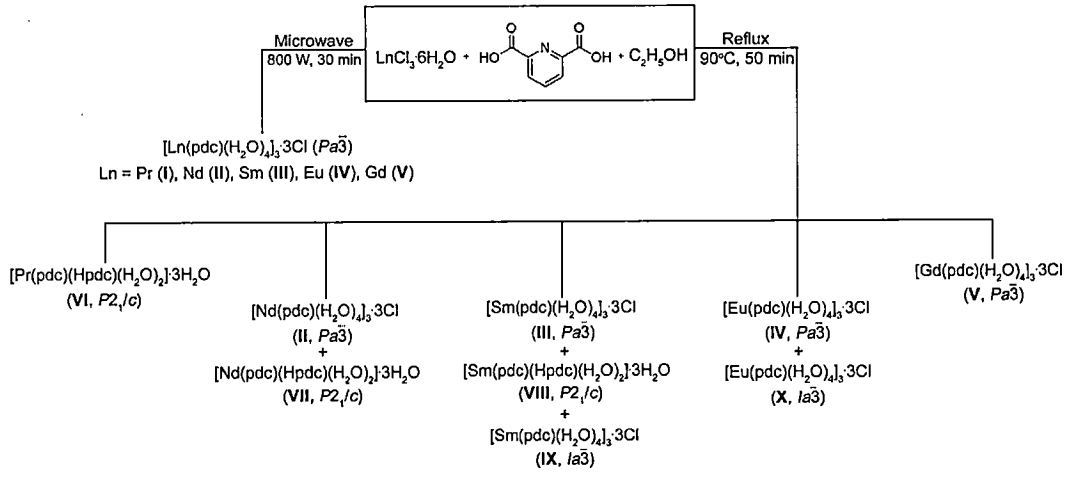

can be classified into three different groups according to their structural symmetries: (i) the cubic $Pa\bar{3}$ structures of $[Ln(pdc)(H_2O)_4]_3{\cdot}3Cl$ where Ln = Pr (I), Nd (II), Sm (III), Eu (IV), and Gd (V), (ii) the monoclinic $P2_1/c$ structures of $[Ln(pdc)(Hpdc)(H_2O)_2]{\cdot}3H_2O$ where Ln = Pr (VI), Nd (VII), and Sm (VIII), and (iii) the cubic $Ia\bar{3}$ structures of $[Ln(pdc)(H_2O)_4]_3{\cdot}3Cl$ where Ln = Sm (IX) and Eu (X). Structural differences and preferences are rationalized and discussed. Thermogravimetric and photoluminescence properties of selected complexes are included.

EXPERIMENTAL SECTION

Materials and Measurements. $PrCl_3{\cdot}6H_2O$, $NdCl_3{\cdot}6H_2O$, $SmCl_3{\cdot}6H_2O$, $EuCl_3{\cdot}6H_2O$, and $GdCl_3{\cdot}6H_2O$ were prepared by dissolving Pr_6O_{11} (99.9%, TJTM), Nd_2O_3 (99.99%, TJTM), Sm_2O_3 (99.5%, TJTM), Eu_2O_3 (99%, Merck), and Gd_2O_3 (99.9%, Sigma-Aldrich), accordingly, in HCl solution (37%, BDH). The solutions were heated to reach supersaturation and crystals of the lanthanide chlorides were crystallized. The amounts of the crystallizing water were determined using thermogravimetric analyses using a Metter Toledo TGA/DSC Simultaneous thermal analyzer. Pyridine-2,6-dicarboxylic acid (H_2pdc; >98%, Fluka) and ethanol (95%, Merck) were obtained commercially and used without further purification. Powder X-ray diffraction (PXRD) experiments were conducted using a Rigaku Mini Flex II X-ray diffractometer operated with Cu K_α radiation (λ = 1.5418 Å, 40 kV, 15 mA). Photoluminescence spectra were collected at room temperature using an Avantes Multichannel spectrometer with the Ocean Optics LED 255 nm excitation source.

Syntheses of I–X. Two synthesis techniques, i.e., the conventional heating under reflux and the dielectric microwave heating, were attempted in the syntheses (Scheme 2). The mixtures of the 1:1:128 for the $LnCl_3{\cdot}6H_2O/H_2$pdc/ethanol mole ratio were employed for every reaction.

Microwave Syntheses. $LnCl_3{\cdot}6H_2O$ (0.100 mmol) and H_2pdc (0.100 mmol) were dissolved in 10.00 mL of ethanol using a Teflon vessel. After the vessel was sealed and placed in the household microwave oven (Samsung MS23F301E), the reaction was conducted at 800 W for 30 min and left to cool down to room temperature. The crystals were obtained after the ethanol solvent evaporated in few days. It has been revealed by the PXRD and the single crystal X-ray diffraction that crystals of $[Ln(pdc)(H_2O)_4]_3{\cdot}3Cl$ {$Pa\bar{3}$; Ln = Pr (I), Nd (II), Sm (III), Eu (IV), and Gd (V)} were obtained. There are nonetheless few diffraction peaks in the collected PXRD patterns which could not be indexed suggesting the existence of other crystalline phases. The attempts to find crystals of other structures besides I–V were however not successful, and further characterization was therefore not performed.

Heating under Reflux. Rather than the use of microwave heating, the reaction mixtures were heated at 90 °C under reflux for 50 min and left to cool down to room temperature. Crystals of similar habits to those obtained from the microwave syntheses were obtained after the

DOI: 10.1021/acs.cgd.6b01389
Cryst. Growth Des. 2017, 17, 1045–1054

Table 1. Crystallographic Data and Refinement Details for I–X

	I	II	III	IV	V
CCDC no.	1448352	1448353	1448354	1494337	1494338
formula[a]	$C_{21}H_{33}N_3O_{24}Cl_3Pr_3$	$C_{21}H_{33}N_3O_{24}Cl_3Nd_3$	$C_{21}H_{33}N_3O_{24}Cl_3Sm_3$	$C_{21}H_{33}N_3O_{24}Cl_3Eu_3$	$C_{21}H_{33}N_3O_{24}Cl_3Gd_3$
formula weight[a]	1240.57	1250.57	1268.93	1273.74	1289.60
temperature (K)	296(2)	296(2)	296(2)	296(2)	296(2)
crystal system	cubic	cubic	cubic	cubic	cubic
space group	$Pa\bar{3}$ (No. 205)	$Pa\bar{3}$ (No. 205)	$Pa\bar{3}$ (No. 205)	$Pa\bar{3}$ (No. 205)	$Pa\bar{3}$ (No. 205)
a (Å)	19.9853(3)	19.9091(6)	19.8330(3)	19.8085(6)	19.7822(6)
V (Å)^3	7982.4(4)	7891.4(4)	7801.3(4)	7772.4(4)	7741.5(4)
Z	8	8	8	8	8
F(000)	4664	4688	4736	4760	4784
ρ (mg·m^{-3})	2.006	2.046	2.100	2.121	2.152
μ (mm^{-1})	3.824	4.112	4.682	5.008	5.307
data/restraints/parameters	4283/6/168	3268/0/168	3966/12/170	2997/0/168	2953/0/168
GOF	1.104	1.153	1.098	1.187	1.199
before SQUEEZE					
R_1 ($I = 2\sigma(I)$)[b]	0.0490	0.0470	0.0569	0.0598	0.0404
wR_2 (all data)[b]	0.1419	0.1433	0.1701	0.1542	0.1116
after SQUEEZE					
R_1 ($I = 2\sigma(I)$)[b]	0.0383	0.0293	0.0389	0.0555	0.0325
wR_2 (all data)[b]	0.0686	0.0627	0.0739	0.0703	0.0565

	VI	VII	VIII	IX	X
CCDC no.	1494339	1494340	1494342	1494341	1494343
formula[a]	$C_{14}H_{14}N_2O_{12}Pr$	$C_{14}H_{14}N_2O_{12}Nd$	$C_{14}H_{19}N_2O_{14}Sm$	$C_{21}H_{33}Cl_2N_3O_{24}Sm_3$	$C_{21}H_{33}Cl_2N_3O_{24}Eu_3$
formula weight[a]	543.18	546.51	589.66	1233.48	1238.28
temperature (K)	298(2)	298(2)	273(2)	298(2)	298(2)
crystal system	monoclinic	monoclinic	monoclinic	cubic	cubic
space group	$P2_1/c$ (No. 14)	$P2_1/c$ (No. 14)	$P2_1/c$ (No. 14)	$Ia\bar{3}$ (No. 206)	$Ia\bar{3}$ (No. 206)
a (Å)	14.785(3)	14.810(3)	13.9892(5)	19.8346(9)	19.8027(10)
b (Å)	10.9727(18)	11.064(2)	11.2046(3)		
c (Å)	12.936(2)	12.944(3)	12.8312(3)		
α (deg)	90.00	90.00(3)	90.00	90.00	90.00
β (deg)	100.256(6)	100.23(3)	102.314(2)	90.00	90.00
γ (deg)	90.00	90.00(3)	90.00	90.00	90.00
V (Å)^3	2065.0(6)	2087.4(7)	1964.93(10)	7803.2(6)	7765.6(7)
Z	4	4	4	8	8
F(000)	1068.0	1072.0	1164.0	4736.0	4760.0
ρ (mg·m^{-3})	1.747	1.739	1.993	2.100	2.118
μ (mm^{-1})	2.421	2.548	3.067	4.681	5.013
data/restraints/parameters	9145/0/270	7906/0/270	4897/0/294	2841/0/88	3670/2/88
GOF	1.049	1.038	1.096	1.194	1.177
before SQUEEZE					
R_1 ($I = 2\sigma(I)$)[b]	0.1407	0.1924	0.0467	0.0720	0.1050
wR_2 (all data)[b]	0.2963	0.2369	0.0799	0.1488	0.1506
after SQUEEZE					
R_1 ($I = 2\sigma(I)$)[b]	0.0836	0.0719	0.0339	0.0532	0.0649
wR_2 (all data)[b]	0.2346	0.1762	0.0799	0.1075	0.1089

[a]Include one chlorine atom approximated using SQUEEZE. [b]$R_1 = \Sigma||F_o| - |F_c||/|F_o|$, $wR_2 = [\Sigma w(F_o^2 - F_c^2)^2/\Sigma w(F_o^2)^2]^{1/2}$.

evaporation of the ethanol solvent in few days. The PXRD and the single crystal X-ray diffraction indicated the yielding of five more distinct crystals: $[Ln(pdc)(Hpdc)(H_2O)_2]\cdot 3H_2O$ {$P2_1/c$; Ln = Pr (VI), Nd (VII), Sm (VIII)} and $[Ln(pdc)(H_2O)_4]_3\cdot 3Cl$ {$Ia\bar{3}$; Ln = Sm (IX), Eu (X)}.

Single Crystal Structures Determination. Crystallographic data of I–V were collected at 296(2) K using a Bruker D8 QUEST CMOS diffractometer equipped with graphite-monochromated Mo K_α radiation (λ = 0.71073 Å), and those of VI–X were collected using a Bruker D8 Venture diffractometer (Photon CMOS detector) equipped with a micro focus sealed tube X-ray source with graphite monochromatic Mo K_α radiation (λ = 0.71073 Å). Empirical absorption corrections were applied to all data using the SADABS program.[18] Every structure was solved by direct methods within the SHELXS program[19] and refined on F^2 by the full-matrix least-squares technique using the SHELXL program[19] via the Olex2 interface.[20]

In order to take the contribution of the disordered chloride anions into account in the cases of I–V, the SQUEEZE option provided in the program PLATON[22] was implemented with every structure after two chloride anions were located. Numbers of electrons per unit cell to be found in the framework accessible voids were determined, and numbers of equivalent chloride anions were calculated: 10 (I and IV), 9 (II and III), and 7 (V) chlorides per unit cell leading to the addition of one chloride per formula. Similar treatment was also required for VI–X. In the cases of VI and VII, numbers of equivalent water molecules were calculated: 10 (VI) and 5 (VII) crystallized water

DOI: 10.1021/acs.cgd.6b01389
Cryst. Growth Des. 2017, 17, 1045–1054

molecules per unit cell. These values led to the approximation of one crystallized water per formula. In the cases of VIII and X, nine chlorides per unit cell was calculated leading to one additional chloride per formula. The application of SQUEEZE on these structures resulted in significant improvement in the *R* and *Rw* values. There is additional site disordering at the chloride anion in every structure possessing the chloride as guest anions. Appreciable improvement in the final residual electron density maxima and minima was achieved after the treatment of such. The crystallographic and refinement data of I–X are summarized in Table 1.

■ RESULTS AND DISCUSSION

Influences of Heating Techniques on Crystal Structures. Despite the different heating techniques, clear solutions of colors characteristic to the corresponding lanthanide ions were yielded alike. Crystals as the sole products appeared after the solvents evaporated in few days. Under an optical microscope, the two different heating techniques provided crystals of similar habits, although qualities and sizes of these crystals varied. There was not any significant correlation between the heating techniques and qualities of the yielded crystals. The PXRD patterns collected on the ground crystals (Figure 1) and the single crystal data however suggest the

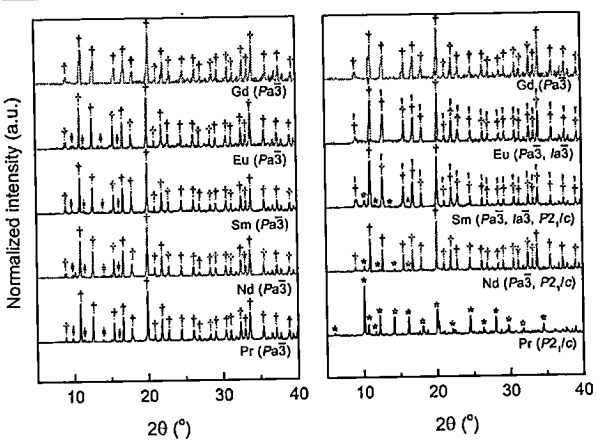

Figure 1. Experimental PXRD patterns collected on bulk solids obtained from the microwave synthesis (left) and the conventional heating (right). Symbols: † = $Pa\bar{3}$, ′ = $Ia\bar{3}$, * = $P2_1/c$, ‡ = unknown.

acquiring of 10 different structures, among which seven structures are new (Scheme 2). The microwave heating apparently led to the formation of the isostructural cubic complexes I–V ($Pa\bar{3}$), which is also isostructural to the previously reported $[La(pdc)(H_2O)_4]_3{\cdot}3Cl$.[8] There are however a few mismatched diffraction peaks between the collected PXRD patterns and the patterns simulated from the single crystal data. These unidentified peaks appear at closely similar 2θ in every pattern. The existence of the other crystalline structure can therefore be concluded, although the attempt to find single crystals of the other structures beside I–V was not successful.

The heating under reflux, on the other hand, led to the formation of different structures which can be classified into three groups of isostructural crystals: (i) the monoclinic $P2_1/c$ structures VI (Pr), VII (Nd) and VIII (Sm), (ii) the cubic $Ia\bar{3}$ structures IX (Sm) and X (Eu), and (iii) the cubic $Pa\bar{3}$ structures II (Nd), III (Sm), IV (Eu), and V (Gd). A few observations are noteworthy. First, there is a tendency in crystal symmetry alteration across the lanthanide series. The crystal symmetry increases from the pure monoclinic $P2_1/c$ in Pr (VI) to the mixtures of the monoclinic $P2_1/c$ and the cubic $Pa\bar{3}$ and $Ia\bar{3}$ in Nd (II + VII) and Sm (III + VIII + IX), to the mixed cubic $Pa\bar{3}$ and $Ia\bar{3}$ in Eu (IV + X), and to the pure cubic $Pa\bar{3}$ in Gd (V). Second, the cubic $Ia\bar{3}$ structures IX (Sm) and X (Eu) are the supramolecular isomers of the cubic $Pa\bar{3}$ structures III (Sm) and IV (Eu). Third, only the monoclinic $P2_1/c$ (VI; Pr) and the cubic $Pa\bar{3}$ (V; Gd) structures can be yielded as pure phases if the heating under reflux was applied. Forth, the cubic structures are more favorable than the monoclinic independent of the heating techniques with the exception of praseodymium complex.

The fact that the crystals were grown after the evaporation of the ethanol solvent in every case suggests the nucleation process to be critical in determining the final structures. Since the nucleation process is kinetically controlled,[23,24] the cubic $Pa\bar{3}$ structures are therefore favored kinetically. The conventional heating, which generally provides thermodynamically favorable structures, however, results in structures of different symmetries and supramolecular assemblies. These structures should therefore be comparatively favored from the thermodynamic point of view, although the $Pa\bar{3}$ structures should be the most favorable structures from both kinetic and thermodynamic viewpoints manifested in the yielding of these structures from every synthesis except the praseodymium case (VI).

An apparent tendency in the changing of the crystal structures across the reported lanthanide series when the conventional heating was employed can be due to the differences in numbers of the coordinating organic ligands and water molecules the latter of which depends on the hydration enthalpies of the lanthanide metal ions. With the lowest hydration preference, only two water molecules are included in the coordination sphere of the praseodymium ion (VI). The number of the coordinating water molecules in the more favorable cubic structures of the heavier lanthanide ions with larger hydration energies is four. In addition, the praseodymium ion of relatively large ionic radius can accommodate more organic ligands compared with the smaller lanthanide metal ions. This is well reflected in the $Ln^{III}/pdc^{2-}/Hpdc^{-}/H_2O_{ligand}$ ratios; 1:2:2 (VI–VIII) compared with 1:1:4 (I–V, IX, and X). The larger number of the coordinating water molecules in the latter group should also be attributed to the coordination requirement of the lanthanide ions. Similar structural variation of the cubic $Pa\bar{3}$ and the monoclinic $P2_1/c$ was notably reported for $[La(pdc)(H_2O)_4]_3{\cdot}3Cl$.[8] The change was however induced by the removal of the chloride anions from the cubic $Pa\bar{3}$ $[La(pdc)(H_2O)_4]_3{\cdot}3Cl$ structure using $AgBF_4$, which led to the formation of the monoclinic $P2_1/c$ ladder-like $[La(pdc)(Hpdc)(H_2O)_2]{\cdot}3H_2O$.[8]

Crystal Structures Description. *The Cubic $Pa\bar{3}$ $[Ln(pdc)(H_2O)_4]_3{\cdot}3Cl$ (I–V).* Complexes I–V are revealed to be isostructural with the previously reported lanthanum complex $[La(pdc)(H_2O)_4]_3{\cdot}3Cl$.[8] According to the results from the SQUEEZE calculations after the assignment of two well-defined chloride anions, the general formula of $[Ln(pdc)(H_2O)_4]_3{\cdot}3Cl$ can be deduced. The presence of the three unbound chlorides in the formula is in good accordance with the tripositive charges of the $[Ln(pdc)(H_2O)_4]_3^{3+}$ framework. Complexes I–V crystallize in the same cubic $Pa\bar{3}$ space group with cell parameters *a* and *V* descending from I (Pr) to V (Gd) consistent with the lanthanide contraction. The asymmetric units of I–V are alike, comprising one unique lanthanide ion, a

DOI: 10.1021/acs.cgd.6b01389
Cryst. Growth Des. 2017, 17, 1045–1054

fully deprotonated pdc^{2-} ligand, four coordinated water molecules, and two unbound chloride anions. The other chloride anion has been treated as a diffuse contribution to the overall scattering without specific atom position by SQUEEZE. One of the well-defined chloride anions in every structure, except III, shows additional disorder over two crystallographic sites, with different site occupancy Cl2A/Cl2B ratios: 0.932:0.068 (I), 0.605:0.395 (II), 0.582:0.418 (IV), and 0.719:0.281 (V). Atom Cl2 in structure III shows similar disorder but over three crystallographic sites with a site occupancy Cl2A/Cl2B/Cl2C ratio of 0.55:0.40:0.05. The attempt to exclude Cl2B and Cl2C from the refinement of I and III, respectively, resulted in judiciously elongated ellipsoids of the corresponding Cl2A and Cl2B.

The Ln ion in I–V is 9-fold coordinated to three pdc^{2-} ligands through the pyridyl N1 and the carboxyl O1–O4 atoms and the water O5–O8 atoms (Figure 2a). The Ln–O and Ln–N bond distances of the structures I–V are in good agreement with those of $[La(pdc)(H_2O)_4]_3{\cdot}3Cl$[8] and consistent with the lanthanide contraction. The bond valence sum calculations based on these bond distances affirm the trivalent state of the lanthanide ions. The nine coordinated atoms delineate the square-face monocapped antiprismatic coordination geometry, *SAPRS*-{LnO_8N} (Figure 2b), with the pdc^{2-} ligand using two μ_2-η^1:η^1 carboxyl groups and the pyridyl N atom in coordination (mode *a* in Scheme 1, Figure 2c). The coordination as described results in almost complete coplanarity between the carboxyl groups and the central pyridyl ring.

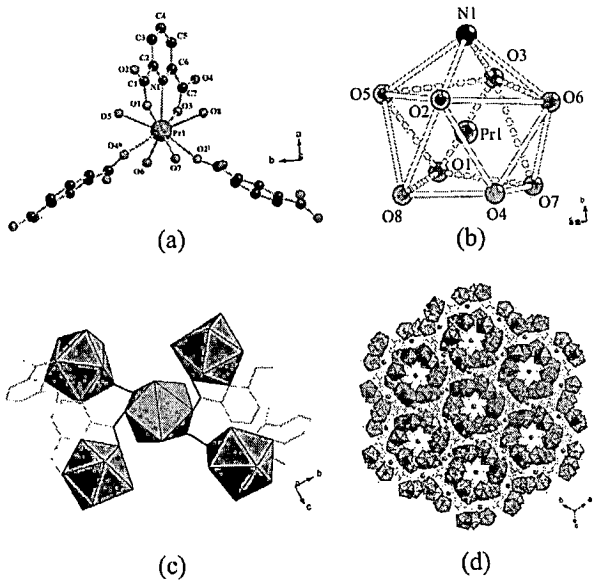

Figure 2. Illustrations showing (a) an extended asymmetric unit, (b) the *SAPRS*-{LnO_8N} unit, (c) the linkage of these units, and (d) the infinite tubular structure of I (as representative of I–V, IX–X).

The infinite frameworks of I–V are built up of the discrete *SAPRS*-{LnO_8N} units, each of which is linked to four adjacent units via three pdc^{2-} linkers. The linkages of the *SAPRS*-{LnO_8N} units result in the formation of four discrete one-dimensional channels extending in four <1 1 1> directions along the 3-fold rotoinversion axes (Figure 2d). The openings of these channels range from 2.96(1) Å to 3.35(3) Å. The interior of these channels is decorated with the coordinated water molecules and therefore is hydrophilic in nature. Inside these channels, there are the unbound chloride anions, some of which are transfixed by the O–H···O and O–H···Cl hydrogen bonding interactions (Table 2), and some are diffused with a high degree of freedom. These channels can therefore be viewed as a microcontainer of the chloride aqueous solution. All the hydrogen donor atoms are intriguingly of the coordinated water molecules. The involvement of every chloride anions including the disordering chlorides in the hydrogen bonding interactions can account for the apparent site disorder of the anions.

The Cubic $Ia\bar{3}$ $[Ln(pdc)(H_2O)_4]_3{\cdot}3Cl$ (IX, X). Complexes IX (Sm) and X (Eu) are isostructural and revealed to be the supramolecular isomers of III (Sm) and IV (Eu), respectively. The asymmetric units of IX and X are closely similar to the corresponding isomers comprising one unique lanthanide ion, half a molecule of the fully deprotonated pdc^{2-} ligand, two coordinated water molecules, and one chloride anion which shows disorder over two crystallographic sites. The occupancy ratios of Cl1A/Cl1B in both structures are closely similar, i.e., 0.256(11):0.744(1) (IX) and 0.262(9):0.738(9) (X). Since IX and X are the isomers of III and IV, the coordination environment about the lanthanide ion and mode of coordination adopted by the pdc^{2-} ligand are principally identical (Figure 3a). If the arrangement and the linkage of the *SAPRS*-{LnO_8N} units in these structures are considered carefully, the *SAPRS*-{LnO_8N} units in IX and X are however not exactly the same as those found in III and IV, but being their enantiomers (Figure 3b). While the spatial arrangement of the ligands about the lanthanide ion in the cubic $Pa\bar{3}$ structures (III and IV) can be defined as the Λ stereoisomer, the configuration in the $Ia\bar{3}$ structures (IX and X) are the enantiomeric counterpart, Δ. Despite the existence of these stereoisomeric building motifs, the packings of these building motifs in the crystal structures according to the operations about the inversion center and the mirror planes result in achiral cubic frameworks. The cubic $Pa\bar{3}$ structures are apparently favored both thermodynamically and kinetically over the cubic $Ia\bar{3}$ structures which exist only in the samarium (IX) and europium (X) cases.

The formation of channels in the $Ia\bar{3}$ structures is similar to those of the cubic $Pa\bar{3}$ structures. The unbound chloride anions are positioned approximately along the 3-fold rotoinversion axes. The hydrogen bonding interactions observed in the cubic $Ia\bar{3}$ structures are also closely similar to the cubic $Pa\bar{3}$ counterparts (Table 2), involving every water molecules as the hydrogen bonding donors and the unbound chloride anions as the acceptors. The alignments of chlorides governed by these hydrogen bonding interactions can therefore be the key factor driving the formation of the tubular structures in these cubic $Pa\bar{3}$ and $Ia\bar{3}$ structures alike.

The Monoclinic $P2_1/c$ $[Ln(pdc)(Hpdc)(H_2O)_2]{\cdot}3H_2O$ (VI–VIII). As the heating under reflux was employed, the lower symmetry structures of the monoclinic $P2_1/c$ space group have been synthesized. Pure monoclinic structure could even be afforded in the case of praseodymium complex (VI), although the cubic structures are favored for the other lanthanides. These $P2_1/c$ structures have been previously reported as can be yielded also by the hydrothermal technique.[11,12] The asymmetric units of VI–VIII are bulky, comprising one unique lanthanide ion, a whole molecule each of the partially deprotonated $Hpdc^-$ and the completely deprotonated pdc^{2-},

DOI: 10.1021/acs.cgd.6b01389
Cryst. Growth Des. 2017, 17, 1045–1054

Table 2. List of Hydrogen Bonding Distances (D···A, Å) and Angles (∠D−H···A,°) for I−X

I[a]

D−H···A	D···A	∠D−H···A
O5−H5A···O2^{i}	3.171(8)	145
O5−H5A···O3^{ii}	2.874(7)	132
O5−H5B···Cl2A	3.141(2)	82
O5−H5B···Cl2B	3.142(2)	111
O6−H6A···O1^{iii}	2.640(1)	160
O8−H8B···Cl1	3.113(1)	131

II[b]

D−H···A	D···A	∠D−H···A
O5−H5A···O3^{i}	2.931(2)	147
O5−H5B···Cl2A^{ii}	3.084(8)	140
O5−H5B···Cl2B	3.281(7)	122
O6−H6B···O3^{i}	2.687(7)	151
O7−H7B···O1^{iii}	2.650(7)	154
O8−H8B···Cl1	3.120(4)	97
O8−H8B···Cl2A	3.481(3)	127

III[c]

D−H···A	D···A	∠D−H···A
O5−H5A···Cl2A	3.260(7)	132
O5−H5A···Cl2B^{i}	3.055(6)	133
O5−H5B···O3^{ii}	2.941(4)	144
O6−H6A···O1^{iii}	2.638(7)	157
O7−H7B···O3^{ii}	2.675(5)	138
O8−H8A···Cl2C	2.750(3)	85
O8−H8B···Cl1	3.131(5)	119

IV[d]

D−H···A	D···A	∠D−H···A
O5−H5B···Cl1	3.136(5)	134
O6−H6A···O3^{i}	2.689(2)	153
O7−H7B···O1^{ii}	2.637(3)	160
O8−H8A···Cl2A^{iii}	3.053(8)	133
O8−H8A···Cl2B	3.242(9)	136
O8−H8B···O3^{i}	2.929(1)	140

V[e]

D−H···A	D···A	∠D−H···A
O5−H5A···Cl2A	3.476(3)	149
O5−H5B···Cl1	3.123(8)	145
O6−H6B···O1^{i}	2.634(8)	161
O7−H7B···O3^{ii}	2.681(9)	158
O8−H8A···O3^{ii}	2.902(3)	151
O8−H8B···Cl2A^{iii}	3.106(8)	139
O8−H8B···Cl2B	3.271(9)	124

VI[f]

D−H···A	D···A	∠D−H···A
O9−H9A···O14^{i}	2.8236	153
O9−H9B···Ol3^{ii}	2.6504	111
O10−H10A···O3^{iii}	2.7788	142
O10−H10B···O7^{iv}	2.7773	147
O13−H13A···O6	2.7464	149
O13−H13B···O14	2.9051	156
O14−H14A···O5	2.9373	170
O14−H14B···O6^{ii}	2.8732	139

VII[g]

D−H···A	D···A	∠D−H···A
O9−H9A···O11^{i}	2.7091	118
O9−H9B···O12^{ii}	2.8173	158
O10−H10A···O2^{iii}	2.7894	103
O10−H10B···O6^{iv}	2.7690	163
O11−H11A···O8	2.7384	142
O11−H11B···O12	2.9132	141
O12−H12A···O5	3.2154	166
O12−H12A···O7	2.9505	113
O12−H12B···O8^{i}	2.9189	165

VIII[h]

D−H···A	D···A	∠D−H···A
O9−H9A···O12^{i}	2.7143	126
O9−H9B···O11^{ii}	2.7526	143
O10−H10A···O1^{iii}	2.7176	129
O10−H10B···O7^{iv}	2.7216	142
O11−H11A···O6^{i}	2.8759	161
O11−H11B···O9^{iv}	2.7526	167
O12−H12A···O6	2.6866	172
O12−H12B···O11	2.9041	145
O13−H13A···O12	3.0075	132
O14−H14A···O13^{v}	2.7926	103
O14−H14B···O13^{v}	2.7926	100

IX[i]

D−H···A	D···A	∠D−H···A
O3−H3A···O1^{i}	3.0782	118
O3−H3B···Cl1B	3.1946	142
O4−H4A···O1^{i}	2.6478	135

X[j]

D−H···A	D···A	∠D−H···A
O3−H3A···O1^{i}	3.0821	109
O3−H3B···Cl1B^{ii}	3.1894	150
O4−H4B···O1^{iii}	2.6539	151

[a]Symmetry codes: (i) = −0.5+x, 0.5−y, 1−z; (ii) = 0.5−x, 0.5+y, z; (iii) = −0.5+x, y, 0.5−z. [b]Symmetry codes: (i) = 0.5−x, 0.5+y, z; (ii) = 0.5+x, y, 0.5−z; (iii) = −0.5+x, y, 0.5−z. [c]Symmetry codes: (i) = 0.5+x, y, 0.5−z; (ii) = 0.5−x, 0.5+y, z; (iii) = −0.5+x, y, 0.5−z. [d]Symmetry codes: (i) = 0.5−x, 0.5+y, z; (ii) = −0.5+x, y, 0.5−z; (iii) = 0.5+x, y, 0.5−z. [e]Symmetry codes: (i) = x, 0.5−y, −0.5+z; (ii) = 0.5+x, y, 0.5−z; (iii) = x, 0.5−y, 0.5+z. [f]Symmetry codes: (i) = x, 1/2 −y, −1/2+z; (ii) = −x, −1/2+y, 1/2−z; (iii) = 1−x, 1/2+y, 1/2−z; (iv) = x, 1/2−y, 1/2+z. [g]Symmetry codes: (i) = −x, −1/2+y, 1/2−z; (ii) = x, 1/2−y, −1/2+z; (iii) = 1−x, 1/2+y, 1/2−z; (iv) = x, 1/2−y, 1/2+z. [h]Symmetry codes: (i) = −x, −1/2+y, 1/2−z; (ii) = x, 1/2−y, −1/2+z; (iii) = 1−x, 1/2+y, 1/2−z; (iv) = x, 1/2−y, 1/2+z; (v) = 1−x, 1−y, 1−z. [i]Symmetry codes: (i) = 1/2−x, 1/2−y, 1/2−z. [j]Symmetry codes: (i) = x, 1/2−y, −1/2+z; (ii) = x, −y, 1/2−z; (iii) = 1/2−x, 1/2−y, 1/2−z.

two coordinated water molecules, and two unbound water molecules. Contrary to the cubic structures, the monoclinic structures include the partially deprotonated $Hpdc^{-}$ ligand and less coordinated water molecules (Figure 4a). Although the coordination about the lanthanide ion in **VI**−**VIII** is the same 9-fold *SAPRS*-9 as those of the cubic structures, it is however highly distorted (Figure 4b). The distorted *SAPRS*-9 unit of the monoclinic structures is delineated with two fully deprotonated pdc^{2-} through the pyridyl N2 and the carboxylate O5, O7, and O8, and one mono-deprotonated $Hpdc^{-}$ through the pyridyl N1 and the carboxyl O1 and O3. Here, two different modes of coordination, namely, modes *a* and *b* (Scheme 1), are adopted

DOI: 10.1021/acs.cgd.6b01389
Cryst. Growth Des. 2017, 17, 1045−1054

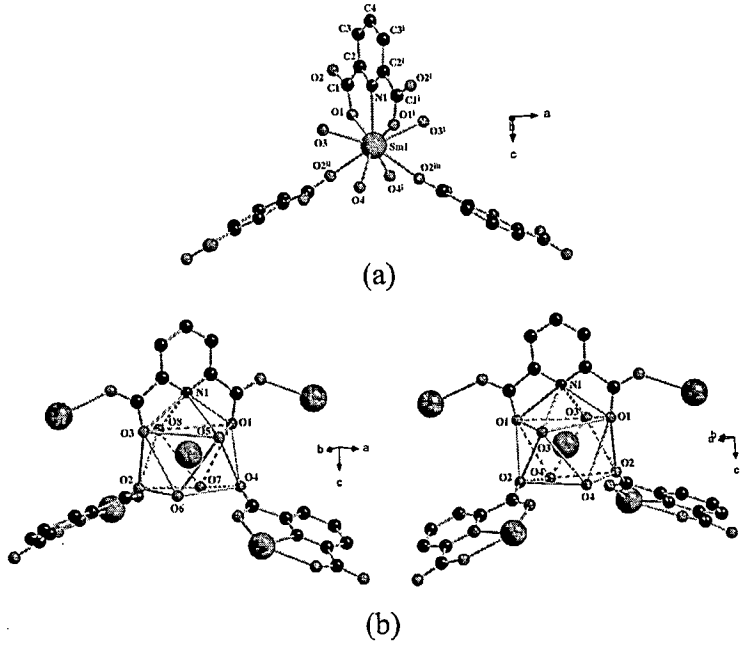

Figure 3. Views of (a) an extended asymmetric unit of IX and (b) the enantiomeric Λ (III, IV) and Δ (IX, X) configurations.

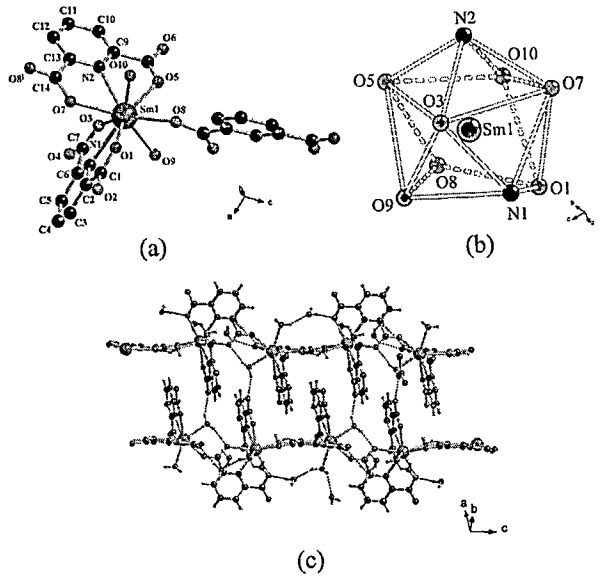

Figure 4. Illustrations of (a) an extended asymmetric unit, (b) the *SAPRS*-{LnO_7N_2} unit, and (c) the infinite ladder-like structure of VIII (as a representative of VI–VIII).

by the pdc^{2-} ligand, whereas mode *k* is adopted by the $Hpdc^-$. Two water O atoms (O9 and O10) complete the coordination requirement and therefore the formation of the *SAPRS*-{LnO_7N_2} structural building unit. Atoms O1 and N1 of the $Hpdc^-$ ligand seem to be the major contribution to the distortion in the *SAPRS*-{LnO_7N_2} unit, which on the other hand accounts for the lower proclivity for the $P2_1/c$ structures to be yielded.

The discrete *SAPRS*-{LnO_7N_2} units are bridged by the pdc^{2-} ligands to form an infinite one-dimensional [Ln(pdc)(Hpdc)$(H_2O)_2$] chain extending along the direction of *c* (Figure 4c). As the $Hpdc^-$ is arranged in an antiparallel fashion to the pdc^{2-}, the derived chain is puckered rather than linear. Compared to the cubic structures reported in this work, the presence of the $Hpdc^-$ ligand forbids the linkage of the adjacent lanthanide ions to form a higher dimensional coordination framework. These chains are bundled up into a dense assembly by the hydrogen bonding interactions between the coordinating and the unbound water molecules (Table 2) The hydrophobic pyridyl rings of these chains are aligned leading to the ladder-like assemblies extending in the *c* direction. According to the statistics on the structures submitted to the CSD,[17] the chelating $Hpdc^-$ ligand tends to give ladder-like structures in both the monoclinic $P2_1/c$ and $P2_1/a$ space groups.[13,17,21,25,26] There is however no π–π interaction in structures VI–VIII. The supramolecular assemblies of these [Ln(pdc)(Hpdc)$(H_2O)_2$] chains into a two-dimensional collugated layer extending in the *ab* plane and to the three-dimensional assembly are directed solely by the hydrogen bonding interactions.

Topology of the Cubic Structures. Despite the different sets of symmetry operations and the Bravais translation adopted by the $Pa\bar{3}$ and the $Ia\bar{3}$ structures, the derived framework topologies of both cubic structures are identical. The cubic $Pa\bar{3}$ and $Ia\bar{3}$ frameworks can be simplified to two interpenetrated uninodal lcs and pcu nets (Figure 5).[27] If the hydrogen bonding interactions between the coordinating water molecules and the unbound chloride anions are disregarded and only the *SAPRS*-{PrO_8N} unit is taken as node, a uninodal 4-connected lcs net with $\{6^6\}$ point symbol is derived. If only the $\{Cl_2(H_2O)_6\}$ motif is, on the other hand, taken as node, the other uninodal 6-connected pcu net with $\{4^{12}.6^3\}$ point symbol is obtained. The interpenetration of the lcs and pcu nets then establishes the networks in I–V and IX–X.

Thermogravimetric Behaviors of V and VI. Because only complexes V ($Pa\bar{3}$; Gd) and VI ($P2_1/c$; Pr) could be obtained with high purity, the thermogravimetric behavior of the two

DOI: 10.1021/acs.cgd.6b01389
Cryst. Growth Des. 2017, 17, 1045–1054

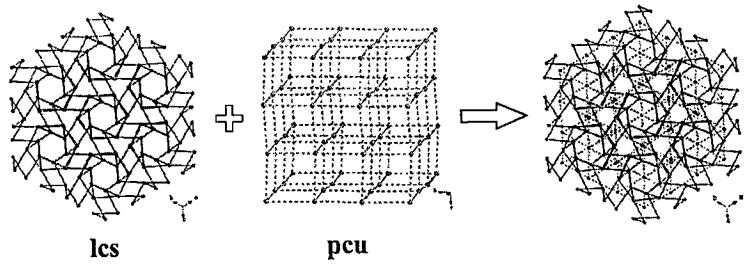

Figure 5. Interpenetrated uninodal lcs and pcu nets of the cubic structures I–V and IX–X.

complexes was studied revealing similar weight loss patterns (Figure 6). The first weight loss in both complexes readily

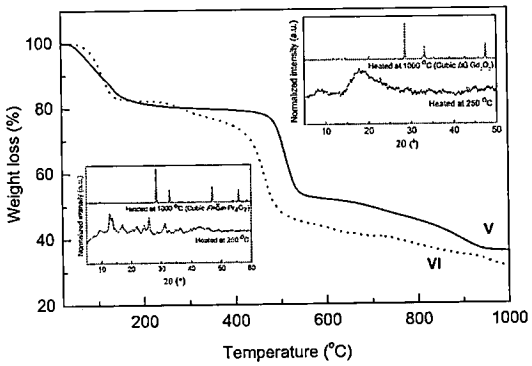

Figure 6. Thermogravimetric curves of V (solid line) and VI (dotted line) with the PXRD patterns of the heated samples shown in the insets.

occurred under the flow of nitrogen gas attributing to the liberation of the water molecules; calc. = 16.76%, exp. = 17.4% for V and calc. = 16.02%, exp. = 17.2% for VI. After the loss of the water molecules, the weight loss gradually proceeded in both cases, although the process was extremely slow in the case of V. The gradual loss led to the collapse of most of the long-range order in both frameworks revealed by the PXRD results, suggesting the successive loss of the other compartments of the frameworks. The second abrupt drops of weight were yet apparent for both complexes during the heat treatment occurring at a higher temperature in the case of V (ca. 470 °C) compared to that of VI (ca. 360 °C). This is consistent with the higher stability of the three-dimensional framework in V relative to the one-dimensional structure in VI. The gradual weight loss then occurred again for both complexes leading to the corresponding cubic lanthanide oxides.

Photoluminescence Properties of VI–X. Because of the purity limitation of the samples yielded from the microwave synthesis, the photoluminescence spectra of only the samples yielded from the conventional heating of which every phase could be identified were collected (Figure 7). The free H_2pdc exhibits a broad feature with multiple maxima covering almost an entire visible region, which can be ascribed to the pyridyl ring $\pi^*-\pi$ emission.[28,29] Different degrees of deprotonation has been reported to negligibly affect the energy of the triplet state of the ligand.[28] Apparently the ligand is a moderately good sensitizer for the reported complexes, especially those of the europium ion (IV + X) of which the intense characteristic emissions incited from the transitions from the first excited $^5D_0$ state to the ground multiplets ^7F_J (J = 0–4) are vivid. The efficiency of the energy transfer process from the ligand to the europium can also be enhanced by the increased molecular rigidity of the ligand after coordination and the singlet pathway of the energy transfer.[30−32] In the case of praseodymium (VI), neodymium (II + VII), and samarium ions (III + VIII + IX), differences between the triplet state of the ligand and the first excited states of the metal ions result in poor energy transfer, and therefore only weak emissions can be observed.[28] Large numbers of the excited states in praseodymium (VI) and neodymium (II + VII) may additionally render energy loss through the nonradiative pathways.[33] In comparison to the spectrum of the free H_2pdc, an emission band at 300 nm in the spectra of these samples may be attributed to the ligand centered $\pi^*-\pi$ emission promoted by the greater molecular rigidity upon the coordination to the metal centers.[34] The photoluminescence spectrum of the gadolinium complex (V) was notably not collected. The remarkably high energies of the excited states of gadolinium ion owing to the exceptional stability of the half-filled f-shell are known to prevent energy transfer from any known ligands, which consequently causes any f–f transition to be unachievable.[35,36]

CONCLUSIONS

In summary, we reported the variation and preference in crystal structures of the lanthanide-H_2pdc complexes synthesized by two different heating techniques, namely, conventional and microwave heating. Microwave heating provides the kinetically favorable cubic $Pa\bar{3}$ structures I–V, while conventional heating results in the formation of three groups of isostructural crystals: (i) the monoclinic $P2_1/c$ structures VI–VIII, (ii) the cubic $Ia\bar{3}$ structures IX and X; and (iii) the cubic $Pa\bar{3}$ structures II, III, and V. The $Pa\bar{3}$ complexes I–V exhibit the tubular structures built up of the *SAPRS*-{LnO_8N} units leading to the formation of four discrete one-dimensional channels extending in four <1 1 1> directions. Inside the channels, the chloride ions are transfixed by coordinating water molecules through hydrogen bonding interactions. The $Ia\bar{3}$ complexes IX and X which are the supramolecular isomers of III and IV, respectively, consist of the Δstereoisomeric *SAPRS*-{LnO_8N} units, while the configuration in III and IV are the enantiomeric counterpart, Λ. Owing to the close similarity between the cubic $Ia\bar{3}$ and $Pa\bar{3}$ structures, their frameworks can be simplified to two interpenetrating uninodal lcs and pcu nets alike. In the case of the $P2_1/c$ complexes VI–VIII, they are different from the other complexes becasuse of the existence of the $Hpdc^-$ ligand, which leads to the construction of highly distorted *SAPRS*-{LnO_7N_2} units. The linkage of these discrete *SAPRS*-{LnO_7N_2} units resulting in the formation of the infinite one-dimensional [Ln(pdc)(Hpdc)$(H_2O)_2$] chains which are further assembled solely by the hydrogen bonding interactions to two- and three-

DOI: 10.1021/acs.cgd.6b01389
Cryst. Growth Des. 2017, 17, 1045−1054

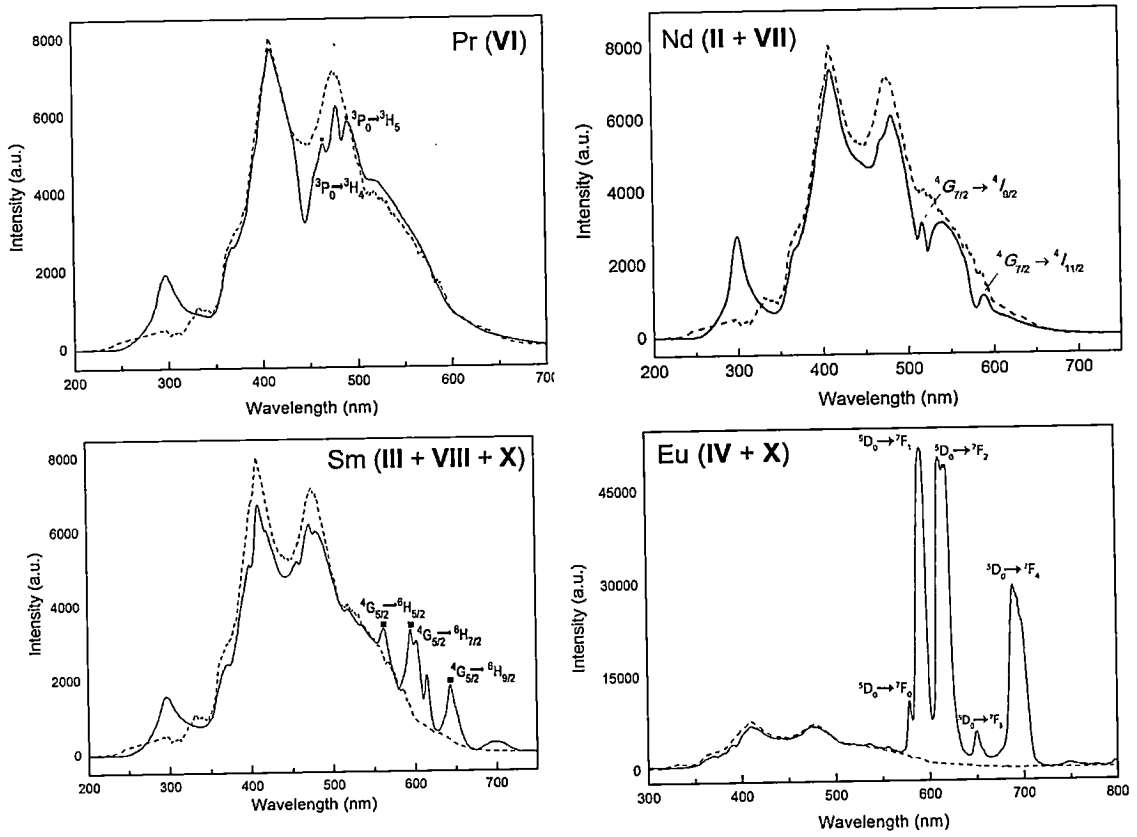

Figure 7. Photoluminescence spectra of the synthesized samples (solid line) compared with that of the free H_2pdc ligand (dashed line).

dimensional framework. The title complexes showed moderate thermal stabilities. The photoluminescence study reveraled a modest ability of the coordinated organic ligand in sensitizing the characteristic emissions of the lanthanide ions.

■ ASSOCIATED CONTENT

Supporting Information

The Supporting Information is available free of charge on the ACS Publications website at DOI: 10.1021/acs.cgd.6b01389.

Extended asymmetric units and simulated powder X-ray diffraction patterns of the reported structures (PDF)

Accession Codes

CCDC 1448352−1448354 and 1494337−1494343 contain the supplementary crystallographic data for this paper. These data can be obtained free of charge via www.ccdc.cam.ac.uk/data_request/cif, or by emailing data_request@ccdc.cam.ac.uk, or by contacting The Cambridge Crystallographic Data Centre, 12 Union Road, Cambridge CB2 1EZ, UK; fax: +44 1223 336033.

■ AUTHOR INFORMATION

Corresponding Author

*Telephone: +66 5394 3341. Fax: +66 5389 2277. E-mail: apinpus.rujiwatra@cmu.ac.th.

ORCID

Apinpus Rujiwatra: 0000-0002-2364-4592

Notes

The authors declare no competing financial interest.

■ ACKNOWLEDGMENTS

This work was cofunded by the Thailand Research Fund and Chaing Mai University. T.C. and P.R. thank the Royal Thai Development and Promotion of Science and Technology Talents Program for Scholarships.

■ REFERENCES

(1) Furukawa, H.; Cordova, K. E.; O'Keeffe, M.; Yaghi, O. M. *Science* **2013**, *341*, 1230444.

(2) Cui, Y.; Yue, Y.; Qian, G.; Chen, B. *Chem. Rev.* **2012**, *112*, 1126−1162.

(3) Sorace, L.; Benelli, C.; Gatteschi, D. *Chem. Soc. Rev.* **2011**, *40*, 3092−3104.

(4) Debroye, E.; Parac-Vogt, T. N. *Chem. Soc. Rev.* **2014**, *43*, 8178−8192.

(5) Xu, J.; Cheng, J.; Su, W.; Hong, M. *Cryst. Growth Des.* **2011**, *11*, 2294−2301.

(6) Zhang, J.; Zheng, B.; Zhao, T.; Li, G.; Huo, Q.; Liu, Y. *Cryst. Growth Des.* **2014**, *14*, 2394−2400.

(7) Li, M.; Li, D.; O'Keeffe, M.; Yaghi, O. M. *Chem. Rev.* **2014**, *114*, 1343−1370.

(8) Ghosh, S. K.; Bharadwaj, P. K. *Inorg. Chem.* **2005**, *44*, 3156−3161.

(9) Ghosh, S. K.; Bharadwaj, P. K. *Inorg. Chem.* **2004**, *43*, 2293−2298.

(10) Gao, H.-L.; Yi, L.; Zhao, B.; Zhao, X.-Q.; Cheng, P.; Liao, D.-Z.; Yan, S.-P. *Inorg. Chem.* **2006**, *45*, 5980−5988.

(11) Ghosh, S. K.; Bharadwaj, P. K. *Inorg. Chem.* **2003**, *42*, 8250−8254.

(12) Liu, S.-H.; Meng, Q.-J.; Li, Y.-Z. *Acta Crystallogr., Sect. E: Struct. Rep. Online* **2005**, *61*, m1111−m1113.

(13) Hao, L.-J.; Yu, T.-L. *Acta Crystallogr., Sect. E: Struct. Rep. Online* **2007**, *63*, m1967–m1967.
(14) Zhao, B.; Yi, L.; Dai, Y.; Chen, X.-Y.; Cheng, P.; Liao, D.-Z.; Yan, S.-P.; Jiang, Z.-H. *Inorg. Chem.* **2005**, *44*, 911–920.
(15) Starynowicz, P. *Acta Crystallogr., Sect. C: Cryst. Struct. Commun.* **1992**, *48*, 1428–1430.
(16) Liu, Y.-R.; Yang, T.; Li, L.; Liu, J.-M.; Su, C.-Y. *Aust. J. Chem.* **2009**, *62*, 1667–1674.
(17) Groom, C. R.; Bruno, I. J.; Lightfoot, M. P.; Ward, S. C. *Acta Crystallogr., Sect. B: Struct. Sci., Cryst. Eng. Mater.* **2016**, *72*, 171–179.
(18) Sheldrick, G. M. *SADABS*; University of Göttingen: Germany, 1996.
(19) Sheldrick, G. *Acta Crystallogr., Sect. A: Found. Crystallogr.* **2008**, *64*, 112–122.
(20) Dolomanov, O. V.; Bourhis, L. J.; Gildea, R. J.; Howard, J. A. K.; Puschmann, H. *J. Appl. Crystallogr.* **2009**, *42*, 339–341.
(21) Ramezanipour, F.; Aghabozorg, H.; Shokrollahi, A.; Shamsipur, M.; Stoeckli-Evans, H.; Soleimannejad, J.; Sheshmani, S. *J. Mol. Struct.* **2005**, *779*, 77–86.
(22) Spek, A. *J. Appl. Crystallogr.* **2003**, *36*, 7–13.
(23) Jhung, S. H.; Jin, T.; Hwang, Y. K.; Chang, J.-S. *Chem. - Eur. J.* **2007**, *13*, 4410–4417.
(24) Rodiguez-Horzedo, N.; Murphy, D. *J. Pharm. Sci.* **1999**, *88*, 651–660.
(25) Wang, P.; Fan, R.-Q.; Liu, X.-R.; Yang, Y.-L.; Zhou, G.-P. *J. Inorg. Organomet. Polym. Mater.* **2012**, *22*, 744–755.
(26) Zou, J.-P.; Wen, Z.-H.; Peng, Q.; Zeng, G.-S.; Xing, Q.-J.; Chen, M.-H. *J. Coord. Chem.* **2009**, *62*, 3324–3331.
(27) Blatov, V. A.; Shevchenko, A. P.; Proserpio, D. M. *Cryst. Growth Des.* **2014**, *14*, 3576–3586.
(28) Massaro, R. D.; Blaisten-Barojas, E. *Comput. Theor. Chem.* **2011**, *977*, 148–156.
(29) Hameka, H. F.; Jensen, J. O.; Jensen, J. L.; Merrow, C. N.; Vlahacos, C. P. *J. Mol. Struct.: THEOCHEM* **1996**, *365*, 131–141.
(30) Rao, X.; Huang, Q.; Yang, X.; Cui, Y.; Yang, Y.; Wu, C.; Chen, B.; Qian, G. *J. Mater. Chem.* **2012**, *22*, 3210–3214.
(31) Yang, C.; Fu, L.-M.; Wang, Y.; Zhang, J.-P.; Wong, W.-T.; Ai, X.-C.; Qiao, Y.-F.; Zou, B.-S.; Gui, L.-L. *Angew. Chem., Int. Ed.* **2004**, *43*, 5010–5013.
(32) Garcia-Torres, J.; Bosch-Jimenez, P.; Torralba-Calleja, E.; Kennedy, M.; Ahmed, H.; Doran, J.; Gutierrez-Tauste, D.; Bautista, L.; Della Pirriera, M. *J. Photochem. Photobiol., A* **2014**, *283*, 8–16.
(33) Cui, Y.; Chen, B.; Qian, G. *Coord. Chem. Rev.* **2014**, *273–274*, 76–86.
(34) Wang, P.; Fan, R.-Q.; Liu, X.-R.; Yang, Y.-L.; Zhou, G.-P. *J. Inorg. Organomet. Polym. Mater.* **2012**, *22*, 744–755.
(35) Vogler, A.; Kunkely, H. *Inorg. Chim. Acta* **2006**, *359*, 4130–4138.
(36) Strasser, A.; Vogler, A. *Inorg. Chim. Acta* **2004**, *357*, 2345–2348.

NOTE ADDED AFTER ASAP PUBLICATION

This paper was published ASAP on February 7, 2017, with some incorrect CCDC numbers in Table 1 and the Accession Codes note. The corrected version with accurate CCDC numbers was posted on February 10, 2017.

DOI: 10.1021/acs.cgd.6b01389
Cryst. Growth Des. 2017, 17, 1045–1054

Inorganic Chemistry
Cite This: Inorg. Chem. 2018, 57, 2620−2630
Article
pubs.acs.org/IC

Lanthanide Coordination Polymers of Mixed Phthalate/Adipate for Ratiometric Temperature Sensing in the Upper-Intermediate Temperature Range

Thammanoon Chuasaard,[†] Athipong Ngamjarurojana,[‡] Sireenart Surinwong,[§] Takumi Konno,[§] Sareeya Bureekaew,[∥] and Apinpus Rujiwatra*[,†]

[†]Department of Chemistry, Faculty of Science and [‡]Department of Physics and Materials Science, Faculty of Science, Chiang Mai University, Chiang Mai 50200 Thailand

[§]Department of Chemistry, Graduate School of Science, Osaka University, Toyonaka, Osaka 560-0043, Japan

[∥]School of Energy Science and Engineering, Vidyasirimedhi Institute of Science and Technology, Rayong 21210, Thailand

Supporting Information

ABSTRACT: Based on the mixed phthalate ($phth^{2-}$) and adipate (ad^{2-}), $[Nd_2(ad)(phth)_2(H_2O)_4]$ (I) and $[Ln(ad)_{0.5}(phth)(H_2O)_2]$ (Ln = Eu^{III} (II), Gd^{III} (III), Tb^{III} (IV), Dy^{III} (V), Er^{III} (VI), Tm^{III} (VII), $1Eu^{III}$:$10Tb^{III}$ (VIII), $3Eu^{III}$:$10Tb^{III}$ (IX), and $5Eu^{III}$:$10Tb^{III}$ (X)) were synthesized and characterized. Complexes VIII−X show excellent ratiometric temperature sensing behavior in physiological and higher temperature ranges (303−423 K) rendered by the Tb^{III}-to-Eu^{III} energy transfer process. The efficiency of the process as illustrated through the lifetime measurements depends on both the Eu^{III}:Tb^{III} mole ratio and the temperature. The performance of X in terms of relative sensitivity (S_r), temperature resolution, and measurement repeatability were determined, revealing the maximum S_r (S_m) of 1.21%·K^{-1} at 303 K with reliable temperature resolution and excellent repeatability.

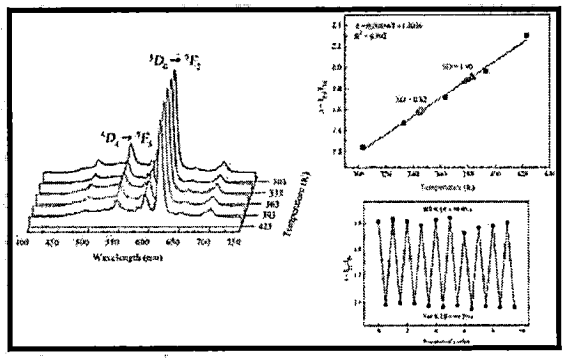

INTRODUCTION

The development of nonevasive thermometry has been recently demanded due to the intrinsic constraints of conventional and evasive thermometry with reference to various applications such as micro- and nanoelectronic diagnoses.[1,2] Amid several potential materials available for noninvasive techniques, those based on lanthanide photoluminescence have gained zealous attention. Since the first and recent report of a lanthanide coordination polymer (LnCP), i.e. $[Eu_{0.0069}Tb_{0.9931}$-DMBDC] (DMBDC = 2,5-dimethoxy-1,4-benzenedicarboxylate), as a potential luminescent thermometer,[3] ardent investigation on other LnCPs and lanthanide metal organic frameworks (LnMOFs) has been escalating. This is partially due to the inexhaustible choices of structural compositions which can be tailored.[4,5] The photoluminescence behavior of previously reported LnCPs is mostly accounted for by an antenna model and Latva's empirical rule.[6] These models have been primarily developed, however, for molecular lanthanide complexes and sometimes cannot be employed with LnCPs possessing infinite frameworks of multidimensions. The inherent photoluminescence features of each structural component of LnCPs may be retained or modulated via interactions with neighboring components. The new approach of band theory, which can be regarded as an extension to the antenna model, has very recently been proposed and successfully applied to several LnCPs.[7]

Photoluminescence thermometry can be developed based on the changes in intensity, lifetime, or wavelength of the emission spectra, among which the ratiometric intensities-based approach offers several benefits.[1,2,4,5] The precision and repeatability of the measurement as well as being self-reference, for examples, are undeniably appealing. To evaluate the performance of ratiometric luminescent thermometers, several parameters, such as relative sensitivity (S_r), temperature resolution (δT), repeatability (R) and working temperature range, have been determined.[1,2] Few observations can be made, nonetheless, for the reported LnCPs thus far. First, most of the materials are based on the use of mixed Eu^{III} and Tb^{III} as dual centers (Eu^{III}/Tb^{III} CPs). Second, the S_r of 2%·K^{-1} or higher have been reported only for the cryogenic (<100 K) and medium temperatures (100−300 K).[4,5] The known materials with high S_r at the physiological (298−328 K) or higher (>350 K) temperature ranges are extremely rare; $[Tb_{0.99}Eu_{0.01}(hfa)_3(dpbp)]_n$ (hfa = hexafluoro acetylacetonato, dpbp = 4,4′-bis(diphenyl phosphoryl)),[8] $Tb_{0.99}Eu_{0.01}(BDC)_{1.5}(H_2O)_2$ (BDC = 1−4-benzene dicarboxylate),[9] and $Tb_{0.8}Eu_{0.2}$BPDA (BPDA = biphenyl-3,5-dicarboxylate).[10] Designing of LnCPs for use as ratiometric luminescent thermometers in such temperature ranges is still,

Received: November 30, 2017
Published: February 14, 2018

DOI: 10.1021/acs.inorgchem.7b03016
Inorg. Chem. 2018, 57, 2620−2630

therefore, of great challenge, and Eu^{III}/Tb^{III} CPs are seemingly eligible choices to embark on. Scrupulous choices of organic antenna with appropriate triplet band energies are also critical in determining the photoluminescence properties of the constructed LnCPs although their triplet band energies are generally lower than the corresponding molecular triplet state energies.[6,7] The efficiency of the sensitization process can, in addition to the concentration and type of Ln luminophores, be modulated by the interactions of the organic antenna with the Ln luminophores and the neighboring motifs, as well as the presence of other species in the framework.[4−7]

Based on the use of rigid phthalic acid (H_2phth) and the flexible adipic acid (H_2ad) with freedom to bend or rotate,[11,12] $[Nd_2(ad)(phth)_2(H_2O)_4]$ (I) and $[Ln(ad)_{0.5}(phth)(H_2O)_2]$ (Ln = Eu^{III} (II), Gd^{III} (III), Tb^{III} (IV), Dy^{III} (V), Er^{III} (VI), Tm^{III} (VII), $1Eu^{III}$:$10Tb^{III}$ (VIII), $3Eu^{III}$:$10Tb^{III}$ (IX) and $5Eu^{III}$:$10Tb^{III}$ (X)) have been synthesized. Their single crystal structures, thermal stabilities, and photoluminescence properties are presented. The ratiometric temperature sensing behavior of VIII−X and the key performance parameters of the measurements based on X are included.

EXPERIMENTAL SECTION

Materials and Methods. All chemicals were obtained commercially and used without further purification; Nd_2O_3 (TJTM, 99.99%), Eu_2O_3 (Merck, 99%), Gd_2O_3 (Sigma-Aldrich, 99.9%), Tb_4O_7 (Sigma-Aldrich, 99.9%), Dy_2O_3 (Fluka, 99.9%), Er_2O_3 (Fluka, 99.9%), Tm_2O_3 (Merck), HNO_3 (Carlo Erba, 65%), phthalic acid (H_2phth; $C_8H_6O_4$, BDH, 65%), adipic acid (H_2ad; $C_6H_{10}O_4$, Sigma-Aldrich, 99%), and 1,4-diazabicyclo[2.2.2]octane (DABCO; Sigma-Aldrich, 98%).

The elemental analysis was performed using a Thermo Scientific Flash 2000 CHN analyzer. Infrared (IR) spectra were collected using a Bruker Tensor 27 FT-IR instrument and KBr discs (BDH, 98.5%). Powder X-ray diffraction (PXRD) data were recorded using a Rigaku Mini Flex II X-ray diffractometer operated with Cu Kα radiation (λ = 1.5418 Å, 40 kV, 15 mA). The amounts of Eu^{III} and Tb^{III} in VIII−X were determined using a Phillips MagiX PRO (PW2540 vrc sample changer) X-ray fluorescence (XRF) spectrometer and an energy dispersive X-ray analysis (EDS) equipped with a field emission scanning electron microscope (SEM; JEOL JSM-6335F). Thermogravimetric analyses were conducted using a PerkinElmer Pyris Diamond TG/DTA Analyzer in a temperature range 35−1100 °C under a nitrogen gas flow with a heating rate 10 °C·min^{-1}. The UV−vis spectra were collected using PerkinElmer Lambda25 UV−vis spectrophotometer.

Room temperature photoluminescence (PL) spectra of I−X and temperature dependent spectra of II, IV, and VIII−X were collected on ground crystals using an ASEQ LR-1T broad range spectrophotometer equipped with an Ultrafire G60 UV 5w 365 nm Ultraviolet LED Flashlight Torch excitation source. The temperature controlling compartment was set up using a Dual Digital F/C PID temperature controller furnace Kiln oven, type K thermocouple and a BOXCAR data collecting analysis system. The stray light was filtered out using a UV optical band-pass (<400 nm), and the temperature was varied from 303(2) K to 423(2) K. The S_r of VIII−X as well as the δT and R of X were determined.

Synthesis of $[Nd_2(ad)(phth)_2(H_2O)_4]$ (I). Nd_2O_3 (0.0673 g, 0.400 mmol Nd^{III}) was dissolved in 7.20 M HNO_3(aq). The pH of the solution was then adjusted to 6 by adding a small amount of 10.00 M NaOH(aq) solution. Separately, a solution of H_2phth (0.0664 g, 0.400 mmol), H_2ad (0.0584 g, 0.400 mmol) and DABCO (0.0448 g, 0.400 mmol) was prepared using 7.00 mL of deionized water. The prepared solutions were mixed in a Teflon vessel which was sealed and hydrothermally heated at 120 °C for 24 h. After the reaction was cooled down to room temperature, light violet block crystals of I were obtained in *ca.* 40% yield based on Nd. Anal. Calcd for $C_{22}H_{24}O_{16}Nd_2$ (%): C, 31.73; H, 2.90. Found: C, 31.62; H, 2.83. IR (KBr pellets, cm^{-1}): 3435(br), 2966(w), 2932(w), 1549(s), 1419(s), 1148(w), 1086(w), 760(m), 696(w), 436(w).

$[Eu(ad)_{0.5}(phth)(H_2O)_2]$ (II). The colorless prismatic crystals of II (45% yield based on Eu) were obtained using the same synthetic procedure as that of I, but replaced Nd_2O_3 with Eu_2O_3 (0.0704 g, 0.400 mmol Eu^{III}). Anal. Calcd for $C_{11}H_{12}O_8Eu$ (%): C, 31.15; H, 2.85. Found: C, 30.99; H, 2.77. IR (KBr pellets, cm^{-1}): 3197(br), 2956(w), 2883(w), 1520(s), 1423(s), 1319(m), 1214(w), 1144(w), 846(m), 775(m), 709(m), 655(m), 417(m).

$[Gd(ad)_{0.5}(phth)(H_2O)_2]$ (III). The colorless prismatic crystals of III (55% yield based on Gd) were obtained using the same synthetic procedure as that of I, but replaced Nd_2O_3 with Gd_2O_3 (0.0726 g, 0.400 mmol Gd^{III}). Anal. Calcd for $C_{11}H_{12}O_8Gd$ (%): C, 30.76; H, 2.82. Found: C, 30.73; H, 2.72. IR (KBr pellets, cm^{-1}): 3209(br), 2955(w), 2883(w), 1531(s), 1431(s), 1319(m), 1213(w), 1148(w), 853(m), 781(m), 717(m), 662(m), 451(m).

$[Tb(ad)_{0.5}(phth)(H_2O)_2]$ (IV). The colorless prismatic crystals of IV (50% yield based on Tb) were obtained using the same synthetic procedure as that of I, but replaced Nd_2O_3 with Tb_4O_7 (0.0748 g, 0.400 mmol $Tb^{III/IV}$). Anal. Calcd for $C_{11}H_{12}O_8Tb$ (%): C, 30.64; H, 2.80. Found: C, 30.70; H, 2.78. IR (KBr pellets, cm^{-1}): 3412(br), 2957(w), 2881(w), 1549(s), 1433(s), 1319(m), 1213(w), 1151(w), 853(m), 781(m), 718(m), 660(w), 451(m).

$[Dy(ad)_{0.5}(phth)(H_2O)_2]$ (V). The colorless prismatic crystals of V (60% yield based on Dy) were obtained using the same synthetic procedure as that of I, but replaced Nd_2O_3 with Dy_2O_3 (0.0746 g, 0.400 mmol Dy^{III}). Anal. Calcd for $C_{11}H_{12}O_8Dy$ (%): C, 30.39; H, 2.78. Found: C, 30.31; H, 2.72. IR (KBr pellets, cm^{-1}): 3204(br), 2955(w), 2880(w), 1566(s), 1435(s), 1402(s), 1319(m), 1211(w), 1153(w), 853(m), 781(m), 716(m), 662(m), 451(m).

$[Er(ad)_{0.5}(phth)(H_2O)_2]$ (VI). The pale pink prismatic crystals of VI (45% yield based on Er) were obtained using the same synthetic procedure as that of I, but replaced Nd_2O_3 with Er_2O_3 (0.0765 g, 0.400 mmol Er^{III}). Anal. Calcd for $C_{11}H_{12}O_8Er$ (%): C, 30.06; H, 2.75. Found: C, 30.04; H, 2.66. IR (KBr pellets, cm^{-1}): 3422(br), 2955(w), 2876(w), 1566(s), 1437(s), 1404(s), 1321(m), 1211(w), 1150(w), 853(m), 781(m), 716(m), 662(m), 451(m).

$[Tm(ad)_{0.5}(phth)(H_2O)_2]$ (VII). The colorless prismatic crystals of VII (60% yield based on Tm) were obtained using the same synthetic procedure as that of I, but replaced Nd_2O_3 with Tm_2O_3 (0.0772 g, 0.400 mmol Tm^{III}). Anal. Calcd for $C_{11}H_{12}O_8Tm$ (%): C, 29.95; H, 2.74. Found: C, 29.95; H, 2.69. IR (KBr pellets, cm^{-1}): 3416(br), 2953(w), 2882(w), 1568(s), 1437(s), 1402(s), 1321(m), 1209(w), 1157(w), 854(w), 779(m), 716(m), 660(m), 451(w).

$[Eu_xTb_y(ad)_{0.5}(phth)(H_2O)_2]$ (VIII−X). The mixed Eu^{III}/Tb^{III} CPs were synthesized using the same synthetic procedure as that of I−VII, except for the use of Eu_2O_3/Tb_4O_7 mixtures: 0.0064 g Eu_2O_3 (0.0364 mmol Eu^{III})/0.0680 g Tb_4O_7 (0.364 mmol $Tb^{III/IV}$) for VIII, 0.0162 g Eu_2O_3 (0.0920 mmol Eu^{III})/0.0575 g Tb_4O_7 (0.308 mmol $Tb^{III/IV}$) for IX, and 0.0235 g Eu_2O_3 (0.134 mmol Eu^{III})/0.0499 g Tb_4O_7 (0.267 mmol $Tb^{III/IV}$) for X. According to the XRF and the EDS results, which are in excellent agreement with the employed amount in the syntheses (Table S1), the Eu^{III}:Tb^{III} mole ratios of 1:10 (VIII), 3:10 (IX) and 5:10 (X) were confirmed.

Single Crystal Structures Determination. The crystallographic data sets of I and III−VII were collected using a Bruker D8 Venture diffractometer equipped with a microfocus sealed tube X-ray source with graphite monochromatic Mo Kα radiation (λ = 0.71073 Å). Empirical absorption corrections were applied to all data using the SADABS program.[13] Crystallographic data sets of II and VIII were collected using a Rigaku FR-E Superbright rotating-anode X-ray source with a Mo-target (λ = 0.71075 Å) equipped with a Rigaku RAXIS VII imaging plate as a detector. The intensity data were collected by the ω-scan technique and empirically corrected for absorption. To study the temperature dependence in the structures of II, IV, and VIII, crystallographic data sets of these samples were collected at 303, 363, and 423 K using a Rigaku Mercury 2 CCD detector with the Synchrotron radiation (λ = 0.6997 Å) at the BL02B1 beamline in Spring-8 with the approval of the Japan Synchrotron Radiation Research

DOI: 10.1021/acs.inorgchem.7b03016
Inorg. Chem. 2018, 57, 2620−2630

Table 1. Crystallographic Data and Refinement Details for I–VIII

	I	II	III	IV	V	VI	VII	VIII
CCDC No.	1548035	1563675	1548036	1548037	1548038	1548039	1548040	-
Empirical formula	$C_{22}H_{24}O_{16}Nd_2$	$C_{11}H_{12}O_8Eu$	$C_{11}H_{12}O_8Gd$	$C_{11}H_{12}O_8Tb$	$C_{11}H_{12}O_8Dy$	$C_{11}H_{12}O_8Er$	$C_{11}H_{12}O_8Tm$	$C_{11}H_{12}O_8Eu_{0.088}Tb_{0.912}$
Formula weight	832.89	424.17	429.46	431.13	434.71	439.47	441.14	430.52
Temperature (K)	235(2)	173(2)	173(2)	173(2)	173(2)	173(2)	173(2)	173(2)
Crystal system	Triclinic	Monoclinic	Monoclinic	Monoclinic	Monoclinic	Monoclinic	Monoclinic	Monoclinic
Space group	*P*1 (No. 1)	$P2_1/n$ (No. 11)	$P2_1/n$ (No. 11)	$P2_1/n$ (No. 11)	$P2_1/n$ (No. 11)	$P2_1/n$ (No. 11)	$P2_1/n$ (No. 11)	$P2_1/n$ (No. 11)
a (Å)	6.2902(9)	13.3183(2)	13.2640(3)	13.2902(7)	13.2574(9)	13.2497(9)	13.3102(7)	13.2848(4)
b (Å)	8.8977(12)	5.9450(1)	5.9170(2)	5.9146(3)	5.8930(4)	5.8577(3)	5.8469(3)	5.9188(1)
c (Å)	12.4234(16)	15.5719(3)	15.4990(3)	15.5575(8)	15.5301(10)	15.5117(10)	15.5139(9)	15.5486(4)
α (deg)	77.185(3)	90.0000	90.0000	90.0000	90.0000	90.0000	90.0000	90.0000
β (deg)	78.934(3)	93.802(7)	93.9700(3)	94.0530(2)	94.2140(3)	94.3450(3)	94.4840(2)	94.035(7)
γ (deg)	70.880(4)	90.0000	90.0000	90.0000	90.0000	90.0000	90.0000	90.0000
V (Å^3)	635.203(15)	1230.23(4)	1213.50(5)	1219.86(11)	1210.02(14)	1200.45(13)	1203.65(11)	1219.56(5)
Z	1	4	4	4	4	4	4	4
Density (mg m^{-3})	2.177	2.290	2.351	2.347	2.386	2.432	2.434	2.348
Abs. coeff. (mm^{-1})	4.123	5.135	5.503	5.835	6.213	7.029	7.409	5.836
F(000)	404	820	824	828	832	840	844	828
Data/restraints/ parameters	7994/3/366	2813/0/183	2126/0/183	5118/0/183	4520/0/183	4730/0/183	2098/0/183	2794/0/183
Goodness-of-fit	0.995	1.122	1.114	1.030	1.033	1.040	1.152	1.075
Final R (all data)								
$R1^a$	0.0330	0.0300	0.0309	0.0363	0.0387	0.0340	0.0157	0.0291
$wR2^b$	0.0621	0.0566	0.0777	0.0530	0.0547	0.0523	0.0357	0.0540

$^aR_1 = \sum||F_0| - |F_c||/|F_0|$. $^bwR_2 = [\sum w(F_0^2 - F_c^2)^2/\sum w(F_0^2)_2]^{1/2}$.

Institute (JASRI). The intensity data were collected by the ω-scan technique and were processed with the Rapid Auto software program.

Every structure was solved by direct methods within the SHELXS program and refined on F^2 by the full-matrix least-squares technique using the SHELXL program via the Olex2 interface.[14,15] The crystallographic and refinement data for I–VIII are summarized in Table 1, while the temperature dependent data sets of II, IV, and VIII are available as Supporting Information (Table S2).

RESULTS AND DISCUSSION

Syntheses and Crystal Structures Description. With the use of lower temperature (120 °C) and shorter reaction time (24 h) relative to the conditions generally employed for the synthesis of LnCPs using mixed rigid and flexible polycarboxylates,[16−22] $[Nd_2(ad)(phth)_2(H_2O)_4]$ (I) and $[Ln(ad)_{0.5}(phth)(H_2O)_2]$ (II–VII) have been synthesized. Despite the addition of DABCO, it is not included in the yielded complexes but acting as a weak base deprotonating the organic ligands' carboxyl groups. According to the PXRD data (Figures S1 and S2), the yielded products from every synthesis are pure phases. Regarding VIII–X, their structures can be confirmed to be isostructural to those of II–VII based on both single crystal X-ray diffraction data (VIII; Table 1) and PXRD results (VIII–X; Figure S2). If the previously reported complexes are taken into account,[20] a series of LnCPs with the same ratio of Ln^{III}:ad^{2-}:$phth^{2-}$:H_2O is noticeably completed, manifesting in two different structures spanning across the lanthanide contraction from Pr^{III} to Tm^{III}.

The structure of $[Nd_2(ad)(phth)_2(H_2O)_4]$ (I) is revealed to be isostructural to $[Pr_2(ad)(phth)_2(H_2O)_4]$,[20] which is three-dimensional and nonporous. The asymmetric unit of I (Figure 1) is composed of two 9-fold coordinated Nd^{III} ions, a whole molecule of ad^{2-}, two molecules of $phth^{2-}$, and four coordinated water molecules. The coordination about both Nd^{III} ions is alike, featuring a distorted tricapped triangular prismatic geometry which is delineated by nine oxygen atoms, *TPRS*-$\{NdO_9\}$, from four $phth^{2-}$, one ad^{2-}, and two water molecules. Every two units of *TPRS*-$\{NdO_9\}$ share an edge to form a $\{Nd_2O_{16}\}$ dimer, each of which is linked to the neighboring dimers by $phth^{2-}$ using the μ_4-η^2:η^1:η^1:η^1 mode of coordination, leading to the formation of an infinite two-dimensional sheet in the *ab* plane. Both crystallographically independent $phth^{2-}$ ligands adopt the same μ_4-η^2:η^1:η^1:η^1 mode of coordination (Figure S3), which can be found only in I and the isostructural $[Pr_2(ad)(phth)_2(H_2O)_4]$.[20] These sheets are then transfixed into a three-dimensional framework by ad^{2-} via the μ_2-η^1:η^1:η^1:η^1 mode of coordination.

Contrary to the three-dimensional framework of I, II–VII feature a two-dimensional framework. The asymmetric units of every complex are similar, composed of one unique Ln^{III} ion which is 9-fold coordinated to a whole molecule of $phth^{2-}$, half a molecule of ad^{2-}, and two coordinated water molecules (Figure 2). The coordination about the Ln^{III} ion in II–VII is intriguingly the same as that of I, *i.e.* *TPRS*-$\{LnO_9\}$. The nine oxygen atoms of the *TPRS*-$\{LnO_9\}$ unit in II–VII are, however, contributed from one ad^{2-}, two water molecules, and three $phth^{2-}$, which is different from the case of I, of which four $phth^{2-}$ are included. This can be well accounted for by the lanthanide contraction.

Rather than the μ_4-η^2:η^1:η^1:η^1 bridging mode found in I, the $phth^{2-}$ in II–VII exhibits the μ_3-η^2:η^1:η^1:η^1 mode which is also very rare for LnCPs (Figure S3). This mode of coordination leads, however, to the formation of the edge-shared $\{Ln_2O_{16}\}$ dimer, which is linked to the adjacent dimers to form an infinite one-dimensional chain along the *b* axis (Figure 2). The established chains are further linked by ad^{2-}, of which the aliphatic chain conforms in an *anti-anti-anti* fashion, leading to the formation of two-dimensional puckered sheet in the *ab* plane. The conformations of the ad^{2-}aliphatic chain in I and II–VII are notably different (Figure S3). The constructed sheets are stacked in the *c* direction and interlocked by weak π–π

DOI: 10.1021/acs.inorgchem.7b03016
Inorg. Chem. 2018, 57, 2620−2630

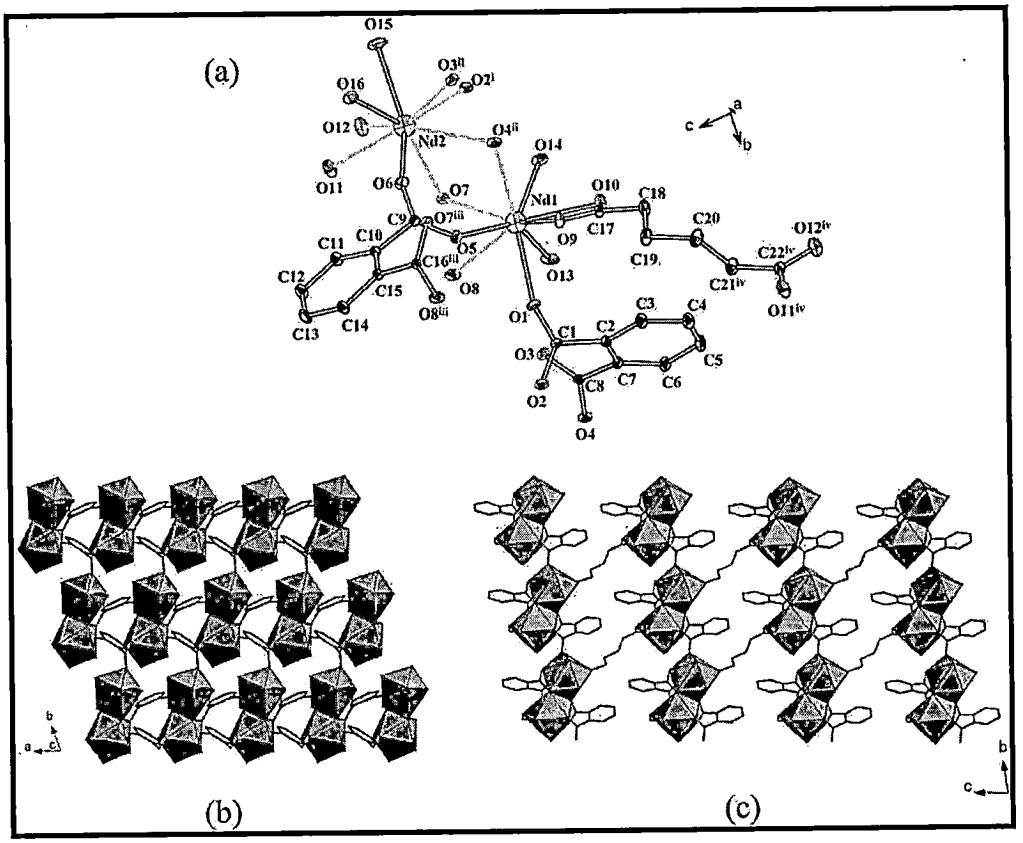

Figure 1. Illustrations of (a) the extended asymmetric unit drawn using 50% thermal ellipsoids with hydrogen atoms omitted, and the fabrication of (b) the two-dimensional and (c) the three-dimensional structures in I. Symmetry codes: (i) $1 + x, -1 + y, z$; (ii) $x, -1 + y, z$; (iii) $-1 + x, y, z$; (iv) $-1 + x, 1 + y, -1 + z$; (v) $1 + x, y, z$.

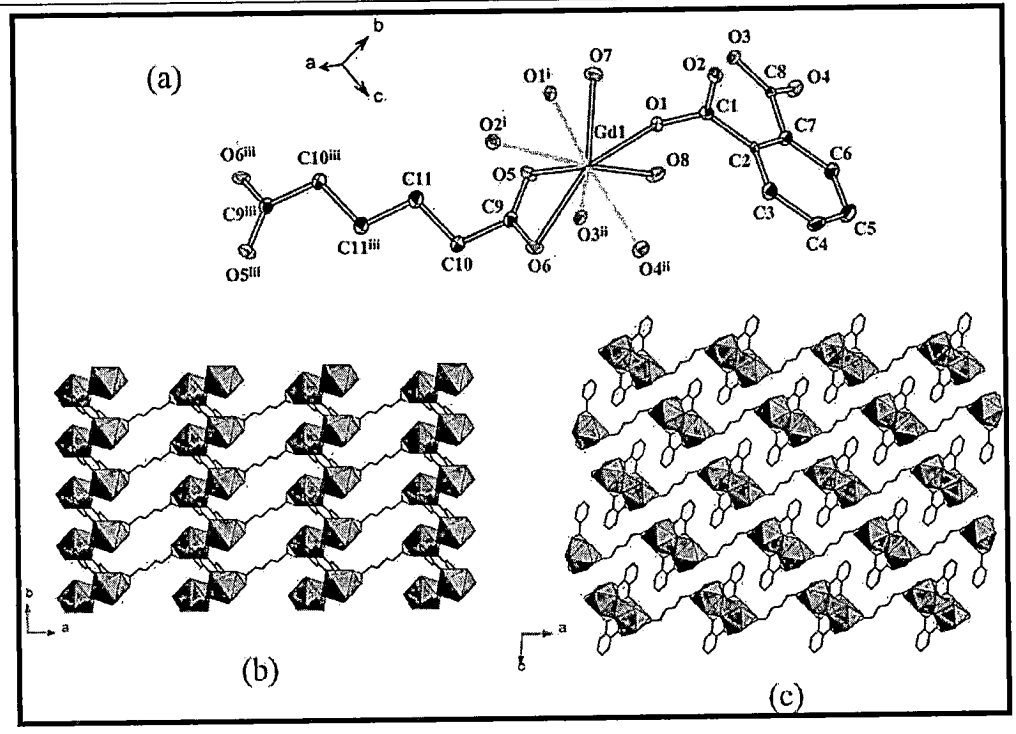

Figure 2. Illustrations of (a) the extended asymmetric unit drawn using 50% thermal ellipsoids with hydrogen atoms omitted, and the fabrication of (b) the two-dimensional structure and (c) the supramolecular packing in III (as a representative of II–VII).

DOI: 10.1021/acs.inorgchem.7b03016
Inorg. Chem. 2018, 57, 2620–2630

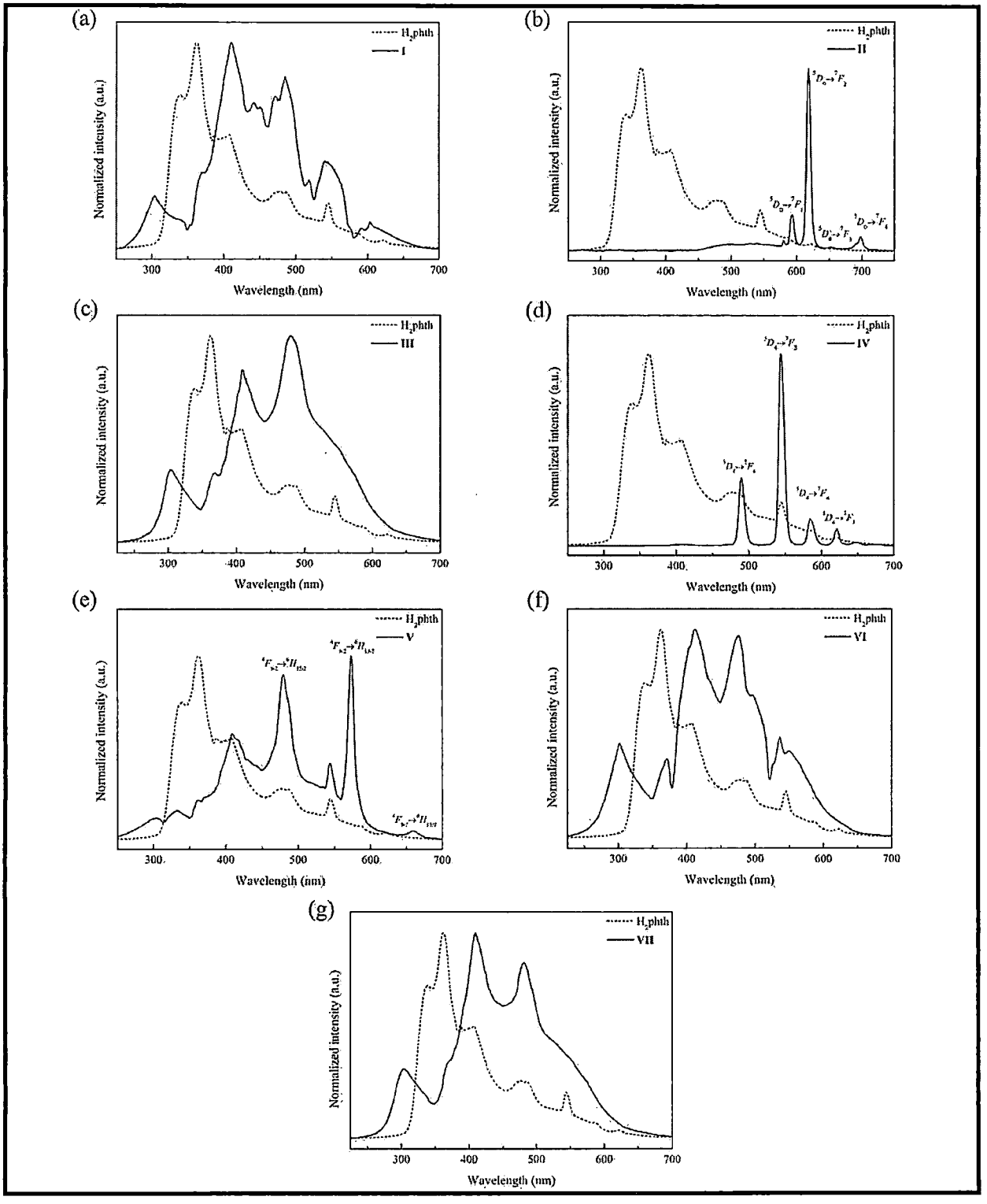

Figure 3. Emission spectra (solid line) of (a) I, (b) II, (c) III, (d) IV, (e) V, (f) VI, and (g) VII compared with that of H_2phth pro-ligand (dash line).

interactions between the phenyl rings of phth^{2-}. The centroid-to-centroid distances and the angles between the two phenyl rings for the $\pi-\pi$ interactions in II–VII are distributed in narrow ranges of 4.78–4.80 Å and 66.84–68.21°, respectively. Noticeably, there is not any hydrogen bonding interaction found in these complexes.

Room Temperature Photoluminescence Behavior of I–VII. Upon the excitation at 255 nm (Figure 3), H_2phth displays a

DOI: 10.1021/acs.inorgchem.7b03016
Inorg. Chem. 2018, 57, 2620–2630

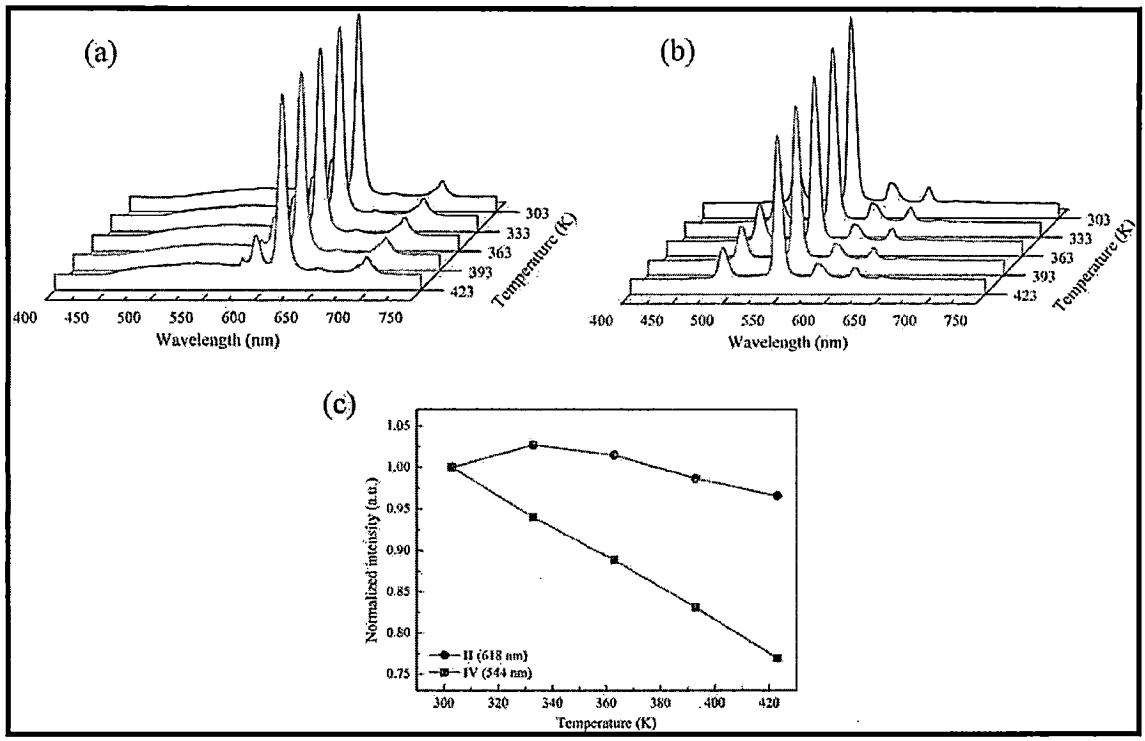

Figure 4. Emission spectra of (a) II and (b) IV recorded between 303 and 423 K excited at 365 nm, and (c) temperature dependent intensity of the emissions at 618 nm (for II) and 544 nm (for IV).

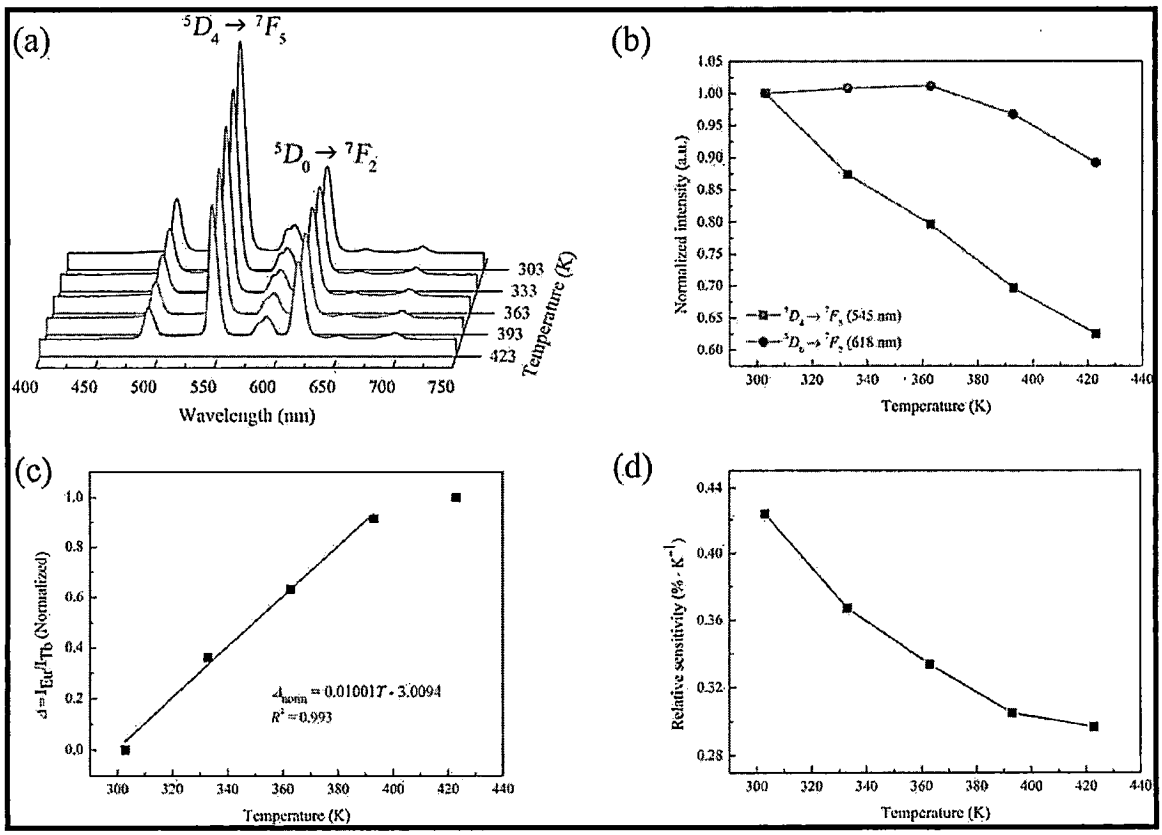

Figure 5. (a) Emission spectra of VIII excited at 365 nm with (b) the temperature-dependent normalized emission intensity of the $^5D_4 \rightarrow {}^7F_5$ and $^5D_0 \rightarrow {}^7F_2$, (c) temperature dependent Δ and linearly fitted curve, and (d) temperature dependent S_r.

DOI: 10.1021/acs.inorgchem.7b03016
Inorg. Chem. 2018, 57, 2620−2630

broad emission band with multiple maxima covering almost the entire spectrum attributed to $\pi^* \rightarrow \pi$ of the phenyl ring.[23] The $phth^{2-}$ centered emission remains vivid in the spectra of I and V–VII although the change in spectral profiles and the red shift are significant, which should be imparted from the increased molecular rigidity upon coordination.[24] According to the band theory,[7] the accumulation of these ligands in the frameworks of LnCPs can also be a significant cause. A distinct display of the ligand centered emission suggests nonetheless the poor energy transfer from $phth^{2-}$ to Nd^{III} (I), Dy^{III} (V), Er^{III} (VI), and Tm^{III} (VII). Characteristic emissions corresponding to $^4F_{9/2} \rightarrow {}^6H_J$ (J = 15/2, 13/2, 11/2) of Dy^{III} (V) are nevertheless visible.[25]

In contrast to I and V–VII, $phth^{2-}$ can effectively sensitize the emission in Eu^{III} (II) and Tb^{III} (IV) even at room temperature, which is reflected via the complete silence of the $phth^{2-}$ centered emission. The characteristic $^5D_0 \rightarrow {}^7F_J$ (J = 1–4) emissions of Eu^{III} are, as planned, distinct in the spectrum of II with the most intense $^5D_0 \rightarrow {}^7F_2$ red emission centered at 618 nm. The characteristic $^5D_4 \rightarrow {}^7F_J$ (J = 6–3) emissions of Tb^{III} are also explicit in the spectrum of IV, with the most intense $^5D_4 \rightarrow {}^7F_5$ green emission centered at 544 nm.[26] Since the lowest excited state energy of Gd^{III} is much higher than the lowest triplet band energy of any ligand, it is therefore common to estimate the triplet band energy of the organic antennae from the PL measurement of Gd^{III} complexes.[27,28] Based on the emission at 480 nm in the spectrum of III, the triplet band energy of 20,833 cm^{-1} can be estimated for $phth^{2-}$, which is in a suitable energy range to promote the sensitization of both Eu^{III} (II) and Tb^{III} (IV) according to Latva's empirical rule.[6]

Temperature Dependent Photoluminescence Behavior of II, IV, and VIII–X. The temperature dependent emission spectra of II and IV were collected in terms of intensity from 303 to 423 K (Figure 4). With increasing temperature, the intensity of the most intense $^5D_4 \rightarrow {}^7F_5$ (Tb^{III}; IV) emission centered at 544 nm dropped approximately 23% while that of the $^5D_0 \rightarrow {}^7F_2$ (Eu^{III}; II) emission centered at 618 nm negligibly changed. The reduction in intensity in the case of IV is commonly explained by thermal activated nonradiative decay.[29,30] Intriguingly, the effect of the thermal vibration of the coordinated water molecules about the Eu^{III} in II is silent. This should be due to the fact that these coordinated water molecules are transfixed in the frameworks and have limited freedom in vibration which is different from the molecular cases.[7] The fact that the coordinated water molecules in II and IV remain intact upon heating has been confirmed by the single crystal data collected at the BL02B1 beamline in Spring-8 (Table S2). This agrees well with thermogravimetric data (Figure S4) revealing no weight lost up to approximately 473 K (200 °C). The enlargement in the unit cell parameters and volumes of every complex is nonetheless apparent (Figure S5).

The apparently different behavior in temperature dependent emission between II (Eu^{III}) and IV (Tb^{III}) brought about the investigation of VIII–X as to if they could exhibit temperature dependent ratiometric photoluminescence behavior.[30−32] The remaining of the coordinated water molecules in VIII (as a representative of VIII–X) was similarly affirmed by the single crystal data (Table S2) and the thermogravimetric analysis (Figure S4). Although the temperature dependent PL spectra of VIII–X

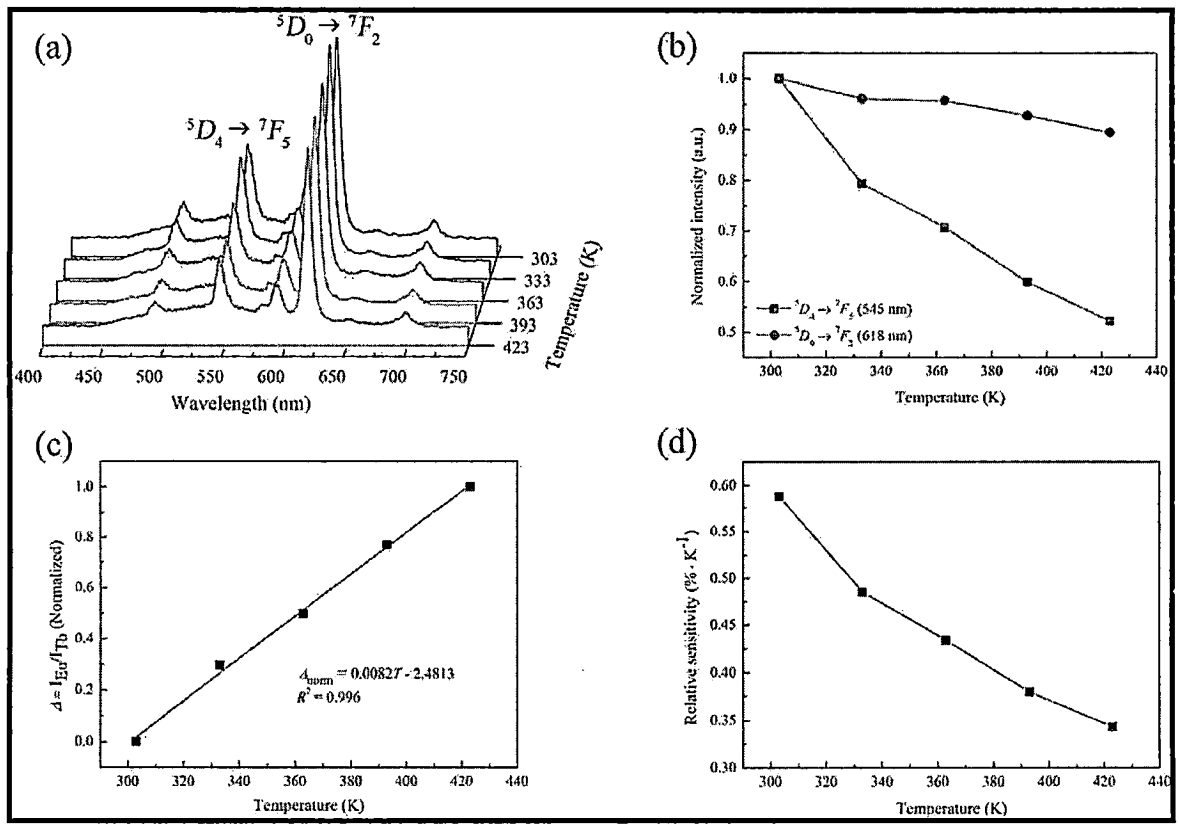

Figure 6. (a) Emission spectra of IX excited at 365 nm with (b) the temperature-dependent normalized emission intensity of the $^5D_4 \rightarrow {}^7F_5$ and $^5D_0 \rightarrow {}^7F_2$, (c) temperature dependent Δ and linearly fitted curve, and (d) temperature dependent S_r.

DOI: 10.1021/acs.inorgchem.7b03016
Inorg. Chem. 2018, 57, 2620–2630

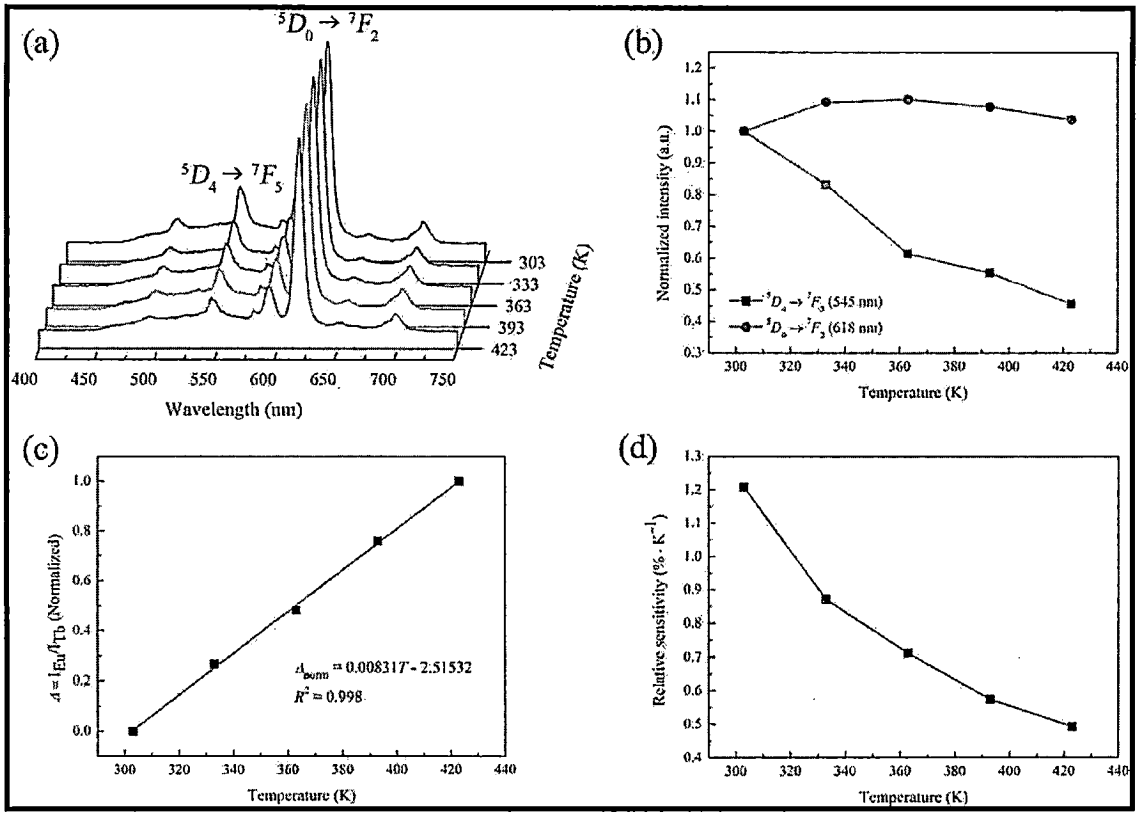

Figure 7. (a) Emission spectra of X excited at 365 nm with (b) the temperature-dependent normalized emission intensity of the $^5D_4 \rightarrow {}^7F_5$ and $^5D_0 \rightarrow {}^7F_2$, (c) temperature dependent Δ and linearly fitted curve, and (d) temperature dependent S_r.

look rather similar at first glance, they are significantly different. In the case of VIII ($1Eu^{III}$:$10Tb^{III}$; Figure S), the intensity of the $^5D_4 \rightarrow {}^7F_5$ (Tb^{III}) emission decreased approximately 37% from 303 K to 423 K, which is more drastic than that observed in IV (23%). The intensity of the $^5D_0 \rightarrow {}^7F_2$ (Eu^{III}) emission, however, negligibly increased and successively diminished at temperatures higher than 365 K. Based on the intensity ratio of $^5D_4 \rightarrow {}^7F_5$ (Tb^{III}) and $^5D_0 \rightarrow {}^7F_2$ (Eu^{III}), the thermometric parameter (Δ) has been calculated, revealing a temperature dependent linear correlation of Δ in a temperature range of 303–393 K (R^2 = 0.993). To evaluate the performance of VIII for use as a ratiometric photoluminescent thermometer, the relative sensitivity (S_r), which is defined as[4,5,33]

$$S_r = \frac{\partial\Delta/\partial T}{\Delta} \quad (1)$$

was calculated, revealing the maximum S_r value of 0.42%·K^{-1} at 303 K.

As the ratio of Eu^{III} was increased, i.e. $3Eu^{III}$:$10Tb^{III}$ (IX; Figure 6) and $5Eu^{III}$:$10Tb^{III}$ (X; Figure 7), the temperature dependent linear correlation of Δ was improved to cover the whole range of the experimented temperatures (303–423 K) with excellent fit to linearity; R^2 = 0.996 (IX) and 0.998 (X). This temperature range intriguingly overlaps with the physiological temperature range (298–328 K). The improvement of the maximum S_r values is also evident. While the S_r for IX brings off the maximum and minimum values of 0.59%·K^{-1} at 303 K and 0.34%·K^{-1} at 423 K, respectively, those for X are 1.21%·K^{-1} at 303 K and 0.49%·K^{-1} at 423 K, respectively. The maximum S_r value of X is intriguingly almost twice that of $Eu_{0.37}Tb_{0.63}$-BTC at similar temperature and corresponding temperature range (0.68%·K^{-1} at 313 K, 313–473 K).[34] Reports on S_r of over 1.2%·K^{-1} at temperatures over 300 K are rare, particularly for the physiological and higher temperature range.[4] According to the PXRD results (Figure S6), the stability of VIII–X over several multiple cycles of heating and cooling during the temperature dependent PL experiments as well as a few months of storage under ambient conditions has been confirmed to be significant.

With the increasing ratio of Eu^{III}, the intensity of the $^5D_4 \rightarrow {}^7F_5$ (Tb^{III}) emission notably declined to a greater extent: 23% (IV), 37% (VIII), 48% (IX), and 54% (X), indicating the energy transfer from Tb^{III} to Eu^{III} in these LnCPs.[10,30,35] This is consistent with the room temperature lifetime measurement results (Table 2), revealing the shorter lifetimes for the $^5D_4 \rightarrow {}^7F_5$ (Tb^{III}) transition with the increasing Eu^{III} ratio. The longer lifetimes were consistently apparent for the $^5D_0 \rightarrow {}^7F_2$ (Eu^{III}) emission in VIII–X compared to that of II although the alteration tendency was not apparent. The efficiency of the energy transfer (η_{ET}) from Tb^{III} to Eu^{III} in VIII–X was also estimated:[10]

$$\eta_{ET} = \frac{\tau_1^{-1} - \tau_0^{-1}}{\tau_1^{-1}} \quad (2)$$

where τ_1 and τ_0 are the lifetimes of the $^5D_4 \rightarrow {}^7F_5$ (Tb^{III}) emission with and without the acceptor (Eu^{III}), respectively. In a similar manner, the η_{ET} was improved with the increasing ratio of the Eu^{III} acceptor (Table 2), which is consistent with the

DOI: 10.1021/acs.inorgchem.7b03016
Inorg. Chem. 2018, 57, 2620–2630

Table 2. List of Photoluminescence Lifetimes and Energy Transfer Efficiencies (η_{ET}) at Room Temperature for II, IV, and VIII–X

	Lifetimes (ms)		
	544 nm	618 nm	η_{ET} (%)
$[Eu(ad)_{0.5}(phth)(H_2O)_2]$ (II)		0.441	
$[Tb(ad)_{0.5}(phth)(H_2O)_2]$ (IV)	1.21		
$[Ln(ad)_{0.5}(phth)(H_2O)_2]$ (Ln = $1Eu^{III}$:$10Tb^{III}$; VIII)	1.04	0.816	14.05
$[Ln(ad)_{0.5}(phth)(H_2O)_2]$ (Ln = $3Eu^{III}$:$10Tb^{III}$; IX)	0.834	0.613	31.07
$[Ln(ad)_{0.5}(phth)(H_2O)_2]$ (Ln = $5Eu^{III}$:$10Tb^{III}$; X)	0.795	0.555	41.65

tendency reported for other materials; $La_{2.85-x}GaGe_5O_{16}$:$0.15Tb^{III}$, xEu^{III} (x = 0, 0.05, 0.07, 0.10, and 0.20),[36] and $(Tb_{1-x}Eu_x)_2Mo_3O_{12}$ (x = 0, 0.1, 0.4, 0.6, 0.8, and 1).[37] Reports on the dependence of η_{ET} on the acceptor concentration are however scarce.

To investigate the performance of X in better detail, the values of temperature resolution (δT) in terms of standard deviation of the temperature read out and repeatability of the measurement (R) were additionally determined:

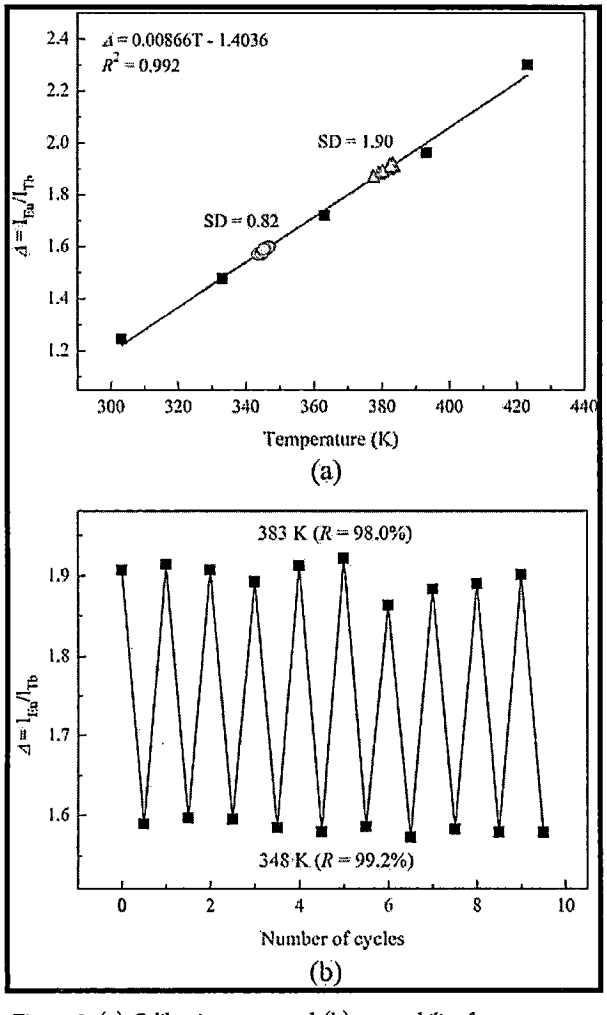

Figure 8. (a) Calibration curve and (b) repeatability for temperature measurement of X.

$$R = 1 - \frac{\max(|\Delta_c - \Delta_i|)}{\Delta} \quad (3)$$

where Δ_c is the thermometric parameter calculated from the calibration curve and Δ_i refers to the value of an individual measurement.[4] Based on ten consecutive temperatures read out at two different temperatures (Figure 8), both the R and δT values are exceptional. The potential of X as a high performance ratiometric luminescent thermometer is therefore illustrated.

CONCLUSIONS

In summary, the three-dimensional $[Nd_2(ad)(phth)_2(H_2O)_4]$ (I) and the two-dimensional $[Ln(ad)_{0.5}(phth)(H_2O)_2]$ (II-VII) have been constructed based on the mixed ligands approach. Every LnCP shows exceptional thermal stability without any liberation of the coordinated water molecules up to approximately 473 K (200 °C), although cell expansion is manifested. The effective sensitization of Eu^{III} and Tb^{III} in II, IV, and VIII-X by $phth^{2-}$ has evidently been illustrated and in good correspondence with the triplet band energy of $phth^{2-}$ estimated from the Gd^{III} complex (III). Complexes VIII–X exhibit temperature dependent ratiometric photoluminescence behavior rendered by the energy transfer process from Tb^{III} to Eu^{III}. The linear temperature dependence of Δ in the range of 303–423 K with the maximum S_r of 1.21%·K^{-1} (at 303 K) and excellent R and δT has been determined for X. In addition to temperature, the efficiency of the Tb^{III}-to-Eu^{III} energy transfer process as illustrated through the lifetime measurements depends, also, on the mole ratio of Eu^{III}:Tb^{III} in the frameworks. If framework structures and composition are considered as a matrix, which is well acknowledged as an important determinant governing the photoluminescence behavior of lanthanide complexes,[38,39] mixed ligand approaches, such as the work reported here, would be worthwhile for further investigation. Use of mixed ligands with varying degrees of sensitization in facile synthesis of new LnCPs is currently being studied by our group.

ASSOCIATED CONTENT

Supporting Information

The Supporting Information is available free of charge on the ACS Publications website at DOI: 10.1021/acs.inorgchem.7b03016.

PXRD, TGA, diagram showing coordination modes of ligands, EDS and XRF analyses, and crystallographic data for II, IV, and VIII at various temperatures (PDF)

Accession Codes

CCDC 1548035–1548040 and 1563675 contain the supplementary crystallographic data for this paper. These data can be obtained free of charge via www.ccdc.cam.ac.uk/data_request/cif, or by emailing data_request@ccdc.cam.ac.uk, or by contacting The Cambridge Crystallographic Data Centre, 12 Union Road, Cambridge CB2 1EZ, UK; fax: +44 1223 336033.

AUTHOR INFORMATION

Corresponding Author

*Tel: +66 5934 3341. Fax: +66 5389 2277. E-mail address: apinpus.rujiwatra@cmu.ac.th; apinpus.rujiwatra@gmail.com.

ORCID

Takumi Konno: 0000-0003-4612-5418

Apinpus Rujiwatra: 0000-0002-2364-4592

Notes

The authors declare no competing financial interest.

DOI: 10.1021/acs.inorgchem.7b03016
Inorg. Chem. 2018, 57, 2620–2630

■ ACKNOWLEDGMENTS

This work is funded by Chiang Mai University (Midcareer research grant) and the Thailand Research Fund (RSA5980026). T. Chuasaard thanks the Development and Promotion of Science and Technology Talents Project for graduate scholarship. Kitt Panyarat is acknowledged for help with the setting of temperature dependent photoluminescence measurements. Synchrotron experiments were carried out at the BL02B1 beamline in Spring-8 with the approval of the Japan Synchrotron Radiation Research Institute (JASRI; Proposal No. 2017A1037).

■ REFERENCES

(1) Brites, C. D. S.; Millán, A.; Carlos, L. D. Lanthanides in Luminescent Thermometry. *Handbook on the Physics and Chemistry of Rare Earths* **2016**, *49*, 339–427.

(2) Wang, X.-d.; Wolfbeis, O. S.; Meier, R. J. Luminescent probes and sensors for temperature. *Chem. Soc. Rev.* **2013**, *42*, 7834–7869.

(3) Cui, Y.; Xu, H.; Yue, Y.; Guo, Z.; Yu, J.; Chen, Z.; Gao, J.; Yang, Y.; Qian, G.; Chen, B. A Luminescent Mixed-Lanthanide Metal-Organic Framework Thermometer. *J. Am. Chem. Soc.* **2012**, *134*, 3979–3982.

(4) Rocha, J.; Brites, C. D. S.; Carlos, L. D. Lanthanide Organic Framework Luminescent Thermometers. *Chem. - Eur. J.* **2016**, *22*, 14782–14795.

(5) Cui, Y.; Zhu, F.; Chen, B.; Qian, G. Metal-organic frameworks for luminescence thermometry. *Chem. Commun.* **2015**, *51*, 7420–7431.

(6) Latva, M.; Takalo, H.; Mukkala, V.-M.; Matachescu, C.; Rodríguez-Ubis, J. C.; Kankare, J. Correlation between the lowest triplet state energy level of the ligand and lanthanide(III) luminescence quantum yield. *J. Lumin.* **1997**, *75*, 149–169.

(7) Einkauf, J. D.; Clark, J. M.; Paulive, A.; Tanner, G. P.; de Lill, D. T. A General Model of Sensitized Luminescence in Lanthanide-Based Coordination Polymers and Metal-Organic Framework Materials. *Inorg. Chem.* **2017**, *56*, 5544–5552.

(8) Miyata, K.; Konno, Y.; Nakanishi, T.; Kobayashi, A.; Kato, M.; Fushimi, K.; Hasegawa, Y. Chameleon Luminophore for Sensing Temperatures: Control of Metal-to-Metal and Energy Back Transfer in Lanthanide Coordination Polymers. *Angew. Chem., Int. Ed.* **2013**, *52*, 6413–6416.

(9) Cadiau, A.; Brites, C. D. S.; Costa, P. M. F. J.; Ferreira, R. A. S.; Rocha, J.; Carlos, L. D. Ratiometric Nanothermometer Based on an Emissive Ln^{3+}-Organic Framework. *ACS Nano* **2013**, *7*, 7213–7218.

(10) Zhao, D.; Rao, X.; Yu, J.; Cui, Y.; Yang, Y.; Qian, G. Design and Synthesis of an MOF Thermometer with High Sensitivity in the Physiological Temperature Range. *Inorg. Chem.* **2015**, *54*, 11193–11199.

(11) Ruan, L.; Wang, H.; Hao, Y.; Zhou, H.; Liu, X.; Xu, B. Intramolecular energy transfer models and energy band characteristic of rare-earth complexes with o-phthalic acid. *J. Lumin.* **2007**, *122–123*, 467–470.

(12) Kim; Suh, M.; Jung, D.-Y. Crystal Structure and Spectroscopic Study of Novel Two- and Three-Dimensional Photoluminescent Eu(III)-Adipate Compounds. *Inorg. Chem.* **2004**, *43*, 245–250.

(13) Sheldrick, G. M. *SADABS*; University of Göttingen: Germany, 1996.

(14) Sheldrick, G. A short history of SHELX. *Acta Crystallogr., Sect. A: Found. Crystallogr.* **2008**, *64*, 112–122.

(15) Dolomanov, O. V.; Bourhis, L. J.; Gildea, R. J.; Howard, J. A. K.; Puschmann, H. OLEX2: a complete structure solution, refinement and analysis program. *J. Appl. Crystallogr.* **2009**, *42*, 339–341.

(16) Hou, K.-L.; Bai, F.-Y.; Xing, Y.-H.; Wang, J.-L.; Shi, Z. A novel family of 3D photoluminescent lanthanide-bta-flexible MOFs constructed from 1,2,4,5-benzenetetracarboxylic acid and different spanning of dicarboxylate acid ligands. *CrystEngComm* **2011**, *13*, 3884–3894.

(17) Feng, X.; Zhao, J.; Liu, B.; Wang, L.; Ng, S.; Zhang, G.; Wang, J.; Shi, X.; Liu, Y. A Series of Lanthanide-Organic Frameworks Based on 2-Propyl-1H-imidazole-4,5-dicarboxylate and Oxalate: Syntheses, Structures, Luminescence, and Magnetic Properties. *Cryst. Growth Des.* **2010**, *10*, 1399–1408.

(18) Hou, K.-L.; Bai, F.-Y.; Xing, Y.-H.; Wang, J.-L.; Shi, Z. Synthesis, structure and luminescence of a new series of rigid-flexible lanthanide coordination polymers constructed from benzene sulfonic acid and glutaric acid. *Inorg. Chim. Acta* **2011**, *365*, 269–276.

(19) Wang, C.-G.; Xing, Y.-H.; Li, Z.-P.; Li, J.; Zeng, X.-Q.; Ge, M.-F.; Niu, S.-Y. A Series of Three-Dimensional Lanthanide-Rigid-Flexible Frameworks: Synthesis, Structure, and Luminescent Properties of Coordination Polymers with 2,5-Pyridine Dicarboxylic Acid and Adipic Acid. *Cryst. Growth Des.* **2009**, *9*, 1525–1530.

(20) Wang, Z.; Xing, Y.-H.; Wang, C.-G.; Sun, L.-X.; Zhang, J.; Ge, M.-F.; Niu, S.-Y. Synthesis, structure and luminescent properties of coordination polymers with 1,2-benzenedicarboxylic acid and a series of flexible dicarboxylate ligands. *CrystEngComm* **2010**, *12*, 762–773.

(21) Hu, D.-X.; Luo, F.; Che, Y.-X.; Zheng, J.-M. Construction of Lanthanide Metal-Organic Frameworks by Flexible Aliphatic Dicarboxylate Ligands Plus a Rigid m-Phthalic Acid Ligand. *Cryst. Growth Des.* **2007**, *7*, 1733–1737.

(22) Wang, P.; Fan, R.-Q.; Liu, X.-R.; Wang, L.-Y.; Yang, Y.-L.; Cao, W.-W.; Yang, B.; Hasi, W.; Su, Q.; Mu, Y. Two-/three-dimensional open lanthanide-organic frameworks containing rigid/flexible dicarboxylate ligands: synthesis, crystal structure and photoluminescent properties. *CrystEngComm* **2013**, *15*, 1931–1949.

(23) Yan, B.; Xu, B. Spectroscopic study on the photophysical properties of novel lanthanide complexes with long chain mono-L phthalate (L = hexadecyl, octadecyl and eicosyl). *Spectrochim. Acta, Part A* **2005**, *62*, 269–275.

(24) Xu, B.; Yan, B. Photoluminescence of Novel Zinc Complexes with Long-Chain Mono (Hexadecyl, Octadecyl, Eicosyl, and Docosyl) Phthalate. *Spectrosc. Lett.* **2006**, *39*, 237–248.

(25) Sahu, I. P.; Bisen, D. P.; Brahme, N.; Tamrakar, R. K.; Shrivastava, R. Luminescence studies of dysprosium doped strontium aluminate white light emitting phosphor by combustion route. *J. Mater. Sci.: Mater. Electron.* **2015**, *26*, 8824–8839.

(26) Ramya, A. R.; Varughese, S.; Reddy, M. L. P. Tunable white-light emission from mixed lanthanide (Eu^{3+}, Gd^{3+}, Tb^{3+}) coordination polymers derived from 4-(dipyridin-2-yl)aminobenzoate. *Dalton Trans.* **2014**, *43*, 10940–10946.

(27) Strasser, A.; Vogler, A. Phosphorescence of gadolinium(III) chelates under ambient conditions. *Inorg. Chim. Acta* **2004**, *357*, 2345–2348.

(28) Ramya, A. R.; Sharma, D.; Natarajan, S.; Reddy, M. L. P. Highly Luminescent and Thermally Stable Lanthanide Coordination Polymers Designed from 4-(Dipyridin-2-yl)aminobenzoate: Efficient Energy Transfer from Tb^{3+} to Eu^{3+} in a Mixed Lanthanide Coordination Compound. *Inorg. Chem.* **2012**, *51*, 8818–8826.

(29) Peng, H.; Stich, M. I. J.; Yu, J.; Sun, L.-n.; Fischer, L. H.; Wolfbeis, O. S. Luminescent Europium(III) Nanoparticles for Sensing and Imaging of Temperature in the Physiological Range. *Adv. Mater.* **2010**, *22*, 716–719.

(30) Yang, Y.; Chen, L.; Jiang, F.; Yu, M.; Wan, X.; Zhang, B.; Hong, M. A family of doped lanthanide metal-organic frameworks for wide-range temperature sensing and tunable white light emission. *J. Mater. Chem. C* **2017**, *5*, 1981–1989.

(31) Wang, K.-M.; Du, L.; Ma, Y.-L.; Zhao, J.-S.; Wang, Q.; Yan, T.; Zhao, Q.-H. Multifunctional chemical sensors and luminescent thermometers based on lanthanide metal-organic framework materials. *CrystEngComm* **2016**, *18*, 2690–2700.

(32) An, R.; Zhao, H.; Hu, H.-M.; Wang, X.; Yang, M.-L.; Xue, G. Synthesis, Structure, White-Light Emission, and Temperature Recognition Properties of Eu/Tb Mixed Coordination Polymers. *Inorg. Chem.* **2016**, *55*, 871–876.

(33) Rodrigues, M.; Piñol, R.; Antorrena, G.; Brites, C. D. S.; Silva, N. J. O.; Murillo, J. L.; Cases, R.; Díez, I.; Palacio, F.; Torras, N.; Plaza, J. A.; Pérez-García, L.; Carlos, L. D.; Millán, A. Implementing Thermometry on Silicon Surfaces Functionalized by Lanthanide-

DOI: 10.1021/acs.inorgchem.7b03016
Inorg. Chem. 2018, 57, 2620–2630

Doped Self-Assembled Polymer Monolayers. *Adv. Funct. Mater.* **2016**, *26*, 200−209.
(34) Wang, H.; Zhao, D.; Cui, Y.; Yang, Y.; Qian, G. A Eu/Tb-mixed MOF for luminescent high-temperature sensing. *J. Solid State Chem.* **2017**, *246*, 341−345.
(35) Wei, Y.; Sa, R.; Li, Q.; Wu, K. Highly stable and sensitive LnMOF ratiometric thermometers constructed with mixed ligands. *Dalton Trans.* **2015**, *44*, 3067−3074.
(36) Zhou, J.; Xia, Z. Multi-color emission evolution and energy transfer behavior of $La_3GaGe_5O_{16}$:Tb^{3+},Eu^{3+} phosphors. *J. Mater. Chem. C* **2014**, *2*, 6978−6984.
(37) Baur, F.; Glocker, F.; Justel, T. Photoluminescence and energy transfer rates and efficiencies in Eu^{3+} activated $Tb_2Mo_3O_{12}$. *J. Mater. Chem. C* **2015**, *3*, 2054−2064.
(38) Gavriluta, A.; Fix, T.; Nonat, A.; Slaoui, A.; Guillemoles, J.-F.; Charbonniere, L. J. Tuning the Chemical Properties of Europium Complexes as Downshifting Agents for Copper Indium Gallium Selenide Solar Cells. *J. Mater. Chem. A* **2017**, *5*, 14031−14040.
(39) Binnemans, K. Lanthanide-Based Luminescence Hybrid Materials. *Chem. Rev.* **2009**, *109*, 4283−4374.

DOI: 10.1021/acs.inorgchem.7b03016
Inorg. Chem. 2018, 57, 2620−2630

Influences of Mixed Antennae on Ratiometric Thermometry of Lanthanide Benzenedicarboxylates

Journal:	*Inorganic Chemistry*
Manuscript ID	Draft
Manuscript Type:	Article
Date Submitted by the Author:	n/a
Complete List of Authors:	Chuasaard, Thammanoon; Chiang Mai University Faculty of Science, Chemistry Ngamjarurojana, Athipong ; Chiang Mai University Faculty of Science, Physics and Materials Science Konno, Takumi; Graduate School of Science, Osaka University Rujiwatra, Apinpus; Chiang Mai University Faculty of Science, Chemistry

Influences of Mixed Antennae on Ratiometric Thermometry of Lanthanide Benzenedicarboxylates

Thammanoon Chuasaard,[a] Athipong Ngamjarurojana,[b] Takumi Konno[c] and Apinpus Rujiwatra[*,a,d]*

[a] Department of Chemistry, Faculty of Science, Chiang Mai University, Chiang Mai 50200 Thailand.

[b] Department of Physics and Materials Science, Faculty of Science, Chiang Mai University, Chiang Mai 50200 Thailand.

[c] Department of Chemistry, Graduate School of Science, Osaka University, Osaka 560-0043 Japan.

[d] Centre of Excellence in Materials Science and Materials Technology, Faculty of Science, Chiang Mai University, Chiang Mai 50200 Thailand.

ABSTRACT

With reference to a series of monometallic and bimetallic $[Ln(bdc)_{0.5}(phth)(H_2O)_2]$ (Ln = Eu (**I**), Tb (**II**), Ho (**III**), Er (**IV**), Tm (**V**), 1.10Eu : 10.0Tb (**VI**), 2.99Eu : 10.0Tb (**VII**), 4.84Eu : 10.0Tb (**VIII**), bdc^{2-} = 1,4-benzenedicarboxylate, $phth^{2-}$ = 1,2-benzenedicarboxylate), influences of the use of mixed bdc^{2-} and $phth^{2-}$ antennae on temperature dependent photoluminescent behavior and temperature sensing performance of the derived complexes are presented. The single crystal structures of **I-V** which are new complexes are included, revealing the unprecedented two-dimensional polymorphism in lanthanide coordination polymers. With reference to the temperature dependent behaviors of **I**, **II** and **VI-VIII**, the segregation of the sensitization processes which imparted unfavorable impact on temperature sensing performance

is demonstrated. An exceptional repeatability (> 98%) as a characteristic feature of photoluminescent sensing and the dependency of the inter-lanthanide energy transfer on the acceptor content are then proposed and discussed.

KEYWORDS Lanthanide; Luminescence; Coordination polymer; Polymorphism; Thermometry

1. Introduction

Ratiometric photoluminescent temperature sensing based on lanthanide coordination polymers (LnCPs) has been profoundly investigated in recent years. A great deal of attention stems from the privileges of being self-reference, fast response, and exceptional accuracy and precision at particularly sub-micrometer scale.[1-3] The sensing performance of LnCPs can however be unforeseeable as several competitive mechanisms are involved, *e.g.* antenna-to-Ln energy transfer or so-called sensitization, Ln-to-antenna back-energy transfer, inter-Ln energy transfer and non-radiative decay.[3-13] Intriguingly, reports on the synergistic or segregation of these processes due to the co-existing of mixed antennae as well as their influences on sensing performance are still deficient to draw any conclusion. In some cases, unexpected results are unfold. For example, a dilution of 1,2-benzenedicarboxylate ($phth^{2-}$) antenna by an ineffective adipate (ad^{2-}) in $[Ln(ad)_{0.5}(phth)(H_2O)_2]$ unanticipatedly promoted their temperature sensing performance.[14] To compare the influences of mixed antennae on sensing performance of LnCPs, the employed LnCPs should be isostructural to eliminate structural factors. However, isostructural LnCPs built up of different combinations of ligands are thus far unknown of.

Inspired by $[Ln(ad)_{0.5}(phth)(H_2O)_2]$,[14] a series of $[Ln(bdc)_{0.5}(phth)(H_2O)_2]$ (bdc^{2-} = 1,4-benzenedicarboxylate; Ln = Eu^{III} (**I**), Tb^{III} (**II**), Ho^{III} (**III**), Er^{III} (**IV**), Tm^{III} (**V**), Gd^{III} (**IX**)), were

fabricated. Single crystal structures of **I-V** were determined revealing the closely relevant framework structures to $[Ln(ad)_{0.5}(phth)(H_2O)_2]$.[14] Details on structural relation of the two series of LnCPs are discussed. Temperature dependent photoluminescent behavior of the titled complexes were investigated and are discussed. In addition, the bimetallic $[Ln(bdc)_{0.5}(phth)(H_2O)_2]$ (Ln = 1.10Eu^{III} : 10.0Tb^{III} (**VI**), 2.99Eu^{III} : 10.0Tb^{III} (**VII**), 4.84Eu^{III} : 10.0Tb^{III} (**VIII**)) were synthesized and characterized. The influences of mixed antennae on the Tb^{III}-to-Eu^{III} energy transfer and consequently the ratiometric temperature-sensing performance were studied.

2. Experimental

2.1 Materials and instrumentation

All chemicals were obtained commercially and used without further purification: Eu_2O_3 (Merck, 99%), Gd_2O_3 (Sigma-Aldrich, 99.9%), Tb_4O_7 (Sigma-Aldrich, 99.9%), Ho_2O_3 (Smart Elements, 99.99%), Er_2O_3 (Fluka, 99.9%), Tm_2O_3 (Merck), HNO_3 (Carlo Erba, 65%), 1,2-benzenedicarboxylic acid (H_2phth; $C_8H_6O_4$, BDH, 99%), 1,4-benzenedicarboxylic acid (H_2bdc; $C_8H_6O_4$, GTI Laboratories Supplies, 99.9%), and 1,4-diazabicyclo[2.2.2]octane (DABCO; Sigma-Aldrich, 98%).

Infrared (IR) spectra were collected using a Bruker Tensor 27 FT-IR instrument and KBr discs (BDH, 98.5%). Powder X-ray diffraction (PXRD) data were recorded using a Rigaku Mini Flex II X-ray diffractometer operated with Cu *K*α radiation (λ = 1.5418 Å, 40 kV, 15 mA). The Eu^{III} and Tb^{III} contents of the bimetallic complexes were determined using an energy dispersive X-ray spectroscopy microanalyzer (EDXA) provided with a JSM 5910 low vacuum scanning electron microscope. The UV-Vis spectra were collected using a Perkin Elmer Lambda25 UV-

Vis spectrophotometer. Photoluminescent spectra were collected on ground crystals using an ASEQ LR-1T broad range spectrophotometer equipped with a fiber coupled CCD detector and an LTB MNL-100 pulsed nitrogen laser excitation source (337 nm). The temperature controlling compartment was installed using a Dual Digital F/C PID temperature controller furnace Kiln oven, type K thermocouple and a BOXCAR data collecting analysis system. The stray light was filtered out using a UV optical band pass (<400 nm).

2.2 Hydrothermal synthesis and crystal growth of I-IX

$[Eu(bdc)_{0.5}(phth)(H_2O)_2]$ (I). Solution **A**: Eu_2O_3 (0.0704 g, 0.400 mmol) was dissolved in 1.00 mL of HNO_3 solution (7.20 mol·L^{-1}). The pH of the solution was then adjusted to 5 using NaOH solution (10.00 mol·L^{-1}). Solution **B**: H_2phth (0.0664 g, 0.400 mmol), H_2bdc (0.0665 g, 0.400 mmol) and DABCO (0.0448 g, 0.400 mmol) were dissolved in 7.00 mL of deionized water. Solutions **A** and **B** were mixed in a 25 mL Teflon lined hydrothermal reactor and made up to 10.00 mL by deionized water. After carefully sealed, the reaction was carried out under autogenous pressure generated at 180 °C for 24 h. Yield: 80% based on Eu. IR (cm^{-1}): 3600-3120(br), 3073(w), 2966(w), 1543(s), 1427(s), 1294(w), 1151(w), 1088(w), 843(m), 750(m), 662(w), 532(w), 440(w).

$[Tb(bdc)_{0.5}(phth)(H_2O)_2]$ (II). The same procedure as that of **I** was adopted but the metal source was changed to Tb_4O_7 (0.0748 g, 0.400 mmol). Yield: 75% based on Tb. IR (cm^{-1}): 3620-3130(br), 3061(w), 2963(w), 1562(s), 1402(s), 1150(w), 1088(w), 847(m), 752(m), 660(w), 532(w), 440(w).

$[Ho(bdc)_{0.5}(phth)(H_2O)_2]$ (III). The same procedure as that of **I** was adopted but the metal source was changed to Ho_2O_3 (0.0756 g, 0.400 mmol). Yield: 60% based on Ho. IR (cm^{-1}):

3620-3130(br), 3061(w), 2963(w), 1562(s), 1402(s), 1150(w), 1088(w), 847(m), 752(m), 660(w), 532(w), 440(w).

$[Er(bdc)_{0.5}(phth)(H_2O)_2]$ (IV). The same procedure as that of **I** was adopted but the metal source was changed to Er_2O_3 (0.0766 g, 0.400 mmol). Yield: 65% based on Er. IR (cm^{-1}): 3620-3130(br), 3061(w), 2963(w), 1562(s), 1402(s), 1150(w), 1088(w), 847(m), 752(m), 660(w), 532(w), 440(w).

$[Tm(bdc)_{0.5}(phth)(H_2O)_2]$ (V). The same procedure as that of **I** was adopted but the metal source was changed to Tm_2O_3 (0.0772 g, 0.400 mmol). Yield: 75% based on Tm. IR (cm^{-1}): 3620-3130(br), 3061(w), 2963(w), 1562(s), 1402(s), 1150(w), 1088(w), 847(m), 752(m), 660(w), 532(w), 440(w).

$[Gd(bdc)_{0.5}(phth)(H_2O)_2]$ (IX). The same procedure as that of **I** was adopted but the metal source was changed to Gd_2O_3 (0.0725 g, 0.400 mmol). IR (cm^{-1}): 3620-3130(br), 3061(w), 2963(w), 1562(s), 1402(s), 1150(w), 1088(w), 847(m), 752(m), 660(w), 532(w), 440(w). Since crystal structure of **IX** has been previously reported,[15] its structure and purity were characterized by PXRD.

$[Eu_xTb_{1-x}(bdc)_{0.5}(phth)(H_2O)_2]$ (VI-VIII). The same procedure as that of **I** was adopted, except for the use of Eu_2O_3/Tb_4O_7 mixtures. The mole ratios of Eu_2O_3 : Tb_4O_7 were: $1Eu_2O_3$: $5Tb_4O_7$ (1Eu:10Tb, **VI**), $3Eu_2O_3$: $5Tb_4O_7$ (3Eu:10Tb, **VII**), and $1Eu_2O_3$: $1Tb_4O_7$ (5Eu:10Tb, **VIII**).

2.3 Single crystal structure determination of I-V

Crystallographic data sets of new complexes **I-V** were collected at 293(2) *K* using a Rigaku XtaLAB SuperNova Diffractometer equipped with a single micro-focus sealed X-ray

tube (Mo K_α, λ = 0.71073 Å) and a Hypix Hybrid Pixel Array detector. Data collection and reduction were performed using CrysAlisPro 1.171.39.46,[16] and empirical absorption corrections were applied to all data sets using spherical harmonics, implemented in SCALE3 ABSPACK scaling algorithm.[16] The structures were solved by intrinsic phasing methods within the SHELXT program[17] and refined on F^2 by the full-matrix least squares technique using the SHELXL program[17] *via* the Olex2 interface.[18] The crystallographic and refinement data for **I-V** are summarized in Table 1.

3. Results and discussion

3.1 Crystal Structure Description of I-V

The crystal structures of **I-V** are revealed to be isostructural with $[Gd(bdc)_{0.5}(phth)(H_2O)_2]$ and $[Dy(bdc)_{0.5}(phth)(H_2O)_2]$ yielded from different synthesis approach,[15] featuring a non-porous three-dimensional framework. More importantly, **I-V** exhibit significant correlation with $[Ln(ad)_{0.5}(phth)(H_2O)_2]$ (Ln = Eu, Gd, Tb, Dy, Er and Tm; H_2ad = adipic acid)[14] in views of both structure and photoluminescent property.

The asymmetric units of **I-V** are alike comprising an eight-fold coordinated Ln^{III} bearing a distorted dodecahedral geometry, denoted as *DD*-{TbO_8}, of which the eight oxygen atoms are from four equivalent $phth^{2-}$, one bdc^{2-} and two water molecules (Figure 1). Due to the μ_4-η^1:η^1:η^1:η^1 coordination mode adopted by $phth^{2-}$, each *DD*-{TbO_8} unit exists as a discreet moiety and is linked to the other eight equivalents through 8×{OCO} bridges of four surrounding $phth^{2-}$ to form a two-dimensional $[Ln(phth)(H_2O)_2]$ sheet in the *ab* plane (Figure 2). The derived sheet can be characterized as a uninodal 4-connected **sql/Shubnikov** with $\{4^4.6^2\}$ point symbol.

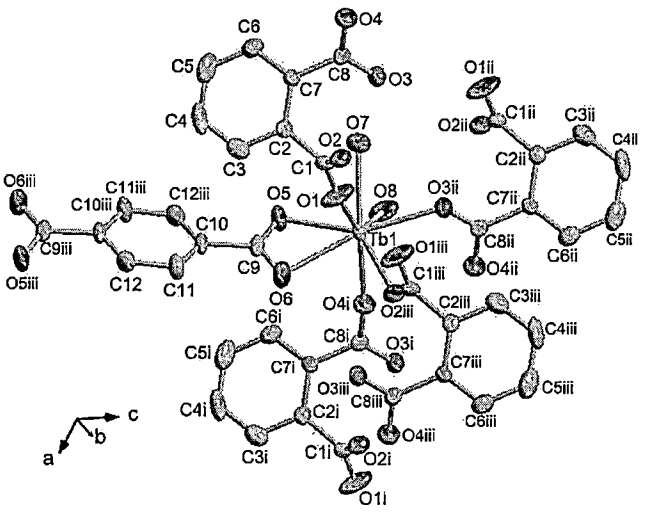

Figure 1. An extended asymmetric unit of **II** as a representative of **I-VIII**, drawn using 70% thermal ellipsoids with H atoms omitted. Symmetry codes: (i) 1+x, 1+y, z (ii) 1-x, 1-y, 2-z (iii) 2-x, 1-y, 1-z.

The completely deprotonated $phth^{2-}$ discernibly tends to provide two-dimensional framework structure of which the architecture is diversified by the adopted coordination mode (Figure S1). Whilst the μ_4-η^1:η^1:η^1:η^1 mode of $phth^{2-}$ leads to a discrete *DD*-{LnO_8} unit as found in **I-V**, the μ_3-η^2:η^1:η^1:η^1 mode in [Ln(ad)$_{0.5}$(phth)(H_2O)$_2$] renders an edge-sharing dimer built up of two *TPRS*-{LnO_9} units.[14] Despite the differences in the primary structure-building units, *i.e.* a discrete *DD*-{LnO_8} and a dimer of two *TPRS*-{LnO_9}, and the three-dimensional framework topology between **I-V** and [Ln(ad)$_{0.5}$(phth)(H_2O)$_2$], chemical composition of the derived sheets of both series is identical, *i.e.* [Ln(phth)(H_2O)$_2$]. The [Ln(phth)(H_2O)$_2$] sheet in **I-V** can therefore be regarded as a polymorph of the [Ln(phth)(H_2O)$_2$] sheet in [Ln(ad)$_{0.5}$(phth)(H_2O)$_2$], which is evidently induced by different coordination modes of $phth^{2-}$. This type of polymorphism which is accounted for by versatile coordination modes of the bridging ligand is markedly atypical for LnCPs.

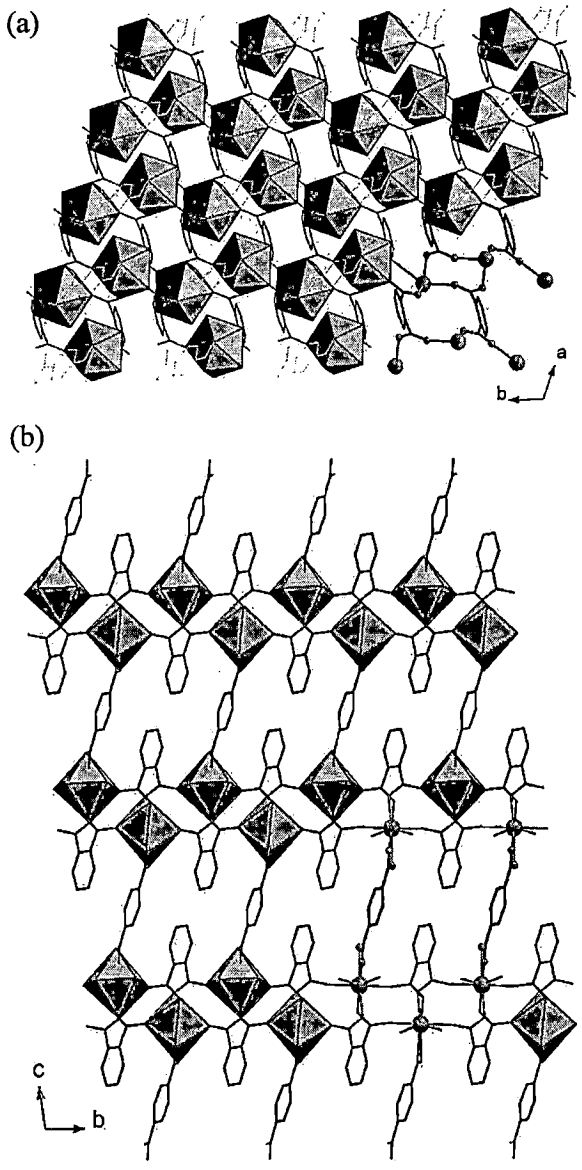

Figure 2. Depictions of (a) two-dimensional and (b) three-dimensional framework structures of **II** and coordination modes adopted by the occluded ligands. H atoms are omitted for clarity.

The $[Ln(phth)(H_2O)_2]$ sheets in structures **I-V** are collectively pillared by bdc^{2-} in *c* direction through the chelating μ_2-η^1:η^1:η^1:η^1 mode, giving rise to the three-dimensional $[Ln(bdc)_{0.5}(phth)(H_2O)_2]$ (Figure 2). Compared with $[Ln(ad)_{0.5}(phth)(H_2O)_2]$,[14] role of the longer

and more flexible ad^{2-} resembles that of the relatively rigid and short bdc^{2-}, *i.e.* being a pillar connecting the polymorphic $[Ln(phth)(H_2O)_2]$ sheets. The two linear bridging bdc^{2-} and ad^{2-} intriguingly adopt the same chelating μ_2-η^1:η^1:η^1:η^1 mode of coordination, although the shorter bdc^{2-} instigates the non-porosity in **I-V**. This is an explicit evidence for the introduction of porosity in pillared layered structures of LnCPs by the pillaring ligands. According to the PXRD (Figure S2), structures of **I-V** deduced from single crystal data were confirmed to be appropriate representatives of the synthesized samples all of which could be yielded as pure phases.

3.2 Photoluminescence Behaviors of I-V

3.2.1 Sensitization Efficiency of Co-existing $phth^{2-}$ and bdc^{2-}. Upon the excitation at 337 nm, the emission spectra of **III-V** were dominated by a broad feature of the ligand-centered $\pi^*\rightarrow\pi$ emissions (Figure 3). The strong and intense Eu^{III}:$^5D_0\rightarrow{}^7F_J$ (J=1-4) (**I**) and Tb^{III}:$^5D_4\rightarrow{}^7F_J$ (J=6-3) (**II**) emissions were, on the other hand, explicit without any trait of the $\pi^*\rightarrow\pi$ emissions. Since both $phth^{2-}$ and bdc^{2-} are well acknowledged for being effective antennae with respect to both Eu^{III} and Tb^{III},[8] the co-existence of both antennae should therefore ensure the effective sensitization in **I** and **II**.

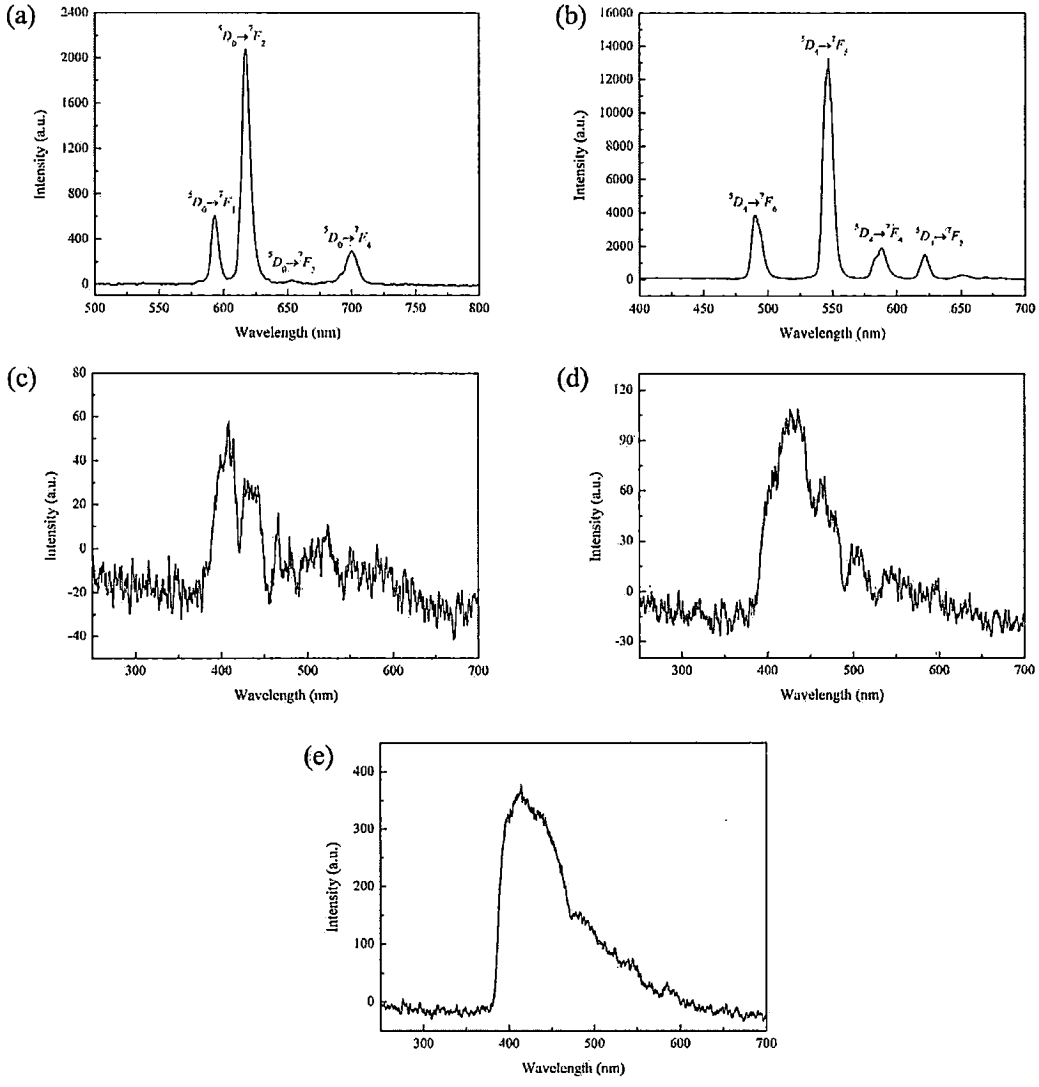

Figure 3. Emission spectra of (a) **I** (b) **II** (c) **III** (d) **IV** and (e) **V**.

According to an antenna model, the primary factor governing effective sensitization is an appropriate energy gap between the triplet state of the organic antenna and the accepting levels of Ln^{III}, *e.g.* $\Delta\{E(^3T)\text{-}E(Eu^{III}:{}^5D_J)\}$ (J = 0-2) and $\Delta\{E(^3T)\text{-}E(Tb^{III}:{}^5D_J)\}$ (J = 3, 4).[7,19] The $E(^3T)$ of an antenna transfixed in coordination framework however differs from that of the corresponding molecular state and depends on its local environment in the framework. To

estimate the E(^{3}T) of phth^{2-} and bdc^{2-} in the titled complexes, [Gd(bdc)$_{0.5}$(phth)(H$_2$O)$_2$] (**IX**) was synthesized using the same synthesis procedure as that of **I-V**. Its photoluminescence spectrum was collected (Supplementary Figure S3). With reference to two emissions at 415 and 466 nm, the E(^{3}T) of 24,096 and 21,459 cm^{-1} could be estimated for phth^{2-} and bdc^{2-}, both of which are consistent with the previously reported values: 23,810 cm^{-1} from [Gd$_2$(phth)$_2$(H$_2$O)$_2$],[6] 23,256 cm^{-1} from [Gd$_2$(bdc)$_2$(H$_2$O)$_2$],[6] 22,220 cm^{-1} from [Gd$_2$(phth)$_3$(H$_2$O)$_3$] and [Gd$_2$(bdc)$_3$(DEF)$_2$(EtOH)$_2$]·2DEF.[8] Contribution of structural diversity to discrepancy of E(^{3}T) is clearly displayed. In comparison with the primary accepting levels of Eu^{III} (^5D_J, J= 0-2) and Tb^{III} (^{5}D$_4$),[20] phth^{2-} and bdc^{2-} should be able to facilitate the *f-f* emissions in both **I** and **II**.

3.2.2 Temperature-dependent Photoluminescence of I, II, VI-VIII. Upon the heating of **I** and **II** from 303 to 423 *K* (Figure 4), intensity of both the red Eu^{III}:$^5D_0\rightarrow{}^7F_2$ (617 nm, **I**) and the green Tb^{III}:$^5D_4\rightarrow{}^7F_5$ (547 nm, **II**) emissions significantly declined, indicating the gravity of the thermally-induced non-radiative decay in both complexes. According to an antenna model and the Latva proposal,[7,8] a reduction in intensity of Tb^{III}:$^5D_4\rightarrow{}^7F_5$ (**II**) should attribute to the energy-back transfer owing to a small Δ{E(^{3}T,bdc^{2-})-E(Tb^{III}:^{5}D$_4$)}. Intensity declining in the Eu^{III}:$^5D_0\rightarrow{}^7F_2$ (**I**) case may however ascribe to a large Δ{E(^{3}T,phth^{2-})-E(Eu^{III}:^{5}D$_0$)} which detracts the sensitization and allows intra-ligand non-radiative decay.

To appraise the Tb^{III}-to-Eu^{III} energy transfer, the bimetallic [Tb$^{III}_x$Eu$^{III}_{1-x}$(bdc)$_{0.5}$(phth)(H$_2$O)$_2$] (**VI-VIII**) were synthesized. Structures of **VI-VIII** were ensured to be isostructural with **I** and **II** by PXRD (Supplementary Figure S4). According to EDXA microanalysis (Supplementary Figure S5), the Eu^{III}-to-Tb^{III} mole ratios are 1.10Eu^{III}-to-10.0Tb^{III} (**VI**), 2.99Eu^{III}-to-10.0Tb^{III} (**VII**) and 4.84Eu^{III}-to-10.0Tb^{III} (**VIII**). In accordance with these

results, the following formulas can be concluded; $[Eu_{0.100}Tb_{0.900}(ad)_{0.5}(phth)(H_2O)_2]$ **(VI)**, $[Eu_{0.230}Tb_{0.770}(ad)_{0.5}(phth)(H_2O)_2]$ **(VII)** and $[Eu_{0.330}Tb_{0.670}(ad)_{0.5}(phth)(H_2O)_2]$ **(VIII)**.

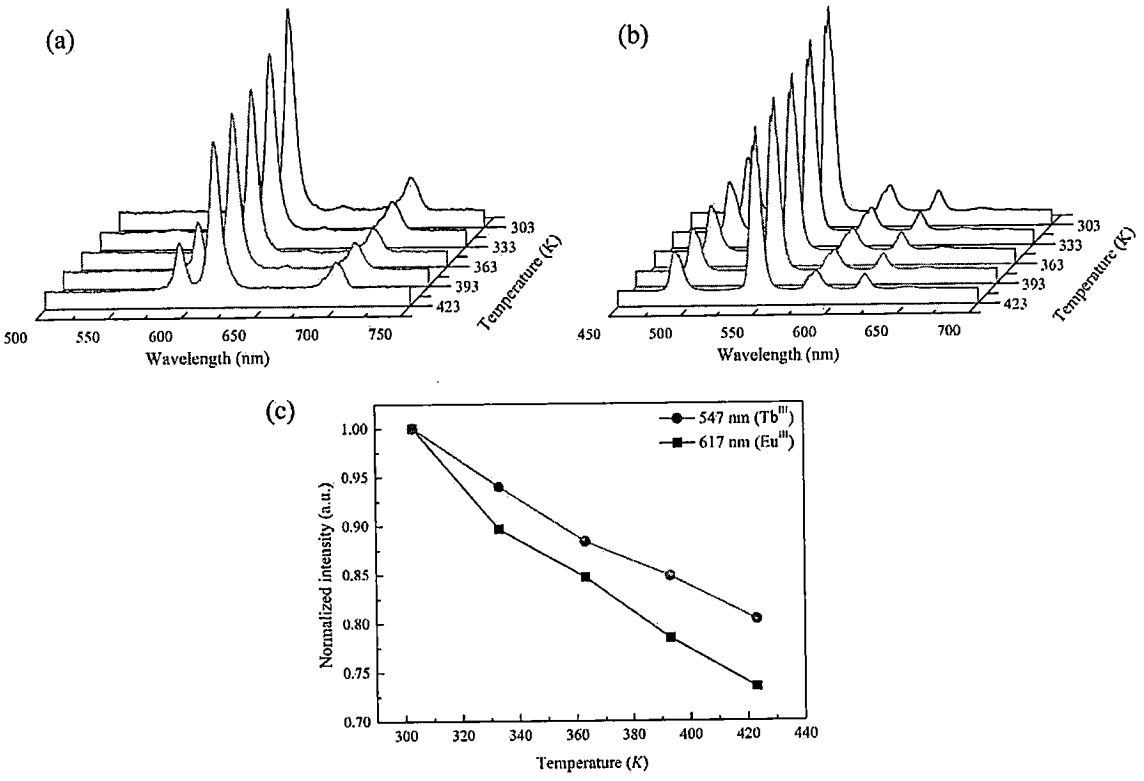

Figure 4. Temperature dependent emission spectra of (a) **I** and (b) **II**, with (c) the corresponding temperature dependent intensities of Eu^{III}:$^5D_0 \rightarrow {}^7F_2$ (617 nm, **I**) and Tb^{III}:$^5D_4 \rightarrow {}^7F_5$ (547 nm, **II**).

Based upon intensities of the red Eu^{III}:$^5D_0 \rightarrow {}^7F_2$ and the green Tb^{III}:$^5D_4 \rightarrow {}^7F_5$ emissions, the grievous effect of heating on photoluminescent properties of the **VI-VIII** were displayed (Figure 5). The declining intensity of the green emission was markedly more substantial than the red emission, which is contrary to the **I-II** cases. The heating effect became successively more drastic with the rising content of Eu^{III}, *i.e.* from 34% **(VI)** to 49% **(VII)** and 51% **(VIII)**. A reduction of the red emission of **VI** containing the lowest Eu^{III} content was less than 10% compared with approximately 20% in the cases of **VII** and **VIII**. These results manifest the Tb^{III}-

to-Eu^{III} energy transfer in **VI-VIII**, and the dependence of the process efficiency on the concentration of Eu^{III}, which is an acceptor.

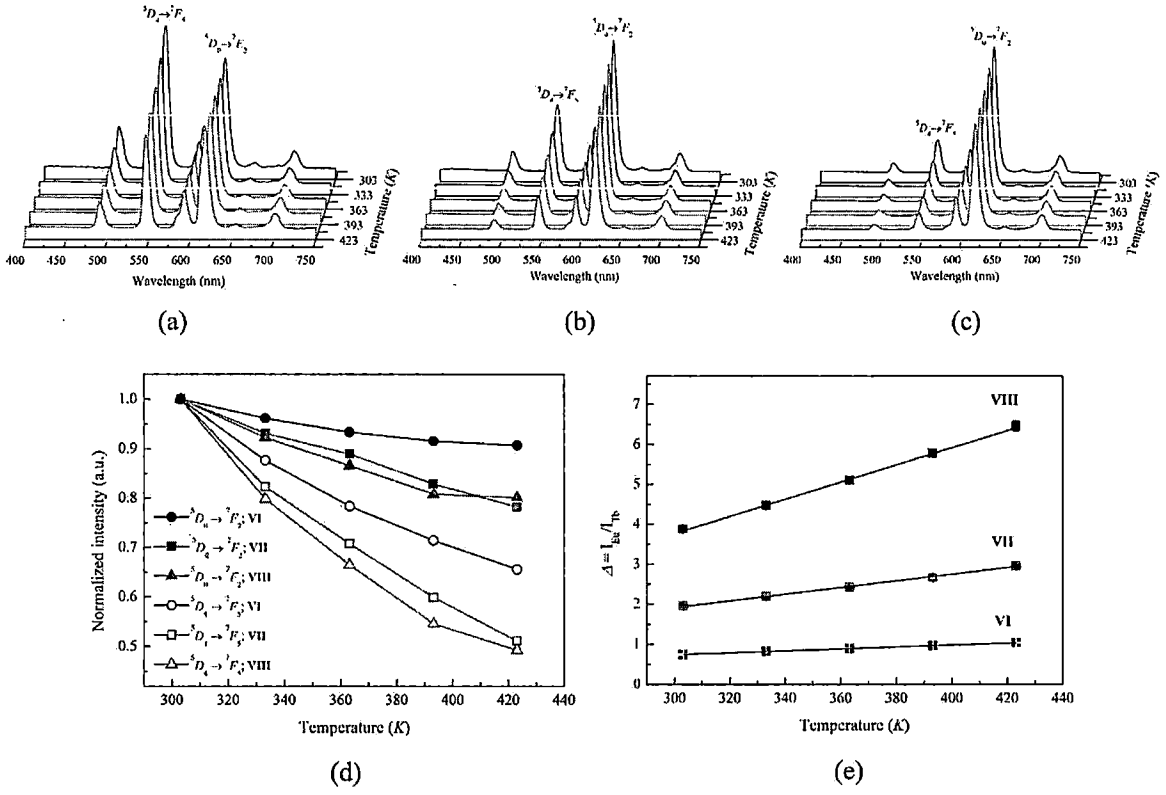

Figure 5. Temperature dependent emission spectra of (a) **VI** (b) **VII** and (c) **VIII**, with the corresponding (d) temperature dependent intensities, and (e) the calculated Δ parameters.

3.2.3 Ratiometric Temperature Sensing Potentiality of VI-VIII. Since the enlarged divergence in temperature dependent characters as found in intensity change of **VI-VIII** is a common indicator of sensitivity in ratiometric thermometry,[21] thermometric parameters (Δ) were thus calculated from intensity ratio of the red Eu^{III}:$^5D_0\rightarrow{}^7F_2$ and the green Tb^{III}: $^5D_4\rightarrow{}^7F_5$ emissions (I_{Eu}/I_{Tb}). An excellent linear correlation has been revealed for the temperature dependent Δ over the 303-423 K for **VI-VIII** (Figure 6). This correlation can be reproduced with

exceptional standard deviations. To evaluate performance of **VI-VIII** in temperature sensing, the relative sensitivity (S_r; $\%\cdot K^{-1}$) were determined, showing the reverse temperature-dependence with the maximal and the minimal S_r at 303 and 423 *K*, respectively; 0.32-0.23 $\%\cdot K^{-1}$ (**VI**), 0.42-0.28 $\%\cdot K^{-1}$ (**VII**), and 0.55-0.33 $\%\cdot K^{-1}$ (**VIII**). The highest S_r was achieved for **VIII** containing the highest content of Eu^{III}, which is an acceptor in the Tb^{III}-to-Eu^{III} energy transfer process. The S_r of **VI-VIII** were however poorer than those of the closely relevant $[Ln(ad)_{0.5}(phth)(H_2O)_2]$ containing only the $phth^{2-}$ antenna.[14] A nullifying affect imparted from the co-existing of bdc^{2-} and $phth^{2-}$ possessing different triplet state energies is therefore revealed. Accordingly, a small $\Delta\{E(^3T,bdc^{2-})-E(Tb^{III}:^5D_4)\}$ in **II** leads to a critical energy-back transfer manifested through a declining of the emission intensity, despite the presence of $phth^{2-}$. These results imply the sensitization process between each antenna and the Ln^{III} to be independent.

With reference to ten successive measurements at two different temperatures (343 and 383 *K*), the values of temperature resolution (δT) in term of percentage deviation of the temperature read outs (%) and repeatability of the measurement (R) were determined. An excellent δT of 1.36% at 343 *K* and 0.71% at 383 *K* with R >98% were achieved for **VIII**. Noticeably, better sensing performance was noticeably yielded at higher temperature.

The room temperature lifetimes (τ) were also determined from the $Eu^{III}:^5D_0\rightarrow{}^7F_2$ (τ_{Eu}) and the $Tb^{III}:^5D_4\rightarrow{}^7F_5$ (τ_{Tb}) emissions (Table 2), showing the truncated τ_{Tb} and the extended τ_{Eu} in **VI- VIII** compared with the corresponding values of **I** and **II**. The Tb^{III}-to-Eu^{III} energy transfer efficiencies (η_{ET}) in **VI-VIII** were calculated, displaying the successive enhancement in η_{ET} from **VI** to **VIII** of which approximately 81% efficiency was revealed. These results are in excellent agreement with aforementioned tendencies. In accordance with the yielded data, the crucial influence of the Tb^{III}-to-Eu^{III} energy transfer of which the efficiency depends on the Eu^{III}

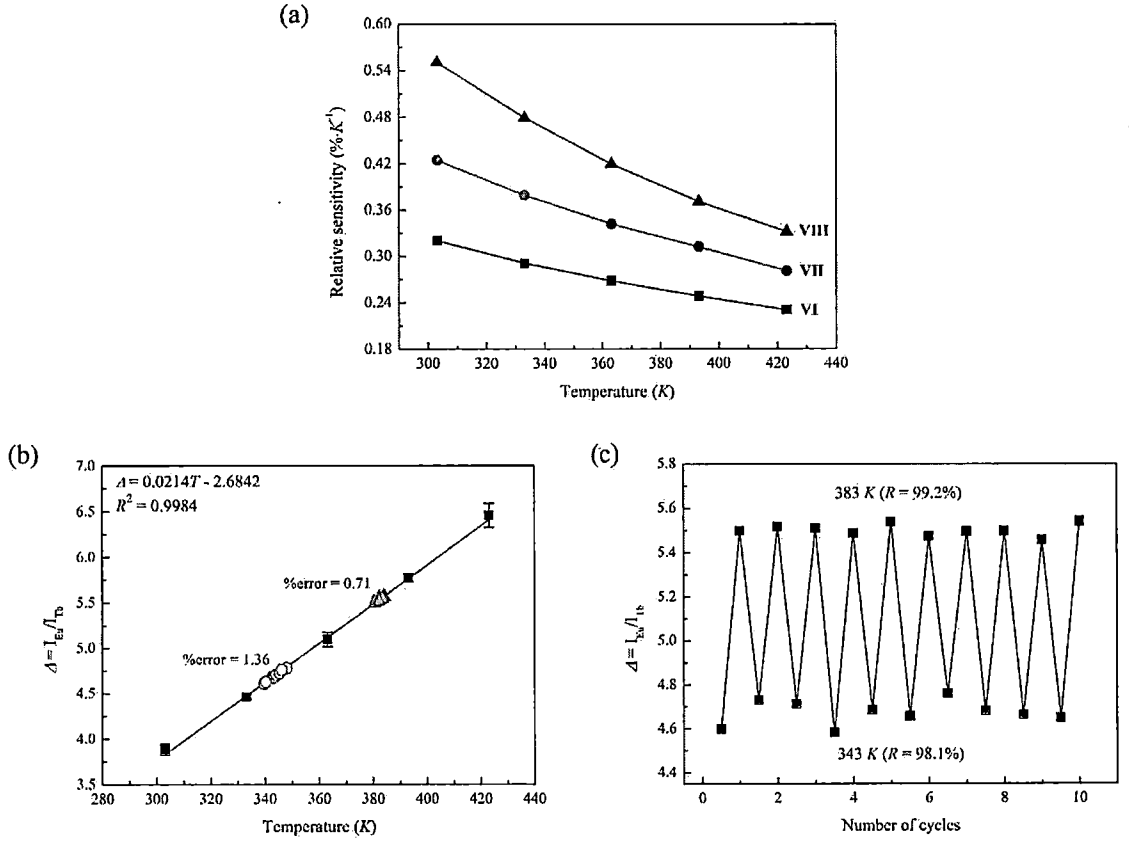

Figure 6. Depiction of (a) the temperature dependent Δ parameters of **VI-VIII**, and the sensing performance of **VIII** in terms of (b) S_r of **VI-VIII**, (c) δT, and (d) R based on ten successive measurements.

content can therefore be concluded. The promotion of the divergence in temperature dependent intensities of the two emitters and the enhanced S_r can also be accounted for. The improved η_{ET} would result in a greater loss in Tb^{III}:$^5D_4 \rightarrow {}^7F_5$ (τ_{Tb}) intensity but a gaining in Eu^{III}:$^5D_0 \rightarrow {}^7F_2$ (τ_{Eu}) intensity leading to their divergent temperature dependency. The S_r which is one of the practical parameters determining the sensing performance is consequently enhanced. This finding is consistent with previous reports on the association between the enhancement of η_{ET} and the Eu^{III}

acceptor content and the evidence for the importance of the Tb^{III}-to-Eu^{III} energy transfer to the improvement of S_r which is notably rare.[14,22,23]

4. Conclusions

Based on a series of monometallic and bimetallic $[Ln(bdc)_{0.5}(phth)(H_2O)_2]$ of which the structures are intimately relevant to $[Ln(ad)_{0.5}(phth)(H_2O)_2]$,[14] the influences of mixed bdc^{2-} and $phth^{2-}$ antennae on temperature dependent photoluminescent behaviour and temperature sensing performance were studied. Despite being effective antennae, the co-existence of $phth^{2-}$ and bdc^{2-} evidently resulted in poorer S_r compared with $[Ln(ad)_{0.5}(phth)(H_2O)_2]$ containing only $phth^{2-}$, over the same working temperature range of 303-423 *K*. The energy gap between the $E(^3T)$ of each antenna and the accepting levels of each Ln^{III} need to be separately considered. The crucial influence of the Tb^{III}-to-Eu^{III} energy transfer on S_r and its dependency on the content of Eu^{III} have been displayed. With reference to **VIII** as a representative of $[Ln(bdc)_{0.5}(phth)(H_2O)_2]$, the maximum S_r of $0.55\%\cdot K^{-1}$ was revealed at 303 *K* before deteriorating to $0.33\ \%\cdot K^{-1}$ at 423 *K*. The δT of 1.36% and 0.71% were however yielded at 343 and 383 *K*, respectively, with $R > 98\%$, indicating the characteristic temperature resolution and precision of the measurements.

ACKNOWLEDGMENT

This work is co-funded by Chiang Mai University and the Thailand Research Fund (RSA5980026). T. Chuasaard thanks the Development and Promotion of Science and Technology Talents Project for graduate scholarship.

Table 1. Crystallographic and refinement details of **I-V**

	I	II	III	IV	V
CCDC No.	1871926	1871927	1871928	1871929	1871930
Empirical formula	$C_{12}H_{10}O_8Eu$	$C_{12}H_{10}O_8Tb$	$C_{12}H_{10}O_8Ho$	$C_{12}H_{10}O_8Er$	$C_{12}H_{10}O_8Tm$
Formula weight	434.16	441.12	447.13	449.46	451.13
Crystal color	Colorless	Colorless	Pinkish orange	Pale pink	Colorless
Temperature (*K*)	293(2)	293(2)	293(2)	293(2)	293(2)
Crystal system	Triclinic	Triclinic	Triclinic	Triclinic	Triclinic
Space group	$P\bar{1}$ (No. 2)	$P\bar{1}$ (No. 2)	$P\bar{1}$ (No. 2)	$P\bar{1}$ (No. 2)	$P\bar{1}$ (No. 2)
a (Å)	6.1203(2)	6.1106(1)	6.1086(1)	6.1089(1)	6.1060(1)
b (Å)	8.8435(4)	8.8120(1)	8.7916(1)	8.7835(1)	8.7537(1)
c (Å)	12.9577(6)	12.8911(2)	12.8634(2)	12.8533(2)	12.8332(2)
α (°)	94.933(3)	94.902(1)	95.117(1)	78.447(1)	78.324(1)
β (°)	99.053(3)	99.170(1)	99.100(1)	80.964(1)	80.976(1)
γ (°)	109.493(3)	109.803(2)	110.154(1)	69.654(1)	69.728(1)
V (Å^3)	645.63(5)	637.439(18)	632.619(17)	630.671(17)	627.319(17)
Z	2	2	2	2	2
Density (Mg·m^{-3})	2.233	2.298	2.347	2.367	2.388
μ (mm^{-1})	4.896	5.586	6.293	6.693	7.111
F(000)	418	422	426	428	430
Data/Restraints/Parameters	2766/0/192	2756/0/192	2728/0/192	2723/0/192	2730/0/192
S	1.006	1.059	1.066	1.067	1.012
$R_1{}^a/wR_2{}^b$	0.0438/0.0964	0.0302/0.0615	0.0282/0.0614	0.0255/0.0468	0.0281/0.0502

$^a R_1 = \Sigma||F_o|-|F_c||/|F_o|$; $^b wR_2 = [\Sigma w(F_o^2-F_c^2)^2/\Sigma w(F_o^2)_2]^{1/2}$.

Table 2. Photoluminescent τ (ms) and η_{ET} (%) at room temperature for **I, II** and **VI-VIII**

	$\tau(Tb^{III}: {}^5D_4 \rightarrow {}^7F_5)$	$\tau(Eu^{III}: {}^5D_0 \rightarrow {}^7F_2)$	η_{ET}
I, $[Eu(bdc)_{0.5}(phth)(H_2O)_2]$	-	0.256	-
II, $[Tb(bdc)_{0.5}(phth)(H_2O)_2]$	1.17	-	-
VI, $[Eu_{0.100}Tb_{0.900}(bdc)_{0.5}(phth)(H_2O)_2]$	0.533	0.524	54.5
VII, $[Eu_{0.230}Tb_{0.770}(bdc)_{0.5}(phth)(H_2O)_2]$	0.308	0.383	73.6
VIII, $[Eu_{0.330}Tb_{0.670}(bdc)_{0.5}(phth)(H_2O)_2]$	0.222	0.389	81.0

REFERENCES

(1) McLaurin, E. J.; Bradshaw, L. R.; Gamelin, D. R. Dual-Emitting Nanoscale Temperature Sensors. *Chem. Mater.* **2013**, *25*, 1283-1292.

(2) Jaque, D.; Vetrone, F. Luminescence nanothermometry. *Nanoscale* **2012**, *4*, 4301-4326.

(3) Cui, Y.; Zhu, F.; Chen, B.; Qian, G. Metal-organic frameworks for luminescence thermometry. *Chem. Commun.* **2015**, *51*, 7420-7431.

(4) Rocha, J.; Brites, C. D. S.; Carlos, L. D. Lanthanide Organic Framework Luminescent Thermometers. *Chem. Eur. J.* **2016**, *22*, 14782-14795.

(5) Zhao, D.; Yue, D.; Jiang, K.; Zhang, L.; Li, C.; Qian, G. Isostructural Tb^{3+}/Eu^{3+} Co-Doped Metal-Organic Framework Based on Pyridine-Containing Dicarboxylate Ligands for Ratiometric Luminescence Temperature Sensing. *Inorg. Chem.* **2019**, *58*, 2637-2644.

(6) Hilder, M.; Junk, P. C.; Kynast, U. H.; Lezhnina, M. M. Spectroscopic properties of lanthanoid benzene carboxylates in the solid state: Part 1. *J. Photochem. Photobiol.* **2009**, *202*, 10-20.

(7) Latva, M.; Takalo, H.; Mukkala, V.-M.; Matachescu, C.; Rodríguez-Ubis, J. C.; Kankare, J. Correlation between the lowest triplet state energy level of the ligand and lanthanide(III) luminescence quantum yield. *J. Lumin.* **1997**, *75*, 149-169.

(8) Einkauf, J. D.; Clark, J. M.; Paulive, A.; Tanner, G. P.; de Lill, D. T. A General Model of Sensitized Luminescence in Lanthanide-Based Coordination Polymers and Metal-Organic Framework Materials. *Inorg. Chem.* **2017**, *56*, 5544-5552.

(9) Zhou, X.; Wang, H.; Jiang, S.; Xiang, G.; Tang, X.; Luo, X.; Li, L.; Zhou, X. Multifunctional Luminescent Material Eu(III) and Tb(III) Complexes with Pyridine-3,5-

Dicarboxylic Acid Linker: Crystal Structures, Tunable Emission, Energy Transfer, and Temperature Sensing. *Inorg. Chem.* **2019**, DOI: 10.1021/acs.inorgchem.8b03319.

(10) Rao, X.; Song, T.; Gao, J.; Cui, Y.; Yang, Y.; Wu, C.; Chen, B.; Qian, G. A Highly Sensitive Mixed Lanthanide Metal-Organic Framework Self-Calibrated Luminescent Thermometer. *J. Am. Chem. Soc.* **2013**, *135*, 15559-15564.

(11) Cui, Y.; Xu, H.; Yue, Y.; Guo, Z.; Yu, J.; Chen, Z.; Gao, J.; Yang, Y.; Qian, G.; Chen, B. A Luminescent Mixed-Lanthanide Metal-Organic Framework Thermometer. *J. Am. Chem. Soc.* **2012**, *134*, 3979-3982.

(12) Cui, Y.; Zou, W.; Song, R.; Yu, J.; Zhang, W.; Yang, Y.; Qian, G. A ratiometric and colorimetric luminescent thermometer over a wide temperature range based on a lanthanide coordination polymer. *Chem. Commun.* **2014**, *50*, 719-721.

(13) Liu, X.; Akerboom, S.; Jong, M. d.; Mutikainen, I.; Tanase, S.; Meijerink, A.; Bouwman, E. Mixed-Lanthanoid Metal-Organic Framework for Ratiometric Cryogenic Temperature Sensing. *Inorg. Chem.* **2015**, *54*, 11323-11329.

(14) Chuasaard, T.; Ngamjarurojana, A.; Surinwong, S.; Konno, T.; Bureekaew, S.; Rujiwatra, A. Lanthanide Coordination Polymers of Mixed Phthalate/Adipate for Ratiometric Temperature Sensing in the Upper-Intermediate Temperature Range. *Inorg. Chem.* **2018**, *57*, 2620-2630.

(15) Thirumurugan, A.; Natarajan, S. Inorganic-Organic Hybrid Compounds: Synthesis and Structures of New Metal Organic Polymers Synthesized in the Presence of Mixed Dicarboxylates. *Eur. J. Inorg. Chem.* **2004**, *2004*, 762-770.

(16) Rigaku Oxford Diffraction, *CrysAlisPRO Software System*, versions 1.171.39.46 (**2018**), Rigaku Corporation, Oxford, UK.

(17) Sheldrick, G. SHELXT - Integrated space-group and crystal-structure determination. *Acta Cryst. A* **2015**, *71*, 3-8.

(18) Dolomanov, O. V.; Bourhis, L. J.; Gildea, R. J.; Howard, J. A. K.; Puschmann, H. OLEX2: a complete structure solution, refinement and analysis program. *J. Appl. Crystallogr.* **2009**, *42*, 339-341.

(19) Bünzli, J.-C. G. In *Handbook on the Physics and Chemistry of Rare Earths*; Bünzli, J.-C. G., Pecharsky, V. K., Ed.; Elsevier: 2016; Vol. 50, pp 141-176.

(20) Peijzel, P. S.; Meijerink, A.; Wegh, R. T.; Reid, M. F.; Burdick, G. W. A complete 4fn energy level diagram for all trivalent lanthanide ions. *J. Solid State Chem.* **2005**, *178*, 448-453.

(21) Cheng, Y.; Gao, Y.; Lin, H.; Huang, F.; Wang, Y. Strategy design for ratiometric luminescence thermometry: circumventing the limitation of thermally coupled levels. *J. Mater. Chem. C* **2018**, *6*, 7462-7478.

(22) Zhou, J.; Xia, Z. Multi-color emission evolution and energy transfer behavior of $La_3GaGe_5O_{16}$:Tb^{3+},Eu^{3+} phosphors. *J. Mater. Chem. C* **2014**, *2*, 6978-6984.

(23) Baur, F.; Glocker, F.; Jüstel, T. Photoluminescence and energy transfer rates and efficiencies in Eu^{3+} activated $Tb_2Mo_3O_{12}$. *J. Mater. Chem. C* **2015**, *3*, 2054-2064.

ASSOCIATED CONTENT

Supporting Information.

The Supporting Information is available free of charge on the ACS Publications website at DOI: 10.1039/x0xx00000x.

Coordination modes of $phth^{2-}$ and bdc^{2-} ligands, PXRD patterns, room temperature photoluminescent spectrum of **IX**, and EDXA spectra (PDF). X-ray crystallographic data for five complexes (**I-V**) (CIF).

CCDC 1871926-1871930.

AUTHOR INFORMATION

Corresponding Author

apinpus.rujiwatra@cmu.ac.th

Notes

The authors declare no competing financial interest.

ACKNOWLEDGMENT

This work is co-funded by the Thailand Research Fund (RSA5980026) and Chiang Mai University. T. Chuasaard thanks the Development and Promotion of Science and Technology Talents Project for graduate scholarship.

For Table of Contents Only

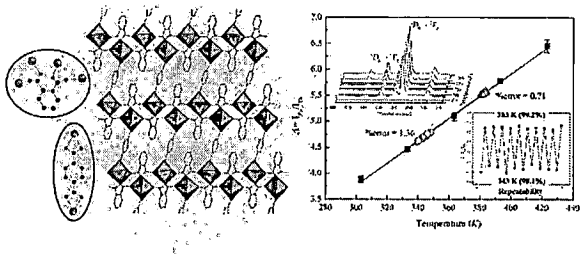

Two-dimensional polymorphism in lanthanide coordination network
and effect of mixed-benzenedicarboxylate antennae on ratiometric temperature sensing